A scoping analysis of the neutronic design for a new South African research reactor

JIC Vermaak

Thesis submitted in partial fulfilment of the requirements for the degree *Master of Engineering in Nuclear Engineering* at the Potchefstroom campus of the North-West University

Supervisors: Mr. S Korochinsky
Prof. E Mulder

November 2011

PREFACE

With any analysis, the representation of one's work is often contained only within the results. This makes it very difficult to indicate the amount of work, innovation and skill that went into this analysis. For this purpose I urge the reader of this thesis to consider the considerable knowledge- and skill base required to operate codes such as MCNP5 and OSCAR-4. Only after I mastered these codes was I able to study the truly wonderful effects of different nuclear fission reactor design concepts. In many ways this thesis only represents halve the knowledge gained during this whole experience, with the other halve being the mastery of the tools needed to make me a true master of nuclear engineering.

The process started with MCNP5 where we speculated how to specify realistic burnup profiles, which led me, out of pure curiosity, to experiment with the history files of OSCAR-4. I quickly became frustrated with the repetitive nature of interfacing with text files and wrote the first of a collection of FORTRAN algorithms to both extract and compile OSCAR-4 data. Soon after, the FORTRAN algorithms proved cumbersome in their own way since I still had to interface with them through a text base console, which led me to explore the VB-script route and Microsoft Excel 2007 as a visual interface. For every piece of cumbersome, repetitive and non-automated action, I wrote an algorithm, usually not pro-actively but as a response to impatiently editing a text file to study the effect of a parameter. After a while, the collection of algorithms grew so complete that the technical fog of interfacing with the codes disappeared and I could focus on the pure nuclear engineering of the analysis. In this aspect I discovered the true value of the OSCAR-4 code system, which I must say is a wonderful tool for any nuclear engineer. The value this thesis added to my career cannot be captured in a report of any kind. I have learned in these last three years that it is not necessarily the physical mathematics and data that makes you a nuclear engineer but the virtual reactor maintained in your mind, as well as the understanding that goes with it. In this light I would like to express my gratitude for the environment in which I could conduct my studies; an environment filled with the greatest minds in this country, if not the world.

Having expressed the technical satiety I gained from this thesis, I would also like to thank all the people that were involved: Sergio Korochinsky, for essentially giving me free reigns to explore, like a child discovering a new world, and for encouraging and appraising my efforts at every point. Together I think we have re-established that science is fun and that learning is the best form of entertainment. I would also like to express my gratitude to my father, not

only for his support, which was immense, but for being my role model since I could remember. I am truly proud to tread in his legacy.

Also, I would like to thank the rest of my family, who had to endure weekend upon weekend of me spending time in front of the computer and trying to explain exciting stuff, of which they had no idea.

ABSTRACT

Together with many other research reactors around the world, the SAFARI-1 reactor has been classified as an ageing research reactor. In order to continue the provision of the current irradiation services, the operator of the reactor, NECSA, needs to consider the replacement of SAFARI-1 with a new large neutron source, and therefore ultimately a new reactor.

A replacement research reactor will have to provide irradiation services that primarily include: radio-isotope production, thermal- and cold neutron beamlines, NTD and material testing. With these specifications, a number of additional design parameters were specified which involved: the fuel design, core layout and beamline layout. The design of the reactor fuel was required to be equivalent to the current plate type MTR-type fuel primarily due to the existing infrastructure for this design. Additionally, the fuel material was specified as uranium-silicide dispersoid (U_3Si_2) in order to support the high uranium-loading required for LEU-fuel. The core layout was ranged from a small 4 by 4 core to a large 9 by 9 core with different amounts of in-core irradiation positions, reflector types and reflector regions (high leakage zones). The neutron beamline designs were varied to investigate the effects of radial orientation.

The design aspects were investigated by utilizing the OSCAR-4 code collection and MCNP5. Two additional software applications, called KNERSIS and MAAS, were developed: one for the automation of the MGRAC code (part of OSCAR-4); and the other for the interface of data between MGRAC and MCNP5. With this collection of software, a number of design iterations could be performed in rapid succession which included elimination of power peaks, optimization of discharge burnup, optimal reload patterns, equilibrium cycle analysis and accurate isotope inventories (with correct burnup profiles) for use in MCNP5.

The study of the fuel design parameters found that for an increased uranium loading per assembly, the reactive life was increased. This increased loading can be achieved by means of a thicker fuel “meat” section, more fuel plates per assembly or a higher uranium-loading fuel material such as uranium 2wt% molybdenum. The reactivity was shown to be weakly dependant on all three these parameters due to the effect of the moderator to fuel ratio.

The study of the radial orientation of beamlines indicated that the epi-thermal- and fast neutron-, as well photon-, output currents from beamlines can effectively be reduced by orientating the beamlines tangentially, an aspect which can reduce beamline noise.

With a fixed fuel design, the study of different core layouts principally shown that the ex-core thermal neutron flux per unit power is inversely proportional to the size of the core design while the total in-core irradiation capacity indicated the opposite.

The investigated parameters allowed for the recommendation of a core design which, for purposes of providing the primary irradiation services, is a medium sized core with sufficient amount of in-core irradiation positions, a heavy water reflector and tangentially orientated thermal- and cold neutron beamlines.

TABLE OF CONTENTS

LIST OF FIGURES

LIST OF TABLES

CHAPTER 1 INTRODUCTION

1.1 BACKGROUND

The first South African Fundamental Atomic Research Installation (SAFARI-1) has been in operation since 1965 when it was commissioned as a research facility. However, during the 1990's the reactor's specialization changed to that of isotope production with the development of in-core irradiation equipment which produces valuable radio-isotopes, making the reactor a fundamental contributor to the worldwide medical isotope industry (IAEA-RRDB, 2011). The reactor is of a Materials Testing Reactor type (MTR) and operates at a nominal thermal power of 20 MW for three- or four-week cycles after which maintenance and reloading operations are performed on it for 5 days. SAFARI-1 is classified as an ageing reactor, and together with factors like the obsolescence of technology and a change in nuclear safety standards (containment building, routing of cables, etc.) the operator of the reactor, the South African Nuclear Energy Corporation (NECSA), needs to evaluate the requirements for another MTR to replace or upgrade SAFARI-1 as part of a feasibility study for a new large neutron source[1].

An integral part of such an evaluation is to determine whether a new large neutron source can attain a level of capacity coherent with the needs of its operator (NECSA), subsidiaries of the operator (such as Nuclear Technology Products, NTP, which processes and delivers all nuclear products), researchers and other users both at present and in future. One of the many characteristics which constitute the capacity of a MTR-type reactor to fulfil the role of a large neutron source is the neutronic design both inside and outside the reactor; and therefore an incentive to determine certain reactor parameters was born. This study therefore pertained to the investigation of preliminary neutronic-design parameters.

[1] Neutron sources can include fission reactors and some high-energy particle accelerators, however, for a capacity equivalent to what SAFARI-1 currently produces, a fission reactor ought to be the source of choice.

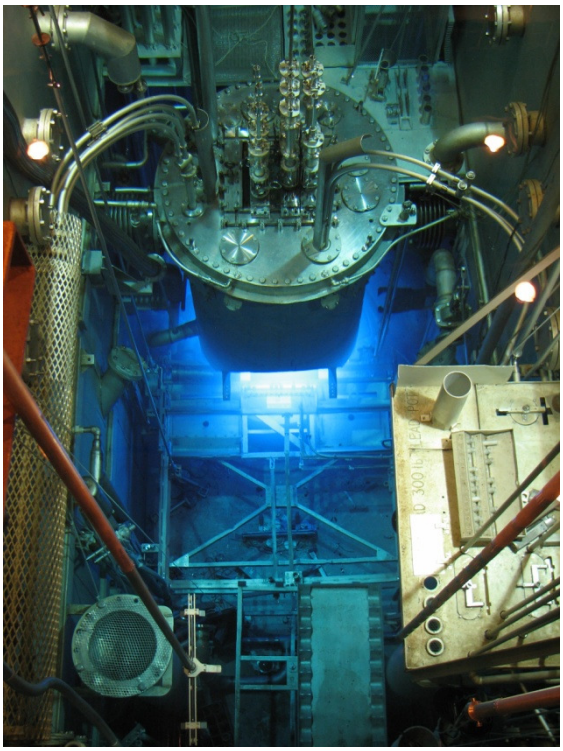

Figure 1 A photograph of the reactor vessel for the SAFARI-1 20 MW nuclear research reactor.

1.2 NUCLEAR RESEARCH REACTOR NEEDS IN SOUTH AFRICA

This section summarizes the requirements within South Africa with regards to the facilities provided by a nuclear research reactor as contained in the preliminary feasibility study for a new large neutron source.

1.2.1 Isotope production

At present the largest consumer of radio-isotopes in the world is the medical industry, which forms an estimated USD3.7 billion industry worldwide (Kahn, 2008), to which the NECSA subsidiary, NTP, contributes a great deal each year. This industry alone requires a major share in the isotope production capability especially that of the production of the valuable isotope ^{99m}Tc, which is used world-wide in diagnostic imaging techniques. Also, other medical isotopes used for treatment, for example the activation of tellurium (Te) and yttrium (Y), which are used to treat thyroid- and liver-illnesses respectively, form part of the production requirements.

1.2.2 Neutron Transmutation Doping (NTD)

A number of complex chemical processes at present are used to produce materials with special- properties, crystal structures and electrical properties. One such material is silicon, in its pure crystalline form, silicone acts almost entirely as an insulator of electricity, however, adding impurities like phosphorous to the crystal structure greatly enhances its semi-conductive properties, essential for use in transistors. These impurities can be included by means of either complex chemical methods or by neutron transmutation doping (NTD). NTD is achieved by means of the radiative capture of a neutron by ^{30}Si (one of the natural isotopes of silicon) whereby unstable ^{31}Si is formed and subsequently β-decays to stable ^{31}P. NTD is a capability for which the need has expanded in the last 10 years and which will continue to do so well into the future and will therefore form an integral part of the use of a MTR.

1.2.3 High neutron-flux material irradiations

The fundamental definition of a Material Testing Reactor inherently includes the testing of materials in a high neutron flux environment. This function includes the irradiation of power reactor fuel prototypes, neutron induced damage studies and long term material transmutation research. In order to maintain this capability, certain design aspects, such as the ability to add complex material testing rigs where pressure, water chemistry and temperature can be controlled, had to be taken into consideration.

1.2.4 Gamma (photon) irradiation facilities

Materials, machines and electronics can be sensitive to gamma radiation. Consequently, gamma[2] irradiation testing of components is a frequent request at any MTR. The SAFARI-1 reactor furnishes a wide array of gamma irradiation facilities which will need to be duplicated in a replacement reactor, or an equivalent thereof.

1.2.5 Thermal neutron beamline facilities

SAFARI-1 furnishes six thermal neutron beam tubes in which a thermal neutron beamline capacity is supplied to both research efforts within NECSA as well as external facilities. Thermal neutron beamlines provide a wide array of possible experiments, ranging from archeology (De Beer et al., 2009) to industrial applications (De Beer, 2005). This functionality not only supports NECSA's mandate (of nuclear research) but also provides

[2] Gamma radiation is used interchangeably to refer to photon radiation. Other variations can include: ϒ-radiation, gamma flux and photon flux.

research platforms for South African universities and therefore, a South African research reactor without thermal neutron beamline facilities would be incomplete.

1.2.6 Cold neutron beamline facilities

By thermalizing neutrons to energies much lower than the nominal upper limit of 0.625 eV; the wavelength[3] of the neutrons, measured in angstrom, Å, can be increased to within the same order of the inter-atomic or inter-molecular distances found in solid materials. Besides the higher reaction rates at low energies (less than 5 meV, (Flocchini et al., 2007)), material micro-structures can be studied due to the neutron diffraction properties of materials at such energies. Although such core technologies do not currently exist in South Africa, the rapid growth in requirements for such research prompts the consideration of a cold neutron beamline facility. Such a facility might however, require specialized design considerations pre-emptive to the design effort (might fundamentally influence the core design), especially if one considers the immense amount of structural infrastructure required for a cold neutron source. Therefore a cold neutron beamline facility needs to be evaluated.

[3] As is the case with other quantum particles; neutrons exhibit both a particle- and a wave behavior. At low energies, the wave behavior of a neutron becomes prevalent and needs to be considered during the analysis of nuclear reactions.

1.3 ASPECTS CONSIDERED

When studying the design of a nuclear fission reactor, at both conceptual- and detail level, it is important to appropriately demarcate the field of study because of the many possible design routes that can appear in modern reactor designs. The first design branch is the purpose of the reactor; more specifically, the question of whether it will primarily produce thermal power (for heat input) or nuclear radiation (neutron-flux, photon-flux, etc.). It is clear that with the mention of the term “research reactor”, the scope of the study was focused towards the selection of the fundamental design concept that will optimize the reactor as a radiation source.

The fundamental design concept governing the optimal capacity of a reactor to produce radiation is the volumetric power density ($W.cm^{-3}$), and originates from the fact that for a given macroscopic fission cross-section (Σ_f), the volumetric energy release is a linear function of the neutron flux (ϕ); in other words, higher flux results in higher reaction rates ($\Sigma_f \cdot \phi$) which generates more power density. Therefore, in order to realize an increase in neutron flux, the volumetric power density needs to be increased; however, this linear increase is limited by the ability of the structure (referring to the heat generating component) to dissipate heat to the coolant. Consequently, the maximum volumetric power density is dependent on the fuel structure and the coolant flow configuration.

1.3.1 Fuel structure

When a fuel structure is selected, which is done primarily from a manufacturability point of view, but also considering heat transfer and structural integrity, the controllable parameter becomes the coolant flow rate (i.e. more flow, results in more surface convection). The effective flow velocity has however, a negative feedback-loop on structural integrity where vibration, drag and pressure drops pose limitations (Miller, 1958). Thus the selection of the fuel structure becomes the first design consideration as it will indirectly define the maximum coolant flow rate, which together with the fuel structure will define the maximum fuel material temperature and therefore the attainable power levels. For this study, a plate-type structure was selected as the fuel structure; primarily because of the experience the operator (NECSA) has with this structure type but also because of considerations including: the existing infrastructure developed during the operation of SAFARI-1, the manufacturability of plate-type structures, heat-dissipation characteristics (i.e. thin plates), and the extensive knowledge-base available for this specific structure type.

1.3.2 Coolant flow rate

As mentioned in the previous section, with the fuel structure established, the maximum coolant flow rate could be determined. This is a convenient selection parameter since the cooling system would not yet have featured in the design. Normally, when establishing the maximum power of a reactor, the coolant system's design is fixed. For this study, the maximum coolant velocity was determined by using a well known reference in the research reactor community; "Critical Flow Velocities for Collapse of Reactor Parallel-Plate Fuel Assemblies" (Miller, 1958), which was a study done by the Knolls Atomic Power Laboratory for General Electric. For each fuel plate thickness and coolant gap configuration, the maximum velocity was determined from the correlations contained in this reference.

1.3.3 Fuel material

With the fuel structure selected, the design aspects of the reactor could be grouped into a large pool of inter-dependant parameters, each of which needed to be considered carefully. However, in-line with completing the selection of the fuel structure one can also evaluate the fuel "meat" material. The fuel "meat" is a term used to refer to the component of a fuel plate containing the uranium fuel. For this study, uranium-silicide was used as a fuel material. This selection is supported by large amounts of data collected during the roll-out of the Reduced Enrichment for Research and Test Reactors (RERTR) program (ANL, 2012), which required a higher uranium-density fuel-material to offset the reduced reactivity effects of converting from High Enriched Uranium (HEU) to Low Enriched Uranium (LEU); as well as a large manufacturing infrastructure both locally and abroad. The characteristics of a single uranium-molybdenum fuel material was evaluated but not used for any core configuration design since it is still largely unproven as a suitable fuel material. The effects of burnable absorbers were also evaluated but not used since it involves analyses associated with a more detailed study of the reactor design.

1.3.4 Fuel uranium content

A major aspect to consider during fuel design is the uranium content per fuel assembly[4]. The primary aspect governing this quantity, namely the ^{235}U enrichment, is normally required to be as high as possible in order to ensure maximum reactivity with minimal dimensional requirements. However, in order to comply with the regulations passed by the Reduced Enrichment for Research and Test Reactors (RERTR) program, a maximum ^{235}U enrichment

[4] A fuel assembly comprises a number of fuel elements which are assembled into a certain structure which rigidly supports the constituent parts. In the case of plate type fuel assemblies, the individual fuel plates form the fuel elements.

of 19.75 wt% may be used. Therefore, within the scope of this enrichment specification, the uranium content per assembly can be altered, for plate type fuel, mainly by means of two distinct methods: increasing the amount of fuel plates per assembly and increasing the fuel meat thickness.

For this study, different fuel plate uranium content designs were studied by defining both a thick- and thin-meat plate configuration for a given amount of fuel plates. An important aspect that arises when changing the number of fuel plates however, is the effect of the dimensional requirements of the assembly on the moderator-to-fuel ratio and heat-dissipation ability of the design where an increase in the number of fuel plates will inadvertently decrease the coolant (also moderator) gap-size. For this study, a maximum of 21 fuel plates were used which represented a good all-round fuel assembly which will fit into the conventional 8 cm square lateral and longitudinal dimensions (2D dimensions), without too great a reduction in coolant gap-size. Together with a meat-thickness of 0.061 cm and the previously mentioned uranium-silicide fuel material (with 4.6 $gU.cm^{-3}$) the resulting fuel assembly mass is approximately 476 g ^{235}U per assembly, which is almost equivalent to the approximate 480 g used in the Australian OPAL reactor (Irwin & De Lorenzo, 2007) and half-way between the 340 g ^{235}U 19 plate fuel assemblies used in SAFARI-1 and the 550 g ^{235}U 20 curved plate fuel as used in the HFR-Petten reactor (Thijssen, 2006).

1.3.5 Control devices

Similar to the many design routes that can be followed for the overall reactor design is that of the control device design. Choices for the basic mechanism range from thin rod-type devices to the more conventional fuel follower type. In this study the follower-type control devices were used primarily because it provided a well known reactivity worth (6 control assemblies for approximately every 30 fuel assemblies) but also because it does not introduce additional difficulty for nodalization in the OSCAR-4 package (Stander & et.al., 2008), which ideally requires row and column heights to be equal throughout (equally spaced nodes). Natural cadmium was used as the absorber material for the control assemblies; however, the study did not encompass the analysis of including different absorber materials like silver (Ag), indium (In), hafnium (Hf) or gadolinium (Gd); all of which entails an additional economical and material processing evaluation.

1.3.6 Reflector material

Materials nominally used as a neutron reflector range between the basic choices of graphite, beryllium (often in combination with light water) and heavy water. For the purpose of this

study the heavy water and beryllium choices were applied; however, the neutronic properties of each type were evaluated in the core design study. General considerations included (besides the neutronic properties): the cost of a specific reflector (i.e. expensive maintenance costs of heavy water), the required size thereof (beryllium compared to graphite) as well as the ability to incorporate experiments or beamlines. For beryllium and graphite reflectors one also needs to consider the solid state of the material, posing both a heating- and spatial logistics[5] concern.

1.3.7 Reactor fuel economy and operation

With the fuel design established and a suitable reflector material selected, the reactor vessel interior detail could in principle be fixed, while the focus could be turned towards only the core configuration design. In this study, realistic core uranium mass distributions (as well as fission product distributions) were assembled by first modeling each core design in the OSCAR-4 package, then in the more accurate flux estimation code MCNP5 (MCNP5: MCNP. X-5 Monte Carlo Team, 2003). This allowed the assembly of an equilibrium core burnup- and fission-product profile whilst simultaneously providing insight into the conceptual economic considerations associated with the fuel- and control assemblies.

1.3.8 In-core irradiation positions

In-core irradiation positions, in practice, are seldom operated without some type of rigging arrangement, which might alter the thermal neutron flux conditions that exist without any rigging arrangement. In this study however, the in-core capacity for each design needed to be approached methodically and therefore all in-core irradiation positions were modeled as assemblies containing nothing but light water.

1.3.9 Ex-core irradiation positions

In reality, the inclusion of irradiation positions, or any kind of neutron absorbing item, in the reflector region of a core will ultimately introduce a flux distribution change and have an effect on the core's overall reactivity. For this study, the typical flux depressions associated with experiments, either due to their absorbing nature, or due to the amount of effective moderator they displace, were not modeled; instead, the reflector tank used in the study was not changed for each core design and therefore provided a firm base of comparison. Also,

[5] The surroundings of a fission reactor are normally heated by energy deposited from photon radiation; this heat needs to be removed by a coolant flow in order to limit the temperature of the components. Also, when a solid material is used as a reflector and an experiment needs to be placed inside it, the component must either have a removable section, into which the experiment can be incorporated, or must be removable.

the effect of beamlines in the reflector ought to reflect on the characteristics of the designs (especially where beamlines are numerous), however, this effect was not analyzed.

1.4 SUMMARY

This chapter established the need to investigate the parameters of a nuclear fission reactor to replace the ageing SAFARI-1 reactor. It then motivated the possible requirements of such a replacement as well as the aspects that formed the field of study. The next chapter details the development of these design aspects into more concise technical specifications which can be used, together with the calculation methods, to study the relevant parameters of the neutronic design of the reactor.

CHAPTER 2 DESIGN PARAMETERS

The neutronic design of a research reactor core, in general, can be a diverse study of different technologies; some of which have been proven, and some of which are in the process of gaining recognition. However, the fundamental areas of the neutronic design of modern research reactors remain the same and can be simplified to; the type of fuel design used, the configuration of the core and finally the characteristics of the irradiation facilities. Worldwide, many research reactors have employed different technologies in each of these areas and for this study it was important to select technologies most suited to the established nuclear industry in South Africa.

Fuel assembly technology can range from annular fuel designs, as used in the High Flux Isotope Reactor (Xoubi N., 2004), to the pin type fuel used in TRIGA reactors (Bakkari et al., 2010); however, one cannot forego the considerable operational experience and established infrastructure concurrent with the use of plate-type Materials Testing Reactor (MTR) type fuel used in the SAFARI-1 reactor for more than 45 years. Additionally, many other research reactors (not in South Africa) also use plate-type MTR fuel and consequently a large industrial infrastructure exists abroad in support of the constant supply surrounding this fuel design (AREVA, CERCA, etc.). Section 2.1 overviews the establishment of the parameters that can be fixed during the consideration of the fuel design.

A research reactor's core configuration[6] is often a dynamically changing aspect of the reactor operation due to constantly changing requirements; however, the basic technology selection involves a combination of two principal technologies: reactors utilizing ex-core[7] neutron leakage exclusively (so called inverse flux-trap designs) and reactors utilizing in-core irradiation exclusively. There are of course reactors that operate with a combination of these technologies, of which the SAFARI-1 reactor is a suitable example. As shown in figure 2, the core is largely reflected with beryllium reflector assemblies, the only exception being the northern face which is in direct contact with the reactor vessel. This face provides a large leakage-based source of neutrons and transforms the SAFARI-1 core into a combination of the before mentioned technologies. Section 2.2 provides an overview of the parameters relating to the core configuration technology.

[6] Core configuration refers to physical arrangement of fuel assemblies, control assemblies and in-core irradiation positions.
[7] Ex-core is a term used to refer to the region outside the core boundary and may include both the reflector and the blanket region.

Section 2.3 overviews the aspects determining the use of modern neutron beam facilities.

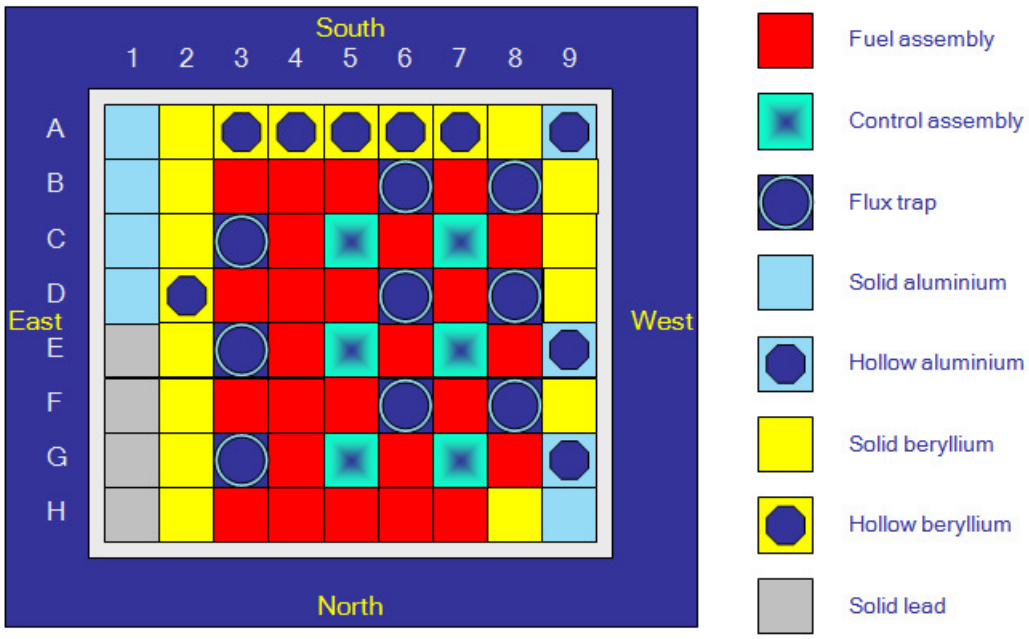

Figure 2 Schematic of a typical SAFARI-1 core configuration **(RR-SAR-0005, 2008)**.

2.1 FUEL DESIGN

The more important parameters in the design of the MTR-type fuel assemblies are the number of fuel plates and associated ^{235}U loading per plate; however, many other generic parameters can be pre-selected without an associated study for each. Therefore, a baseline fuel design could be selected together with a collection of fixed parameters and is detailed in section 2.1.1.

The first parameter to be considered is the overall size of the fuel assembly which is primarily governed by strength versus slenderness considerations but also modularity and over-all core dimensions (defining assembly height from a volume-to-surface ratio). Secondly, the materials have to be selected which fundamentally define the fuel design's structural- and thermal performance. Other parameters also include the fuel meat material, coolant gap size, number of plates and total plate thicknesses. The following sections detail the consideration of both fixed and variable parameters used during the study.

2.1.1 A baseline fuel assembly design

As a baseline design, the SAFARI-1 LEU uranium-silicide fuel assembly design is used in order to limit the scope of the design to the fuel plates only. The fuel assembly is of a general MTR-type and consists of a number of plates arranged in a rectangular geometry with a top and bottom end-adapter, as shown in figure 3.

The fuel plates contained in the base-line assembly design are swaged into grooves within the aluminium-alloy side plates, which essentially bounds the assembly of the active fuel region. The plates used for the assembly are of two types: inner plates and outer plates. Both types of plates consist of an aluminium-alloy cladding and an internal fuel material section termed the “meat”. The cladding provides confinement of fission products as well as heat transfer from the fuel to the coolant. For the outer plates, the upper and lower inactive sections of the cladding are slightly longer in order to form a closed assembly box.

The end-adapters of the assembly are also of an aluminium-alloy and are welded to the top and bottom of the active fuel region where they serve the purpose of firstly, locating the fuel assembly within a seating grid (bottom adapter) and secondly, to provide a means of handling the assembly (top adapter). Due to the relatively low concentration of impurities (usually contained in the alloying elements), these end adaptors do not suffer much neutron activation and can be removed from spent fuel assemblies in order to minimize radio-active waste volume (a process known as cropping).

The approximately square 8 cm by 8 cm lateral and longitudinal dimensions of this fuel assembly design is commonly used by MTR’s because of its strength and modularity which has been established as satisfactory over a period of many years. The specific dimensions can be justified from a collection of viewpoints:

i) MTR-type cores require certain degrees of modularity in order to alter core power distribution, refueling and planning. Therefore, fuel assemblies must be small in order to provide more loading combinations, however, if the assemblies are too small, assemblies will be numerous and the complexity of fuel shuffling during refueling or handling will increase. Additionally, cores that have too large a degree of modularity will inevitably have very slender assemblies which pose concerns regarding stiffness and fragility of the assemblies. With a core cross-sectional geometry of 56 cm wide and 56 cm long (typical for a MTR core), an 8 cm by 8 cm assembly will provide 49 modular positions with which to arrange a core configuration.

ii) MTR-type fuel assemblies utilize plate type fuel. If plates are too slender (i.e. much longer than they are wide), they have no stiffness and are fragile to handle. When the plates are wide, they are easy to manufacture but penalize modularity and stability under flow conditions; conversely, if they are very narrow, they are harder to manufacture and become slender. An 8 cm wide plate, 0.127 cm thick and 70 cm tall provides for suitable manufacturability as well as structural integrity.

iii) Fuel assemblies must provide a certain ratio of moderator to fuel (heterogeneity) which is facilitated by coolant gaps. The nature of the gaps spaces fuel plates an optimal distance from each other which defines the longitudinal character of the core. When such a core is then modularized into a matrix, 8 cm by 8 cm assemblies, it provides for realistic manufacturing whilst also facilitating the required modularity.

Fuel plate geometry is dependent on many design factors stretching from neutronics to manufacturability. The height of the fuel plates is specified to be identical to that of fuel plates used in SAFARI-1 fuel assemblies and can be justified in consideration of a finite cylinder or parallelepiped, which needs to comply with the surface area to volume ratio optimizations in order to provide for maximum reactivity.

The non-fuel materials are all of a certain aluminium-alloy which varies according to the function of each component. The choice of aluminium-alloys as a material for non-fuel components is a common design-choice for many MTR-designs and can be justified as follows:

i) Aluminium-alloys are a low cost, low neutron absorption cross-section material with desirable mechanical properties at the nominal operating temperatures of typical MTR's. The alternate option, Zircaloy, also exhibits desirable neutronic properties but is more expensive both in monetary- and manufacturability terms.

ii) MTR's require a high power density (thermal power per unit volume of fuel material) in the order of 1880 $MW.m^{-3}$ in comparison to that of typical PWR power densities of approximately 260 $MW.m^{-3}$ (Duderstadt & Hamilton, 1976). This requires adequate heat removal from the meat which can be accomplished with thin plate type elements covered with a material with good thermal conductivity, k, for which aluminium-alloys are well suited. Aluminium-alloys have a thermal conductivity of

nominally 180 $W.m^{-1}.K^{-1}$ (Cengel, 2006) in comparison to that of Zircaloy (used in power reactors) which is less than 10 $W.m^{-1}.K^{-1}$ (Lamarsh & Baratha, 2001). Additionally, in order to limit fuel temperatures (which also impacts reactivity), heat generating volumes need to be as thin or narrow as possible in order to maximize the heat diffusivity over the power generating profile, which can effectively be facilitated by plate type fuel. Also, plate type fuel can be easily constructed utilizing aluminium.

iii) Being that the assembly elements are of plate type, aluminium possesses optimal ductility and yielding strength to be able to perform a cladding function whilst also not posing manufacturing difficulties or, material degradation during neutron irradiation.

A selection of baseline material properties are shown in table 1.

Table 1 Material specifications for the SAFARI-1 19 plate LEU uranium-silicide fuel assemblies with a ^{235}U loading of 340 grams per assembly **(RR-SAR-0005, 2008)(RR-TGL-1103, 2003)**.

Description	Parameter value
Material types	
Fuel material	Uranium-silicide (U_3Si_2) dispersed in Aluminium
Cladding and side plate material	Aluminium alloy AG3 NE
Assembly adapter material	Aluminium alloy 6082-T6
Fuel material composition	
Uranium-density (g/cm^3)	4.8 (4.6 used for this study)
^{235}U mass per element (g) *^{235}U mass per plate (g)*	340.1 *17.9*
Total uranium mass per element (g) *Total uranium mass per plate (g)*	1722.0 *90.63*

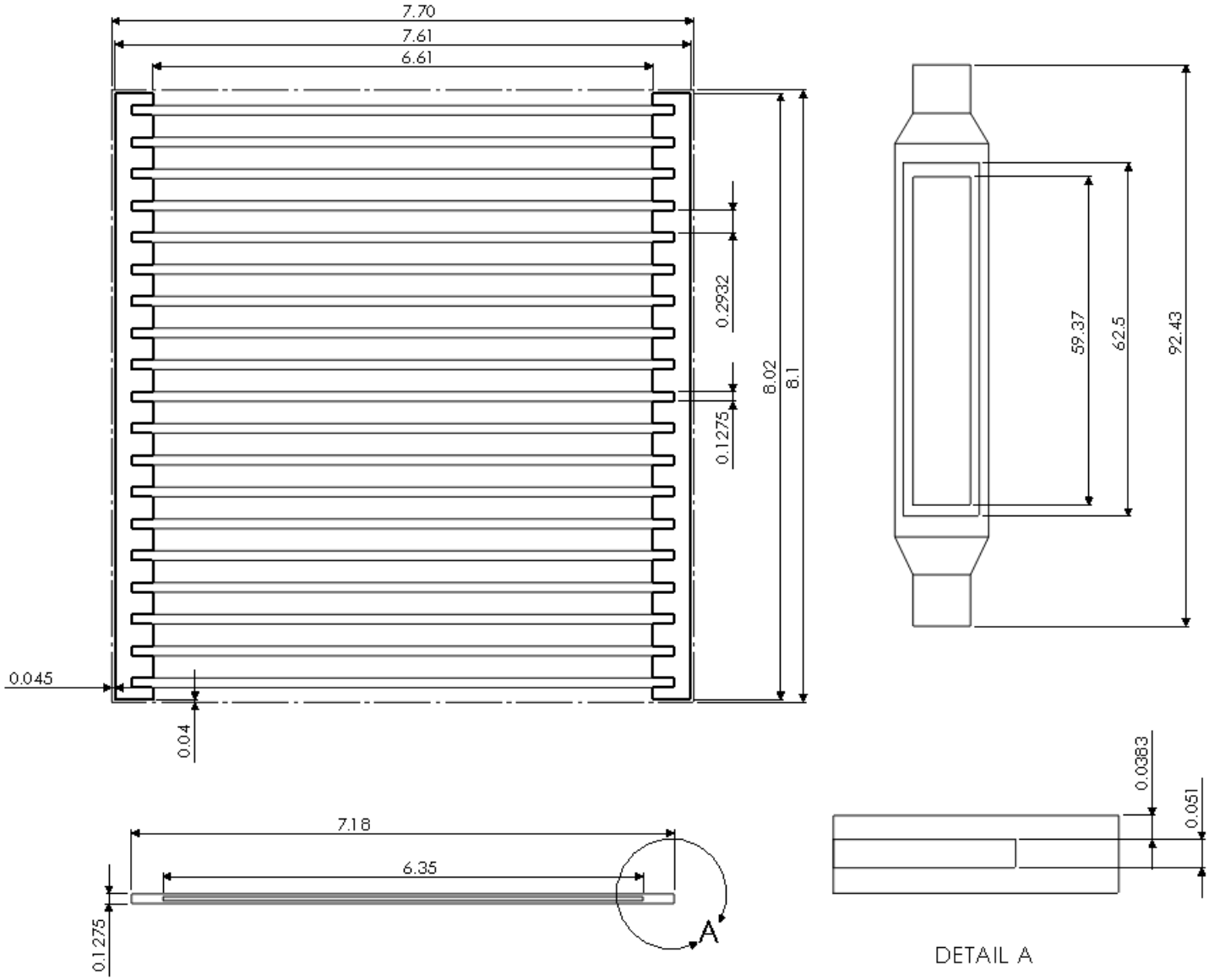

Figure 3 Schematic of a SAFARI-1 fuel assembly (RR-SAR-0005, 2008) (RR-TGL-1103, 2003).

2.1.2 Fixed fuel design parameters

With the base-line fuel design established, this section continues to detail parameters which could be fixed during the study.

Fuel material and uranium-density

With the establishment of the Reduced Enrichment for Research and Test Reactors (RERTR) program, and its non-proliferation goal, it has become necessary around the world for research reactors to use higher uranium-loading fuel materials. The increased uranium loading is necessary because the fissile properties of the fuel must remain relatively

unchanged. This entails that the amount of ^{235}U must be kept equivalent[8] to the previously used enrichment, which necessitates the loading of more total uranium to achieve less than 20% ^{235}U enrichment. However, the heat transfer characteristics (i.e. fuel centerline temperature) provided by thin fuel plates with high enrichment needs to be preserved and consequently the increase in fuel meat volume needs to be limited, which necessitates the use of a fuel material allowing a higher uranium-density.

According to a study (Finlay et al., 2004), material compositions which allow high uranium-density includes U_3SiAl, USi, U_3Si_2, U_3Si, U_6Mn and U_6Fe; however, of these compositions the silicide compounds exhibit both desirable neutronic characteristics and irradiation stability (IAEA-TECDOC-643, 1992). The study by Finlay (2004) found that the U_3Si_2 compositions demonstrated the least fuel particle swelling brought on by the build-up of fission-gas bubbles and exhibits a crystalline to amorphous transformation of its metallurgical structure, further enhancing its swelling resistance at higher burnup. Therefore it is concluded that U_3Si_2 is the high uranium-loading composition of choice with regards to irradiation behavior.

The maximum uranium-density that can be achieved with the U_3Si_2-compound is mostly limited by manufacturing processes, with arc or induction melting providing densities up to 6 gU/cm^3 (Sinha et al., 2008). However, with the major research reactor fuel manufacturers focused on the much less complicated process of the production of U_3Si_2 powder dispersoid; densities of 4.8 gU/cm^3 can reliably be achieved (Finlay et al., 2004) and are currently qualified as a long-term fuel material.

Therefore in the ensuing studies, the maximum uranium-density will be limited to 4.8 gU/cm^3 (4.6 gU/cm^3 was used for the study), while the fuel material will initially be identical to that used in SAFARI-1 fuel assemblies (U_3Si_2 powder dispersed in aluminium). This choice of fuel material is used in other reactors as well: ISIS and OSIRIS in France, HANARO in Korea, NRU in Canada, HFR in the Netherlands, and the collection JRR-3M, JRR-4 and JMTR in Japan (IAEA-RRDB, 2011). In order also to encapsulate the possibility of using even higher uranium density fuel material technology, a uranium-molybdenum alloy is also included in the evaluation of the fuel material performance; however, since this technology is

[8] The word “equivalent” is used specifically here. This is because, in reality, the addition of more ^{238}U will introduce a significant reactivity penalty which needs to be compensated by adding more ^{235}U than was necessary for an HEU fuel material.

very much still under development, it was not included in the ensuing core configuration study.

2.1.3 Variable fuel design parameters

This section details parameters involved with the fuel design that were considered to be variable, focussing on the thickness of the meat section and the coolant gap size.

Thickness of the meat section

The specification of the fuel plate thickness is a parameter which is dependent on both thermal-hydraulic requirements and uranium-loading which will be varied in the ensuing studies of plate configurations. At SAFARI-1 a cladding thickness of at least 0.383 mm has been established as sufficient to perform both a heat-diffusion and fission product containment function (RR-SAR-0005, 2008) even during extreme damage scenarios (plate bending tests); therefore the plate thickness (variable meat thickness plus fixed cladding thickness) will be determined by the uranium-loading because of its dependence on the uranium-density (more fuel material volume for more uranium).

A limitation on the maximum plate thickness is however incurred by the allowable maximum fuel temperature which, according to a United States of America regulatory document (NUREG-1313, 1988), may not exceed the blistering threshold temperature of 515˚C. This limitation will be considered when reviewing the safety characteristics of the fuel design during which the limit will be conservatively set at 415˚C in order to account for uncertainty (from a basis of interviews with experienced persons).

According to a study on plate coolant velocities (Miller, 1958), in parallel to the temperature requirement for the plate thickness, is the requirement for resistance to flow induced stress and strain. The critical coolant velocity (V_{crit}), at which the flow-induced turbulence within the coolant will resonate with the natural frequency of the flat fuel plates, must be taken into consideration during the specification of the plate- and meat thicknesses, coolant gap size and core coolant requirements. A correlation for this critical velocity is given in the equation below (Miller, 1958):

$$V_{crit} = \left[\frac{15 \times 10^5 E({t_p}^3 - {t_m}^3)t_w}{\rho W^4(1-\upsilon^2)}\right]^{\frac{1}{2}} \quad \text{Eq.1)}$$

Where the symbols, with SAFARI-1-specific nominal values, are as follows:

V_{crit} = Critical coolant velocity [cm.s^{-1}]
E = Young's Modulus [bar] = 6.98x10^5 bar for 6082-T6 Aluminium cladding material
t_p = fuel plate thickness [cm] = 2*0.0383 + t_m
t_m = fuel meat thickness [cm] = variable
t_w = water gap size [cm] = 0.2932 cm (i.e. plate-to-plate separation)
ρ = water density in [kg.m^{-3}] = 990 kg.m^{-3} at 45℃ (mean coolant temperature in core)
W = water channel width [cm] = 6.61 cm.
υ = Poisson's ratio = 0.35 for most Aluminium alloys

For a plate thickness of 0.1275 cm (t_m=0.051), the critical velocity is approximately 19 m.s^{-1} while the operational coolant velocity for SAFARI-1 is unlikely to exceed 8 m.s^{-1} with a total core coolant flow of 3400 m^3.hr^{-1}.

For a ^{235}U-loading of 17.5 g per plate, a meat thickness of 0.051 cm was initially used (constitutes a uranium-density of approximately 4.6 g/cm^3). For higher ^{235}U-loadings, meat thickness were adjusted while maintaining the uranium-density specification of 4.6 g/cm^3. This was done by critically evaluating the effect on structural stability.

Coolant gap size

The coolant gap size[9] between fuel plates contributes to the following two reactor performance parameters: The moderator-to-fuel ratio, and the coolant flow resistance. Of a lesser concern is the effect on flow resistance since the gap must be quite small before pressure drop would become a major concern. Such a small gap is however, much more likely to cause the reactor to become under-moderated and consequently the specification of the coolant gap size will be governed in consideration of the moderator-to-fuel ratio only.

A study was conducted (Ahmed et al., 2005) on the effect of coolant gap size on the infinite multiplication factor, k_∞, for infinite reactors consisting of fuel assemblies with 23 fuel plates per assembly, with variations in the fuel loading per plate. This study is however, applicable to fuel assemblies with different amount of fuel plates as well, since the infinite reactor concept, as used in the study, inherently dismisses the effect of modular assemblies. Figure 4 represents an extract from this study.

[9] The coolant gap size refers to the longitudinal spacing between fuel plates and does not relate to the width of the gap, which is determined by the fuel plate width.

For a ^{235}U loading of 17.9 grams per plate (as used in SAFARI-1 fuel assemblies), figure 4 indicates an optimal coolant gap size of approximately 0.29 cm. It is therefore suitable to use the 0.2975 cm coolant gap size as specified for SAFARI-1 fuel assemblies.

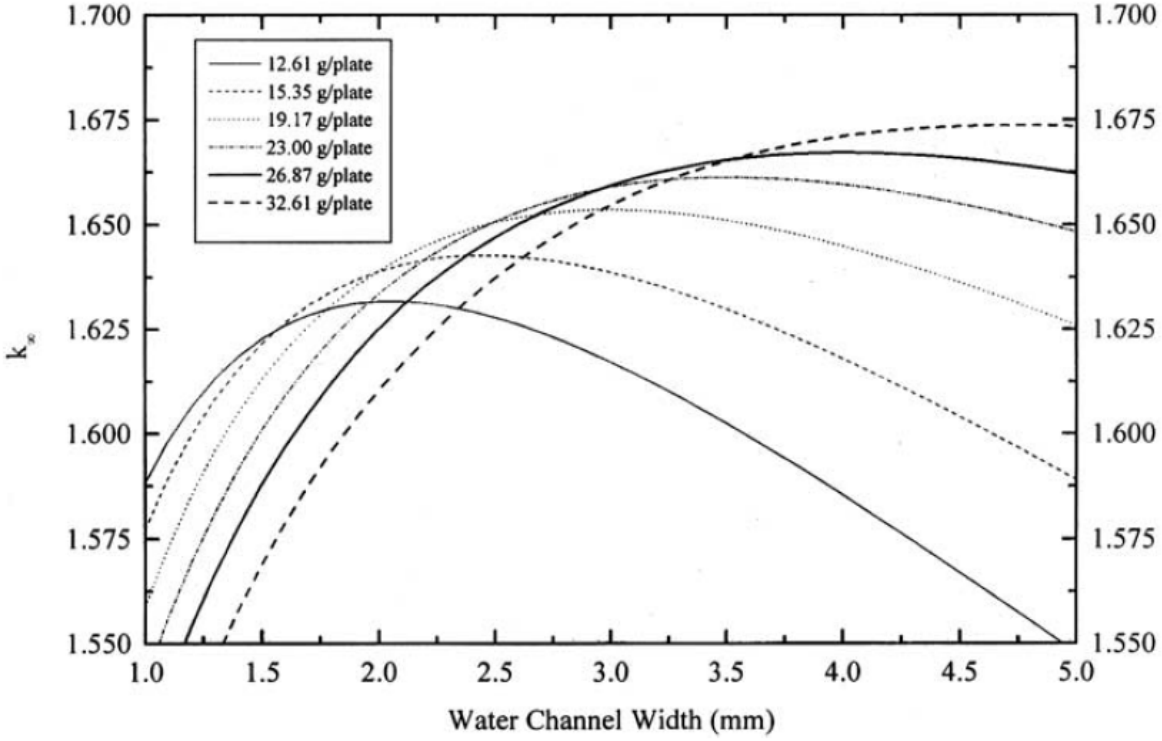

Figure 4 Variation of k_∞ with water gap size in a 23 plate fuel assembly with variations in the ^{235}U loading per plate utilising uranium-silicide as fuel material. Different fuel loadings are represented by different meat thicknesses. **(Ahmed et al., 2005)**.

Important effects that need to be considered during the evaluation of figure 4 are whether or not the moderating ratio will have an effect on the moderator-temperature reactivity feedback performance of the reactor. If the reactor is under-moderated (i.e. set point to the left of the peak multiplication factor as indicated in figure 4), an increase in coolant temperature and therefore a decrease in density, will have the effect of shifting the k_∞ curve to the right of the set point since effectively less moderator resides within the coolant gap, thereby decreasing k_∞ for the assembly and causing a negative reactivity feedback. However, if the reactor is sufficiently over-moderated, k_∞ will increase causing a positive reactivity feedback. What needs to be established in this consideration is whether or not this increase in k_∞ will cause an increase in reactivity comparable to the decrease in reactivity worth caused by both a hardening of the neutron spectrum and a decrease in the moderating strength ($\xi\Sigma_s$). This

effect is taken into account during the analysis of fuel designs in the form of moderator temperature and density feedback coefficients.

2.2 CORE DESIGN

The core configuration design is an outcome of an integral consideration of all design parameters. These parameters can be broadly categorized as; Neutron flux characteristics, safety and economy. The sections below detail the design parameters considered during the evaluation of different core designs.

2.2.1 Neutron flux characteristics

In chapter 1, the requirements were specified that the reactor will need to facilitate three main irradiation services:

- Isotope production,
- Neutron beamline supply and
- Material testing.

In order to compete with modern reactors around the world, the thermal neutron flux in both in-core and ex-core irradiation positions need to be as high as possible; however, the degree to which this parameter is optimized largely depends on the core technology.

2.2.2 Thermal-Hydraulic Safety

The major thermal hydraulic requirement for the safety of the reactor is fuel integrity, which relates directly to the temperatures reached under conditions still within the design basis. The design basis for the fuel temperature will be to avoid nucleate boiling during low flow conditions, which is usually around 90% nominal flow, but also at 120% of the nominal operating power (SCRAM trip point) and the trip limit for the inlet temperature (SCRAM inlet temperature). The primary reason for avoiding nucleate boiling in any part of the reactor is to limit the neutronic effect of voids in the moderator, which can cause power fluctuations and, if power peaks remain undetected, might cause local power excursions.

In order to maintain a sufficient margin to the onset of nucleate boiling, it is necessary to specify the maximum allowable plate power density which will define the reactor power. This is done as follows:

- The maximum allowable coolant velocity is determined from the viewpoint of the plate structural stability (Miller, 1958). It is also reduced with a 10% calculation uncertainty and a 2/3 margin (RR-SAR-0005, 2008) for safety and finally another 10% compensation for the low flow condition (90% of nominal flow),
- The maximum allowable plate heat flux, which could cause the cladding surface to reach the temperature of the onset of nucleate boiling, is determined with the Bergles-Rohsenow correlation; utilizing both the conservative Dittus-Boelter correlation for determining the forced convection coefficient, and the trip limit for the inlet temperature (SCRAM inlet temperature),
- The calculated maximum allowable plate heat flux is then reduced by the over-all hot spot factor which takes into account the statistical variation of the fuel manufacturing (or total uncertainty factor),
- The power peaking factor is applied to the heat flux by ignoring the local power peak, f_p. This is justified by the efficiency with which the aluminium cladding (with a high thermal conductivity) can dissipate heat from a local peak to the rest of the plate surface, thus negating the use of the local power peak,
- Finally this heat flux is compensated with 20% corresponding to a 120% overpower condition, thus arriving at the allowable average plate heat flux, which can be used to calculate the allowable average assembly power and thus the reactor power.

A more detailed description of each of these steps is provided in the paragraphs below.

Maximum coolant velocity:

Since the purpose of this exercise is to evaluate a design, one can afford the luxury of specifying the flow rate; however, one must do so within reasonable limits. The first consideration is to limit the flow to the critical coolant velocity causing the excitation of the fuel plates with a frequency co-incident with their natural frequency which could cause plate damage. This method is detailed in section 2.1.3 and provides an absolute maximum for plate coolant velocity (e.g. V_{crit}). Additionally, three conservative corrections are made to this velocity. First the correlation is assumed to have an uncertainty of 10%, thus decreasing the critical velocity; second; in order to maintain a sufficient margin to this critical velocity the maximum velocity is set to two thirds that of the adjusted maximum. Finally, in order to adjust for low flow conditions, 90% of this flow is taken as the limiting flow condition. This is explained mathematically below:

$$V_{max} = V_{crit} \times 0.9 \times \frac{2}{3} \times 0.9$$
$$V_{max} = 0.54\, V_{crit} \quad \text{Eq.2)}$$

Sub-cooled heat transfer:

The Bergles-Rohsenow correlation (recommended in (IAEA-TECDOC-133, 1980)) relates the heat flux for the onset of nucleate boiling to the operating temperatures and pressure with the following relation:

$$Q_{ONB} = 1.10 \times 10^{13} \times P_{atm}^{1.156} \left(\frac{9}{5}\Delta T_{sat}\right)^{\frac{2.16}{P_{atm}^{0.0234}}} \quad \text{Eq.3)}$$

In this equation (Bergles AE, 1964):

Q_{ONB} = Heat flux for the onset of nucleate boiling [W.cm^{-2}]
P_{atm} = Absolute pressure [atmospheres]
ΔT_{sat} = Wall super heat = $(T_w - T_s)$ [˚C]
T_w = Fuel plate surface temperature (Wall temperature) [˚C]
T_s = Coolant saturation temperature [˚C]

The wall temperature, T_w, can be calculated from a simple convection heat transfer equation (Cengel, 2006), using the bulk coolant temperature, with:

$$T_w = T_b + \frac{Q_{ONB}}{h} \quad \text{Eq.4)}$$

Where:

T_b = Bulk coolant temperature [˚C]
h = Convection heat transfer coefficient

Combining equations 3 and 4 as well as making adjustments to the units, one arrives at the following formula (RR-SAR-0005, 2008) of which an iterative solution- example is demonstrated in section 4.4.3:

$$Q_{ONB} = h\left[0.556 \times \left(\frac{Q_{ONB}}{1.796 \times 10^{-3} \times P^{1.156}}\right)^{\frac{P^{0.0234}}{2.828}} + (T_s - T_b)\right] \quad \text{Eq.5)}$$

Where:

P = Coolant absolute pressure [Pa]

Convection coefficient:

The parameter which connects the coolant flow to the heated surface is the convection heat transfer coefficient, h, which can be determined from the Dittus-Boelter correlation (Cengel, 2006). It should be noted that the Sieder-Tate equation (Cengel, 2006) accounts for the change in coolant viscosity caused by a changing temperature and therefore more accurately predicts the convection coefficient; however, under most conditions the use of the Dittus-Boelter correlation yields more conservative values and is therefore generally used for the safety evaluation of nuclear reactors:

$$Nu = \frac{h \,.\, D_h}{k} = 0.023 \, Re^{0.8} Pr^{0.4} \qquad \text{Eq.6)}$$

Where:

Nu = Dimensionless Nusselt number
Re = Dimensionless Reynold's number
Pr = Prandtl number
D_h = Hydraulic diameter [m]
k = Thermal conductivity of the coolant [$W.m^{-1}.K^{-1}$]

Using equations 4 and 5, one can iteratively calculate the heat flux for the onset of nucleate boiling given the maximum fluid velocity, which can be determined with the method detailed in section 2.1.3, and the coolant gap size.

Overall hot spot factor

The overall engineering hot spot factor is a component of design which takes into account the engineering uncertainties (or total uncertainties) and includes the following sub-factors (RR-SAR-0005, 2008):

- Variation in the homogeneity of the meat material,
- Variation in the thickness of the meat material,
- Enrichment variations,
- Variation of total plate uranium content,
- Core power uncertainty (instrumentation),
- Core power distribution uncertainty,
- Variation in coolant gap-size,
- Coolant flow distribution uncertainty,
- Heat transfer coefficient uncertainty,
- Total fuel plate thickness variation and
- Thermal conductivity of fuel plate materials.

The calculation of the value for the overall engineering hot spot factor is an exercise best done on an existing design since many parameters influence it; however, considering the fact that a new South African research reactor will in all likelihood function in the same engineering quality assurance environment as SAFARI-1 currently does, the engineering hot spot factor for SAFARI-1 can be used:

$$\boldsymbol{HSF = 1.34}$$

This value can now be used to adjust the maximum allowable heat flux calculated in the previous steps to produce the maximum allowable power density (e.g. heat generation rate).

Power Peaking factor

The power peaking factor (PPF) is a product of three sub-factors. These factors are defined as; the transverse assembly-averaged peaking sub-factor across the width of the core, f_{xy}; the axial peaking sub-factor, f_z; and the local peaking factor across the radial direction within a single assembly (internal radial peaking factor), f_p.

$$PPF = f_{xy}.\, f_z.\, f_p \qquad \text{Eq.7)}$$

In order to establish the overall PPF, the design envelope of SAFARI-1 has been chosen which stipulates:

$$f_{xy} < 1.60$$
$$f_z < 1.68$$
$$f_p < 1.30$$
$$\therefore \boldsymbol{PPF} < 3.5$$

This parameter needs to be considered during the evaluation of different core configurations.

Bubble-detachment criterion

In conjunction with the requirement for having sub-cooled heat transfer (i.e. liquid phase only), is that of the margin against flow-instability induced fuel plate burn-out (IAEA-TECDOC-643, 1992). A relation for this condition is prescribed as:

$$P_{plate} \leq \frac{v.\, l_h.\, w_h.\, (T_S - T_i)}{f_p \left[f_z.\, n_c + \frac{4}{\rho C_p} \cdot \frac{l_h}{D_h} \right]} \qquad \text{Eq.8)}$$

Where:

P_{plate} = Plate power [Watt]

v = Coolant velocity [m.s^{-1}]

l_h = Heated length [m]
w_h = Heated width [m]
T_S = Coolant saturation temperature [˚C]
T_i = Coolant inlet temperature [˚C]
f_p = Internal radial peaking factor
f_z = Axial peaking factor
n_c = Critical bubble detachment parameter [˚C.cm^3.W^{-1}.s^{-1}]
ρ = Coolant density [kg.m^{-3}]
C_p = Coolant heat capacity [J.kg^{-1}.K^{-1}]
D_h = Hydraulic diameter [m]

As specified in the IAEA guidebook (IAEA-TECDOC-643, 1992); the critical bubble detachment parameter must have a value greater than 32.5˚C.cm^3.W^{-1}.s^{-1} which will prevent steam bubbles from detaching from the coolant surface, thus inhibiting excursive flow instability. The temperature at which bubble-formation becomes a concern is however, above the temperature for the onset of nucleate boiling and therefore this parameter will not be used to specify the maximum reactor operating power but rather as an additional safety parameter in the form of a margin.

2.2.3 Neutronic Safety

Unique to nuclear facilities is the specification of neutronic safety parameters. These primarily include shutdown systems and the shutdown margin.

Shutdown margin

The first concept relating to the shutdown margin is the reactor's excess reactivity which is defined as the maximum core reactivity for a cold, Xenon-free BOC core, with the control assemblies fully withdrawn and all experiments loaded in their most reactive state. The shutdown margin is then defined (IAEA Safety Standards Series NS-R-4, 2005) by the absolute value of the reactivity of the core in the most reactive state with the control assemblies fully inserted and with the control assembly with highest reactivity worth fully withdrawn (i.e. to account for any single failure). In some cases the regulating authority for a specific country defines the shutdown margin for the entire control bank, as opposed the control bank minus the most reactive assembly; however, in these cases the shutdown margin requirement is also altered (increased). Mathematically, the shutdown margin can be represented as:

$$SM = \left| \rho_{fully\ inserted} + \rho_{highest} \right| \quad \text{Eq.9)}$$

The South African National Nuclear Regulator (NNR) defines the shutdown margin as pertaining to the entire control bank[10] and prescribes that the shutdown margin must be greater than the excess reactivity (RR-SAR-0005, 2008).

$$\boldsymbol{SM > \rho_{excess}}$$

The specification indicates that a reactor may not be overloaded and that the loading of fuel must be conducted in a fashion so as to support the cycle length (i.e. minimum amount of control assemblies versus fuel assemblies).

Total shutdown system worth

The total control bank worth (shutdown system worth) is defined as the difference of the excess reactivity and the reactivity of the core with the control assemblies fully inserted.

$$\rho_{bank} = \rho_{excess} - \rho_{fully\ inserted} \qquad \text{Eq.10)}$$

The South African regulator again specifies (RR-SAR-0005, 2008) the total bank worth to be greater than 15000 pcm (~$20).

$$\boldsymbol{\rho_{bank} > 15000\ pcm}$$

[10] According to this definition of the shutdown margin, it is: $SM = |\rho_{fully\ inserted}|$, without consideration of having failure in the most reactive control device, but with all experiments in their most reactive condition.

2.2.4 Economy

The primary considerations with regards to the feasibility of the reactor are:

- The reactor power,
- The operating cycle length, and
- Fuel economy.

Fundamental to the design of the reactor is the thermal power. With higher thermal power, the reactor's neutron flux output increases linearly and therefore constitutes greater yield in all irradiation activities conducted in the reactor; however, it also influences other factors. With higher power, the energy requirements increase and therefore, for a certain fuel loading, a higher power will result in a shorter cycle length. Also, higher power will require more excess reactivity for a given cycle length since the reactor will ultimately burn more fuel and therefore plays a role in the specification of the shutdown margin. From a safety perspective, the power requirement determines the power density and peak power profiles which need to be accommodated by the coolant system. In summary, a higher reactor power will:

- increase the neutron flux,
- decrease cycle length (for constant fuel loading),
- increase the excess reactivity requirement (to keep cycle length),
- decrease the shutdown margin,
- increase the power density and
- increase capital and operational costs

In a direct relationship with all the other parameters is the operating cycle length, which is important for the reactor's overall availability. Modern standards require approximately 85% (310 days of operation each year) availability annually, which normally allows for 11 operating cycles of 28 days each and 5 days of shutdown time per cycle.

Fuel economy is a composite requirement of both the amount of fuel assemblies used per annum as well as the percentage burnup reached (discharge burnup). In addition to the physical usage of fuel and control assemblies per annum, one can evaluate the economic feasibility of any core configuration with the method detailed in the following paragraphs.

Estimation of operating envelope

An assumption which is necessary to formulate the operating envelope is that both a fuel and control assembly produces the same average assembly power during each burnup cycle, which is a justifiable assumption from the viewpoint that each assembly will be loaded in all the different assembly power positions and thus effectively experience the true average assembly power.

Thus the average assembly powers are given by:

$$P_{avg,fuel} = \frac{P_{reactor}}{N_{FA} + pfN_{CA}} \quad \text{Eq.11)}$$

$$P_{avg,ctl} = \frac{pf\ P_{reactor}}{N_{FA} + pfN_{CA}} \quad \text{Eq.12)}$$

Where:

$P_{avg,fuel}$ = Average fuel assembly power [MW]
$P_{avg,ctl}$ = Average control assembly power [MW]
$P_{reactor}$ = Reactor power [MW]
N_{FA} = Number of fuel assemblies
N_{CA} = Number of control assemblies
pf = Average fraction of the power produced in the control assemblies compared to a fuel assembly

In order for the reactor to operate at a given thermal power for a specified cycle length, it will require a certain amount of ^{235}U mass. In fact, reactors that utilize low enriched uranium fuels, often use a fair percentage of ^{239}Pu as fuel (4 to 10 percent of the power is produced by ^{239}Pu) due to the conversion of ^{238}U; however, this formulation does not encompass it. The amount of ^{235}U mass added during each reload, is a function of the difference between an assembly's depletion ^{235}U mass content and its fresh ^{235}U mass content as well as the amount of assemblies changed. Thus the following relation can be derived:

$$P_{reactor} l_c \dot{m}_{235} = BUP_{fuel}.m_{i,fuel}.N_{chg,fuel} + BUP_{ctl}.m_{i,ctl}.N_{chg,ctl} \quad \text{Eq.13)}$$

Where:

l_c = Cycle length [days]
$\dot{m}_{235}$ = ^{235}U mass consumption per unit energy produced [g.MWD^{-1}]
$m_{i,fuel}$ = ^{235}U mass content of a fresh fuel assembly [g]
$m_{i,ctl}$ = ^{235}U mass content of a fresh control assembly [g]
$N_{chg,fuel}$ = Average number of fresh fuel assemblies loaded each cycle
$N_{chg,ctl}$ = Average number of fresh control assemblies loaded each cycle
BUP_{fuel} = Average discharge burnup of fuel assemblies [fraction]
BUP_{ctl} = Average discharge burnup of control assemblies [fraction]

The equation reads as follows: The product of the reactor power and the cycle length equals the energy produced per cycle, in MWD, multiplied by the ^{235}U mass consumption rate (g.MWD^{-1}) provides the total ^{235}U mass consumption for the cycle. This term then balances the mass addition which is provided by exchanging either spent fuel assemblies or spent control assemblies with a respective fresh assembly. Therefore, the net amount of mass that is added to the core is the product of the mass consumed in an assembly (product of the discharge burnup and the initial mass) and the number of respective assemblies that are changed. In explanation:

$$\begin{aligned} mass\ added &= (m_i - m_f) \times N_{chg} \\ &= \frac{(m_i - m_f)}{m_i} \times m_i \times N_{chg} \\ &= BUP \times m_i \times N_{chg} \end{aligned} \qquad \text{Eq.14)}$$

In this equation:

m_f = ^{235}U mass content of a depleted assembly [g]

The number of burnup steps an assembly undergoes during its lifetime in the core is given by the amount of the specified assembly divided by the number of assemblies changed each cycle:

$$n_{BUsteps,fuel} = \frac{N_{FA}}{N_{chg,fuel}} \qquad \text{Eq.15)}$$

And,

$$n_{BUsteps,ctl} = \frac{N_{CA}}{N_{chg,ctl}} \qquad \text{Eq.16)}$$

Where:

$n_{BUsteps,fuel}$ = Average number of burnup steps for fuel assemblies

$n_{BUsteps,ctl}$ = Average number of burnup steps for control assemblies

In order to calculate the discharge burnup for a given assembly, the amount of mass consumed during all burnup steps needs to be calculated. Therefore:

$$BUP_{fuel} = \frac{m_{i,fuel} - m_{f,fuel}}{m_{i,fuel}} = \frac{n_{BUsteps,fuel}.P_{avg,fuel}.l_c.\dot{m}_{235}}{m_{i,fuel}} \quad \text{Eq.17)}$$

And,

$$BUP_{ctl} = \frac{m_{i,ctl} - m_{f,ctl}}{m_{i,ctl}} = \frac{n_{BUsteps,ctl}.P_{avg,ctl}.l_c.\dot{m}_{235}}{m_{i,ctl}} \quad \text{Eq.18)}$$

By taking the ratio between the discharge burnup in a control assembly to that of a fuel assembly, one arrives at:

$$\frac{BUP_{ctl}}{BUP_{fuel}} = \frac{\frac{n_{BUsteps,ctl}P_{avg,ctl}.l_c.\dot{m}_{235}}{m_{i,ctl}}}{\frac{n_{BUsteps,fuel}.P_{avg,fuel}.l_c.\dot{m}_{235}}{m_{i,fuel}}}$$

$$\frac{BUP_{ctl}}{BUP_{fuel}} = \frac{n_{BUsteps,ctl}}{n_{BUsteps,fuel}} \cdot \frac{m_{i,fuel}}{m_{i,ctl}} \cdot \frac{P_{avg,ctl}}{P_{avg,fuel}}$$

By exchanging the respective burnup steps with equations 15 and 16, while also exchanging the respective assembly averaged power with equations 11 and 12, one arrives at:

$$\frac{BUP_{ctl}}{BUP_{fuel}} = \frac{\frac{N_{CA}}{N_{chg,ctl}}}{\frac{N_{FA}}{N_{chg,fuel}}} \cdot \frac{m_{i,fuel}}{m_{i,ctl}} \cdot \frac{\frac{pfP_{reactor}}{N_{FA} + pfN_{CA}}}{\frac{P_{reactor}}{N_{FA} + pfN_{CA}}}$$

Thus:

$$BUP_{ctl} = BUP_{fuel} \cdot pf \cdot \frac{N_{CA}}{N_{FA}} \cdot \frac{N_{chg,fuel}}{N_{chg,ctl}} \cdot \frac{m_{i,fuel}}{m_{i,ctl}} \quad \text{Eq.19)}$$

And by inserting this equation into equation 13, one arrives at:

$$P_{reactor} l_c \dot{m}_{235} = BUP_{fuel}.m_{i,fuel}.N_{chg,fuel} + BUP_{fuel} \cdot pf \cdot \frac{N_{CA}}{N_{FA}} \cdot \frac{N_{chg,fuel}}{N_{chg,ctl}} \cdot \frac{m_{i,fuel}}{m_{i,ctl}}.m_{i,ctl}.N_{chg,ctl} \quad \text{Eq.20)}$$

This simplifies to:

$$P_{reactor} l_c = \frac{BUP_{fuel}.m_{i,fuel}}{\dot{m}_{235}}.N_{chg,fuel} \cdot \left(1 + pf \cdot \frac{N_{CA}}{N_{FA}}\right) \quad \text{Eq.21)}$$

This equation shows that the cycle energy delivery is a hyperbolic function of:

- the fuel discharge burnup,
- fuel initial mass,
- number of fuel assemblies changed per cycle (fuel economy),
- fraction of the power produced in the control assemblies,
- the number of control assemblies,
- the number of fuel assemblies and finally
- the ^{235}U mass consumption per unit energy.

For a given core configuration, the only unknown parameters are usually the core power, cycle length and fuel discharge burnup. It is of interest to note that this equation is independent of both the number of control assemblies changed during each cycle and the ^{235}U mass content of a fresh control assembly because this information is captured within the fraction, pf. The effect of these parameters is however, evident if one tracks the core control bank position versus the cycle's duration. For a constant cycle length, the power changes the slope of the curve (thus changing the fuel assembly discharge burnup), while the control assembly reloading frequency shifts the curve up or down while leaving the fuel assembly discharge burnup unchanged. This is an important concept to consider during core optimization studies.

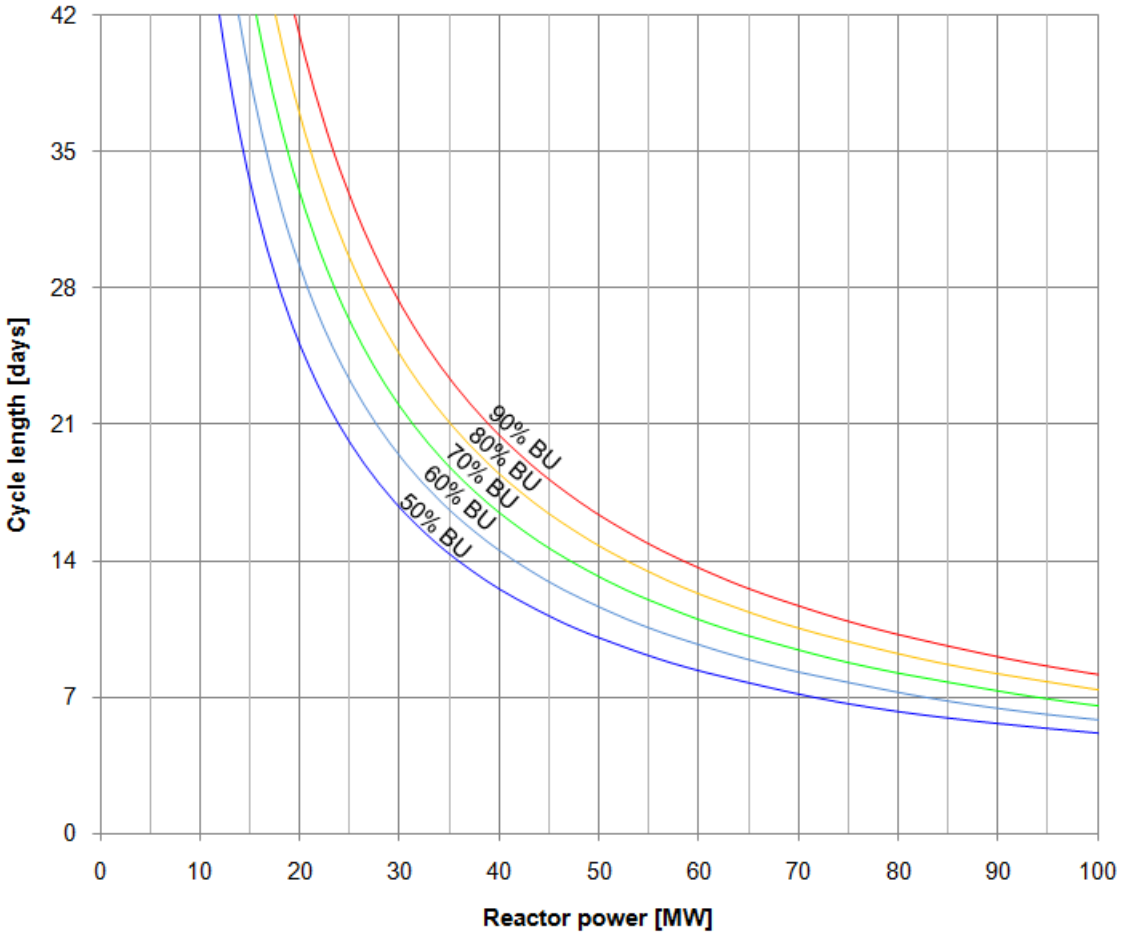

Figure 5 Graphical representation of equation 21 showing the isometric-burnup-lines for the SAFARI-1 reactor's operation. SAFARI-1 operates at 20 MW with a cycle length of 30 days and assembly discharge burnup percentage is approximately 60%.

This correlation can therefore be used to initially determine if a core configuration is feasible, for example, if a given core loading with 12 fuel assemblies is used the isometric-lines will shift to the lower left; however, from a practical point of view one will have to replace about two fuel assemblies each cycle which allows only six burnup steps and this will again shift the isometric-lines much further to the upper right.

In order to meet modern discharge burnup standards, a minimum discharge burnup of at least 50% must be achieved.

$$BU_{discharge} \geq 50\%$$

The upper limit for the discharge burnup is defined by a combination of three parameters; reactor power, cycle length and discharge burnup.

Maximum allowable fission density

The fission density inside the fuel material is a measure of the fuel burnup. In order to limit fuel particle swelling which might increase fuel plate thickness, the maximum fission density is specified to correspond with a fuel particle swelling of 10% at 2 x 10^{27} fissions.m^{-3}. This specification is justified by the nominal porosity of 4 to 10% for uranium-silicide fuels, whereby the swelling of the fuel particle can be accommodated within the porous cavities (NUREG-1313, 1988). For each fuel design the corresponding fission density must therefore be translated to a maximum burnup percentage (or fraction) with:

$$BU_{max} < \frac{2 \times 10^{27} \times V_{meat} \times M_{U235}}{N_A m_i} \qquad \text{Eq.22)}$$

Where:

BU_{max} = Maximum burnup fraction
V_{meat} = Volume of meat [m^3]
M_{U235} = Molar mass of ^{235}U [$g.mole^{-1}$]
N_A = Avogrado's number [6.022 x 10^{23} $mole^{-1}$]
m_i = Assembly fresh mass [g]

For an assembly with a ^{235}U content of 550 g (similar to the assemblies used in the HFR, Petten), this equation evaluates to a maximum burnup of approximately 79%.

Number of fuel assemblies per year

Due to the flexible nature of a core configuration with regards to power, cycle length, shutdown margin, discharge burnup and loading pattern; it would be impossible to determine accurately what the fuel assembly usage per annum will be. Instead, the physical economy will have to be determined on the basis of a trial and error calculation.

In order to determine the reactor limits, a simple linear programming exercise can be executed for each core configuration concept. This is done as follows:

- For a given core configuration, the fuel and control assembly replacement frequency can be specified to produce isometric burnup lines such as those contained in figure 5,
- The lower limit for the reactor cycle length is four weeks which provides a horizontally limiting line on the chart,
- For the given fuel assembly design, as well as the amount of assemblies in the core the thermal-hydraulic safety parameters can be used to evaluate the maximum reactor power which provides a vertically limiting line,
- Finally, the burnup limitation will provide an isometric burnup line which will limit fuel assembly burnup.

As a last parameter, the fuel assembly discharge burnup will affect the linear decrease in fuel assembly mass as an assembly undergoes burnup steps; thus for an increase in burnup (with the fuel replacement frequency constant) the total core mass will decrease unless compensated for by the more frequent replacement of control assemblies. Therefore, this parameter introduces the concept of criticality. For a low discharge burnup, the core mass will be high and criticality will be easily reached but decreasingly so with increases in discharge burnup. Thus, the criticality of the reactor cannot be determined on the hand of this linear programming exercise and has to be determined by means of a calculation.

Two examples of linear programming charts are shown below for SAFARI-1 nominal values.

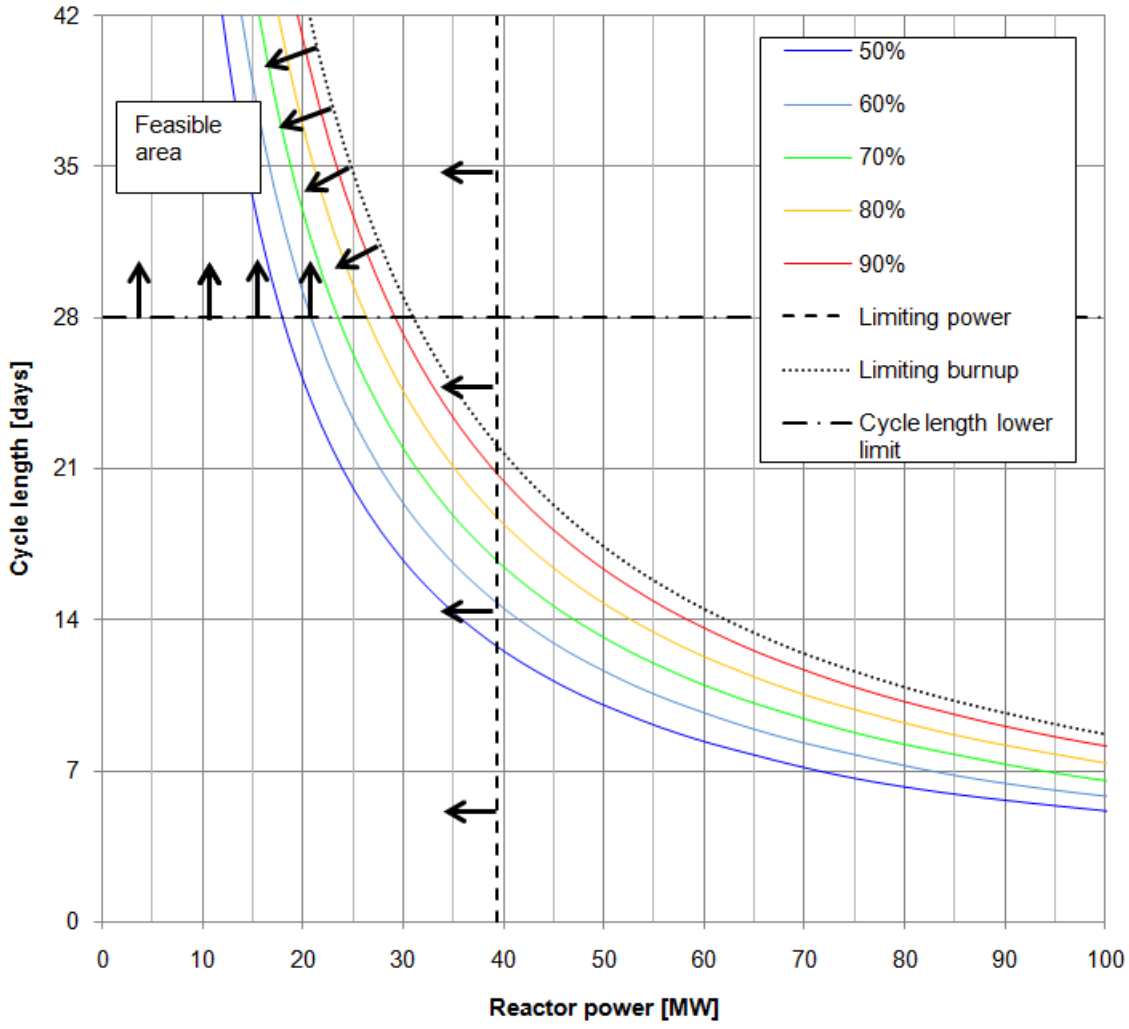

Figure 6 An example of a linear programming exercise used to determine the feasibility of fuel replacement strategies versus cycle length, reactor power and burnup. The example is for the SAFARI-1 reactor, replacing an average of 2.8 assemblies per cycle with a core of 26 fuel assemblies and 6 control assemblies replaced at an average rate of 2 control assemblies every four cycles.

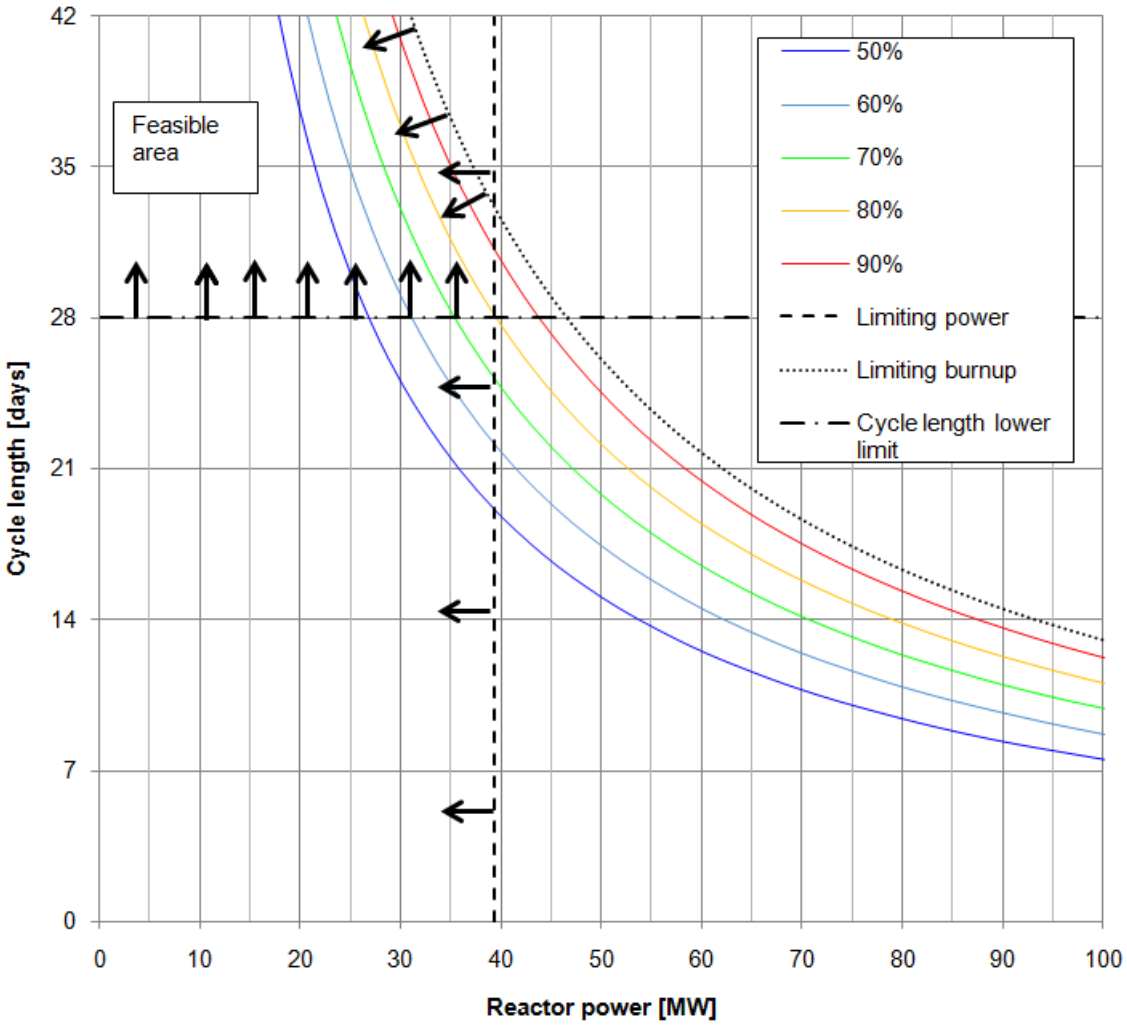

Figure 7 An example of a linear programming exercise used to determine the feasibility of fuel replacement strategies versus cycle length, reactor power and burnup. The example is for the SAFARI-1 reactor, replacing an average of 4.2 assemblies per cycle with a core of 26 fuel assemblies and 6 control assemblies replaced at an average rate of 1 control assemblies every cycle.

2.3 BEAMLINE DESIGN

A design exercise of equal diversity to that of core design is that of the design of neutron beam irradiation facilities (beamlines[11]). The aspects for the design of beamlines impacting the selection of a particular core design are detailed in the ensuing paragraphs.

From a conceptual point of view: neutrons scatter in many directions when entering any medium (after being produced inside the core). In order to utilize these neutrons, a beamline can be pointed towards the medium to shield away all but a small portion of the neutrons. These unshielded neutrons can then be channeled towards a target which is usually situated away from the harsh environment around the core. Hence, with the target situated in a better shielded low-radiation area, sophisticated equipment can effectively be installed in order to perform a wide variety of functions.

2.3.1 Thermal neutron sources

An integral term associated with the requirements of a neutron beamline irradiation facility is the characteristics of the neutron source used to supply the neutrons. The term “neutron source”, associated with neutron beamlines, is an often ambiguous term used to refer to the medium or component from which neutrons, at a specific energy, scatter before entering the neutron beamline device. For beryllium-reflected core designs with light water filled blanket regions (like SAFARI-1 and HFR) the thermal neutron flux rapidly decreases beyond the extent of the physical Beryllium assemblies. Therefore, in order to maximize the amount of thermal neutrons scattered into the beamline, the source (or origin of the beamline) should ultimately be located against the core face - directly adjacent to the beryllium reflector assemblies. The core face is then referred to as a “thermal neutron source”. For heavy water reflected core designs, the thermal neutron flux peaks approximately 16 to 20 cm beyond the bare core face (Shen & Yuan, 2002), which makes this location of the component referred to as the thermal neutron source for such cases.

2.3.2 Cold neutron sources

Modern beamline technologies tend to require neutrons with less energy than that nominally associated with thermal neutrons (E_n<0.625 eV). For these technologies, specialized designs are developed to reduce the up-scattering energy transfer due to the molecular

[11] The definition of a beamline is: a line leading to the experimental end-station which utilizes particle beams from a particle accelerator, synchrotron light obtained from a synchrotron, or neutrons from a spallation source or research reactor (Wikipedia, 2011).

thermal motion associated with the medium's thermodynamic temperature. With sub-cooled low melting point substances, such as liquid- hydrogen or deuterium (at approximately 20K), a high atomic density- low thermal motion medium can be placed in the thermal neutron flux close to the core to thermalize the already thermal neutrons to lower energies. A typical energy boundary for these low energies is 5 meV (Flocchini et al., 2007), and neutrons at and below this energy are referred to as cold neutrons.

In order to optimize the production of cold neutrons, the cold neutron source (i.e. the medium which contains the sub-cooled substance) should be located in the peak thermal neutron flux location and should be of the appropriate dimensions. The dimensions (and shape) of the source is a diverse subject in itself since newer designs already feature oddly shaped source structures like oval- and annulus-structures (Shen & Yuan, 2002); however, in order to provide comprehensive data regarding the ability of a particular core design to deliver cold-neutrons, the study was confined to a cylindrical shape and a corresponding height to diameter ratio of approximately unity. The scope of the cold neutron beamline study is then confined to the fundamental variables; the source medium (H_2 or D_2) and the volume thereof.

The rationale behind selecting the source medium is economically coupled to the volume required since larger volumes require both larger cooling systems and greater amount of space, which are both closely related to the initial- and operating costs. For hydrogen sources, the scattering cross-section is high, therefore, a small volume is required; however, the absorption cross-section is also high. For deuterium, the scattering cross-section is lower and a larger volume is required but the absorption cross-section is lower. Thus, both mediums have specific advantages and disadvantages which need to be evaluated carefully. For this study, a liquid hydrogen (H_2) source was used. A short study on the optimal source volume was conducted using a 5 by 5 core design as discussed in annexure B. The study found that for nominal conditions, a 2000 cm^3 (2 liters) H_2 cylindrical cold-neutron source at 20K will produce an optimal cold-neutron output for the beamline (figure included in annexure B). For all the evaluated core designs, the same volume was used to compare the cold neutron beamline output neutron current.

As a final consideration there are two isomeric forms of ordinary room temperature hydrogen (or deuterium), which comprises a 50%-50% ratio of the two isomeric forms of hydrogen; para-hydrogen and ortho-hydrogen. These forms refer to the nuclear spin of the two protons of the molecule and fundamentally influence the molecule's magnetic behavior. When the hydrogen is liquefied and cooled to below -200˚C, there is a natural conversion of the

hydrogen to 100% para-hydrogen which influences the thermal behavior (Kasai et al., 2003) and therefore the neutron up-scattering behavior due to thermal motion, S(α,β). For this study, it was assumed that the cold-neutron source would be used directly after a refill with cooled hydrogen and therefore a 50%-50% ratio was used in all the designs. Typically, the conversion process takes place over a period of approximately 10 days (Ooi et al., 2006).

2.3.3 Direction and location of beamlines

Neutron beamlines have traditionally been located directly against the core face with a radial orientation with the core center; however, with the use of heavy water reflectors becoming more common, where the core in essence is transformed into an inverse flux trap, beamlines no longer need to be orientated radially. This is because the peak thermal neutron flux, at the before mentioned 16 cm peak location away from the core face, is mostly isotropic (i.e. the same in all directions). This means that the beamline can theoretically be placed in any direction for which it should experience the same output regardless of the direction.

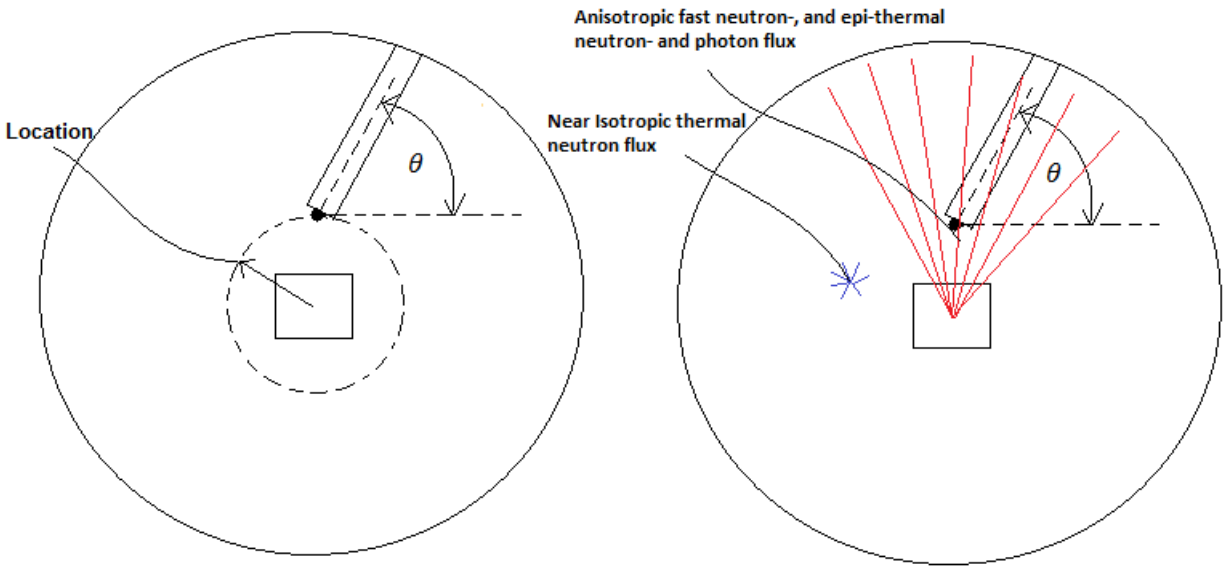

Figure 8 [Left] A schematic of the definition of the beamline location and directionality. [Right] Illustration of the isotropy of different fluxes at the beamline source location.

Another consideration of beamline directionality is the effect of the accompanying fast neutron-, epi-thermal neutron- and photon flux which considering the nominal sensitivity of targets and the associated equipment, is undesirable with respect to noise, radiation levels and material damage. These fluxes are however, unlike the thermal neutron flux, very much

still anisotropic even at 16 cm away. Thus in theory, if the beamline is pointed away from the core, the amount of fast neutron-, epi-thermal neutron- and photon flux should decrease.

2.3.4 Beamline diameter or equivalent dimension

The neutron beamline shape and internal detail is another aspect which can take on many forms, especially considering new developments in collimator design and materials. In order to compare the output of the evaluated core designs with that of SAFARI-1, the beamlines were modeled as round with an internal diameter of 17.6 cm (7 inch) and with an aluminium wall thickness of 1 cm. The internals of the beamline were modeled as a volume filled with low pressure helium which allows for a near neutron-transparent medium to be placed in the void of the beamline (instead of modeling an unrealistic void).

2.4 SUMMARY

This chapter detailed the development of the technical specifications from design aspects discussed in chapter 1. The three primary aspects, namely; the design of the fuel, the core design and the design of the beamlines were overviewed and the relevant items that needed to be studied were indicated. The next chapter describes the calculational methods employed to study the relevant parameters by detailing the calculational software codes, and their associated models, used for the analysis of the before mentioned primary aspects. The chapter also contains an evaluation of the models used in each codes and discusses the relevance of the different phenomena.

CHAPTER 3 CALCULATIONAL METHODS

This chapter covers all the topics relevant to the calculation methods used to perform the various studies. Section 3.1 describes the methodologies used in the HEADE (Heterogeneous Assembly Depletion) code to perform the evaluation of fuel designs as well as cross-section homogenization. Section 3.2 describes the methodologies used to assemble the nodal diffusion models from homogenized cross-sections for the MGRAC code (Vogel & Weiss, 2011). Section 3.3 details the setup of MCNP5 models while section 3.4 describes how the MGRAC code was interfaced with MCNP5 as well as other codes (some of which were developed specifically for this study). Section 3.5 depicts the evaluation of the discharge prediction correlation developed in chapter 2 as well a MGRAC to MCNP5 comparison of complete core models.

3.1 TRANSPORT CODE HEADE

HEADE (Joubert & Weiss, 1992) is a collision probability neutron transport-equation solver, utilizing a response matrix formalism to solve a two dimensional fine-group transport problem for an infinite array. It includes capabilities such as: burnup analysis, analysis of temperature feedback effects, coolant boron-concentration modeling, xenon-poison concentrations modeling and burnable absorber (BA) modeling. These capabilities allow the simulation of the infinite multiplication factor, k_∞, with progression of burnup for a range of state parameters[12] in sufficient geometric detail. Additionally, the code is also used to prepare few-group homogenized cross-sections for use in the nodal diffusion based neutronic calculation code, MGRAC, which is discussed in section 3.2.

3.1.1 Modeling fuel

This section describes the modeling of the fuel, and therefore includes both the modeling of active sections of fuel assemblies as well as the active sections of the fuel follower for control assemblies.

Geometrical modeling in the HEADE code requires the representation of a planar (2D) mesh of regions, termed cells, represented with simplistic rectangular-, slab- or cylindrical- (pin) geometries. For each of the subsequent sub-cell geometries (detail within each cell),

[12] State parameters refer to the varying parameters relating to a specific operating state and include: the operating temperature of the fuel, coolant boron-concentration, temperature- and density of the coolant and xenon-concentration changes.

defined by the before mentioned selection of geometries, a unique material can be specified in order to arrive at a representation of a realistic core component.

Geometry

In order to model fuel sections, the materials were divided into four material groups: fuel material, cladding- and side plate material, burnable absorber (BA) material and coolant. These materials were mostly incorporated into slab geometries with the exception of the modeling of burnable absorber wires which required a cylindrical geometry. These geometries were then assembled into the before mentioned cells, and then arranged into a two dimensional mesh as shown in figure 9.

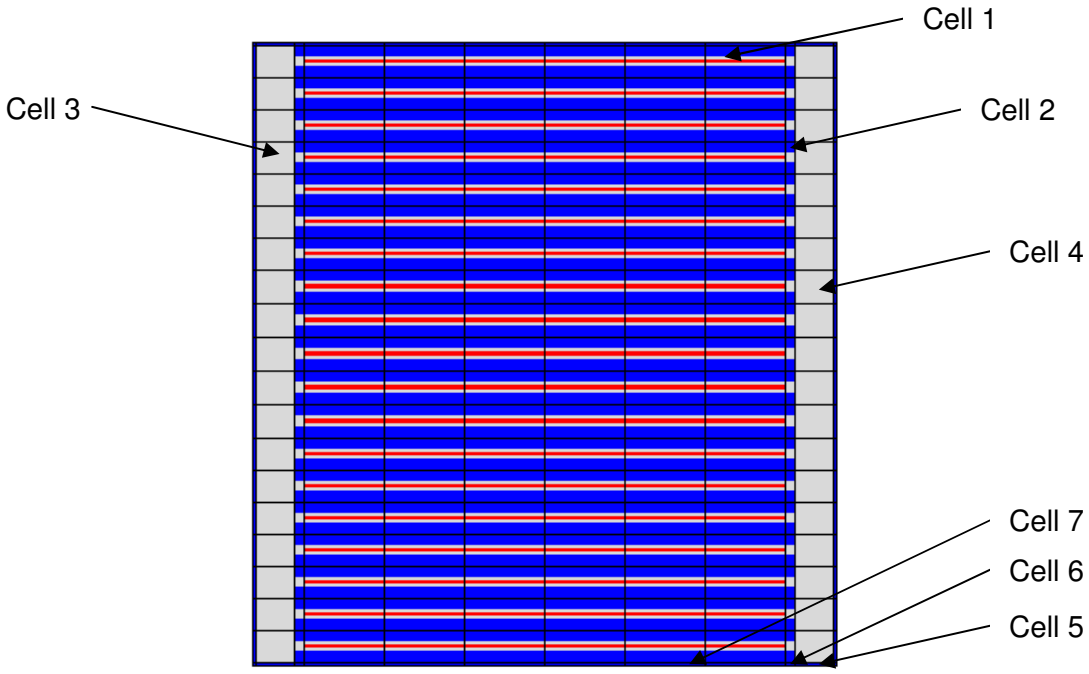

Figure 9 Schematic representation of the two dimensional mesh used to simplistically model sub regions called cells for a 19 plate fuel assembly in the HEADE code.

Cells which define plates containing fuel material are modelled within cell 1, and comprise 5 horizontal slab regions which accommodate: the coolant on either side of a fuel plate, the two cladding surfaces and the fuel meat. Cells defining plates containing no fuel material are modelled within cell 2 and consist of 3 horizontal slab regions used to define the coolant on either side of a plate and a single slab for the plate. Cells 3 and 4 consist of two vertical slabs for both the assembly side plates and inter-assembly coolant gap. Cells 5, 6 and 7 consist of single slab geometries and are used to model the top and bottom inter-assembly coolant gaps.

Materials

Material compositions within the HEADE code are specified with isotopic number densities (with unit: atoms.barn^{-1}.cm^{-1}). For the fuel material, fresh LEU fuel is modelled with the isotopic break down of the typical chemical specification used for SAFARI-1 uranium-silicide LEU fuel, as shown in table 2 (RR-SAR-0005, 2008) as well as typical specifications for a high uranium-density LEU fuel material, for which the 2 wt% Molybdenum alloy (Kim et al., 1997) was used. The composition of the cladding material, in practice, depends largely on the selection of an appropriate alloy; however, due to the normally low concentrations of impurities within alloys normally used for cladding, the cladding and side plate material was modelled as pure Aluminium ($^{27}_{13}Al$). Coolant was modelled as ordinary light water.

Table 2 Chemical and isotopic compositions used to model fresh fuel material in the HEADE code.

Uranium-silicide-aluminium dispersoid	
uranium wt%	78.6%
aluminium wt%	15.0%
silicon wt%	6.4%
Uranium-aluminium with 2% molybdenum	
uranium wt%	44.2%
aluminium wt%	52.9%
silicon wt%	0.9%
molybdenum wt%	2.0%
Uranium Isotopic composition	
uranium-234 wt%	0.24%
uranium-235 wt%	19.75%
uranium-236 wt%	0.10%
uranium-238 wt%	79.91%

In order to track fission product build up, particularly Xenon, a number of isotopes needed to be included in the burnup analysis of the fuel. These isotopes needed to encompass all the fissionable and heavily absorbing actinides as well the fission product isotopes which will sufficiently exhibit the poisoning character of the fuel material. A list of these isotopes is indicated in table 3.

Table 3 Isotopes tracked during the burnup progression of fresh fuel. Burnable absorbers are not included in the list.

Actinides	Fission products
uranium-234	iodine-135
uranium-235	xenon-135
uranium-236	cerium-141
uranium-238	cerium-142
neptunium-237	cerium-144
neptunium-239	praeseodymium-143
plutonium-238	neodymium-143
plutonium-239	neodymium-144
plutonium-240	neodymium-145
plutonium-241	neodymium-146
plutonium-242	neodymium-147
americium-241	neodymium-148
americium-243	promethium-147
californium-242	promethium-148
californium-243	promethium-148 Metastable
californium-244	promethium-149
californium-245	samarium-147
-	samarium-148
-	samarium-149

Energy group structure

In order to incorporate a fine-group representation of cross-sections, 172 energy groups were used for energy discritization in the HEADE code and were collapsed to a 6 group structure for assembly- homogenized cross-sections. For the homogenization of control assembly cross sections an intermediate 24 energy group structure was used. The energy group boundaries are shown in annexure C.

Burnup steps

Depending on the ^{235}U loading per assembly, up to 50 burnup steps were used in order to simulate fuel assembly performance for up to 440 MWD energy delivered. Burnup-step duration varied according to four time periods:

- An initial “startup” period during which fission product build-up is quite significant, which was simulated with steps of a maximum of 6 hours, for up to 1 day exposure;
- A transient period of minor fission product build-up, simulated with 1 day steps, for up to 10 days exposure;

- Larger time steps, 10 days, in duration for up to 100 days exposure;
- Depletion up to end-of-life, with steps of 20 days in duration, up to the maximum exposure duration of 640 days.

This selection of time-spans allows the MGRAC code to interpolate burnup data, in the homogenized cross-section library, with sufficient accuracy.

Off-base state parameters

In order to investigate the moderator temperature- and density feedback performance of the fuel, the coolant temperature is varied by 5˚C for each burnup step. In this way, the Moderator Temperature Coefficient (MTC) can be calculated and analyzed over the entire lifetime of the fuel.

3.1.2 Modelling control assembly absorber sections

Due to the fact that the HEADE code uses a low order response matrix formalism to couple nodes, the solution of the transport equation across a heavily absorbent medium becomes challenging, especially considering the large flux gradient practically experienced in such cases. In order to limit the possible inaccuracies introduced by the collapsing of cross-sections from 172 energy groups to 6 energy groups by the HEADE code, an intermediate step is facilitated by the STYX code (Ball & Weiss, 1993), which utilizes an intermediate 24 energy group structure as an output from the HEADE code, to produce the homogenous nodal diffusion cross-sections for 6 energy groups. The energy group boundaries for this intermediate structure are shown in annexure C.

For the HEADE modelling of the geometry, which will generate the intermediate energy-group cross-sections, an ordinary fuel region is modelled as shown in figure 9 but with an additional row on the bottom representing three different control materials, i.e. absorber, coolant and aluminium. The detailed structure of the control absorber is not modelled due to the fact that the character of the energy spectrum is not lost during the collapse from 172 energy groups to 24. This is because 24 energy groups largely capture the detailed flux weighted reaction rates in the areas of importance, i.e. fast, unresolved-resonances, resolved-resonances and thermal. The calculation then produces a STYX data file containing the four major homogenized materials (the before mentioned materials plus the homogenized fuel) used to model the control region in STYX. The two modelling approaches are indicated in figure 10 and figure 11 below.

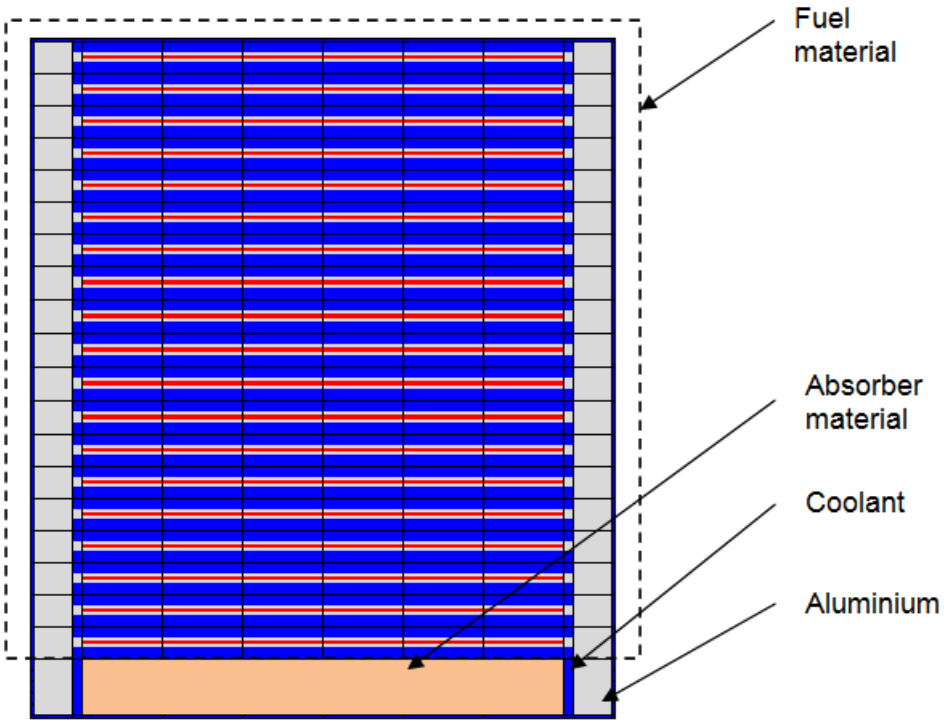

Figure 10 Schematic representation of the two dimensional mesh used to extract 24 energy group cross-sections from the HEADE code for use by the STYX code.

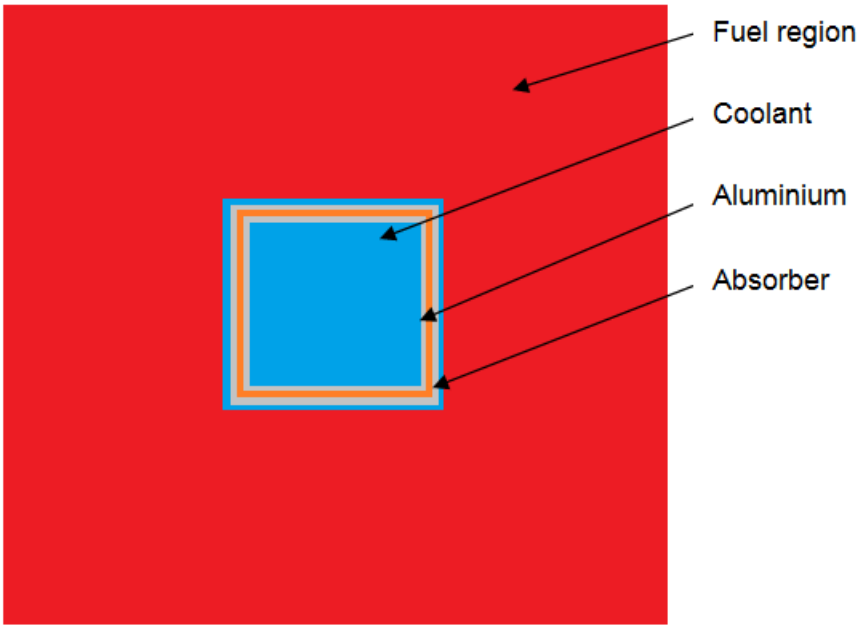

Figure 11 Schematic representation of the configuration used to produce 6 energy group cross-sections for control material using the STYX code

3.1.3 Modelling burnable absorbers

Burnable absorbers were incorporated in the study by means of cadmium wires. In the specific case of using cadmium wires, flux self-shielding becomes a concern and therefore, when representing very thin wires typically in the order of 0.05 cm in diameter, one has to consider the amount of cylindrical layers modelled in HEADE in order to represent the wire node (see figure 12).

In order to determine the appropriate number of layers, a short study was performed on the infinite multiplication factor versus burnup. The results of this study are shown in figure 13 for a 19 plate fuel assembly with cadmium wires located on either side of the fuel plate, as shown in figure 12 below.

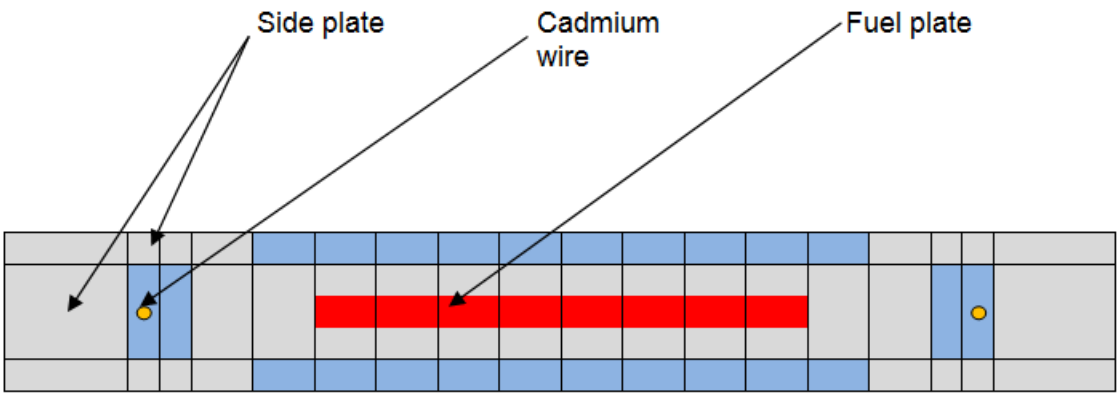

Figure 12 A scaled representation of the nodalization used to model Cadmium wires in the fuel regions of assemblies.

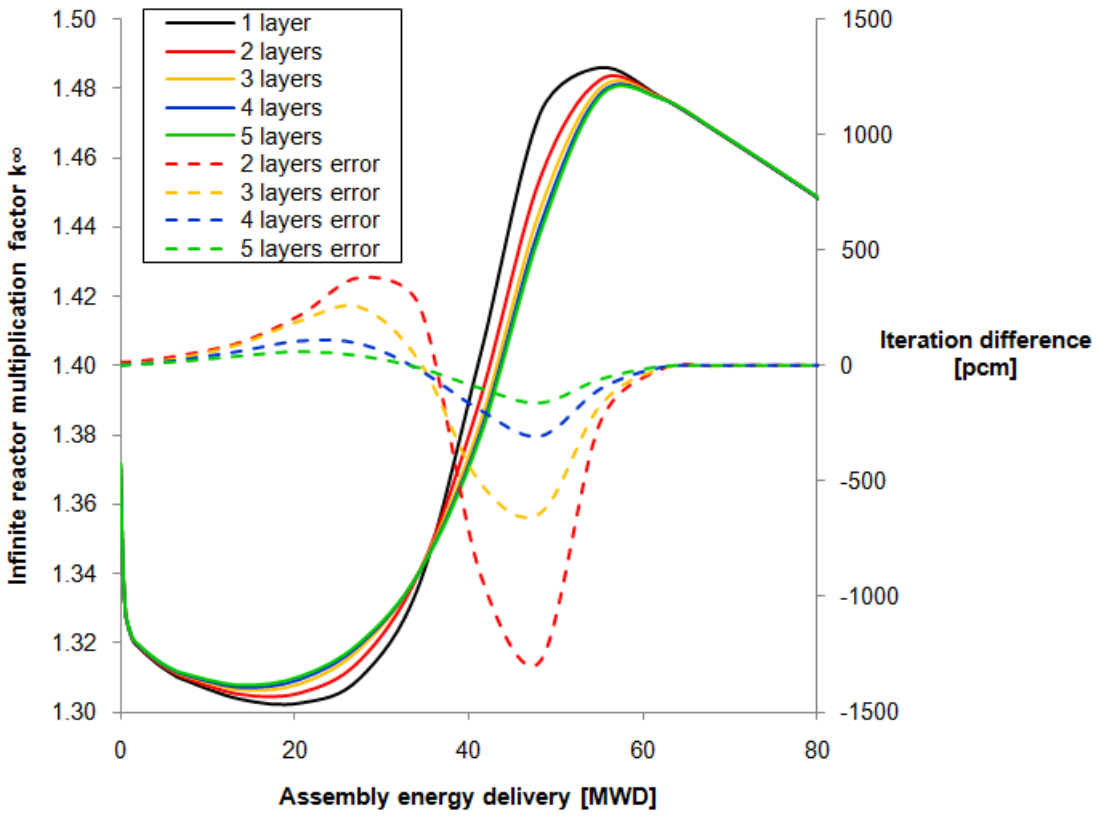

Figure 13 Results of a study to determine the appropriate amount of layers to use when representing a 0.05 cm diameter Cadmium wire.

The study shows that the modelling of 0.05 cm diameter cadmium wires as cylindrical nodes with five radii is sufficient to reduce the error to below 150 pcm. The major calculational variance occurred both at the initial reactivity decrease (first local minima) and at the reactivity recovery peak (first local maxima).

It is of importance to note the diminishing self-shielding effect of the Cadmium wires where; initially self-shielding is high and the criticality reduces approximately at the normal burnup reduction rate, but as the wire depletes, so does the self-shielding and consequently the depletion of the wire accelerates (increasing reactivity) from 10 MWD to approximately 55 MWD where the criticality reduction again resumes the normal burnup reduction rate.

3.2 NODAL-DIFFUSION MODELS DESCRIPTION

The Multi-Group Reactor Analysis Code (MGRAC) is a three dimensional nodal diffusion code used to analyze MTR type reactors and forms part of the OSCAR-4 code package. It utilizes modular input files to define: assembly homogenized cross-section configurations

(.BASE files), core designs (.CONFIG file), fuel- and control assembly loading configurations (.LOAD files) and a simulation input file (.INP file). These files are used in conjunction with the few group homogenized cross-section library (.LNX file), to calculate nodal neutron flux, power generation and burnup. The burnup of fuel assemblies are tracked by means of fuel- and control assembly history files (.HIST files). Collectively these processes allow the code to simulate a number of important effects such as Xenon and Samarium build up as well as reactor economics and reactivity effects.

In order to utilize the MGRAC code, a homogenized cross-sections library needs to be prepared with the HEADE code for the following components:

- Homogenized fuel for each fuel design
- Absorber (control) sections
- Inter-sectional pieces and end-adaptor sections
- Non-fuel, homogenized sections for reflector assemblies
- Irradiation facilities
- Axial reflector regions
- Radial reflector regions (light water, heavy water and beryllium)

Once these homogenized cross-sections are prepared, they are assembled into a library by the codes: POLX (polynomial cross-section fitting code) and LINX (cross-section library linking code).

Assembly definitions

In order to appropriately place the homogenized cross-sections in the correct nodes, assembly definition files and a core configuration file was required. The active region of fuel assemblies define the active core section for the MGRAC simulation and therefore have been defined with 8 equally spaced nodes (7.5 cm in height). Fuel assemblies therefore have twelve nodes in total in order to define the eight active nodes, the bottom end-adaptor and the top-end adaptor. The end-adaptors were split into two nodes in order to incorporate the effect of the changing aluminium to water ratio along the adaptor height, especially along the bottom adaptor where it is inserted into the spacing grid, which increases the effective aluminium volume. A fuel assembly configuration is shown in figure 14 below.

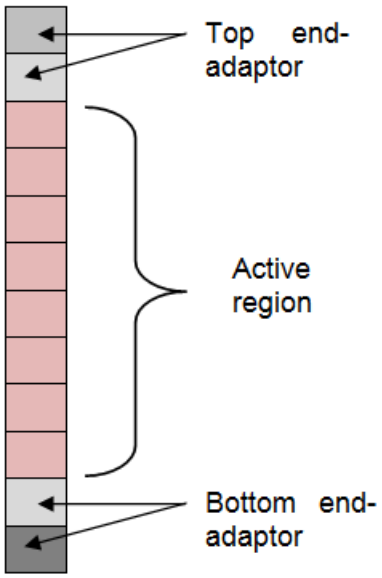

Figure 14 Schematic representation of the nodalization used to define fuel assembly configurations in the MGRAC code.

The modeling methodology of the control assemblies was similar to that of the fuel assemblies except for the additional nodes used to define the absorber section. Other assemblies such as reflector assemblies and irradiation facilities are modeled in the same manner as fuel assemblies but with the active fuel node cross-sections swapped with the relevant cross-sections from the library (i.e. light water, beryllium, etc.).

Core Configuration

In the case where the reactor was modeled with a light water reflector or blanket region, the core was modeled with up to three additional planar nodes extending outside the core perimeter, without the use of equivalent reflector treatment. If however, the reflector consisted of heavy water, the core was modeled with only two additional nodes outside the core perimeter, after which an equivalent reflector treatment was applied in the form of an albedo matrix calculated in an iterative manner with MCNP5 (see section 3.5.2). As an example of a core design specification (.CONFIG file), consider figure 15 below.

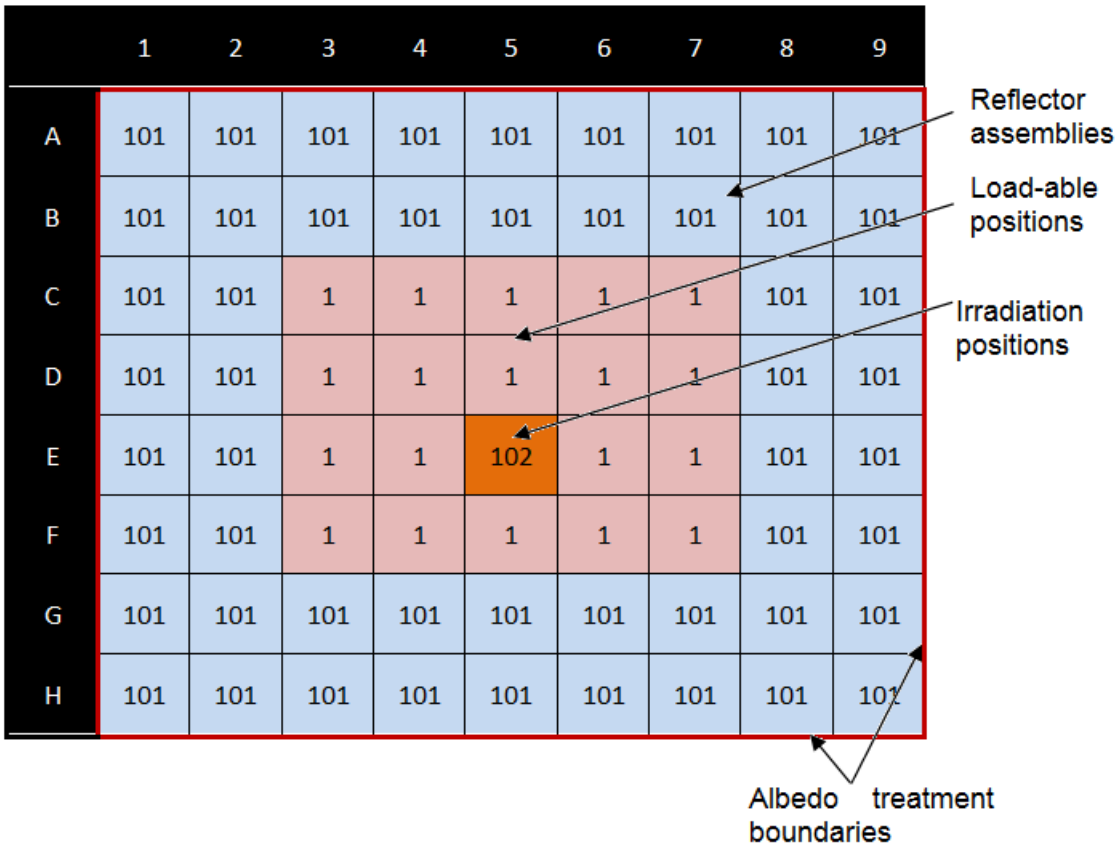

Figure 15 A schematic of the core configurations used to represent different core designs utilizing albedo treatments.

3.3 MCNP5 MODELS DESCRIPTION

MCNP5 (Monte Carlo N-particle) is a particle transport code commonly used to simulate steady-state neutronics of reactors. It implements statistical particle collision tracking to generate particle tracks, which can be used to estimate nuclear reaction rates, fluxes and currents. Due to the fact that MCNP5 is relatively computationally intensive, it was not used for performing burn-up calculations and only for accurate flux- and current calculations (neutron, β and ϒ).

3.3.1 Modeling

In order to model fuel- and control assemblies as accurate as possible, isotopic number densities were extracted from equilibrium core data, which are contained in assembly history files generated by the MGRAC code. The number densities, contained within history files, do however only contain isotopes that can induce reactivity effects over the course of an assembly's burnup (see section 3.1) and therefore do not contain the necessary alloying

elements such as aluminium and silicon (for uranium-silicide fuel materials) or molybdenum (for uranium-molybdenum fuel materials). These materials, consequently, had to be added to the isotopic number densities extracted from the history files, be appropriately treated, and packaged into nodal material specifications to be used by MCNP5. Also, for a specific axial node, the material density and material number needed to be correctly specified and coupled to the correct cell. Thus the fuel sections of fuel- and control assemblies were defined from the fuel meat outwards as follows:

- All eight nodes of a single plate's meat is constructed cell-by-cell.
- The eight nodes are enclosed by a single cladding cell which excludes the inner meat cells.
- Another single cell is defined which excludes the meat nodes as well as the cladding but only extends until half the coolant gap size in both lateral directions.
- The meat nodes, cladding and coolant cell together are assigned to a single universe which is compiled into a lattice universe used to fill the entire fuel plate region.
- A single cell is defined to contain the universe in which the fuel plate lattice is defined. The surfaces which define this cell can be modified in the lateral direction to change the number of plates without redefining the fuel plates.
- Once the fuel plates have been defined, the side plates are added and the surrounding coolant volumes are added all of which are assigned to a third unique universe number used to completely define a single core position. (see figure 16)
- This process is then followed for all fuel- and control assemblies with the exception that control assemblies are constructed out of surfaces which are coupled to transformation input cards in order to facilitate movement. Fuel assemblies on the other hand can all share common surfaces since none of them require any movements. (see figure 17)
- The entire core configuration is then defined by means of a finite lattice universe. (see figure 18)

Figure 19 shows the assembly of a 5 by 5 core as a 3D visualization.

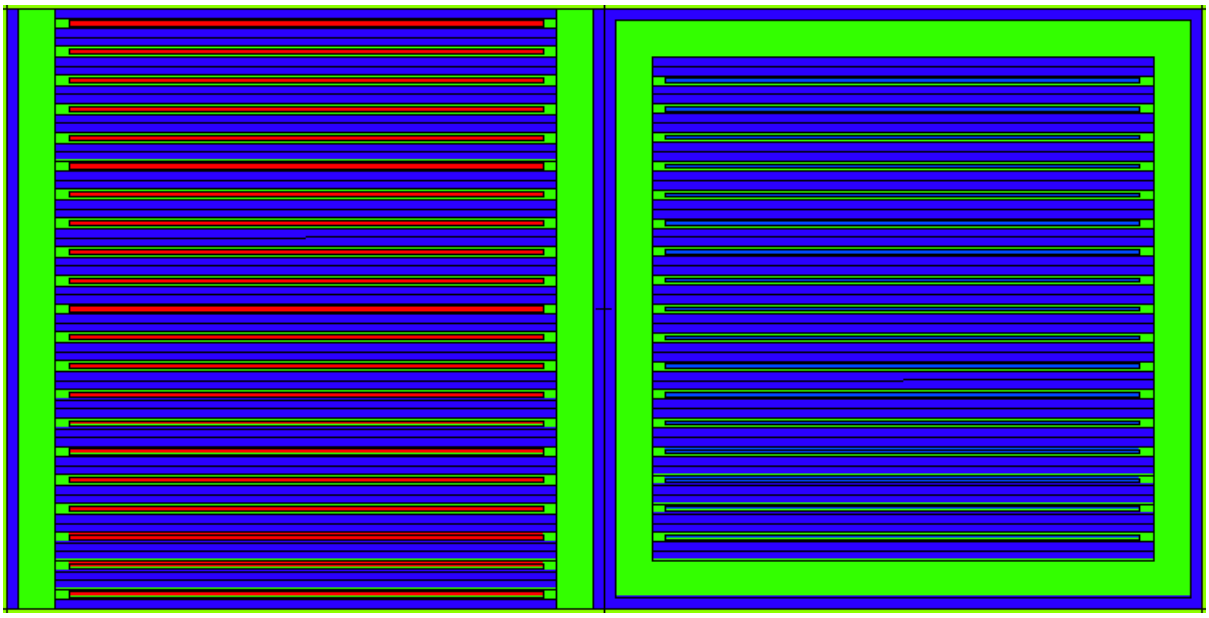

Figure 16 Visualization of the MCNP modelling of fuel- and control assemblies using lattices and universes.

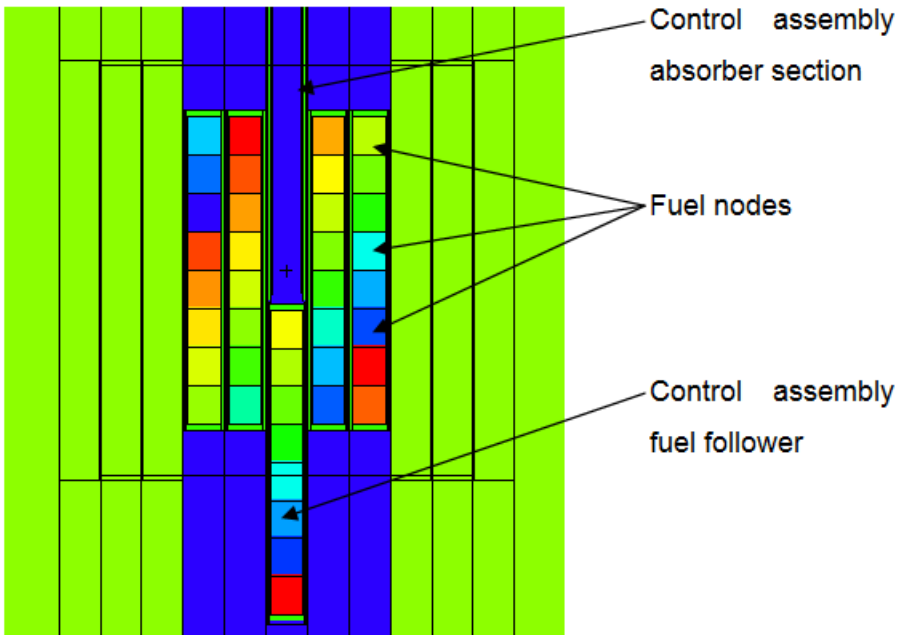

Figure 17 A visualization of an axial section through the core showing the modelling of fuel nodes.

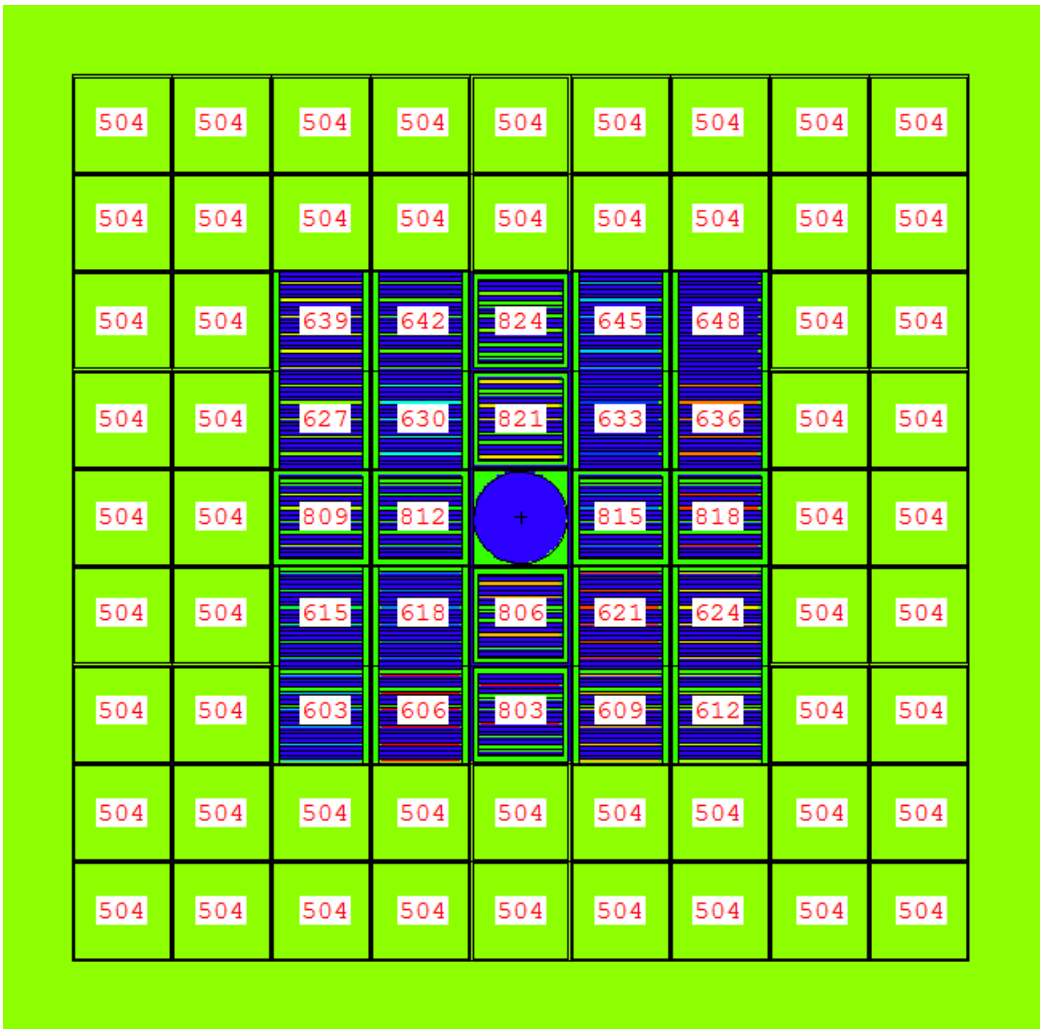

Figure 18 A visualization of a section through a core modelled with MCNP, showing the universe numbers.

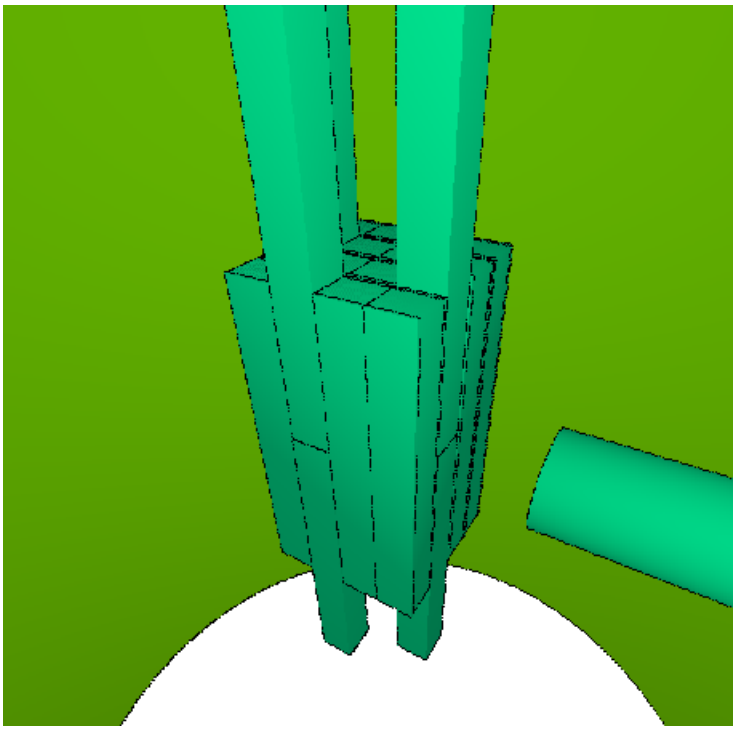

Figure 19 A 3D perspective visualization of a core model showing the active region of fuel assemblies, control assemblies (active section and absorber section) and a thermal neutron beam line. The internal side of the vessel can be observed in the background.

3.3.2 Tallies

In order to find the various flux values, an MCNP5 mesh tally was used (fmesh card). The mesh was based on the same 8 cm by 8 cm square lattice used for both the MGRAC and MCNP5 models and corresponded, throughout the height, to the nodalization used within MGRAC. Values from this tally provided volume averaged flux.

For determining the output current from beamlines, an ordinary surface tally was used on the output-surface[13]. A cosine angular tally boundary was applied to provide the output current in a 5 degree cone around the surface normal (positive sense) and was done to dismiss currents which were unlikely to traverse through the surrounding concrete shield.

[13] The output-surface refers to the surface used to define the output end of a beamline.

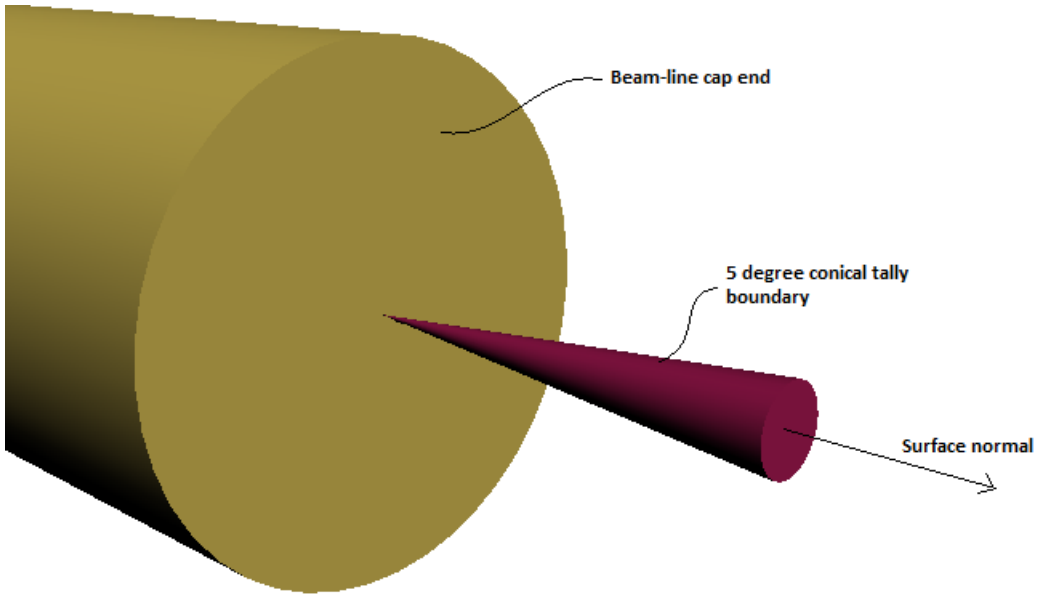

Figure 20 Illustration of the conical angular boundary used to estimate the effective current output of a beamline.

3.3.3 Variance reduction

The only aspect of the MCNP5 studies which required variance reduction was that of beamline output currents. The method applied was to, use a single DXTRAN sphere surrounding the before mentioned tally surface at the end-cap of a beamline cylinder.

A DXTRAN sphere is a variance reduction utility in the MCNP5 code which creates a special DXTRAN particle for each source particle (after either its first collision or after leaving the source). This special particle is then deterministically transported to the DXTRAN sphere's outer surface (whilst adjusting the particle weight) from where a normal MCNP5 particle track is resumed. The original source particle is tracked as per normal with the exception that if it should enter the DXTRAN sphere, it would be "killed" as to not doubly contribute to the tally contained within the sphere. If correctly applied, a DXTRAN sphere results in more calculations per source particle but with greater amount of samples in the tally region and thus, for low complexity tally regions the figure of merit (FOM) should increase dramatically with only a small increase in total computing time. For this study, applying a single DXTRAN sphere around the output-end beamline surface tally, the average convergence rate was increased almost three-fold.

3.3.4 Tally multiplication factor

Tallies in MCNP5 are by default normalized to the particle population per source particle. Therefore, in order to determine the actual tally value, the actual amount of source particles needs to be determined for any given core design. In a nuclear fission reactor, the core

power directly defines the fission rate which can be used, together with the energy- and neutrons released per fission, by the isotope undergoing fission, to calculate the effective amount of source particles. In reality there are other actinides, besides ^{235}U, which contribute to the overall fission power and consequently one can define the following equation for each actinide i (of a total number of N):

$$S_0 = \sum_{i=1}^{N} \frac{\bar{\nu}_i P_i}{\bar{E}_i} \qquad \text{Eq.23)}$$

Where:

S_0 = Number of source particles [s^{-1}]
$\bar{\nu}_i$ = Average amount of neutrons released per fission of actinide i [$fission^{-1}$]
P_i = Total power produced by actinide i [Watt]
$\bar{E}_i$ = Average energy released per fission of actinide i [Joule]

An interesting phenomenon observed with the use of the equation above was that, when applied to energy deposition tallies (F6 and F7 cards in MCNP5); the calculated power is in the order of 3% to 4% lower than the input value. It was found that this difference corresponded directly to the amount of delayed energy per fission reaction since MCNP5 does not include delayed β- or ϒ-energy release.

For this study, the power produced per actinide *i* was calculated by the MGRAC code for all the evaluated core designs. For the SAFARI-1 core, the calculation details are shown below:

Table 4 Calculation of the tally multiplication (source multiplier) for the SAFARI-1 core. The power-share per major power producing isotopes was calculated by the MGRAC code. *Values extracted from ENDF/B 6.8. Yellow fields indicate input data.

Fissile isotope	MGRAC Power (%)	Average neutron rel. ν *	Q-Value (eV)*	Delayed β&ϒ (eV)*	Delayed β&ϒ (%)*
^{235}U	93.38	2.437	1.9372E+08	6.50E+06	3.36%
^{238}U	0.59	2.492	1.9806E+08	8.48E+06	4.28%
^{239}Pu	5.48	2.881	1.9992E+08	5.31E+06	2.66%
^{241}Pu	0.51	2.945	2.0198E+08	6.58E+06	3.26%

Weighted ν	Weighted Q-value	Th power (MW)	Delayed β&ϒ (%)
2.463	1.9405E+08	20.00	3.32%

Calculated source multiplier	Predicted power reading of energy tallies
1.584E+18	19.34

3.4 AUTOMATION OF CALCULATIONAL ENVIRONMENT

After generating a homogenized cross-section library with the combination of codes; HEADE, STYX, POLX and LINX; the MGRAC code could be used to simulate the operation of any given reactor design. A drawback of the MGRAC code is the use of text based input files which require manual input of parameters and typing of input cards which unnecessarily takes a lot of time (and might lead to mistakes). In order to increase the efficiency with which core simulations are conducted a number of Visual Basic algorithms have been created and packaged into two different Excel 2007 spreadsheet (which serves as graphical interfaces). The first spreadsheet, called KNERSIS[14], performs the following functions:

- Generates core configuration files (.CONFIG files)
- Generates fresh fuel- and control assembly history files (.HIST files) and updates the component directory (COMP.DIR)
- Generates the core loading file (.LOAD)
- Generates the MGRAC input files (.INP)
- Extracts power-, flux- and mass-profiles

[14] The word KNERSIS is not an abbreviation, it originated from a cartoon series in which the characters; Oscar and Knersis featured.

- Extracts assembly isotopic mass contents (for assembly inventories)
- Provides a graphical loading platform
- Provides concise version control

The KNERSIS package is mainly used to interface with the OSCAR-4 code package. The second package of algorithms, called MAAS (MCNP Automation Algorithm Spreadsheet), is used to interface with MCNP and performs the following functions:

- Extracts isotopic number densities from MGRAC history files for a specific burnup history.
- Treats isotopic number densities for the inclusion of non-tracked isotopes such as aluminium, silicon or molybdenum.
- Converts isotopic number densities to mass quantities
- Calculates node mass densities
- Assigns MCNP material numbers per assembly
- Macro processes lists of fuel- and control assemblies used in OSCAR-4
- Produces input cards for cells and surfaces defining fuel- and control assemblies according to predefined formats in MCNP
- Produces input cards for materials defining nodes in fuel- and control assemblies

Under some cases (see section 3.5.2), the MAAS package was used in an iterative manner to determine surface albedo-matrix values for the MGRAC code input files which greatly simplified the calculation process which was conducted as follows:

- An equilibrium core is first determined with either a best estimate 6 energy group boundary Albedo matrix or a light water surrounded[15], beryllium reflected core as input to OSCAR-4. This core is not realistically representative of a core which will be heavy water reflected, however, the purpose of this step is only to provide for relatively realistic burnup profiles and core actinide mass distributions for the generation of more accurate albedo values.
- The core geometry and isotopic number densities are then extracted using the MAAS package and an MCNP5 simulation is conducted to determine albedo values.

[15] The light water surrounding forms the blanket region. For designs which completely surrounded by only heavy water the term blanket region can be omitted since it forms part of the reflector.

- The MGRAC code is again used in conjunction with the KNERSIS spreadsheet in order to find another equilibrium core (minimizing power peaks) after which the process is repeated until the albedo values converges sufficiently.

The code package relationships are indicated in the diagram below:

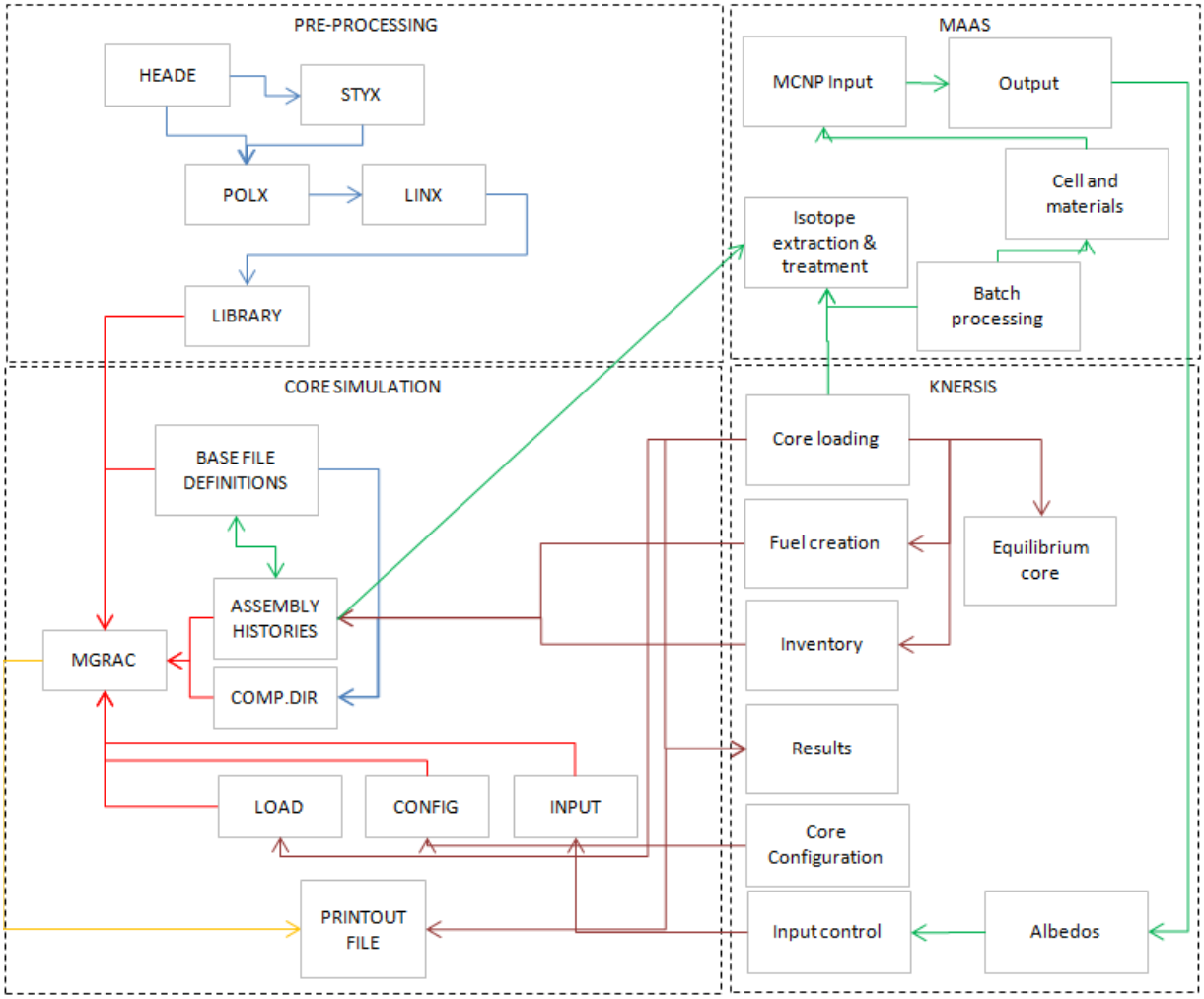

Figure 21 Diagram of the relationships between the different code-packages used for analysing core configurations of varying complexity.

3.5 EVALUATION OF CALCULATIONAL MODELS

This section details the evaluation of different calculation models used for the various studies. Section 3.5.1 details the evaluation of the method used for estimating the operating envelope of a given core design and fuel discharge burnup percentage as described in

section 2.2.4. This section is followed by an evaluation of the MGRAC models, with specific reference to the difference in calculated thermal neutron flux between MGRAC and MCNP5.

3.5.1 Estimation of fuel discharge burnup

A simplified calculational method was developed in section 2.2.4 to enable the estimation of a given core-design's operating envelope (power versus cycle length). This method, which is represented as a correlation (equation 22), can be compared to equilibrium cycle analyses performed with MGRAC by means of comparing discharge burnup percentages for fuel assemblies. The data for this evaluation was, however, only available after the core design study was compiled (chapter 5) and therefore the same designs, as was used for the design study, were used for this comparison. It is important to note, that the predicted burnup data contained in this section does not correspond to those found in the annexure. This is because the prediction used in this section was updated with data from the final equilibrium cycle designs, as opposed to the predictions contained in the annexure which contain estimated pre-equilibrium cycle data.

3.5.1.1 Results

Table 5 Comparison of predicted versus calculated discharge burnup percentages utilizing the correlation depicted in section 2.2.4.

Core design	4 x 4, no in-core irradiation positions	4 x 5, 1 in-core irradiation position	5 x 5, 4 in-core irradiation positions	7 x 7, 7 in-core irradiation positions
Average core power fraction input for control assemblies	0.60	0.66	0.36	0.45
^{235}U-mass consumption [g.MWD^{-1}]	1.15	1.14	1.17	1.08
Predicted average discharge burnup percentage	52.5%	66.3%	57.6%	72.7%
Average discharge burnup percentage calculated in MGRAC	60.5%	69.8%	57.9%	73.2%
Percentage difference (i.t.o. MGRAC)	-13%	-5%	-0.5%	-0.7%

3.5.1.2 Discussion

Table 5 depicts discharge burnup percentages calculated by the correlation described in section 2.2.4 as well as discharge burnup percentages calculated by equilibrium cycle

studies with MGRAC. The data supplied to the correlation originated from calculated data from the core design study.

The correlation used for the prediction, required the following parameters:

- Fuel- and control assembly ^{235}U mass content,
- Amount of fuel- and control assemblies,
- Frequency of changing fuel- and control assemblies (average amount per cycle),
- Average control assembly power divided by average fuel assembly power,
- Core average ^{235}U mass consumption (grams per MWD),
- Total core power, and
- Cycle length.

The prediction correlation shows fairly large differences for the smaller core designs (13% and 5% respectively) and smaller differences for the two larger designs (less than 1%). The 8 by 9 and 9 by 9 core designs were not included in this study since the designs are based on actual, known operating envelopes (no predictions are done).

3.5.1.3 Conclusion

The discrepancy in discharge burnup percentage is most likely to be incurred by the fundamental assumption that each assembly experiences the same average power; however, this assumption is sensitive to the amount of burnup steps experienced by a given fuel assembly, which in turn is sensitive to both the frequency of change and the amount of fuel assemblies (few assemblies changed infrequently or many assemblies changed frequently). It can also be attributed to the differing length of each burnup chain for a given design. It is therefore expected that the assumption should be more accurate for core designs with more fuel assemblies. Given the simplicity of the correlation, it provides an adequate prediction of the operating envelope of any given design.

3.5.2 Core modeling in MGRAC

Two different cases were applied to the modeling of the evaluated core designs in MGRAC; the first is for a light water surrounded (mostly beryllium reflected) design and the second is for a heavy water reflected design. For the light water case the behavior of the core was captured, in sufficient accuracy, by modeling only 2 additional rows of light water (beyond the physical core boundary). This is because the reduction in neutron flux within the light water surrounding occurs so rapidly that additional rows do not improve either the accuracy of the calculation or the prediction of reactivity. This was not however, the case for the heavy

water reflected designs where significant changes in both the predicted reactivity and the calculated flux values were found for each additional row. In reality, the effect of additional heavy water increases up until 300 cm of additional heavy water. Therefore, in order to keep the MGRAC models small and to ensure convergence at all stages, two layers of heavy water were modeled after which the outer surfaces were given equivalent albedo treatments (in contrast to the light water case were black surfaces were used). This approach does, however, incur a problem which needs to be detailed:

The physical requirements for the specification of albedo values in MGRAC is: the specification of the albedo values, β_j, for reflecting from energy group j to both the same group again as well as to all the other energy groups N (with j ϵ [1,N]). Therefore, the following matrix is required:

$$\begin{bmatrix} \beta_{1,1} & \beta_{1,2} & \cdots & \beta_{1,N} \\ \beta_{2,1} & \beta_{2,2} & & \\ \vdots & & \ddots & \\ \beta_{N,1} & & & \beta_{N,N} \end{bmatrix}$$

By constructing an MCNP5 model from MGRAC history files for an equilibrium core modeled as a beryllium reflected core, an initial estimate of the diagonal terms of the matrix can be obtained. The off-diagonal terms, however, are not trivial to determine and for this study were set to zero. This matrix was then used as input to the same MGRAC model but without beryllium reflection and only 2 rows of heavy water, after which another equilibrium core was calculated. The equivalent diagonal albedo matrix was then recalculated (with MCNP5) and the process repeated until convergence was satisfactorily achieved.

Because this study involved only a conceptual design study, for which the specification of fuel burnup profiles, reload strategies and power profiles would normally have involved averaged values, which are merely representative of actual profiles and reload strategies; the inaccuracies introduced by approximating reflection boundaries with equivalent albedo-values needed to be evaluated. This was done by comparing MGRAC axially averaged thermal neutron flux distributions as well as axial thermal neutron flux profiles, for the active core sections and within relevant assemblies, to that of MCNP5.

In order to comprehensively compare both fuel assembly- and control assembly fluxes together with the effect of in-core irradiation positions, a medium sized core (5 x 5) was prepared with 4 in-core irradiation positions (core designs are discussed in later sections, the

specific core used for this comparison is among the evaluated designs). The core design was prepared according to the process outlined in section 3.3. The in-core axially-averaged thermal fluxes (E_n< 0.625 eV) were then calculated with MGRAC and MCNP5 for both a light water reflected design and a heavy water reflected design (to which equivalent albedo surfaces were applied in MGRAC). In order to generate the MCNP5 model, the process as depicted in section 3.4 was followed. The results are shown below:

3.5.2.1 Results

With equivalent albedo treatment

0.86	1.06	1.01	1.08	0.86
0.92	1.07	0.96	1.08	0.95
0.92	1.08	0.86	1.09	0.93
0.93	1.07	0.96	1.07	0.93
0.86	1.07	1.00	1.06	0.85

No albedo treatment (H_2O blanket region)

0.82	1.02	0.96	1.05	0.82
0.89	1.02	0.92	1.04	0.91
0.87	1.04	0.82	1.04	0.88
0.90	1.03	0.92	1.03	0.90
0.82	1.04	0.96	1.03	0.81

Figure 22 Comparison of the axially averaged thermal neutron flux calculated over the active core height. Values indicate OSCAR-4 to MCNP5 calculated value ratio.

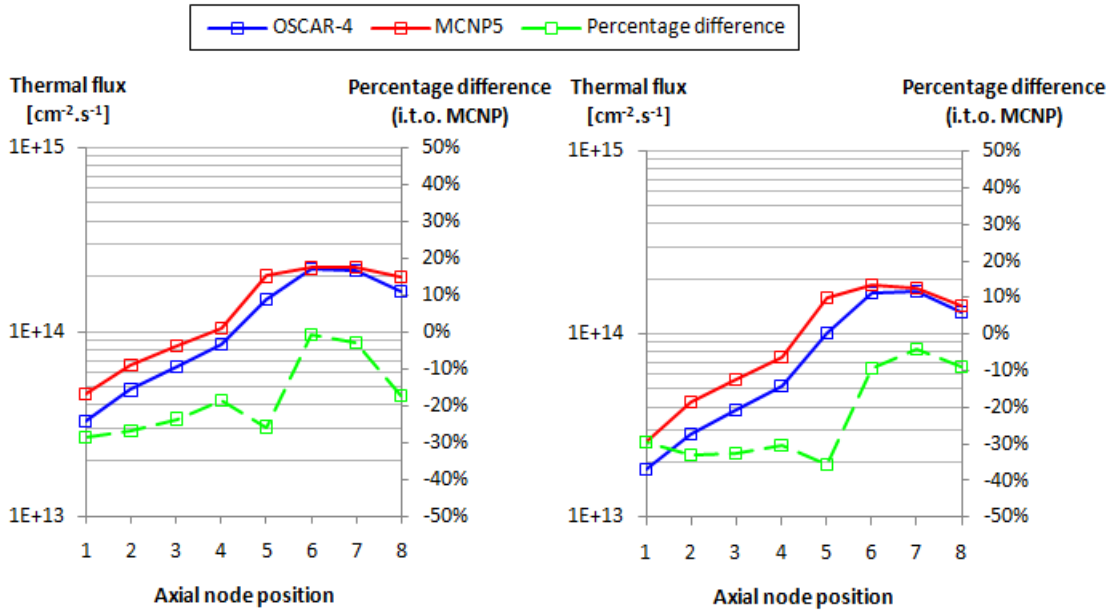

Figure 23 Axial comparisons for control assemblies. (Left) Thermal flux comparison with equivalent albedo treatment. (Right) Thermal flux comparison without albedo treatment. Results includes flux profiles over the active core height.

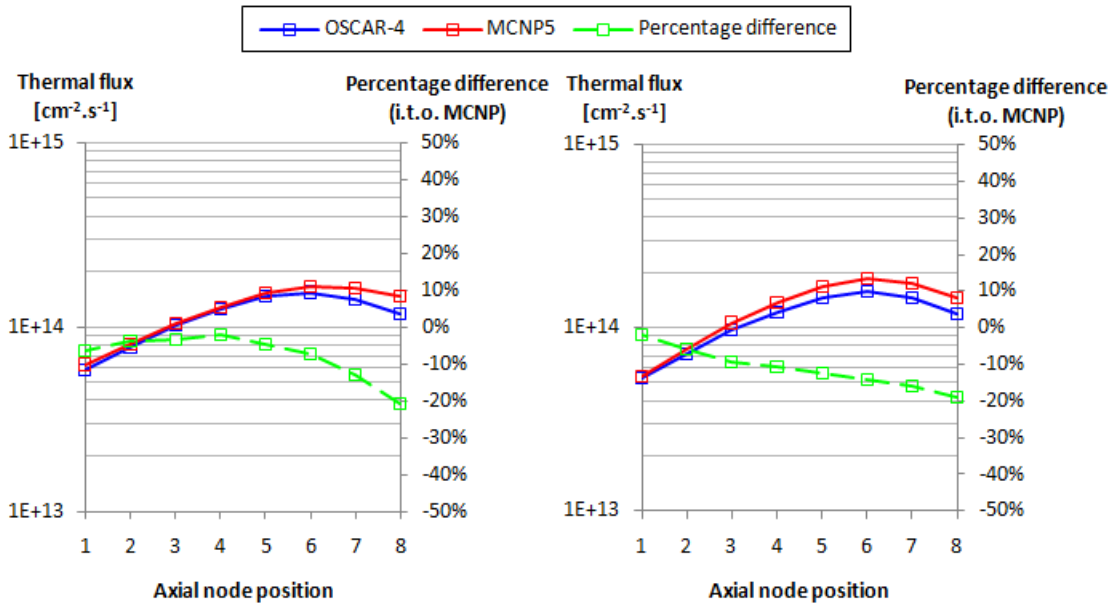

Figure 24 Axial comparisons for fuel assemblies. (Left) Thermal flux comparison with equivalent albedo treatment. (Right) Thermal flux comparison without albedo treatment. Results includes flux profiles over the active core height.

3.5.2.2 Discussion

The axially averaged thermal neutron flux distribution calculation comparisons between MGRAC and MCNP5 are shown in figure 22 for both a case where an equivalent albedo treatment was used and a case where it was not. For the albedo treated, heavy water reflected case, the calculation indicated a critical core at a control bank height of approximately 50% withdrawn; however, for the case where the core was light water reflected, the calculation indicated a sub-critical design regardless of control bank height. Therefore, in order to comprehensively compare the two cases, a control bank withdrawal of 50% was applied to both the MGRAC model and the MCNP5 model, in both cases. This approximation can be done because the calculation of k_{eff}-eigenvalues with MGRAC and MCNP5 is weakly dependant on the calculation of the flux distribution. The results indicated that for both cases (with albedo treatment and without), the percentage difference between MGRAC and OSCAR-4 within fuel assemblies is within 10%. For control assemblies however, the difference is on average 14% for the albedo treated case and on average 18% for non-treated case.

Axial profiles of the thermal neutron flux within selected control- and fuel assemblies, respectively, are shown in figure 23 and figure 24. The profiles were selected for representing the most axial differences. For the fuel assemblies, the difference is up to 20%

in both cases and for the control assemblies, predominantly more than 30% within the absorber section and predominantly below 20% in the fuel follower section (for both cases).

3.5.2.3 Conclusion

For conceptual investigations of neutronic performance; burnup-profiles, loading patterns and power profiles are normally specified as averaged values, representing an overall realistic condition for any given core rather than explicit parameters. By approximating the modeling of reflector boundaries with equivalent diagonal-albedo-matrices, the results indicate that the accuracy of the calculation remains relatively unchanged.

A matter of concern is the fairly large differences in axial thermal neutron flux profiles between MGRAC and MCNP5. This difference is a possible congregation of many factors;

- Firstly, the codes (OSCAR-4 and MCNP5) use different isotope neutron cross-section libraries, with OSCAR-4's HEADE code utilizing a Winfrith Improved Multi-group Scheme Library (WIMS Library) and MCNP5 utilizing the Evaluated Nuclear Data Files B VII Library (ENDF/B VII Library).
- Secondly, the approximations introduced by diffusion theory. However, homogenized cross-sections are utilized to solve the diffusion equation for nodalized geometry. Together with correct equivalence parameters (between the diffusion solution and the transport solution) and correct region-wise homogenization, the nodal diffusion solution should be able to recover the transport solution calculated with HEADE. This then reveals the third and possibly most influential factor, which is:
- The calculation of equivalence parameters and the effect of homogenization. HEADE is used to assemble a library of homogenized cross-sections from 2D representations of assembly geometries and materials. The environment, in which these assemblies are modeled, fundamentally influences the accuracy of the associated homogenized cross section (i.e. generating homogenized cross-section for an assembly directly adjacent to a control absorber but using the cross-section, in MGRAC, 16 cm away from a control absorber). In practice, it would require the generation of many different cross-sections (perhaps even in 3D instead of 2D), in all the possible configurations, to be able to properly represent the equivalent nodal fluxes. This factor is evident in the differences calculated for control assemblies since the homogenization of control absorber cross-sections requires the STYX code, which does not generate equivalence parameters.

With consideration of the factors introducing differences in the thermal neutron flux profiles, the conceptual nature of the study remains the most important factor justifying the use of MGRAC to develop realistic core configurations and burnup profiles. Should MGRAC not be used as a burnup estimator, it would become challenging to estimate realistic core mass distributions and profiles. Thus, it is concluded that for purposes of a conceptual study, the results are sufficiently realistic.

3.6 SUMMARY

This chapter detailed the calculational methods used to study different fuel and core designs whereby the constituents of the OSCAR-4 package were utilized to derive realistic material inventories to be used in MCNP5. The chapter also detailed the methodology through which the different software codes were interfaced with each other as well the inaccuracies and uncertainties that were introduced. In the next two chapters, the results that were produced by applying these methods are detailed and discussed.

CHAPTER 4 FUEL ASSEMBLY DESIGN

Parameters of interest during the design of fuel assemblies include the following:

- Plate geometry,
- Cladding material,
- Meat-material metallurgy,
- Plate uranium-content,
- Number of plates,
- Burnable absorbers and
- Coolant gap size.

Of these parameters, the plate width and height as well as the cladding material can be specified generically as motivated in section 0. Therefore the investigation of the design is limited to the effects of the variation of the coolant gap size, fuel plate meat material, the number of plates and burnable absorbers.

The general strategy for determining the fuel design is to assemble a library of fuel assemblies with a range of performance characteristics. From the baseline, 340 g ^{235}U per 19 plate assembly, the assembly ^{235}U-mass content and the number of fuel plates need to be varied and the effects observed. For a different amount of fuel plates, the assembly might no longer fit into the desired 8 cm by 8 cm grid geometry and therefore an additional modification needs to be considered, which is to reduce the size of the coolant gap.

4.1 COOLANT GAP SIZE

4.1.1 Method

The baseline fuel assembly's coolant gap is 0.2932 cm; however, the size of this coolant gap influences the fuel-to-moderator ratio and therefore determines whether the core will be over- or under-moderated as well the extent of the given fuel-to-moderator ratio for any burnup state. This influence is largely determined by the fuel loading per plate. By analyzing the infinite reactor multiplication factor, k_∞, with the HEADE code, the effect of different amount of fuel plates can be ignored since the infinite reactor concept dismisses any modular character.

For the analyses, coolant gap thicknesses were varied and corresponding k_∞ values were determined. This was done for the following meat material configurations with the same enrichment and cladding thickness:

1. Uranium-silicide-aluminium dispersoid with 17.5 grams ^{235}U per plate corresponding to a meat uranium density of 4.6 $gU.cm^{-3}$ and a meat thickness of 0.051 cm.
2. Uranium-silicide-aluminium dispersoid with 22.7 grams ^{235}U per plate corresponding to a meat uranium density of 4.6 $gU.cm^{-3}$ and a meat thickness of 0.066 cm.
3. Uranium- 2 wt% molybdenum -aluminium alloy with 30 grams ^{235}U per plate corresponding to a meat uranium density of 7.8 $gU.cm^{-3}$ and a meat thickness of 0.051 cm.

4.1.2 Results

The HEADE code generates multiple output files for each meat material configuration with each file corresponding to a specified coolant gap size. The results are graphically depicted in figure 25.

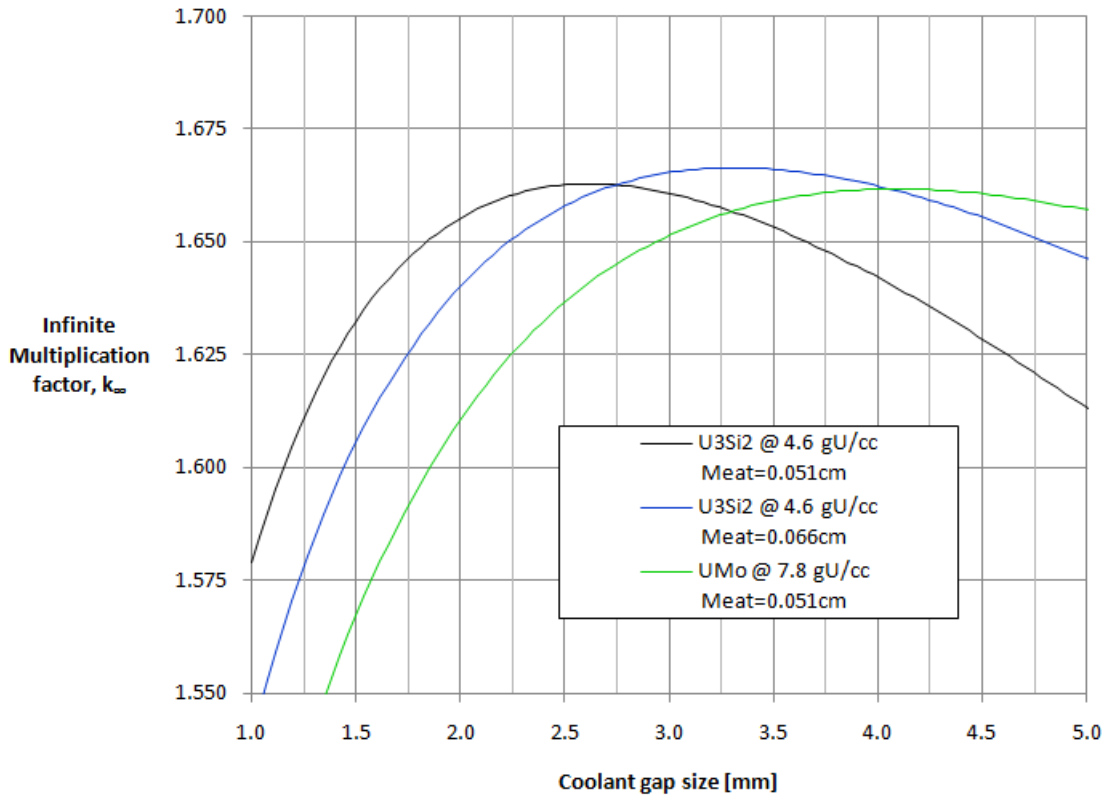

Figure 25 Variation of k_∞ with coolant gap size for a plate type MTR-fuel assembly, for varying meat material configurations.

4.1.3 Discussion

For the uranium-silicide meat material, the coolant gap-size corresponding to the peak infinite multiplication factor is approximately 0.26 cm for a meat thickness of 0.051 cm, and 0.33 cm for a meat thickness of 0.066 cm. The corresponding peak for the high density uranium-molybdenum meat material correlates to a coolant gap size of approximately 0.42 cm. The peak k_∞-factor for all of the meat materials do not differ by more than 0.3%, indicating that no adverse reactivity penalty is effected by using any specific meat material composition.

If a 2 mm coolant gap-size is used (representing a relatively small gap), all of the fuel designs will be under-moderated and the maximum reactivity difference between the designs is about 1700 pcm. If a 4 mm coolant gap-size is used (representing a relatively large gap), the maximum reactivity difference is approximately 730 pcm. Considering the fact that the assembly's longitudinal dimensions will increase with an increase in gap-size as well as the fact that a smaller gap-size will allow more plates to be added to the fuel assembly, it would be of more benefit to keep the gap-size as small as possible than to attempt to optimize the reactivity of a fresh assembly. Also, with the addition of more fuel plates, core mass and thus effective reactivity, will increase while the reactivity-penalty per MWD burnup will decrease.

From figure 25 it was also observed that with a decrease in ^{235}U mass-density, the k_∞ versus coolant gap-size curve for an assembly shifts to the left. This means that for a fresh assembly, in an under-moderated state, the assembly will become less under-moderated as burnup increases, since the ^{235}U density effectively decreases (k_∞ curve shifts to the left for a given gap-size). This effect continues up to a certain peak value, after which the assembly enters the over-moderated regime. The expected behaviour of a fuel assembly with an increase in burnup is depicted in the figure below:

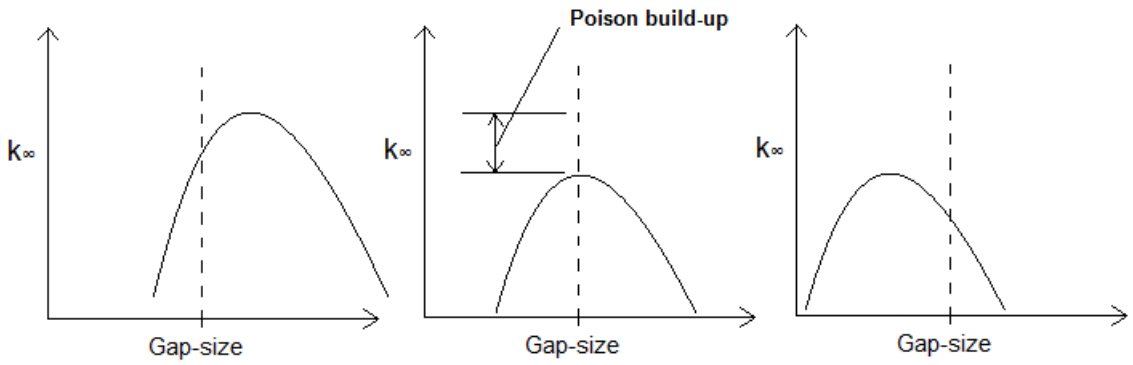

Figure 26 Depiction of the possible response of a fuel assembly's criticality behaviour with an increase in burnup.

4.1.4 Conclusion

As depicted in figure 25 and figure 26, the study found that a coolant gap-size in the range between 2 and 4 mm should not introduce adverse fuel-to-moderator penalties. Also, it was found that an assembly will inadvertently become over-moderated as burnup progresses which poses a concern regarding the moderator-density reactivity feedback-coefficient (hotter and less dense moderator will lead to an increase in reactivity); however, this factor needs to be evaluated in the same scope as the moderating power ($\xi\Sigma_s/\Sigma_a$) of the moderator which might still indicate a negative moderator-temperature feedback.

4.2 NUMBER OF FUEL PLATES

4.2.1 Method

With the selection of meat materials defined in section 4.1, a collection of fuel assembly configurations were modeled in the HEADE code. Fuel assemblies with 19 plates, 21 plates and 23 plates were investigated. For each of these configurations, the following options were evaluated, keeping the enrichment and cladding thickness constant:

- Uranium-silicide-aluminium dispersoid with a meat uranium density of 4.6 gU.cm^{-3} and a meat thickness of 0.051 cm and a coolant gap size of 0.29 cm.
- Uranium-silicide-aluminium dispersoid with a meat uranium density of 4.6 gU.cm^{-3} and a meat thickness of 0.066 cm and a coolant gap size of 0.29 cm.
- Uranium-silicide-aluminium dispersoid with a meat uranium density of 4.6 gU.cm^{-3} and a meat thickness of 0.066 cm. The gap size is reduced in order to allow the assembly to fit within the desired 8 cm square.

- Uranium- 2 wt% molybdenum aluminium alloy with meat uranium density of 7.8 $gU.cm^{-3}$ and a meat thickness of 0.051 cm and a coolant gap size of 0.29 cm.

For each option, the HEADE code was used to calculate the infinite multiplication factor, k_{∞}, versus assembly burnup.

4.2.2 Results

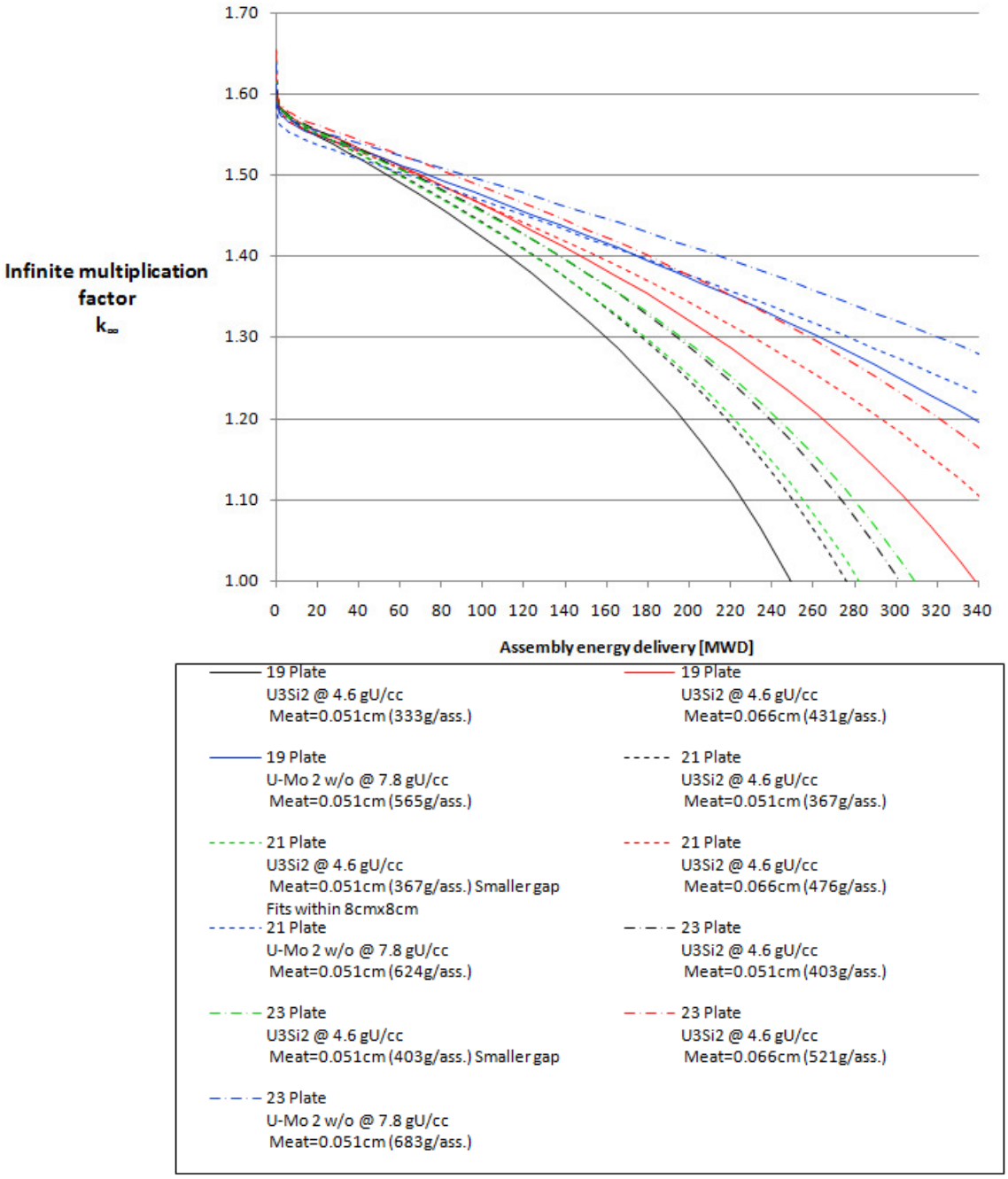

Figure 27 Fuel assembly infinite multiplication factor versus energy delivered.

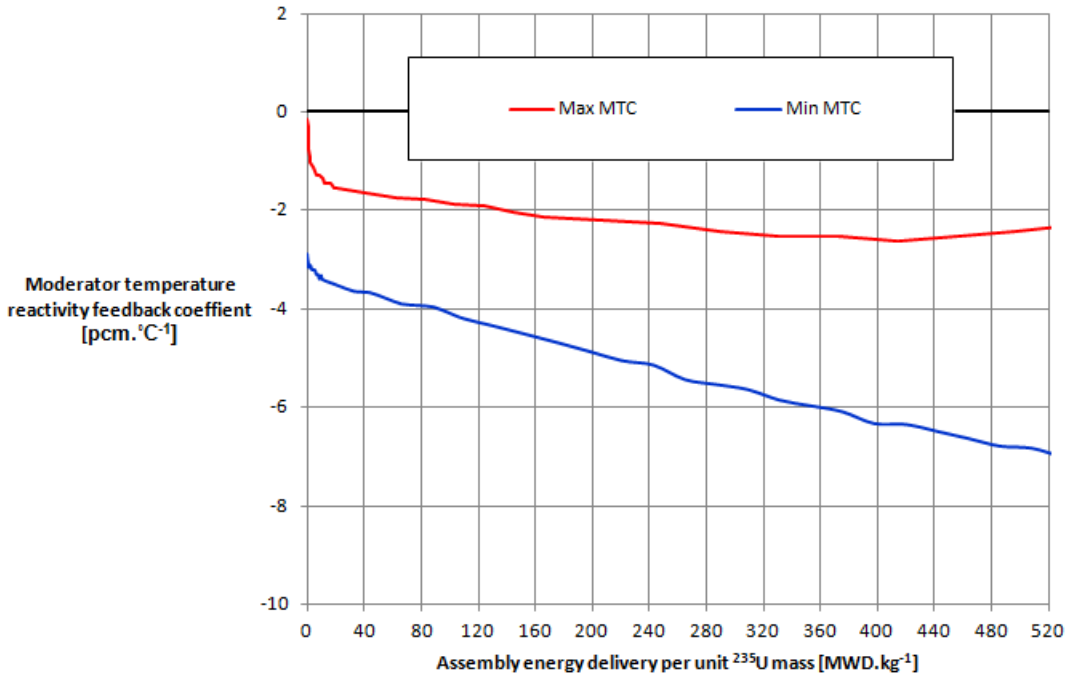

Figure 28 Maximum and minimum calculated moderator-temperature reactivity-feedback coefficient for the evaluated fuel assembly designs. Nominally the ^{235}U consumption for research reactors is 1.21 g ^{235}U per MWD.

4.2.3 Discussion

The inherit advantage of using high uranium-loading fuel materials is evident in figure 27. In this figure, the solid lines represent 19 plate fuel assemblies, the singularly dashed lines represent 21 plate fuel assemblies and the dashed-to-dot lines represent 23 plate fuel assemblies. All lines black in color denote the uranium-silicide material with a meat thickness of 0.051 cm while all green lines denote the same material and meat thickness but with a coolant gap suitably chosen to keep the assembly 8 cm by 8 cm in size. Red lines indicate the uranium-silicide material with a meat thickness of 0.066 cm. Finally, the blue lines denote the uranium-molybdenum material with a meat thickness of 0.051 cm.

For all the designs, the initial reactivity was found to be high, but decreased rapidly during the initial burnup period. This effect is a result of the build-up of fission product poisons, especially ^{135}Xe, in the fuel material. Other differences in the initial reactivity are mostly due to the different moderator-to-fuel ratios of the designs.

The designs with adjusted coolant gap sizes showed a minor delay in the decrease of reactivity, which can directly be contributed to the moderator-to-fuel ratio since the curve, as contained in figure 25, will also be shifted to the left. This means that these designs first experience a relative increase in reactivity (opposed negatively by the fuel burnup) before

resuming the ordinary burnup profile (i.e. the designs first climb the hump of moderator-to-fuel ratio before going down).

As expected, with more uranium loading per assembly, the assembly can remain reactive for longer and is approximately coherent with the nominal 1.21 g ^{235}U per MWD consumption. Therefore, for a ^{235}U increase of 100 grams, a corresponding 83 MWD increase in energy delivery capacity can be expected. Another interesting observation is the characteristic shape of each curve, with a downwards “droop” as lifetime progresses, which is a result of the continual build-up of absorbing fission products, like samarium.

For a design with uranium-silicide as meat material and with less than 23 plates, i.e. the 21 plate design, with a meat thickness of 0.066 cm and resultant 476 g ^{235}U loading, resulted in the maximum energy delivery.

The maximum and minimum moderator-temperature reactivity-feedback coefficient profiles are shown in figure 28. These profiles were chosen amongst the entire selection of profiles calculated for each fuel design. Both profiles indicate a negative feedback coefficient, which remains negative over the entire lifetime of a fuel assembly.

4.2.4 Conclusion

For an assembly with a given amount of fuel plates, coolant gap size and meat thickness, it was found that the infinite core reactivity increased with an increase in uranium loading. In cases where the coolant gap size was decreased, in order to make the assembly fit into an 8 cm by 8 cm square, the net effect was a delayed decrease in reactivity value with burnup progression. Therefore, reducing the coolant gap size will mostly be beneficial to the design from the neutronic point of view, although the effect on the thermal-hydraulic performance needs to be evaluated and might be a limiting factor.

Considering the fact that 23 fuel plates, within an 8 cm by 8 cm square assembly, apparently challenges the thermal-hydraulic and structural design elements judging by the lack of these designs in existing reactors, it would be fitting to select a known and proven design with 21 fuel plates. Therefore, the 21 plate uranium-silicide assembly, with a meat thickness of 0.066 cm, is selected as the design basis fuel assembly for the core evaluation study.

As discussed in section 4.1.4, the fact that a design operates in the over-moderated regime could incur concerns regarding the reactivity feedback coefficient; however, for all the

designs the feedback coefficient indicates no such concern since the coefficient remains sufficiently negative.

4.3 BURNABLE ABSORBERS

4.3.1 Method

In order to investigate the effect burnable absorbers would have on the burnup performance of a fuel assembly, thin natural cadmium wires, 0.05 cm in diameter, embedded on both sides of each fuel plate were modeled. The configuration was only modeled for the 19 plate fuel assembly with the uranium-silicide material and a meat thickness of 0.051 cm. The wires were located over an active length of 30 cm, centered on the fuel centerline.

4.3.2 Results

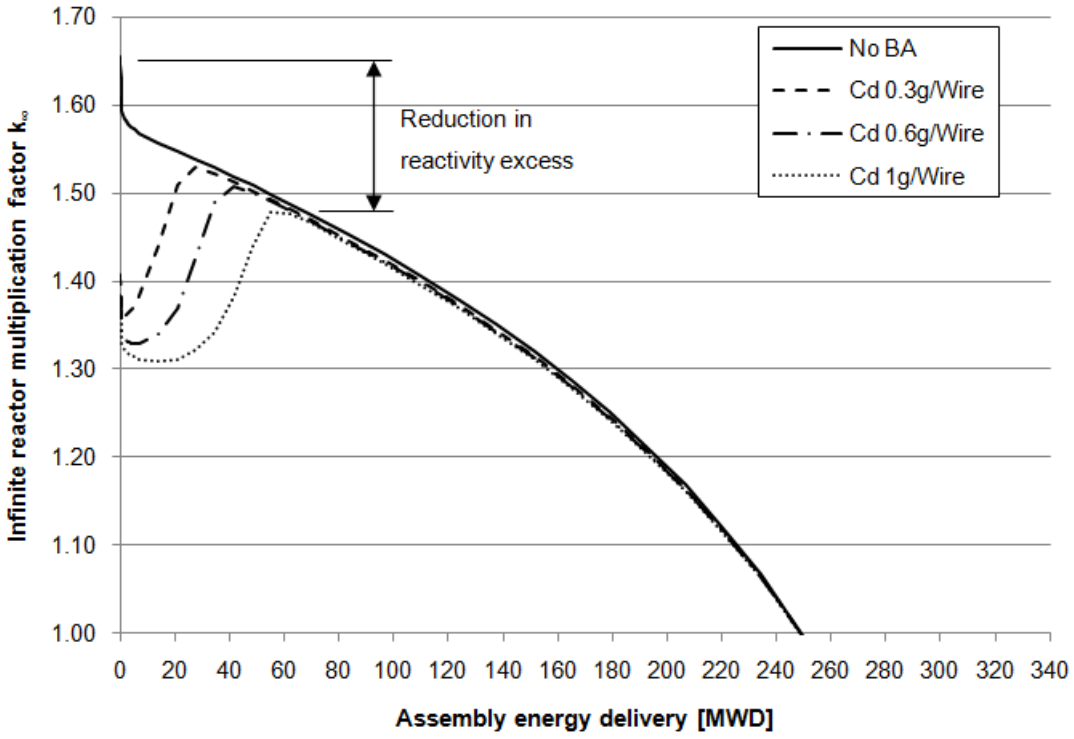

Figure 29 Infinite multiplication factor versus assembly depletion for a 19 plate fuel assembly with uranium-silicide as meat material, a meat thickness of 0.051 cm, and 0.05 cm diameter natural cadmium wires embedded on both sides of each fuel plate. The uranium density is approximately 4.6 gU/cm^3.

4.3.3 Discussion

Figure 29 shows that the initial reactivity worth of a fuel assembly can effectively be decreased by means of embedded cadmium wires. The assembly reactivity shows a rapid

increase after approximately 30 MWD with a natural cadmium wire of 0.05 cm in diameter (modeled with the same density as natural Cadmium). This occurs because of the thermal neutron flux self-shielding native to cadmium wires, i.e. because the cadmium is being depleted, the absorption in the area of the wires decrease, which in turn increases the flux, and thus the burnup rate of the cadmium. After approximately 70 MWD the reactivity penalty of this configuration is mostly dissipated.

4.3.4 Conclusion

Using cadmium wires as a means to reduce the initial reactivity worth of a fuel assembly is shown to be quite effective. For core designs where power peaking factors and shutdown margin requirements become challenging to keep within limits, burnable absorbers will provide a suitable remedy with the only cost being, a small increase in design complexity.

4.4 FUEL OPERATING ENVELOPE

This section contains the evaluation of the operating envelope for the fuel assembly design selected in section 4.2.4, according to the design parameters indicated in section 2.2.2.

4.4.1 Maximum coolant velocity

By using equation 1 (section 2.1.3), the critical coolant velocity can be determined:

Table 6 List of input parameters used to determine the critical coolant velocity for the 21 fuel plate design with a uranium-silicide meat material, 0.066 cm in thickness.

Parameter	Symbol	Unit	Value	Reference
Young's modulus for cladding material	E	bar	7.00 x10^5	(Hyde et al., 2005)
Fuel plate thickness	t_p	cm	0.1275	Section 2.1.1
Fuel plate meat thickness	t_m	cm	0.066	Section 4.2.4
Coolant gap size	t_w	cm	0.2936	Section 4.2.4, implicit in fitting the assembly into 8x8 cm square
Coolant pressure	P	Pa	225 000	Estimated design value
Coolant saturation temperature	T_{sat}	˚C	124	(Cengel, 2006)
Bulk coolant temperature	T_b	˚C	43	Estimated design value
Coolant density, at inlet temperature of 40˚C	ρ	kg.m^{-3}	992.1	(Cengel, 2006)
Poisson's ratio	ν	-	0.35	Estimated for common Aluminium alloys

Water channel width	W	cm	6.61	Section 4.2.4, implicit to the modeling of the assembly
Fuel plate heat flux transmitting height	H	cm	70	Section 2.1.1, active fuel height + 5 cm top and bottom
Coolant viscosity	μ	$kg.m^{-1}.s^{-1}$	6.53×10^{-4}	(Cengel, 2006)
Prandtl number for coolant at inlet temperature of 40˚C	Pr	-	4.32	(Cengel, 2006)
Thermal conductivity of the coolant at 40˚C	k	$W.m^{-1}.K^{-1}$	0.631	(Cengel, 2006)

$$V_{crit} = \left[\frac{15\times10^5 E({t_p}^3 - {t_m}^3)t_w}{\rho W^4(1-\upsilon^2)}\right]^{\frac{1}{2}}$$

$$V_{crit} = \left[\frac{15\times10^5 (7\times10^5)((0.1275)^3-(0.066)^3)(0.2936)}{(992.1)(6.61)^4(1-(0.35)^2)}\right]^{\frac{1}{2}}$$

$$V_{crit} = 18.19\, m.s^{-1}$$

Applying equation 2:

$$V_{max} = 0.54\, V_{crit}$$
$$V_{max} = 0.54\ (18.06)$$
$$V_{max} = 9.82\, m.s^{-1}$$

4.4.2 Convection coefficient

From the velocity, the Reynold's number can be determined:

$$Re = \frac{\rho V_{max} D_h}{\mu}, \qquad D_h = \frac{2(W\times t_w)}{W + t_w}$$

$$Re = \frac{1\times10^{-2}(992.1)(9.75)(2\times6.61\times0.2936)(6.61+0.2936)}{6.53\times10^{-4}}$$

$$Re = 8.39 \times 10^4$$

Using equation 6;

$$h = \frac{0.023\times k\times Re^{0.8}\times Pr^{0.4}}{D_h}$$

$$h = \frac{0.023\ (0.631)(8.39\times10^4)^{0.8}(4.32)^{0.4}}{1\times10^{-2}(2\times6.61\times0.2936)(6.61+0.2936)}$$

$$h = 40\,258\,W.m^{-2}.K^{-1}$$

4.4.3 Iterative calculation of the limiting heat flux

With all the required parameters in place, equation 5 can be applied; however, the solution of the equation requires an iterative solution. The initial step of the iteration is shown below:

$$Q_{ONB} = 460\,000\,W.m^{-2} \qquad (Estimated\ guess)$$

$$Q_{ONB} = h\left[0.556 \times \left(\frac{Q_{ONB}}{1.796 \times 10^{-3} \times P^{1.156}}\right)^{\frac{P^{0.0234}}{2.828}} + (T_s - T_b)\right]$$

$$Q_{ONB} = 40\,258\left[0.556 \times \left(\frac{460\,000}{1.796 \times 10^{-3} \times (225\,000)^{1.156}}\right)^{\frac{(225\,000)^{0.0234}}{2.828}} + (124 - 43)\right]$$

$$Q_{ONB} = 3.510903\ \times\ 10^{6}\ W.m^{-2} \qquad (New\ guess)$$

The final result for the heat flux is:

$$Q_{ONB} = 3.92\ \times\ 10^{6}\ W.m^{-2} \qquad (Final\ iteration\ guess)$$

$$Q_{ONB} = 40\,055\left[0.556 \times \left(\frac{3.92 \times 10^{6}}{1.796 \times 10^{-3} \times (225\,000)^{1.156}}\right)^{\frac{(225\,000)^{0.0234}}{2.828}} + (124 - 43)\right]$$

$$Q_{ONB} = 3.928\ \times\ 10^{6}\ W.m^{-2}$$

In order to translate this limiting heat flux to an allowable average it was required to apply the overall hot spot factor (see section 2.2.2), the transversal power peaking factor, f_{xy}, the axial power peaking factor, f_z, and the 20% over power condition (usually a SCRAM limit). Thus the allowable average heat flux, Q_{avg}, for the before mentioned fuel design is:

$$Q_{avg} = \frac{Q_{ONB}}{HSF \times f_{xy} \times f_z \times 1.2}$$

$$Q_{avg} = \frac{3.928 \times 10^{6}}{1.34 \times 1.60 \times 1.68 \times 1.2}$$

$$Q_{avg} = 9.08\ \times\ 10^{5}\ W.m^{-2}$$

4.4.4 Conclusion

The average assembly power can be calculated by multiplying the heat flux by the total number of plates, N_{plates}, and their associate active area:

$$P_{avg} = Q_{avg}.N_{plates}.W.H \times 2$$
$$P_{avg} = 9.08 \times 10^5(21)(6.61)(70)(2 \times 10^{-4})$$
$$P_{avg} = 1.765\ MW\ per\ assembly$$

Thus for a 16 assembly core, the maximum allowable total power is $P_{avg} \times 16 = 28.2\ MW$.

It should be noted that this value differs slightly from that found in the annexure; however, the difference can be attributed to the inaccuracy of the hand calculations where only a limited amount of significant digits were used.

4.5 SUMMARY

This chapter detailed the establishment of a suitable fuel assembly for use in the core design study. The coolant gap size, number of fuel plates, and fuel operating envelope were analyzed for their effects on the overall power production. In the next chapter, different core designs are compiled with these fuel selections.

CHAPTER 5 CORE DESIGN

This chapter contains the evaluation of different core designs according to the design parameters established in preceding chapters. Firstly, it details the selection of the reflector design which was a critical design component that allowed a suitable platform for assembling different designs, and since the reflector (or blanket region) forms part of the core exterior (ex-core) it allows the ensuing design to focus on the configuration of interior core components (in-core) only. The chapter then proceeds to the second part, by detailing the evaluation of certain parameters relating to the neutron beam facilities after which, the third part of this chapter details the logical arguments followed during the assembly of core configuration. This part is then followed by the results of the core neutronic design calculations, as well as the discussion thereof. The data for the core design evaluations was compiled with both the OSCAR-4 code package and the MCNP5 code; according to the methodology described in chapter 3 for which most of the data is included in annexure A.

5.1 SELECTION OF THE REFLECTOR TECHNOLOGY

A critical component in the design of the reactor is the combination of materials in the reflector- and or blanket region. Many reactors employ beryllium reflectors (SAFARI-1 is an example) with a light water (H_2O) filled blanket region while newer reactors tend to use a single large heavy water (D_2O) reflector, which inherently dismisses the concept of a blanket region. The primary investigation relating to the reflector design is to compare the flux and reactivity benefits of different reflectors by considering the following configurations:

- A beryllium reflected core with a light water (H_2O) filled blanket region,
- A graphite reflected core, and
- A heavy water (D_2O) reflected core.

5.1.1 Methodology

In order to evaluate the above mentioned reflector designs, a suitable core design was needed as a neutron driver. For this purpose a small 4 by 4 core was used to dismiss the effects of in-core irradiation positions. This core was initially assembled as a heavy water reflected core which had to conform to all the realistic requirements of a safe and economic core as well as to have an equilibrium loading pattern established with as little as possible power peaks. Consequently, the core design was also included in the evaluation of the core designs since all the proper design principles had to be applied.

The core-, reflector- and blanket region configuration used for the study of a quadruple beryllium-assembly reflector is shown in figure 30 and the in-core configuration is shown in figure 40 (section 5.2). The core includes four control assemblies and twelve fuel assemblies. The reflector tank is modelled as a 260 cm diameter tank and was selected as such to correspond approximately to the design of the OPAL reactor.

In order to evaluate the effectiveness of multiple rows of beryllium reflector assemblies the two branch cases were considered; a reflector with 2 rows of beryllium, and a reflector with 4 rows of beryllium.

The effect of the variation of the reflector tank diameter was studied by calculating the core reactivity change from an 80 cm diameter tank to a 320 cm diameter tank.

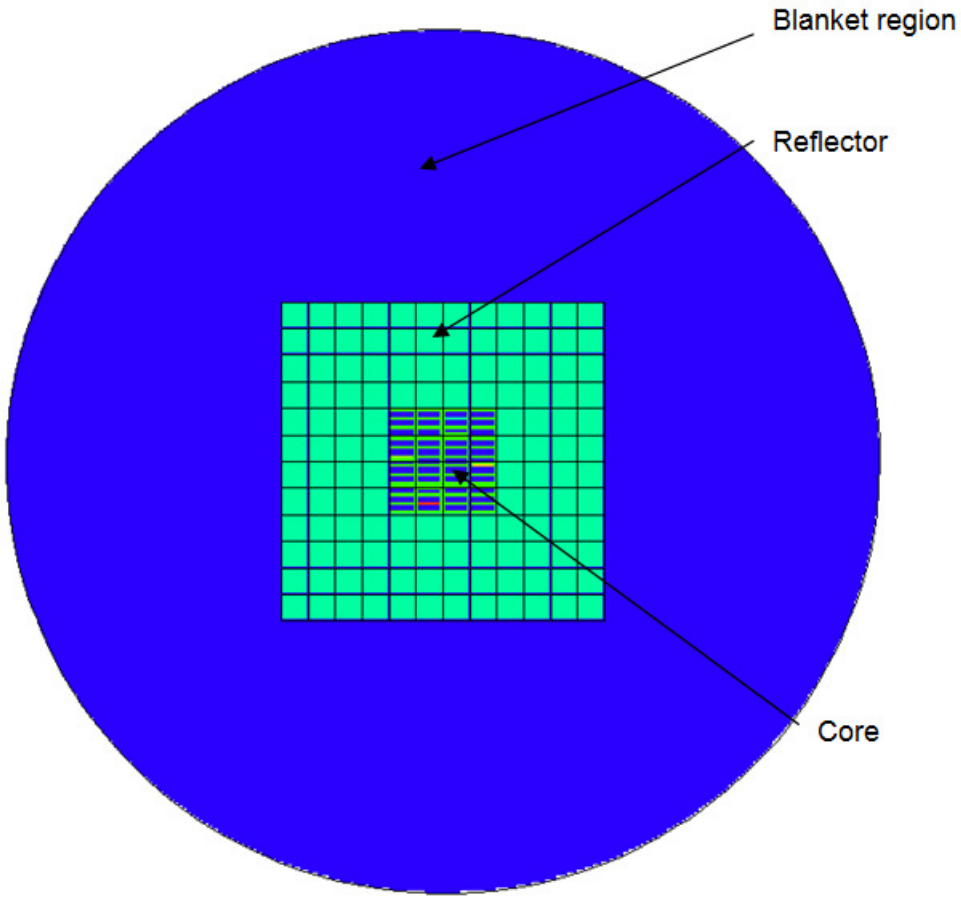

Figure 30 MCNP visualization of the configuration used to investigate different reflector technologies.

5.1.2 Results

Using the 4 by 4 core design as described above, isotopic number densities produced as output from the equilibrium core configuration study were imported from MGRAC assembly history files, into an input file for MCNP5. This was done in order to calculate radial thermal-neutron flux for each reflector design. The results are shown below.

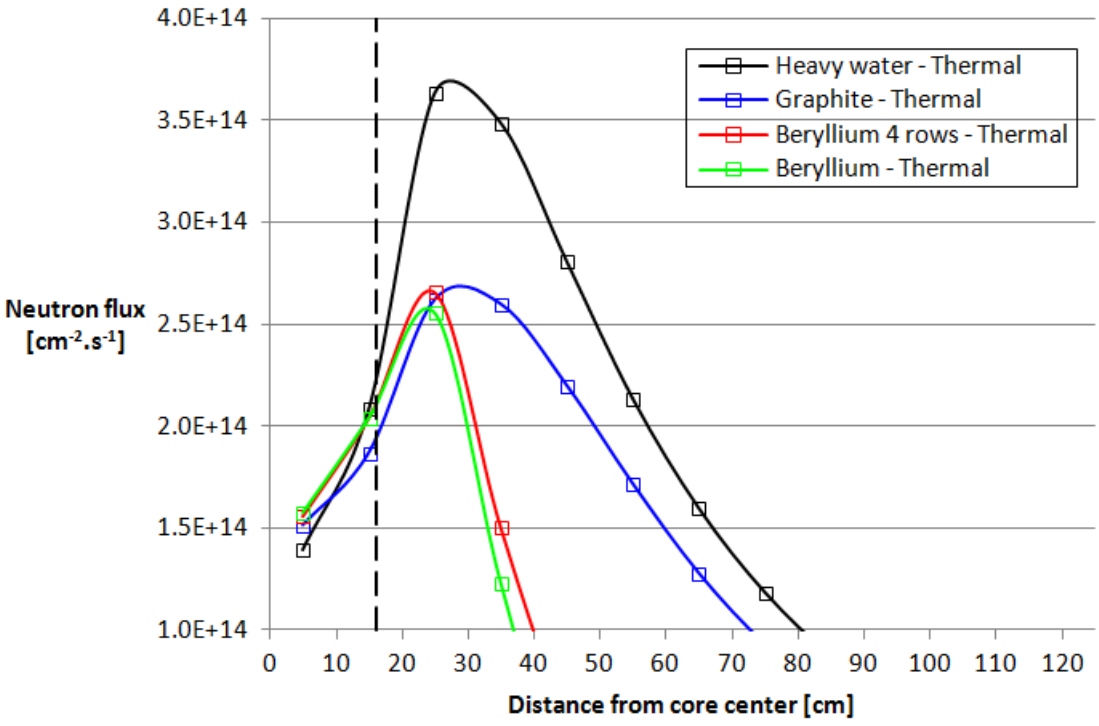

Figure 31 Comparison of the thermal-neutron fluxes (E_n<0.625 eV) surrounding a 4 by 4 core for different reflector materials.

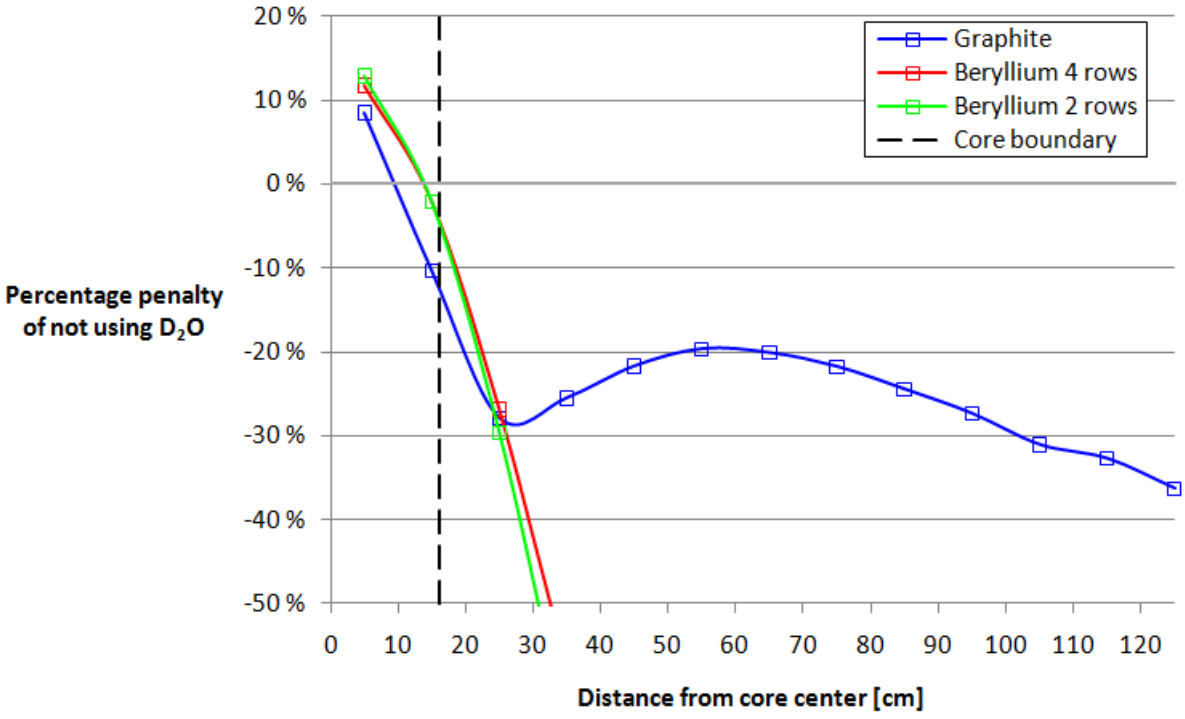

Figure 32 Percentage penalty on the thermal-neutron flux in comparison to the use of a heavy water reflector.

Table 7 Summary of the reactivity changes as a result of different reflector designs, relative to a heavy water reflected 4 by 4 core.

Reflector configuration	Reactivity difference
Heavy water reflected	-
Beryllium reflected, 2 rows	-953 pcm
Beryllium reflected, 4 rows	-694 pcm
Graphite reflected	+919 pcm

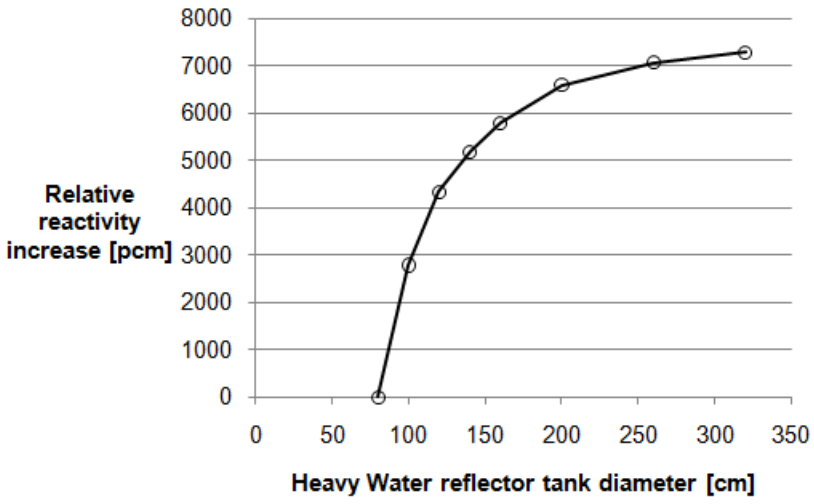

Figure 33 Relative reactivity increase as a function of heavy water reflector tank diameter. Reactivity values calculated with MCNP and normalized to the core reactivity corresponding to an 80 cm diameter reflector tank.

5.1.3 Discussion

From figure 32, it can be observed that the thermal flux for the beryllium- and graphite reflected core differs significantly from a heavy water reflected core. Also, the flux penalty increases considerably from the core boundary outwards. The beryllium reflected core designs display a monotonous decrease in flux to beyond 50% of the heavy water reflected flux within 16 cm (2 row widths) and continues to decrease further. The graphite reflected core shows a decrease in flux down to approximately 30% of the heavy water reflected flux at 28 cm away from the core centerline, after which it shows a slight increase to 20% at 57 cm from the core centerline and then decreases beyond.

The reactivity effects contained within table 7 indicate that the beryllium reflected configurations have the lowest reactivity while the graphite configuration has 919 pcm (~1.3β) more reactivity than a heavy water reflected configuration.

5.1.4 Conclusion

Considering the high flux levels that can be obtained in the blanket region of heavy water reflected core configurations it is clear why modern reactors employ this option. A graphite reflected configuration, although relatively inexpensive, requires many practical considerations such as; gamma-heating, cooling, modularity provided for experiments, the possibility of an independent shutdown system as well as reactivity temperature-feedback. There is no clear distinction between the reactivity of a core reflected with 2 rows of

beryllium and a core reflected with 4 rows of beryllium, indicating the accepted and widespread use of only 2 rows.

A heavy water reflected core configuration is therefore implemented in all ensuing investigations and according to figure 33 a reflector tank diameter of 260 cm is sufficiently optimal for the associated design calculations.

5.2 NEUTRON BEAMLINE ORIENTATION

The effect of orientating the neutron beamlines in non-radial angles is detailed in this section. For each evaluated core design, the peak and optimal (with regards to neutron-photon ratio) output current is contained in section 5.4.4; however, in order to comprehend the observed orientation effects, the beamline study for the same 4 by 4 core (as used in the previous section) will be detailed.

5.2.1 Methodology

As discussed in section 3.3.3, a DXTRAN sphere was applied to the MCNP5 model of each core design, to produce the models as shown figure 34 and figure 35 below. The beamline orientation was then varied, from the 90˚ as shown, to -15˚ in both the thermal neutron- and cold neutron cases (as discussed in section 2.3.3).

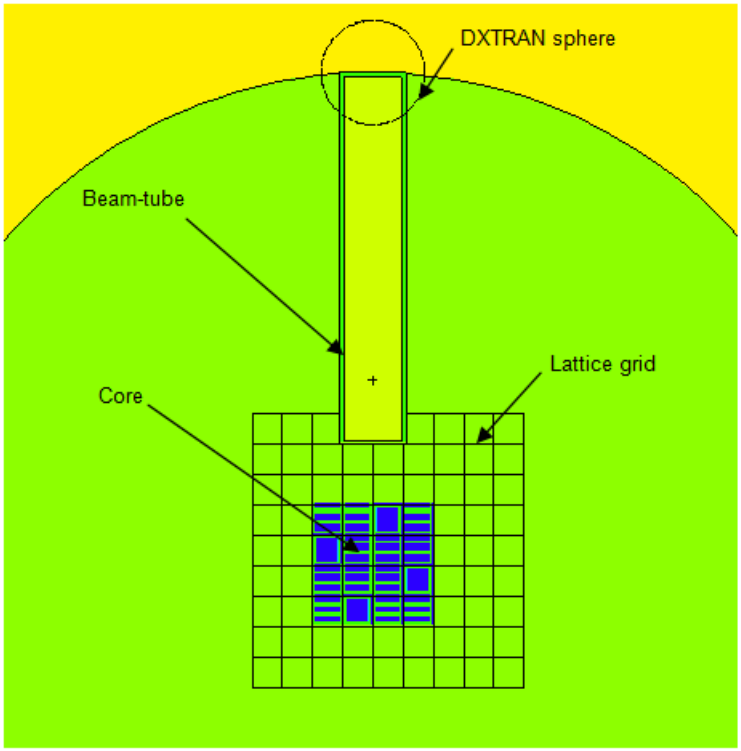

Figure 34 Visualization of the MCNP5 model used to study the directional effects of a thermal neutron beamline. The circular region in the figure indicates the extent of the heavy water reflector tank after which a concrete shielding area was modelled.

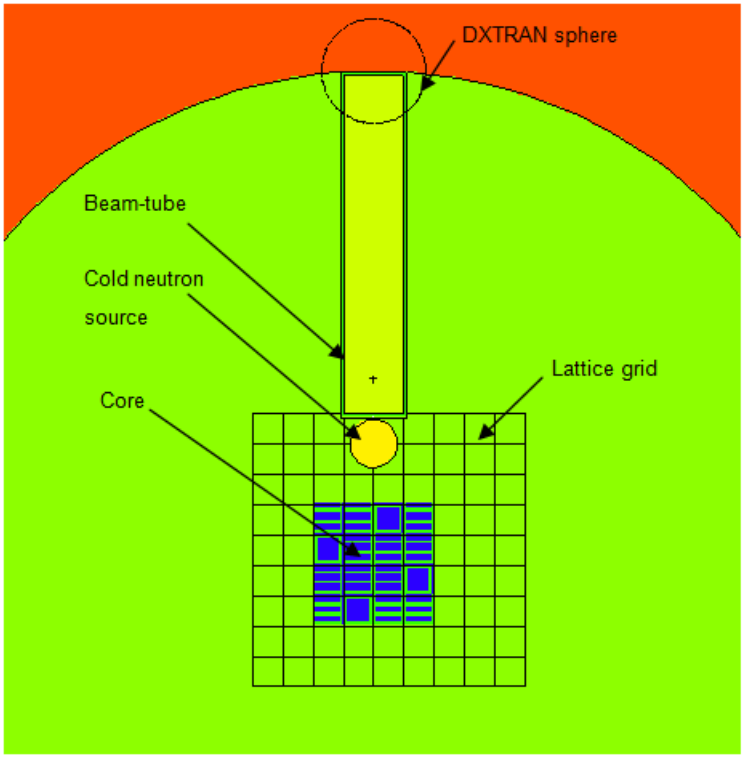

Figure 35 Visualization of the MCNP5 model used to study the direction effects of a cold neutron beamline. The circular region in the figure indicates the extent of the heavy water reflector tank after which a concrete shielding area was modelled.

5.2.2 Results

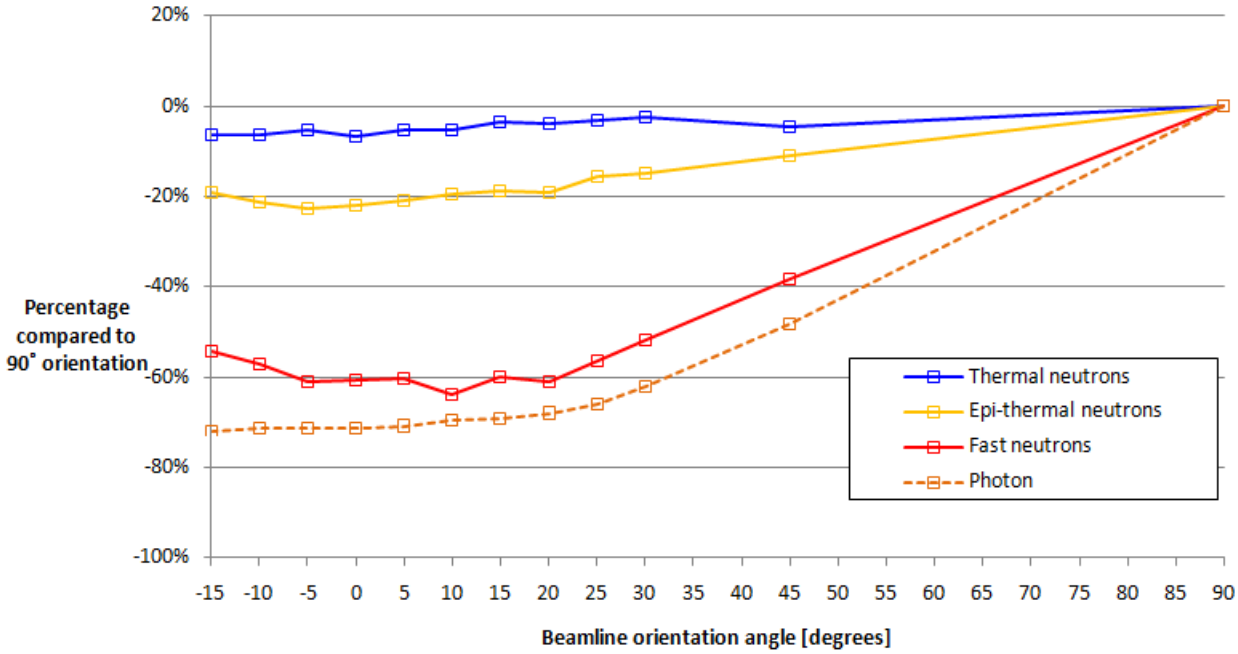

Figure 36 Beamline output current for a thermal neutron (E_n< 0.625 eV) beamline applied to a 4 by 4 core design. Angular orientation is relative to the north core face, where 90˚ corresponds to the radial orientation. Values were calculated with MCNP5 utilizing DXTRAN-spheres.

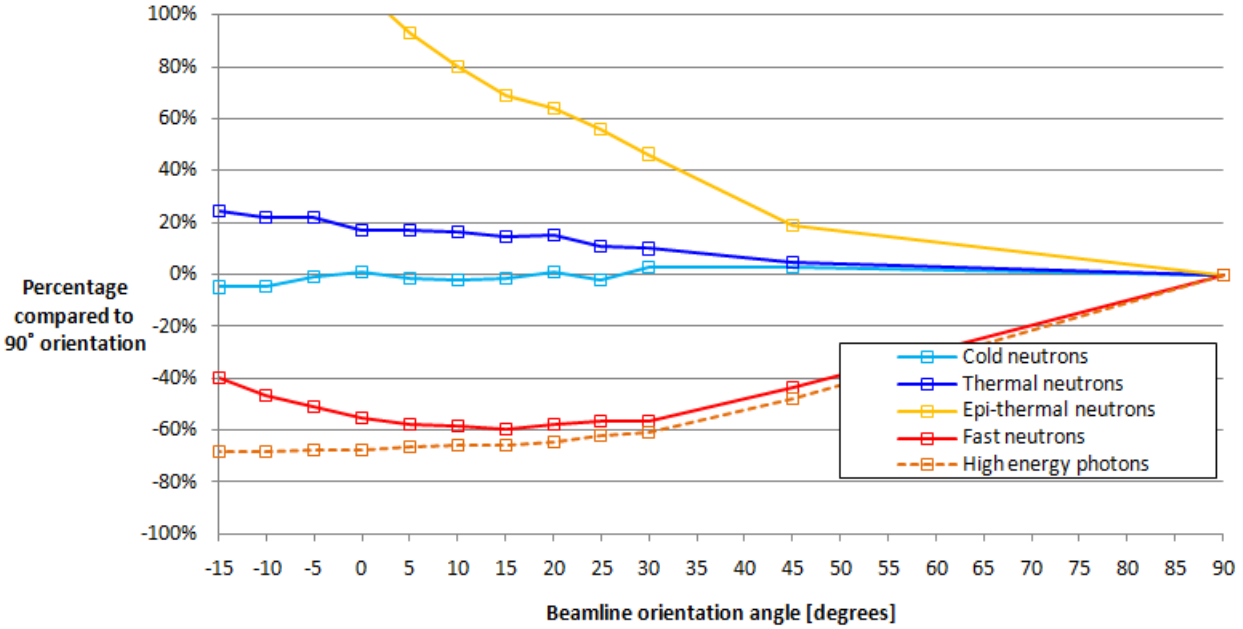

Figure 37 Beamline output current for a cold neutron (E_n< 5 meV) beamline applied to a 4 by 4 core design. Angular orientation is relative to the north core face, where 90˚ corresponds to the radial orientation. Values were calculated with MCNP5 utilizing DXTRAN-spheres.

5.2.3 Discussion

Thermal neutron beamline

The neutron and photon current from the output end of the investigated thermal neutron beamline is shown, as percentages of the 90˚ orientation, in figure 36. The thermal neutron current shows a slight decrease from the 90˚ orientation for all other orientations, indicating the validity of the predicted near isotropic thermal neutron current. The difference in all orientations is less than 10%. The photon current shows a decrease for each additional rotation (from 90˚), indicating a radially-orientated anisotropic photon current at the source location. The maximum decrease in photon output current is slightly more than 70%.

The effects of orientation on the epi-thermal- and fast neutron currents were similar to the photon currents; however, after moving through the tangential orientation (0˚) these currents showed a slightly less decrease. The epi-thermal neutron current, decreases down to approximately 20% with the minimum located at a -5˚ orientation in relation to the tangent, while the fast neutron current decreases to a minimum of approximately 60% at orientations from 20˚ to -5˚ in relation to the tangent. These decreases also indicate radially-orientated anisotropy, however, the effect of a slight increase in the output currents at orientations less than tangential (< 0˚) needs to be considered. This effect occurs because of the radial distribution of iso-fluxes and iso-currents as shown in figure 38 below.

When the beamline is orientated tangentially, it is also orientated tangentially to these iso-fluxes; however, if additional orientation is applied, the beamline moves into areas of higher epi-thermal and fast neutron fluxes and currents. Consequently, these increases are observed not because of an increase at the source location but by additional contributions from regions along the beam tube.

The same increases are however, not seen with the photon currents and can be attributed to the fact that the inclusion of higher photon current regions, which decreases much faster than the neutron currents due to the optical thickness of the heavy water, does not compare to the exclusion of the anisotropic “beams” at the source location (beamline origin).

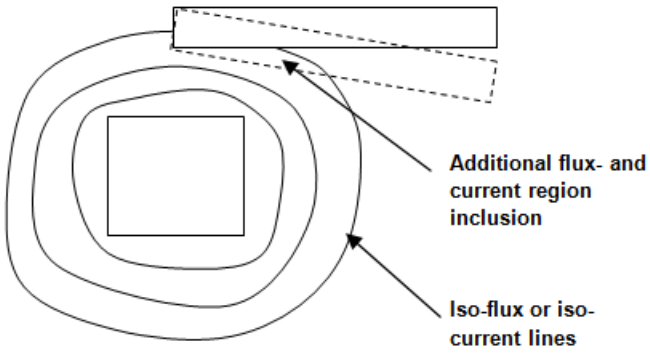

Figure 38 Schematic of the beamline tangential orientation showing the inclusion of higher flux- or current regions when additional rotation is applied.

Cold neutron beamline

The neutron and photon current from the output end of the investigated cold neutron beamline is shown as percentages of the 90˚ orientation in figure 37. The parameter of interest, namely the cold neutron current, shows almost no decrease (other than the statistical variance) up to the tangential orientation, from where a slight decrease of approximately 5% is observed. The photon output current values show very much the same tendency as for the thermal neutron beamline case with decreases up to 70%.

Interesting effects are again observed when observing the output currents for epi-thermal- and fast neutrons; however, the thermal neutron current can also form part of the discussion. The fast neutron current shows a considerable decrease up to an orientation of 30˚ after which it exhibits a near constant decrease of approximately 60% for the range from 30˚ to 5˚; after which it increases at a steeper rate than for the thermal beamline case. Both the epi-thermal and thermal neutron currents show a non-monotonous increase for each additional rotation, with the epi-thermal neutron current increasing beyond 100% while the thermal neutron current increases up approximately 25%.

All of the increases mentioned above can again be attributed to the distribution of iso-fluxes and currents, however, since the beamline is rotated around the centre of the cold neutron source rather than around its origin, the current increasing effects are amplified. This is because instead of the beamline just sweeping (rotationally) over a larger flux- and current region it is also moving, radially, closer to the core centre. These effects are captured in figure 39 below.

The same increases in photon currents are not observed for the same reason as that for the thermal neutron beamline case.

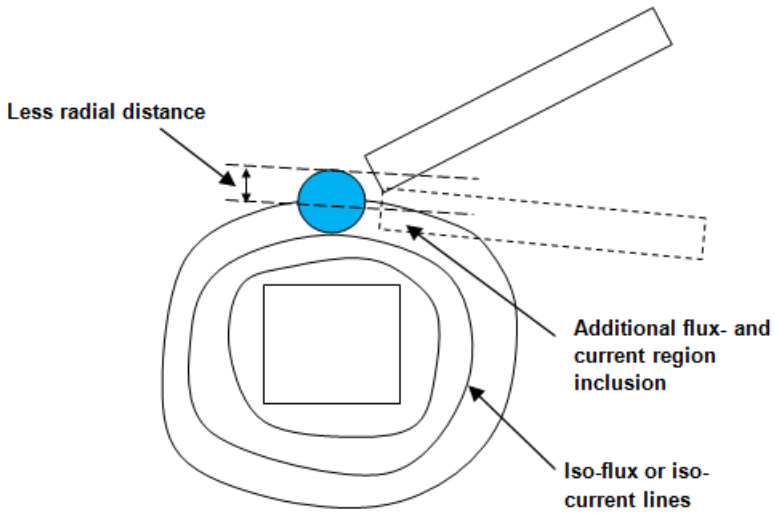

Figure 39 Schematic of the beamline tangential orientation showing the inclusion of higher flux- or current regions when additional rotation is applied as well as the decrease in radial distance from the core due to the rotation around the cold neutron source.

5.2.4 Conclusion

In both the thermal neutron and cold neutron beamline designs, the results show that the corresponding thermal neutron-to-photon current ratio and cold neutron-to-photon current ratio can effectively be increased by rotating the beamline to a more tangential orientation. The results also show that the same adjustment can be made to reduce the fast neutron output current, and in the case of the thermal neutron beamline also the epi-thermal neutron current. Consideration should however, be exercised when applying the same adjustments to the cold neutron beamline design where the results show that a dramatic increase in epi-thermal neutron current will be obtained.

5.3 EVALUATED CORE DESIGNS

For the initial attempt of each core design, the core configuration was assembled according to a logical argument of required attributes: placement of fuel assemblies, placement of control assemblies, reflector assemblies and irradiation positions. Many of these configurations were sampled until suitable selections were available. The selected designs produced by this process are evaluated in this section.

For the initial configuration of each design, a suitable refuelling pattern was established to support the maximum allowable reactor power and cycle length as determined in sections 2.2.2 and 2.2.4. The loading pattern was then modified to:

- minimize the PPF,
- provide for a sufficient shutdown margin, and
- maximize the reactor's energy delivery (product of the operating power and cycle length).

Once the loading pattern produced an acceptable equilibrium state, the core design was used to evaluate the neutronic properties.

The different core designs that were considered varied from a simplified inverse flux trap (flux utilized only ex-core) to a beryllium reflected core with a multitude of irradiation positions. The following sections contain a summary of each design, for which detailed results are included in the annexure.

5.3.1 4 by 4 core with no in-core irradiation positions

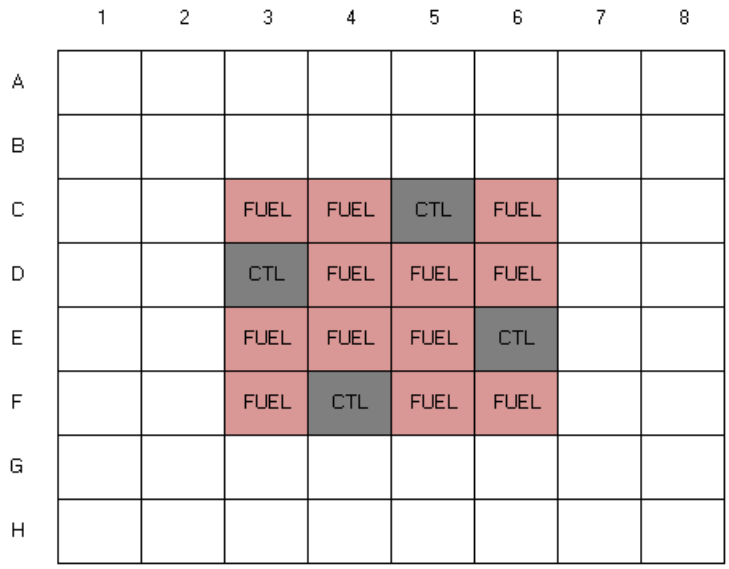

Figure 40 Diagram of the 4 by 4 core configuration.

This core design is an example of an inverse flux trap where no in-core irradiation positions are incorporated. The 4 by 4 geometrical layout was chosen in order to correspond approximately with the OPAL reactor; however, since MGRAC only allows nodal meshes with aspect ratios (width to length ratio) of less than 8, the modelling of the true OPAL control assemblies was not replicated. Instead the core was modelled with 12 fuel assemblies and 4 fuel-follower type control assemblies. The maximum allowable power for this design as determined by the method in section 2.2.2, was found to be approximately 20 MW.

The design evaluation indicated a surprisingly reactive core (large excess reactivity) with the replacement of 2 fuel assemblies per cycle (see annexure A1); however, with the core ^{235}U-mass being relatively low, the burnup rate and consequent reactivity loss rate was found to be high (control bank withdrawal occurs rapidly). Therefore, as an optimization of this design, to allow for more energy production (either higher power or longer cycle length), the design will have to allow for the loading of more ^{235}U mass without exceeding the shutdown margin limitation. This can be done by incorporating burnable absorbers into the fuel assembly design, which will decrease the initial reactivity of fresh fuel assemblies while recovering some reactivity during the operating cycle (see section 4.3). In reality this optimization is applied to the fuel assemblies of the OPAL reactor, which is of a similar design, and which allows operation at 20 MW for up to 35 days with a considerable BOC shutdown margin.

5.3.2 4 by 5 core with a single in-core irradiation position

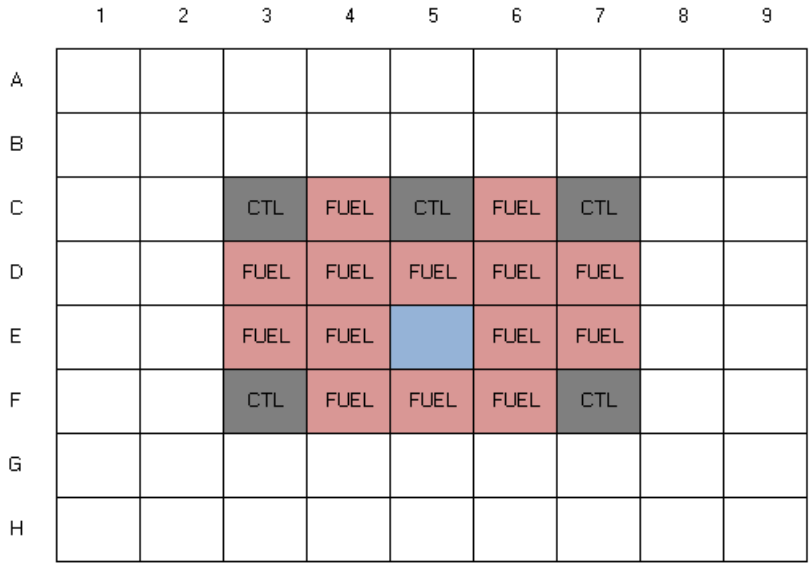

Figure 41 Diagram of the 4 by 5 core configuration.

The inclusion of a single irradiation position was incorporated by adding a column to the 4 by 4 core design, and also adding a single irradiation position to this column. A control assembly was added to position C5 in order to reduce the power peaks in the central fuel assemblies as well to allow for a “none prime number” amount of fuel assemblies (which allows the specification of a trivial loading pattern). The allowable power for this design was found to be slightly higher than that of the 4 by 4 core, at approximately 25 MW, which can be attributed to the increased amount of fuel assemblies (14 fuel assemblies in total) which reduces the average power per assembly. (see annexure A2)

With a higher control-to-fuel assembly ratio than that of the 4 by 4 core, it was found that the design features a relatively large shutdown margin, which allows for many optimizations to be applied. Together with burnable absorbers for increased energy delivery, the design can incorporate a highly neutron-absorbing irradiation target, like a fuel irradiation rig, which would normally adversely affect the operation of a design with a smaller shutdown margin.

Another advantage of this design is that, since it allows for a higher power whilst maintaining a small modular shape, the ex-core thermal neutron flux is much higher than that for the 4 by 4 core.

5.3.3 5 by 5 core with 4 in-core irradiation positions

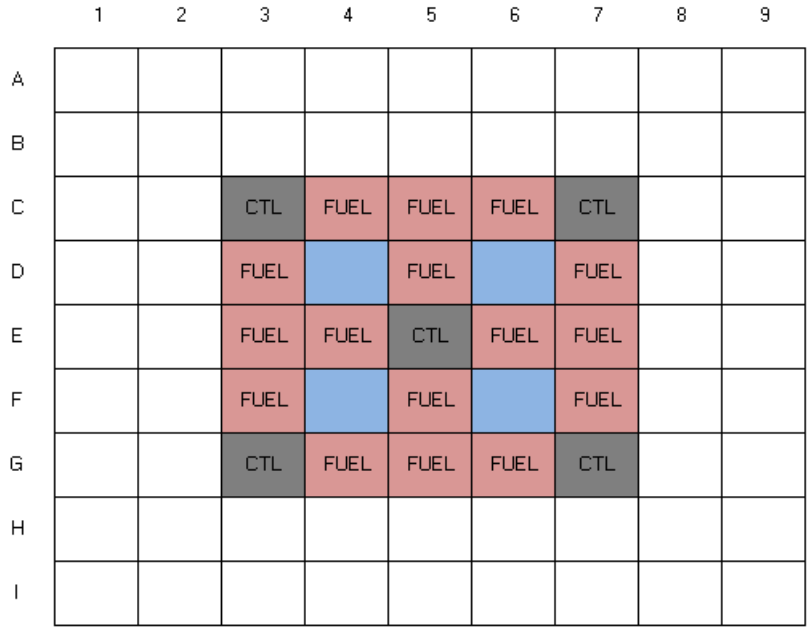

Figure 42 Diagram of the 5 by 5 core configuration.

For another incremental change to the amount of in-core irradiation positions, a symmetric 5 by 5 core was assembled. This design represents a medium-sized core with a considerable amount of in-core irradiation positions in comparison with the previously mentioned designs. With a total of 16 fuel assemblies and 5 control assemblies, the maximum allowable power was found to be approximately 28 MW, which represents an increase of the allowable power for the previous 4 by 5 design in approximately the same proportion as to the increase in the amount of fuel assemblies. Since additional in-core irradiation positions were added, which incur more of a reactivity penalty than the gain brought forward by more fuel assemblies, the amount of control assemblies could be left unchanged. (see annexure A3)

The design evaluation indicated that the core has a relatively high excess reactivity with the replacement of, on average, 3 fuel assemblies per cycle. Suitable optimizations for this could include; a reduced frequency of control assembly change (which needs to be evaluated against the control assembly depletion criteria) and thermal-hydraulic optimizations for increased power production.

With a good combination of in-core irradiation positions and ex-core leakage (performing similar to inverse flux trap), the design should be able to provide a configuration which is easy to cool and inexpensive to operate. These advantages should be weighed against the in-core irradiation capacity which might not be sufficient.

5.3.4 7 by 7 core with 7 in-core irradiation positions

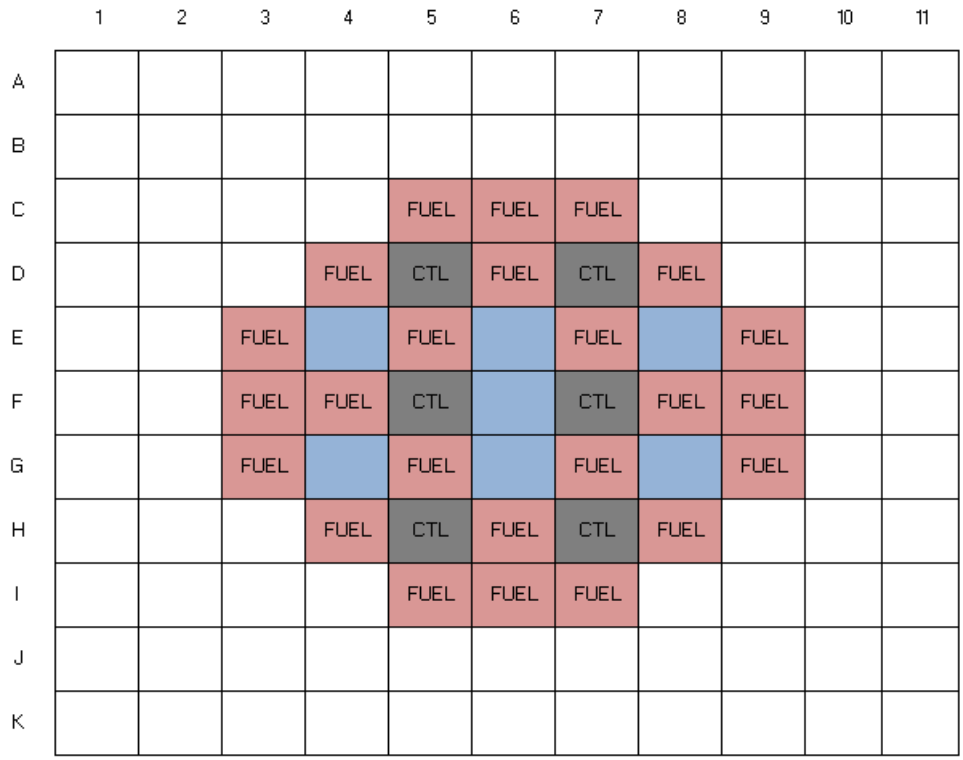

Figure 43 Diagram of the 7 by 7 core configuration.

While maintaining a square symmetry, the 5 by 5 core was enlarged by adding 2 rows to each side to form a 7 by 7 configuration. Due to the size of the core, assemblies which would normally have been located in the corners of the grid could be omitted without introducing an unacceptable reduction in reactivity whilst allowing better control of power peaks. These regions would normally be filled by beryllium filler assemblies in order to maintain a square core-box construction but modelled with heavy water for this study. The centre position, F6, was initially filled with a fuel assembly allowing a slightly higher total power; however, it was instead filled with an irradiation position for the following reasons: firstly, placing an irradiation position in F6 instead of a fuel assembly resulted in a very high thermal flux peak in this position (higher than that found in the other positions); secondly, the placement added to the in-core irradiation capacity of the design; and thirdly, an additional fuel assembly would have resulted in an uneven number of fuel assemblies which posed a reloading pattern challenge (25 fuel assemblies instead of 24). (see annexure A4)

The allowable power for this design was found to be approximately 40 MW and even with a large amount of in-core irradiation positions a suitable operating envelope could be established by replacing 4 fuel assemblies per cycle. In order to allow for even more energy production, a larger amount of fuel will have to be loaded which in turn will cause the

shutdown margin limit to be violated, and therefore would necessitate the use of burnable absorbers or any other means of increasing the shutdown margin.

5.3.5 8 by 9 core with 9 in-core irradiation positions (SAFARI-1)

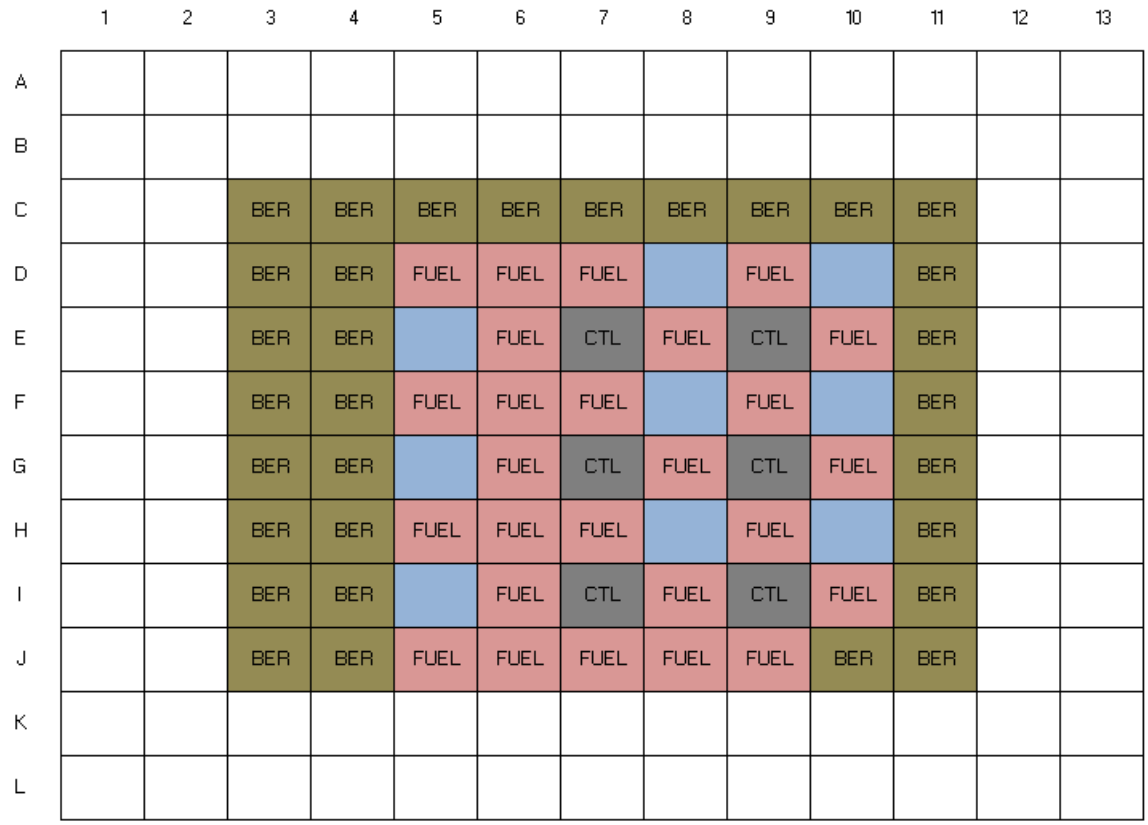

Figure 44 Diagram of the SAFARI-1 core configuration. The core is beryllium reflected with a light water filled blanket region.

With core designs ranging from small (12 fuel assemblies) to fairly large (24 fuel assemblies) it is required to compare these conceptual designs with designs already in operation. For this reason the SAFARI-1 core is resembled in this design. The design utilizes both in-core and ex-core irradiation positions to provide a wide array of utilization.

Aspects that can be compared to the previous heavy water reflected conceptual designs include the in-core irradiation positions and the thermal flux profiles on the leakage side of the core (bottom section not reflected with beryllium). The SAFARI-1 reactor operates at a nominal power of 20 MW which is largely a limit imposed by the existing cooling system. Theoretically, the allowable power could be much higher if the method as contained in section 2.2.2 is followed; however, in order to establish this design as a reference, the limitations of the existing cooling system is reflected in the 20 MW power specification. For the study of the design resembling the SAFARI-1 core, a power of 20 MW was used in the

analyses to provide insight into the quantitative comparison, of the SAFARI-1 core, to the other evaluated designs. (see annexure A5)

5.3.6 9 by 9 core with 19 in-core irradiation positions (HFR Petten)

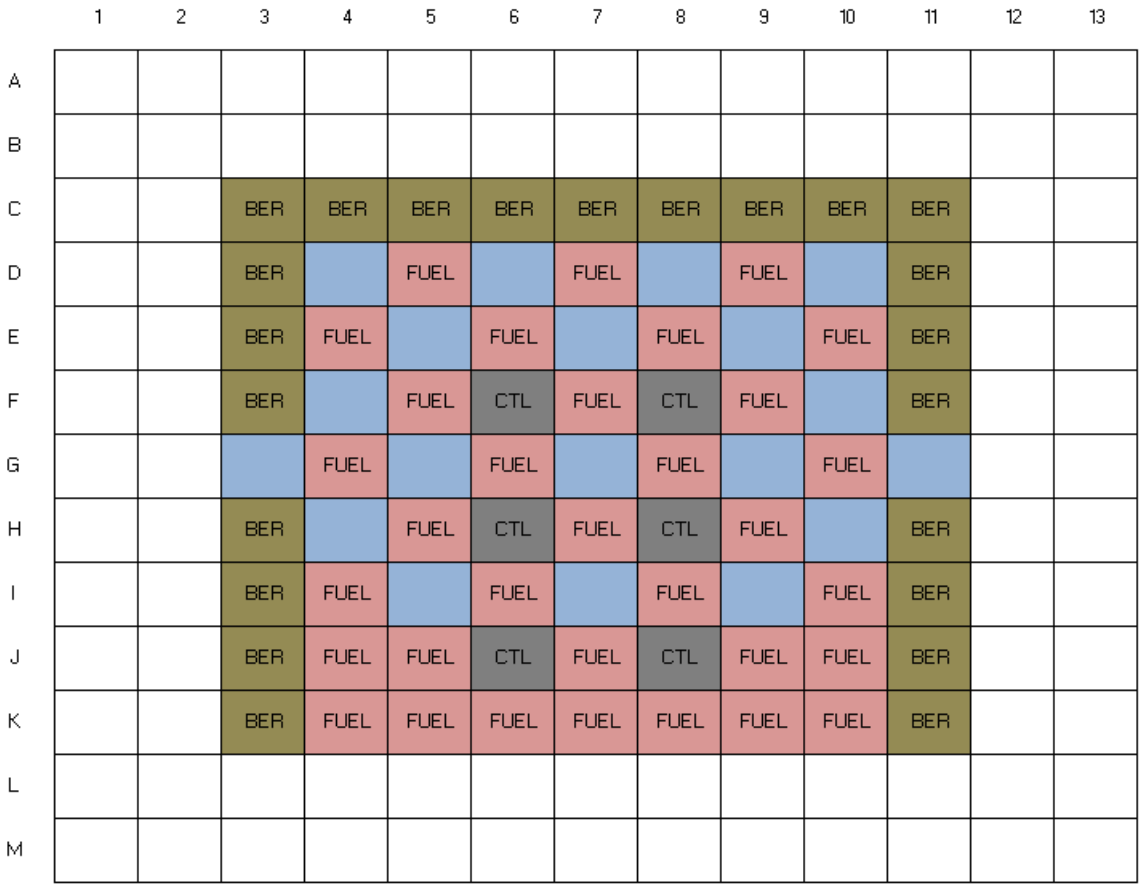

Figure 45 Diagram of a core design resembling that of the HFR Petten.

Together with the evaluation of the SAFARI-1 core design the consideration of a design resembling the HFR Petten core, which represents a similar yet larger core with much more in-core irradiation positions, was required. The design is unique in the fact that it operates at a very high power and consequently requires a few additional design optimizations which include:

- High ^{235}U fuel loadings per assembly (550 g ^{235}U per assembly) to allow for sufficient cycle length and burnup characteristics
- Curved fuel plates to allow for better structural integrity under increased coolant flow
- Burnable absorber wires (cadmium) to reduce BOC excess reactivity and to allow for a sufficient shutdown margin
- A slightly pressurized reactor vessel which offsets nucleate boiling

The HFR Petten reactor operates at a nominal power of 50 MW in cycles of up to 30 days. In order to allow for the same quantitative comparison as that for the SAFARI-1 core design, the design was analyzed for this specific power and cycle length; however, with the fuel assembly design used for all the other core designs, only containing 476.2 g ^{235}U per assembly, the reloading pattern could not be replicated. Also, with the fuel designs not containing burnable absorbers, the core unavoidably exceeded the shutdown margin limitation; however, by assembling a relatively equivalent design (regardless of the shutdown margin and loading pattern) a quantitative comparison was still made possible. (see annexure A6)

5.4 RESULTS OF THE CORE DESIGN EVALUATION

5.4.1 In-core irradiation position total thermal neutron flux capacity

Table 8 List of the total (sum of) in-core irradiation position axially averaged thermal flux for the evaluated core designs. Results are for BOC only.

Core design	Total irradiation flux capacity [$cm^{-2}.s^{-1}$]	Total irradiation flux capacity per unit power [$cm^{-2}.s^{-1}.MW^{-1}$]
4x4 core with no in-core irradiation positions	-	-
4x5 core with 1 in-core irradiation position	5.55E+14	2.22E+13
5x5 core with 4 in-core irradiation positions	1.86E+15	6.63E+13
7x7 core with 7 in-core irradiation positions	3.37E+15	8.42E+13
8x9 core with 9 in-core irradiation positions	1.91E+15	9.54E+13
9x9 core with 19 in-core irradiation positions	6.16E+15	1.23E+14

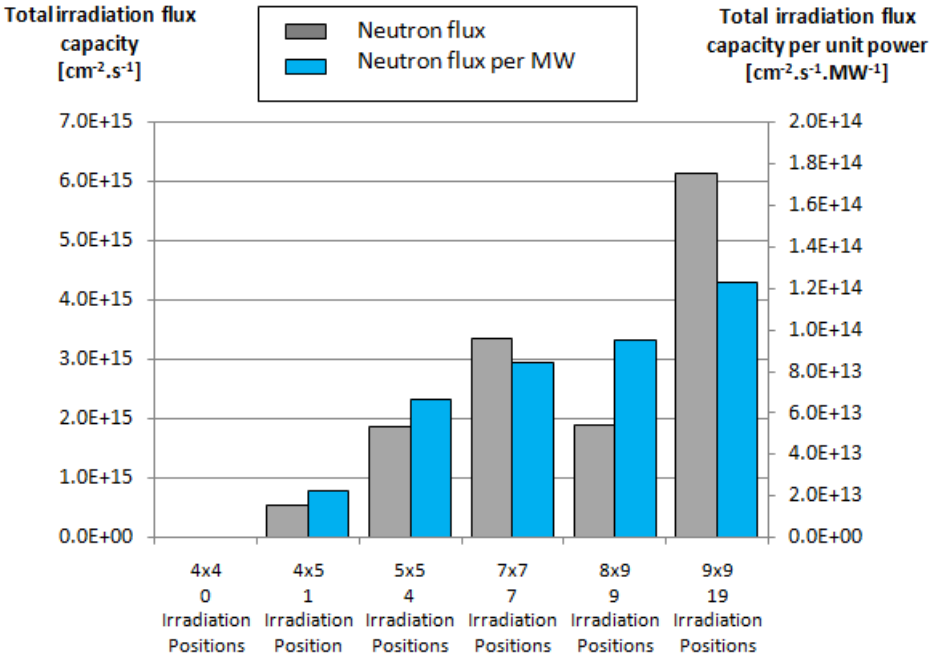

Figure 46 Total (sum of) in-core irradiation position thermal flux for the evaluated core designs. Results are for BOC only.

5.4.2 Maximum in-core irradiation position, axial-peak thermal neutron flux

Table 9 List of the axial peak in-core irradiation position thermal neutron flux for the position with the maximum thermal flux. Results are for BOC only.

Core design	Total irradiation flux capacity [$cm^{-2}.s^{-1}$]	Total irradiation flux capacity per unit power [$cm^{-2}.s^{-1}.MW^{-1}$]
4x4 core with no in-core irradiation positions	-	-
4x5 core with 1 in-core irradiation position	7.81E+14	3.13E+13
5x5 core with 4 in-core irradiation positions	4.86E+14	1.74E+13
7x7 core with 7 in-core irradiation positions	8.49E+14	2.12E+13
8x9 core with 9 in-core irradiation positions	4.42E+14	2.21E+13
9x9 core with 19 in-core irradiation positions	8.81E+14	1.76E+13

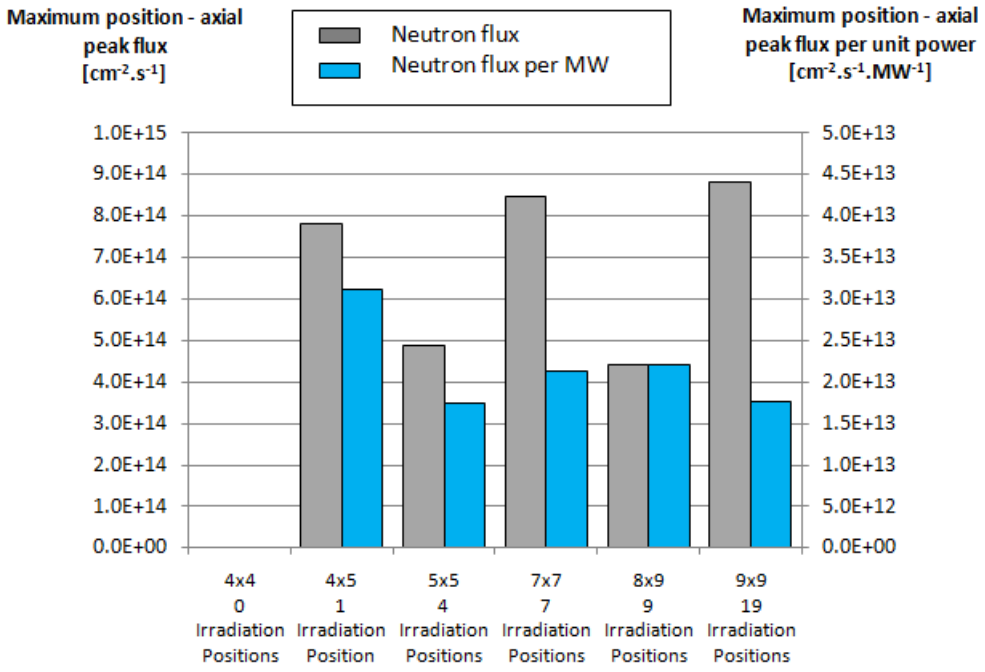

Figure 47 Axial peak in-core irradiation position thermal neutron flux for the position with the maximum thermal flux. Results are for BOC only.

5.4.3 Ex-core neutron flux distribution

Table 10 List of ex-core axially averaged- and peak thermal neutron flux values for the evaluated core designs.

Core design	Maximum axially averaged thermal flux [$cm^{-2}.s^{-1}$]	Axial peak - thermal flux [$cm^{-2}.s^{-1}$]	Maximum axially averaged thermal flux per unit power [$cm^{-2}.s^{-1}.MW^{-1}$]	Axial peak - thermal flux per unit power [$cm^{-2}.s^{-1}.MW^{-1}$]
4x4 core	3.51E+14	4.31E+14	1.76E+13	2.16E+13
4x5 core	4.00E+14	5.02E+14	1.60E+13	2.01E+13
5x5 core	3.35E+14	4.06E+14	1.20E+13	1.45E+13
7x7 core	3.75E+14	4.30E+14	9.38E+12	1.07E+13
8x9 core	1.45E+14	1.95E+14	7.25E+12	9.75E+12
9x9 core	3.30E+14	4.87E+14	6.60E+12	9.75E+12

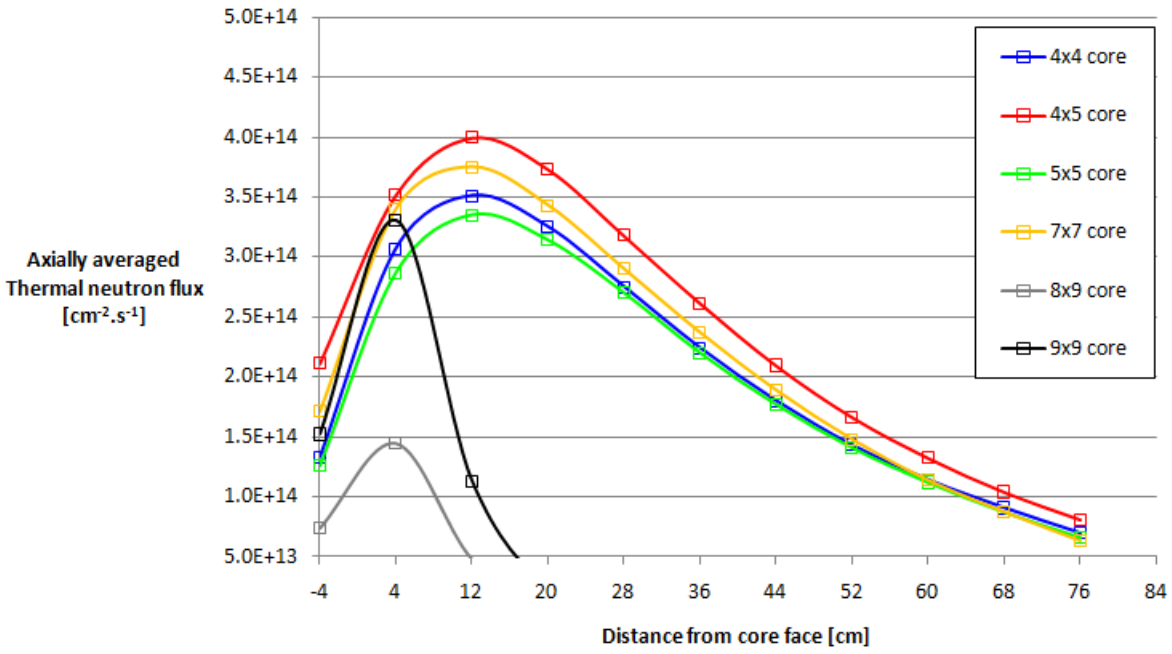

Figure 48 Ex-core, axially averaged, thermal neutron flux distribution for the evaluated core designs.

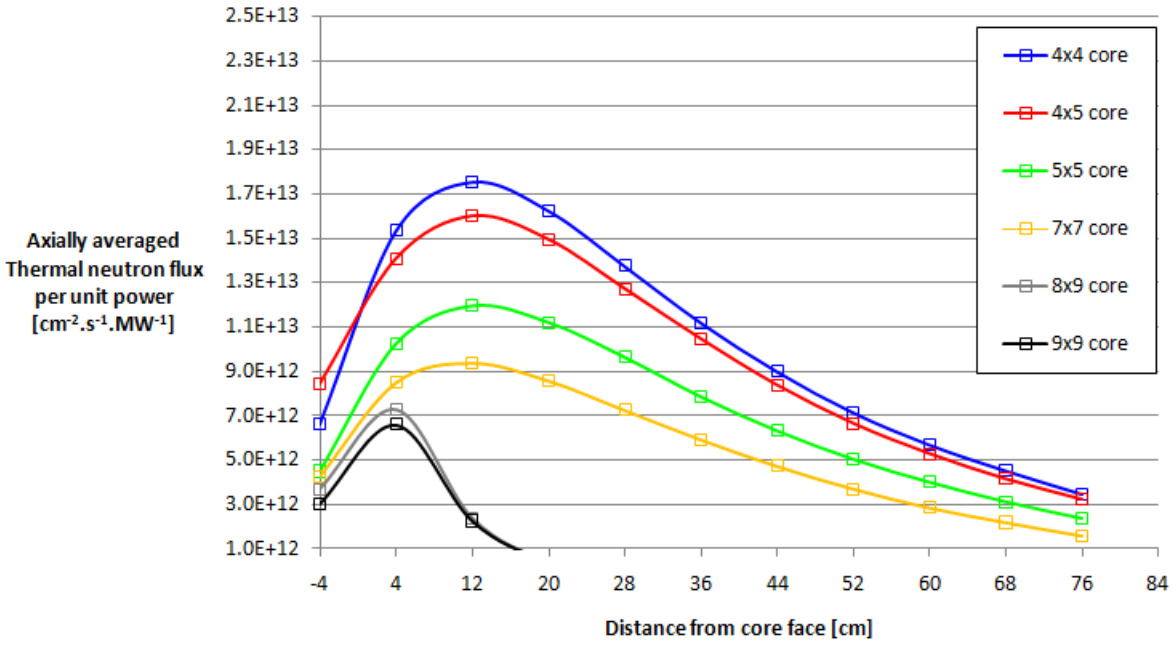

Figure 49 Ex-core, axially averaged, thermal neutron flux distribution per unit power, for the evaluated core designs.

5.4.4 Neutron beamline output capacity

Table 11 List of ex-core axially averaged- and peak thermal neutron flux values for the evaluated core designs.

Core design	Thermal neutron current [$cm^{-2}.s^{-1}$]	Cold neutron current [$cm^{-2}.s^{-1}$]	Thermal neutron current per unit power [$cm^{-2}.s^{-1}.MW^{-1}$]	Cold neutron current per unit power [$cm^{-2}.s^{-1}.MW^{-1}$]
4x4 core	8.005E+13	4.147E+12	4.0025E+12	2.0735E+11
4x5 core	8.805E+13	4.687E+12	3.522E+12	1.8748E+11
5x5 core	7.763E+13	4.113E+12	2.7725E+12	1.46893E+11
7x7 core	8.84E+13	4.731E+12	2.21E+12	1.18275E+11
8x9 core	3.002E+13	-	1.501E+12	-
9x9 core	1.722E+13	-	3.444E+11	-

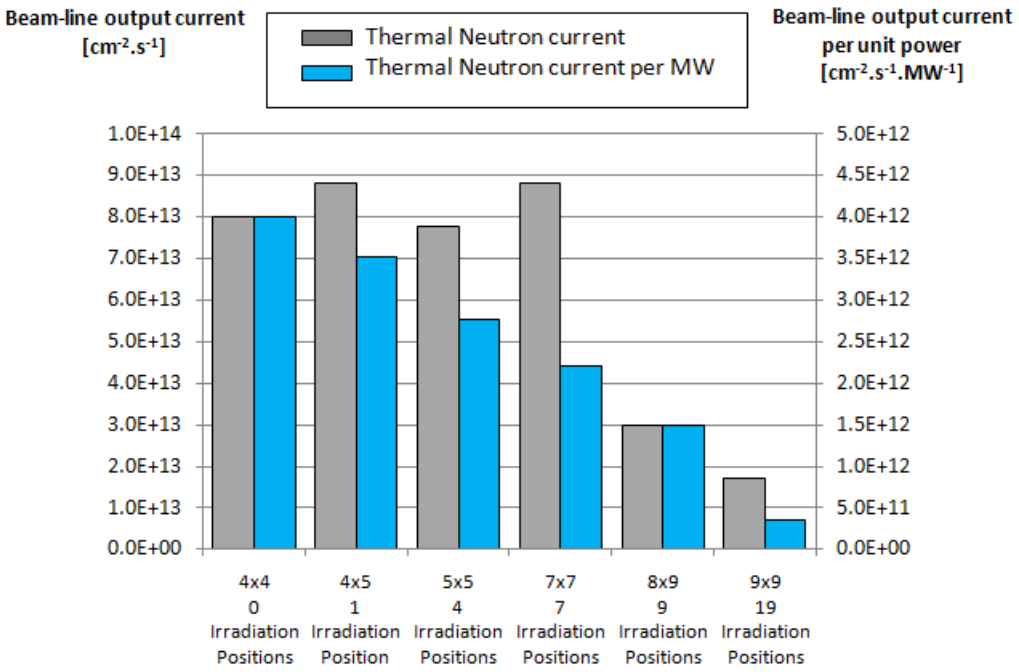

Figure 50 Thermal neutron output current comparison for thermal-source beamlines.

5.4.5 Core economy

Table 12 List of core design economic parameters.

Core configuration	Irradiation positions	Power - Cycle length		Fuel economy Cntl economy
4x4	0	20 MW	28 days	2 per cycle ~0.5 per cycle
4x5	1	25 MW	30 days	2 per cycle 1 per cycle
5x5	4	28 MW	30 days	~3 per cycle 1 per cycle
7x7	7	40 MW	35 days	~4 per cycle 1 per cycle
8x9, SAFARI-1	9	20 MW	30 days	~3 per cycle ~0.5 per cycle
9x9, HFR Petten	19	50 MW	30 days	~4 per cycle ~0.5 per cycle

5.5 DISCUSSION OF CORE DESIGN EVALUATION RESULTS

5.5.1 In-core irradiation positions

The summation of the axial-average thermal neutron flux within in-core irradiation positions for each evaluated core design is shown in figure 46. This summation is a representation of the total in-core irradiation capacity of a given core design, for which the results follow an almost linear increase for each incremental increase in core size, with the exception 8 by 9 core design. However, for capacities normalized by the total core power (also shown in figure 46), all the designs showed that the overall capacity per unit power is proportional to the core size.

The axial-peak thermal neutron flux for the in-core irradiation position with the maximum average, for each core, is depicted in figure 47. The results indicate that the large 9 by 9 core exhibits the largest thermal neutron flux peak at 8.81×10^{14} neutrons.cm^{-2}.s^{-1}. The 4 by 5 core, and 7 by 7 core, also exhibit a high peak flux with both being within 12% of that for the 9 by 9 core. For the other core designs (with in-core irradiation positions), peak fluxes of more than 4×10^{14} neutrons.cm^{-2}.s^{-1} are indicated. The normalized peaks show no clear dependency on core size, whilst the 4 by 5 core shows a relatively high normalized peak.

For core design without any in-core irradiation positions, the thermal neutron flux within the core (and total flux) will normally decrease with an increase in core size, due to the smaller geometrical buckling. An effect which can also be justified by considering the homogenous reactor one-group equation which, if solved for a rectangular parallelepiped, indicates the amplitude of the flux to be inversely proportional to the core volume (Lamarsh & Baratha, 2001). Therefore, it would be expected that the average flux in in-core irradiation positions will decrease for an increase in core size (for constant power); however, this aspect does not reflect in the total in-core irradiation capacity of a given core design. This is because the expected decrease does not compare to the effects of both the power distribution in each core design and the effect of having physically more in-core irradiation positions. On the foundation of having more of a flux-trap volume, the increase in total capacity with an increase in core size, can be explained satisfactorily. The peaks on the other hand are more likely to be dependent on the configuration in the immediate vicinity of the irradiation positions, with the surrounding power production playing a major role.

5.5.2 Ex-core neutron flux

The thermal neutron flux outside the northern core face of each core design is shown in figure 48. The flux profiles contained in the figure indicates a considerably larger flux

capacity in the heavy water reflected designs than that for the beryllium and light water reflected designs. This effect is largely due to the same influential conditions as was found for the study of different reflector technologies (moderation ratio, moderator absorption, etc.).

The physical thermal neutron flux does not show any clear dependence on either core size or power; however, when these values are normalized by the core power (as shown in figure 49) there is a clear indication that the ex-core thermal neutron flux per unit power decreases with core size. This is due to the same dependency on core total volume as indicated in section 5.5.1, with the smaller core designs allowing for more leakage from their external surfaces.

5.5.3 Beamline output capacity

The thermal neutron output current for each core design is compared in figure 50. The figure indicates that for the four heavy water reflected designs there is no clear dependency on core size with each design delivering a thermal neutron current of approximately $8x10^{13}$ neutrons.cm^{-2}.s^{-1}. The two light water reflected designs show a much lower output; however, because the source locations were placed directly against the core face, it would be incorrect to compare this output with that of the heavy water reflected designs.

The effect of the beamline output current displays approximately the same dependence on the core size as that seen in the ex-core thermal neutron flux and can be attributed to the same cause.

The cold neutron output current for the heavy water reflected designs, with an applied cold-neutron source, is contained in table 11. The values indicate approximately the same behaviour as that for the thermal neutron flux, which can be attributed to the fact that the same cold neutron source volume was used for each design which inherently places the dependence on the thermal neutron flux at the source location.

5.5.4 Core economy

The core power, cycle length and fuel- and control assembly change frequency, used for each core design study, is contained in table 12. The values indicate that in general the amount of fuel assemblies used per cycle increases slightly with core energy delivery; however, this minimal dependence can be attributed to the inherently smaller power share carried by the more numerous fuel assemblies in large designs compared to that of smaller designs. This effect also follows the core operating envelope development, as presented in

section 2.2.4, in which the core energy delivery has been found to be linearly dependant on the frequency of fuel change (see equation 21), but with the gradient being a number much greater than one; a small change in the frequency of fuel change will result in a large difference in possible energy production.

5.6 SUMMARY

This chapter detailed the results of the core design study by discussing: the selection of the reflector technology, the investigation of the effect of beamline orientation, the different core designs that were studied, and the results. As this marks the final chapter of the study component, the next chapter contains the conclusions and recommendations.

CHAPTER 6 CONCLUSIONS AND RECOMMENDATIONS

6.1 INTRODUCTION

Using the software codes, OSCAR-4 and MCNP5; a number of core configurations were assembled and evaluated on the basis of design parameters detailed in chapter 2. This was done after a plate-type fuel- and control assembly design was specified. The fuel assembly design, used for the core design study, features a square 8 cm by 8 cm (laterally and longitudinally) structure with an active height of 60 cm. An aluminium alloy was used for the non-fuel material of the assembly designs while both a uranium-silicide-aluminium alloy and a uranium-molybdenum-aluminium alloy was used (alternately) for the fuel material. The combined effect of using different amounts of fuel plates, different fuel meat thicknesses and different fuel materials were evaluated and presented in chapter 4. The study showed that the reactivity worth of a fuel assembly is largely dependent on the total ^{235}U-loading per assembly, with a larger ^{235}U-mass resulting in a considerable increase in the possible energy production. The effect of the fuel-to-moderator ratio on the moderator-temperature reactivity feedback coefficient was evaluated by calculating the coefficient for each fuel design. None of the designs exhibited a positive coefficient; indicating that the moderator-to-fuel ratio does not greatly influence the feedback mechanism.

6.2 FUEL TECHNOLOGY

A fundamental parameter identified in the study of the fuel designs is the concept of having a fuel assembly with a ^{235}U-mass as high as possible. Higher loadings allow a given core design to produce more energy (product of core power and cycle length) but needs to be balanced with the effects of excess reactivity and the core's shutdown margin. Fuel assembly total ^{235}U-mass can be increased mainly by means of either increasing the fuel meat thickness, increasing the number of plates or by using a fuel material capable of a higher total uranium loading. An increase in meat thickness beyond 0.061 cm, as well as an increase in the number of fuel plates beyond 21 plates, was shown to be beneficial but would, however, require proper justification from a thermal-hydraulic perspective since it will lead to an increase in the fuel centreline temperature and a decrease in coolant gap size. The alternate option, of using a higher uranium-loading material, would also be beneficial but needs to be evaluated from a metallurgical perspective as well as a manufacturability perspective, especially considering radiation damage effects and fission product build up.

The effect of burnable absorbers on the reactivity of fuel assemblies was analyzed by evaluating cadmium wires in the side section of fuel plates. The study shows that the initial reactivity of a fuel assembly can effectively be decreased and can therefore be applied to increase a core design's beginning of cycle (BOC) shutdown margin and allows the design to achieve a longer cycle length.

For a given fuel design, the maximum allowable assembly power (or operating envelope) could be determined by using a combination of correlations and equations deduced from both IAEA technical documents and SAFARI-1 technical documents, all of which is detailed in chapter 2. This methodology was fundamentally based on the maximum attainable coolant velocity, which was based on structural considerations, and the specification of sub-cooled heat transfer. Both predictions were based on rather conservative approaches which, if analyzed in greater depth, will result in a higher allowable fuel assembly power. Also, suitable measures can be put in place to increase the performance of a cooling system, such as a pressurized reactor vessel (as applied in the China Advanced Research Reactor) or curved fuel plates to allow for greater coolant flow (as applied in the HFR Petten reactor).

6.3 NEUTRON BEAMLINES

Before the core designs were evaluated, a suitable reflector technology needed to be chosen. A short study indicated that a heavy water reflected core would allow for the greatest amount of thermal neutron-flux in the reflector (or blanket) region. A selection which could make any given core design a potential inverse flux trap.

An analysis of the angular orientation of neutron beamlines delivered interesting results with respect to the reduction of noise-inducing fast and epi-thermal neutron currents as well as photon currents. The analysis indicated a clear benefit of rotating a beamline from a radial orientation to a more tangential orientation with the thermal or cold neutron output currents decreasing only slightly. The eventual placement and orientation of beamlines however, needs to be evaluated in conjunction with the eventual facility construction since each beamline needs to be accommodated in a suitable environment allowing for the placement of the required shielding and equipment.

6.4 CORE DESIGN

With the fuel operating envelope and reflector technology established, core configurations were assembled on the basis of ranging from a small core design to a very large one. Realistic actinide- and fission product distributions were compiled using the MGRAC code, which forms part of the OSCAR-4 code package, and were imported into MCNP5 input files in order to calculate accurate flux and current values. The stream-lining of this operation was carried out by a complex interaction of scripts, programs and spreadsheets which were all developed specifically for this study. The methods used to model and process all the relevant elements are depicted in chapter 3 and allowed the evaluation of core designs to be conducted at a very high rate.

A selection of four heavy water reflected core designs, ranging from a small 12 fuel assembly design to a large 30 fuel assembly design, as well as an additional two- beryllium and light water reflected core designs representing the SAFARI-1 and HFR Petten core designs respectively, were evaluated. Therefore, a total of six core designs were used to for this study, for which the results are depicted in chapter 5.

The study found that the maximum axially-averaged ex-core thermal neutron flux, at the maximum allowable power, for all of the core designs ranged from 1.76×10^{13} neutrons.cm^{-2}.s^{-1}, for the smallest core (4 by 4 core), to 6.60×10^{12} neutrons.cm^{-2}.s^{-1} for the largest core (9 by 9 core). The flux per unit power was found to be inversely proportional to the core size, with a smaller core resulting in a higher thermal neutron flux, a result which was expected (see chapter 1). The in-core irradiation capacity evaluation however, indicated the opposite, with the total irradiation capacity being proportional to the core size, that is; a larger core provides more capacity. This result also is not unexpected since the marginal decrease in effective neutron leakage is not comparable to the addition of a physical irradiation volume (one more in-core irradiation position) when a larger core size is used.

Another two additional neutron flux parameters were investigated: the peak in-core irradiation position thermal neutron flux, and the beamline thermal and cold-neutron output. The study found that the peak thermal neutron flux inside in-core irradiation positions does not follow a clear dependence on the core size, and is understandable from the fact that peak fluxes are dependant more on the power distribution (and therefore configuration) in the immediate vicinity of the irradiation position than on the overall core size. Therefore, peak fluxes are more likely to be influenced by power peaks. Since the neutron beamlines

derive their sources from the ex-core leakage, it was not a surprise to find that the output currents from the beamlines showed the same inverse proportional dependence on the core size. Therefore, smaller core designs will allow for greater output currents in both the thermal and cold neutron beamlines.

A final consideration regarding the evaluation of core designs was the core economy. A simple method for estimating the operating envelope of a core design was developed in chapter 2 and was used to predict the discharge burnup of fuel assemblies for a number of parameters. The parameter of interest to the neutronic economy of the designs is the consumption of fuel and control assemblies, which in all cases showed a clear dependence on core power, with larger powers requiring more fuel. Again, this conclusion was expected but an interesting phenomenon observed was the weak dependence of the energy production capability of a core design to the amount of fuel assemblies. This phenomenon can also clearly be observed in equation 21, which was used for the discharge burnup predictions.

6.5 OVERALL CORE DESIGN CONCLUSION

Based on the fact that a new South African research reactor is required to provide in-core irradiation facilities for high fast neutron flux to be used for fuel irradiation and material testing; ex-core irradiation facilities for high thermal neutron flux to be used in radio-isotope production; and neutron beam facilities for general research; it can be concluded that a medium sized core design, with an intermediate amount of in-core irradiation positions, be used. This will allow sufficient leakage from the core to drive ex-core irradiation facilities whilst allowing sufficient in-core irradiation capacity. The total amount of in-core irradiation positions however, need to be assessed carefully since currently SAFARI-1 produces most isotopes in-core; however, with a heavy water reflector offering such a large volume of irradiation, with attractive flux values, the optimal utilization of the volume needs to be considered. It is also clear that the thermal-hydraulic limitations of the fuel assemblies need to be assessed carefully since this will define the total core power and therefore directly the output fluxes and currents.

6.6 RECOMMENDATIONS

A new South African research reactor should be able to offer a good balance of in-core and ex-core irradiation facilities but should also remain simple and easy to both build and

operate. Like most mechanical assemblies, the fewer the constituent components, the easier the assembly will be to maintain; a fact which can be applied to the core design. It is therefore recommended to use a core design similar to the 5 by 5 core design which consists of 16 fuel assemblies, 5 control assemblies and 4 irradiation positions, all of which represents a simple design. It is also recommended to evaluate all the possible enhancements to this design such as:

- Higher fuel assembly ^{235}U-loadings with burnable absorbers to counter the decrease in shutdown margin, and
- Different absorber materials in control assemblies which will increase the total worth of the control bank (and in doing so the shutdown margin)

Also, a fundamental recommendation is to revise the entire thermal-hydraulic design of current – established – reactor designs in order to increase the maximum allowable core power to as high as possible.

It is therefore believed that the conceptual nature of different core designs are thoroughly captured in this study, but that the eventual deliverable flux values lies with the thermal-hydraulic design of the reactor as a whole, since it governs the eventual operating power.

ANNEXURE A. CORE DESIGN DATA

A1 4 X 4 CORE WITH NO IRRADIATION POSITIONS

The core configuration with this design is shown in the figure below:

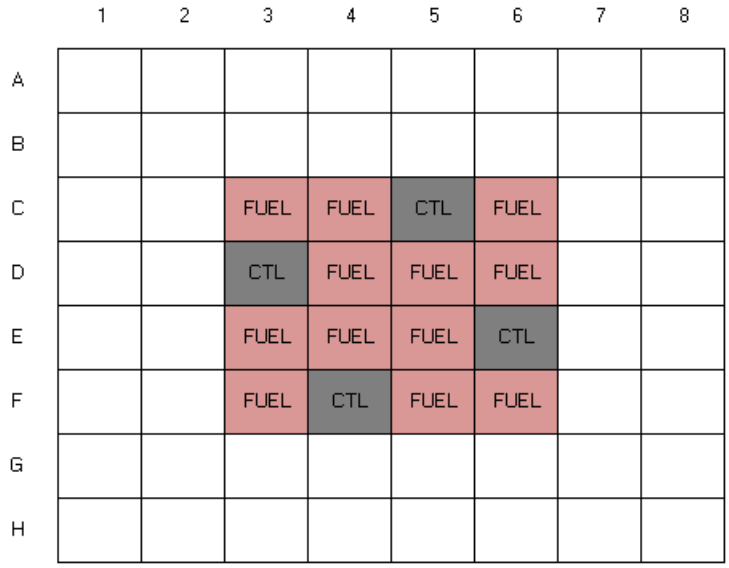

Figure 51 Diagram of the 4 by 4 core configuration.

A1.1 Loading pattern and equilibrium core power distribution

The core configuration is shown in figure 51. It includes four control assemblies and twelve fuel assemblies. Control assembly fuel followers have 17 uranium-silicide fuel plates with a meat thickness of 0.066 cm resulting in 297 grams of ^{235}U per assembly. Fuel assemblies have 21 uranium-silicide fuel plates with a meat thickness of 0.066 cm resulting in 476 grams of ^{235}U per assembly. The reflector tank is modelled as a 260 cm diameter tank and was selected as such to correspond approximately to the design of the OPAL reactor. Utilizing equation 21, figure 52 shows the initial operating envelope.

Table 13 Initial operating envelope for the 4 by 4 core with 12 fuel assemblies and 4 control assemblies.

Parameter	Symbol	Value
Limiting power to prevent nucleate boiling	P_{ONB}	< 21.4 MW
Discharge burnup for 28 days of operation		
Discharge burnup, replacing 1 assembly per cycle	-	@20 MW > 100%
Discharge burnup, replacing 2 assemblies per cycle	-	@20 MW = 55%
Discharge burnup, replacing 3 assemblies per cycle	-	@20 MW < 50%

In this table, replacing 2 assemblies per cycle (of 28 days length) yields a suitable discharge burnup of approximately 55% which allows an operating envelope as indicated in figure 52.

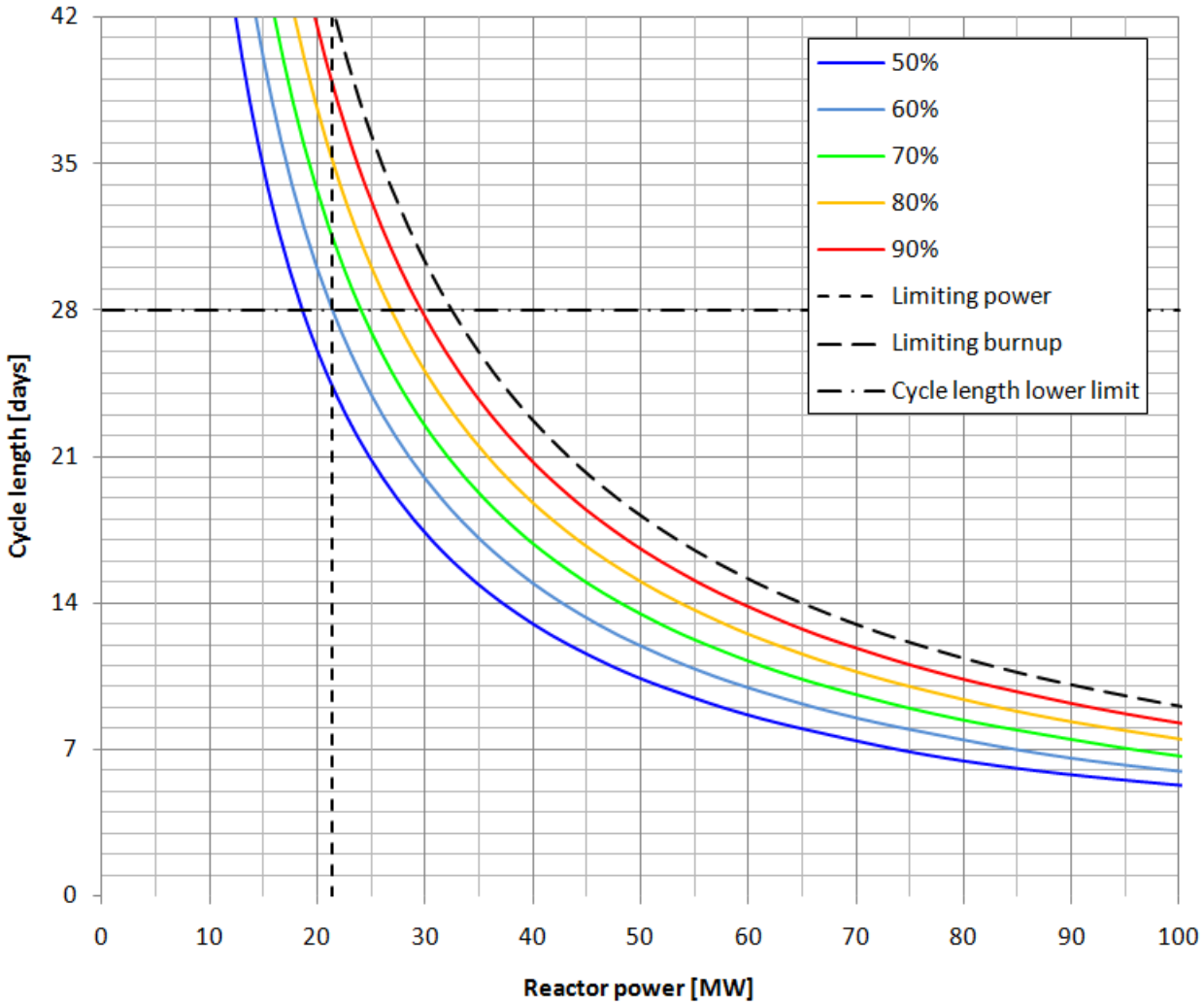

Figure 52 Operating envelope for the 4 by 4 core utilizing 4 control assemblies and 12 fuel assemblies. Two fuel assemblies are replaced per cycle.

Below is the equilibrium core mass distribution and reload pattern. Control assemblies were replaced every four cycles resulting in the following loading cycles:

- Cycle A: 2 fuel assemblies + 2 control assemblies
- Cycle B: 2 fuel assemblies
- Cycle C: 2 fuel assemblies
- Cycle D: 2 fuel assemblies
- Repeat starting at Cycle A

For each cycle, the reload path as indicated in figure 54 was used and the corresponding bank-height versus cycle progression is shown in figure 53 below.

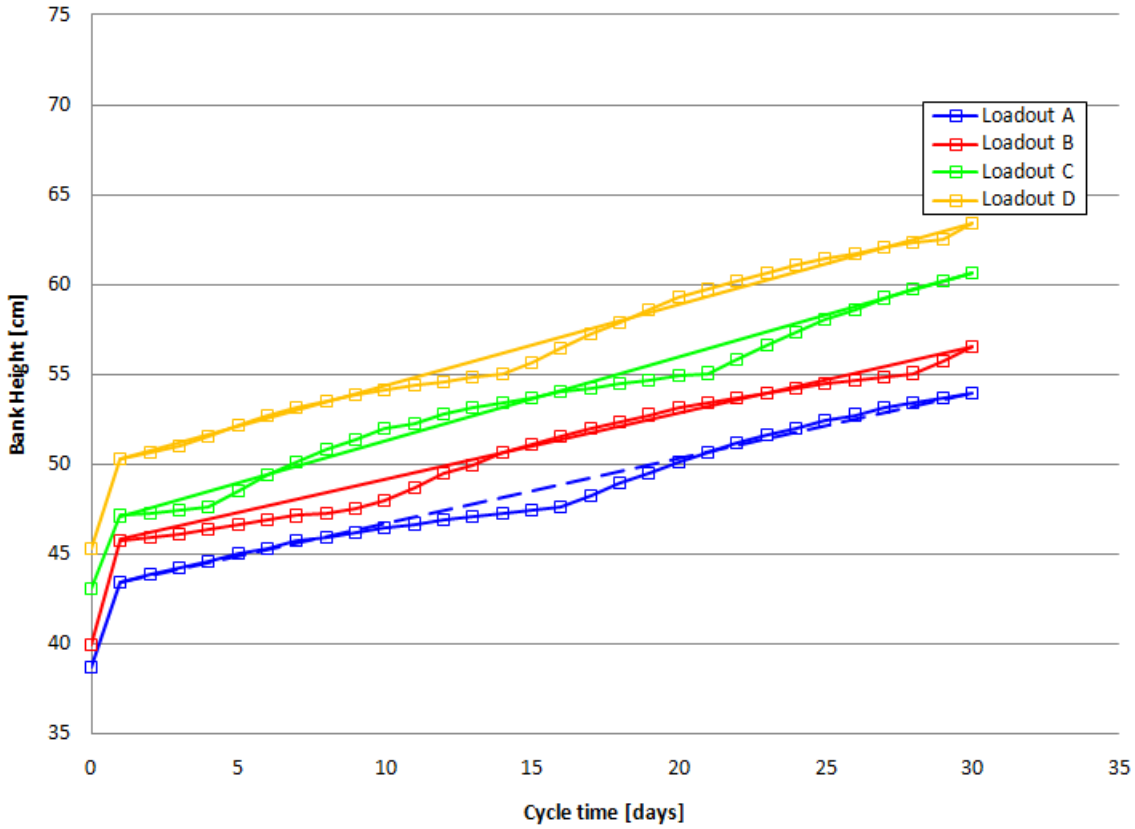

Figure 53 Bank height versus cycle length for the 4 by 4 core.

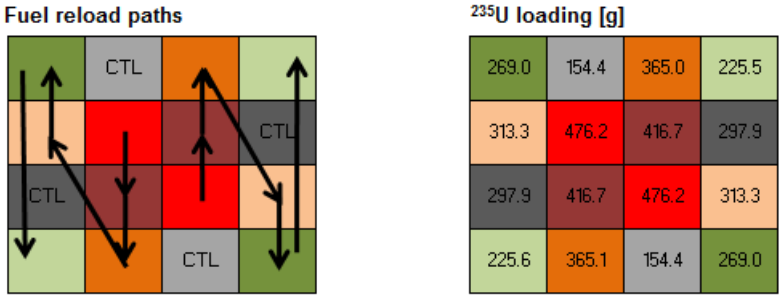

Figure 54 Loading pattern and mass distribution used to reload the 4 by 4 code numbers indicate ^{235}U content in grams.

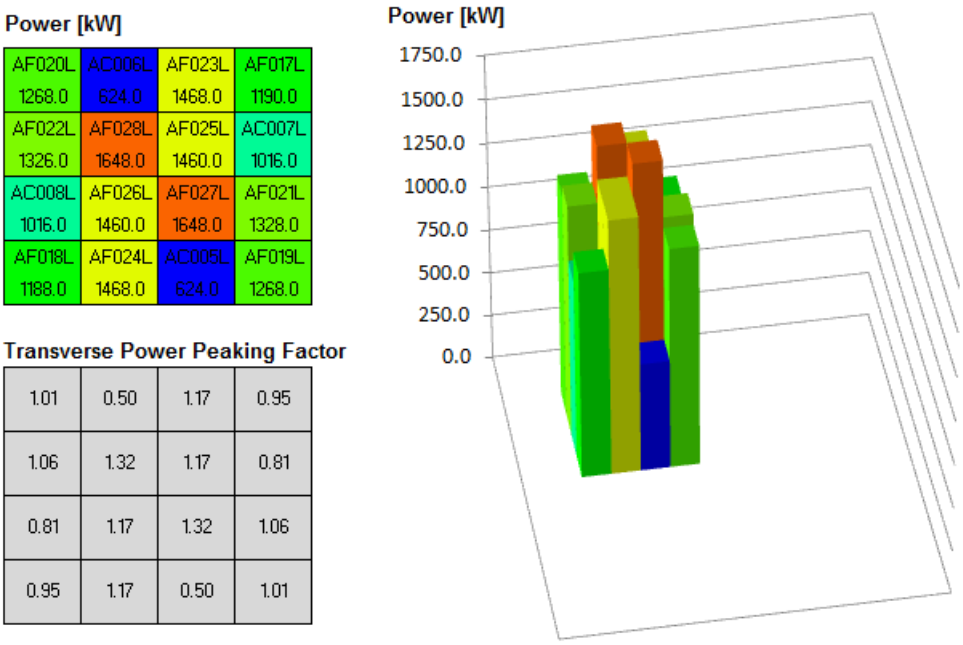

Figure 55 Core power distribution for the 4 by 4 core, for the most reactive cycle.

A1.2 Safety parameters

Table 14 List of relevant safety parameters associated with the 4 by 4 core.

Parameter		Value
BOC ^{235}U mass		5036 g
EOC ^{235}U mass		4346 g
Shutdown margin		-20 929 pcm (k_{eff} = 0.82693)
Excess reactivity		+12 191 pcm (k_{eff} = 1.13884)
Control bank reactivity worth		+33 120 pcm
Power peaking factor:	- f_{xy}	1.32
	- f_z	1.44
	- f_p	1.3 (assumed)
	- PPF	2.47 (<3.5)
Limiting power to prevent the onset of nucleate boiling		21.4 MW
Limiting power to prevent bubble detachment instability		28.1 MW

A1.3 OSCAR-4 axially averaged thermal neutron flux distribution

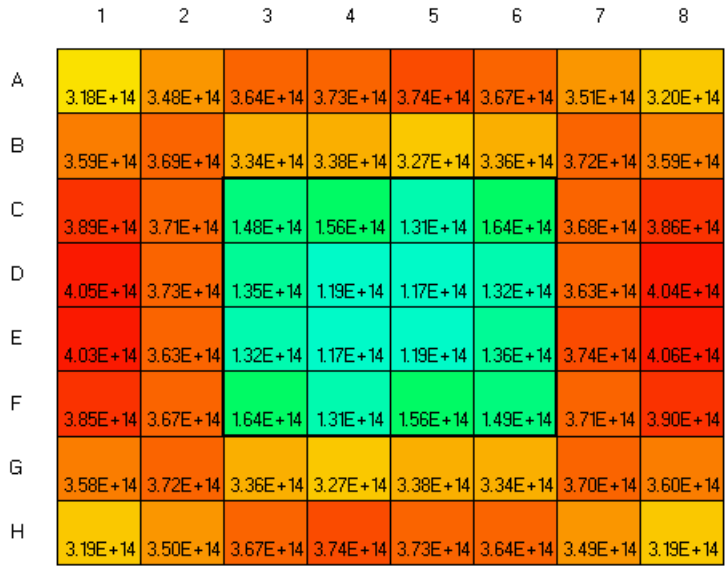

Figure 56 Thermal flux-distribution (E_n<0.625 eV) for the 4 by 4 core, for the most reactive cycle. Values calculated over the active core region (±30 cm) with OSCAR4.

A1.4 MCNP5 In-core axially averaged thermal neutron flux distribution

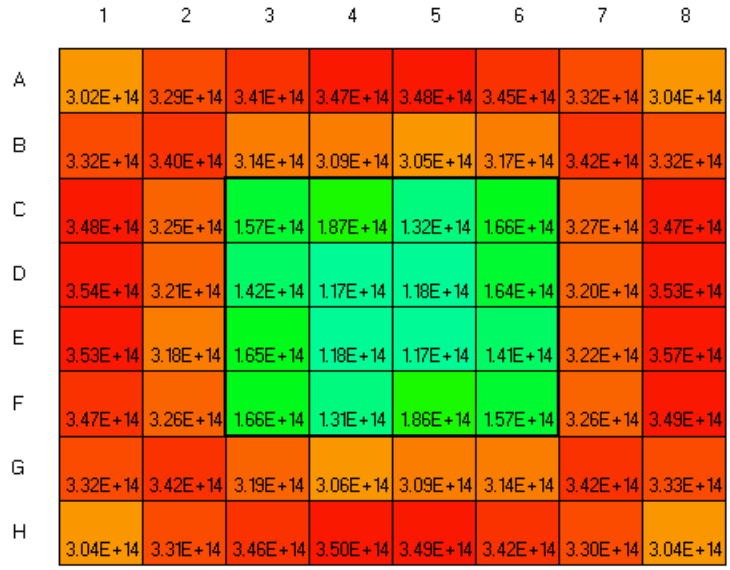

Figure 57 Thermal flux-distribution (E_n<0.625 eV) for the 4 by 4 core, for the most reactive cycle. Values calculated over the active core region (±30 cm) with MCNP5.

A1.5 MCNP5 In-core axially averaged epi-thermal neutron flux distribution

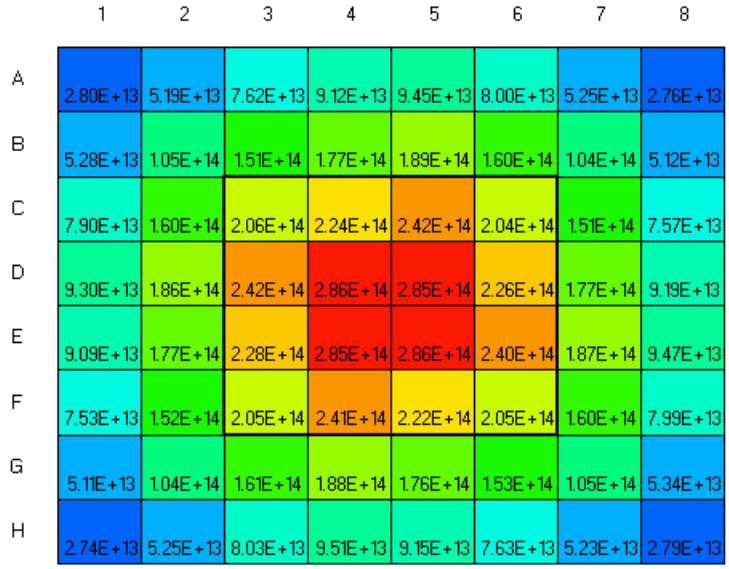

Figure 58 Epi-thermal flux-distribution (E_n>0.625 eV & E_n<100 keV) for the 4 by 4 core, for the most reactive cycle. Values calculated over the active core region (±30 cm) with MCNP5.

A1.6 MCNP5 In-core axially averaged fast neutron flux distribution

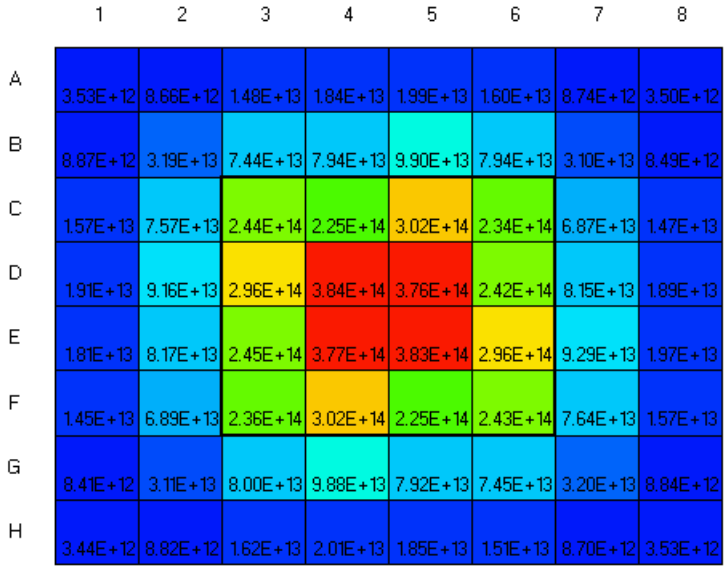

Figure 59 Fast flux-distribution (E_n>100 keV) for the 4 by 4 core, for the most reactive cycle. Values calculated over the active core region (±30 cm) with MCNP5.

A1.7 MCNP5 Ex-core neutron flux distribution

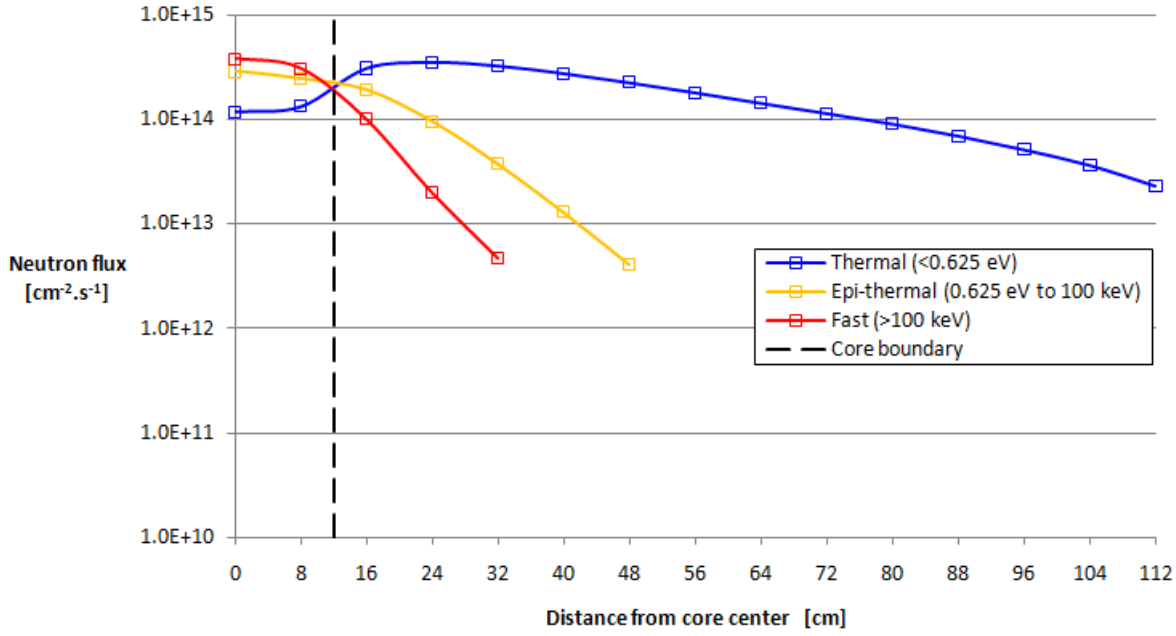

Figure 60 Flux-distribution in the reflector (blanket region) of the 4 by 4 core, for the most reactive cycle. Values were calculated over the active core region (±30 cm) with MCNP5 and only include statistically converged data.

Table 15 Numerical values for the Flux-distribution in the reflector (blanket region) of the 4 by 4 core, for the most reactive cycle. Values were calculated over the active core region (±30 cm) with MCNP5 and only include statistically converged data.

Distance from center [cm]	Thermal (E_n<0.625 eV)	Epi-thermal (E_n 0.625 eV to 100 keV)	Fast (E_n>100 keV)
0	1.184E+14	2.870E+14	3.793E+14
8	1.325E+14	2.436E+14	3.044E+14
16	3.075E+14	1.902E+14	9.970E+13
24	3.508E+14	9.520E+13	2.003E+13
32	3.253E+14	3.737E+13	4.782E+12
40	2.750E+14	1.291E+13	-
48	2.244E+14	4.128E+12	-
56	1.800E+14	-	-
64	1.432E+14	-	-
72	1.144E+14	-	-
80	9.065E+13	-	-
88	6.961E+13	-	-
96	5.152E+13	-	-
104	3.662E+13	-	-
112	2.320E+13	-	-

A1.8 MCNP5 Thermal neutron beamline characteristics

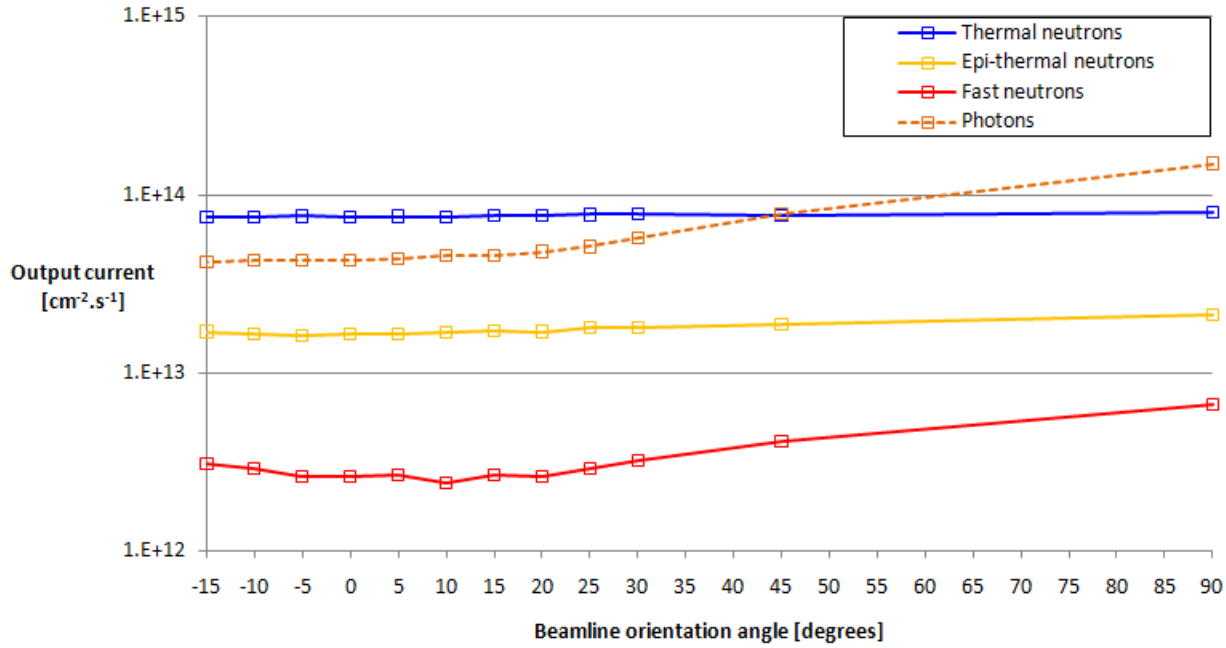

Figure 61 Beamline output current for a thermal beamline for the 4 by 4 core. Angular orientation is relative to the north core face. Values calculated with MCNP5 utilizing DXTRAN-spheres.

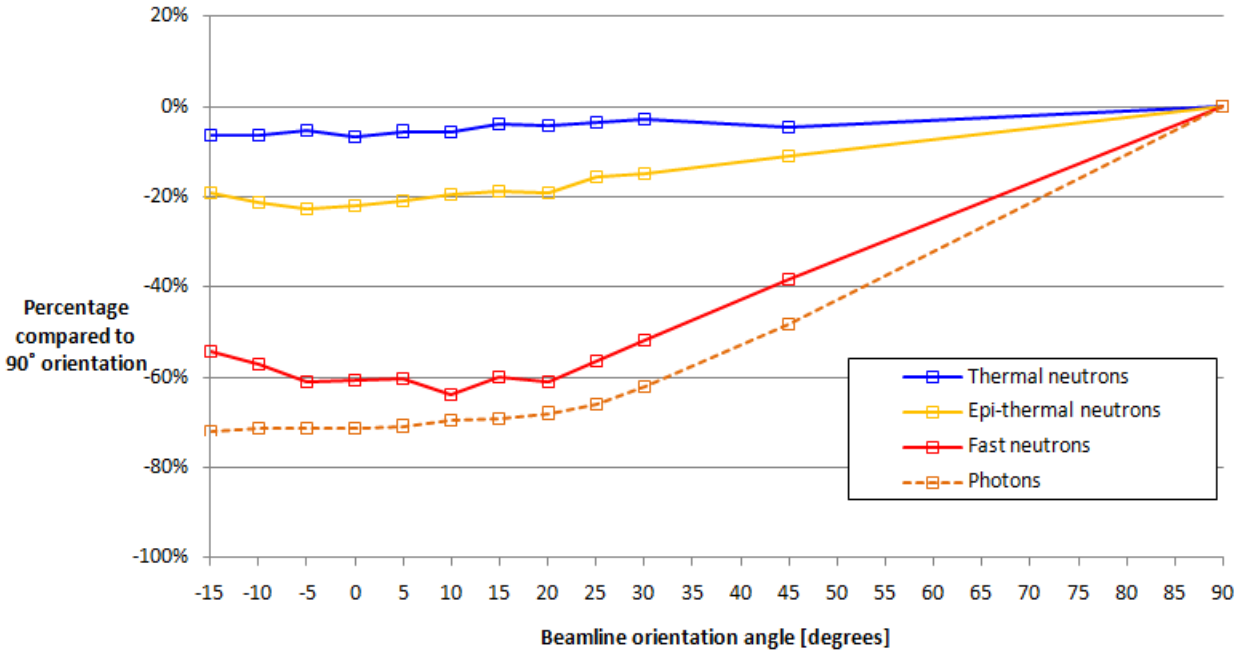

Figure 62 Beamline output current for a thermal beamline for the 4 by 4 core. Angular orientation is relative to the north core face. Values calculated with MCNP5 utilizing DXTRAN-spheres.

Table 16 Numerical values for the output currents, for the 4 by 4 core, at the end of the thermal beamline. The currents only includes directional values within a 5° difference of the output normal.

Orientation Angles (degrees)	Thermal (E_n<0.625 eV)	Epi-thermal (E_n 0.625 eV to 100 keV)	Fast (E_n>100 keV)	Photons (Total)
90	8.005E+13	2.110E+13	6.706E+12	1.498E+14
45	7.627E+13	1.881E+13	4.135E+12	7.735E+13
30	7.778E+13	1.796E+13	3.241E+12	5.691E+13
25	7.731E+13	1.779E+13	2.926E+12	5.111E+13
20	7.664E+13	1.704E+13	2.601E+12	4.797E+13
15	7.692E+13	1.710E+13	2.682E+12	4.596E+13
10	7.548E+13	1.696E+13	2.429E+12	4.557E+13
5	7.564E+13	1.668E+13	2.651E+12	4.372E+13
0	7.457E+13	1.643E+13	2.636E+12	4.288E+13
-5	7.575E+13	1.630E+13	2.618E+12	4.270E+13
-10	7.485E+13	1.663E+13	2.878E+12	4.315E+13
-15	7.491E+13	1.705E+13	3.074E+12	4.192E+13

Table 17 Numerical values for the output currents, for the 4 by 4 core, at the end of the thermal beamline as percentages of the 90° orientation. The currents only includes directional values within a 5° difference of the output normal.

Orientation Angles (degrees)	Thermal (E_n<0.625 eV)	Epi-thermal (E_n 0.625 eV to 100 keV)	Fast (E_n>100 keV)	Photons (Total)
90	100.0	100.0	100.0	100.0
45	95.3	89.1	61.7	51.6
30	97.2	85.1	48.3	38.0
25	96.6	84.3	43.6	34.1
20	95.7	80.8	38.8	32.0
15	96.1	81.1	40.0	30.7
10	94.3	80.4	36.2	30.4
5	94.5	79.1	39.5	29.2
0	93.2	77.9	39.3	28.6
-5	94.6	77.3	39.0	28.5
-10	93.5	78.8	42.9	28.8
-15	93.6	80.8	45.8	28.0

A1.9 MCNP5 Cold neutron beamline characteristics (Hydrogen source, H_2 at 20K)

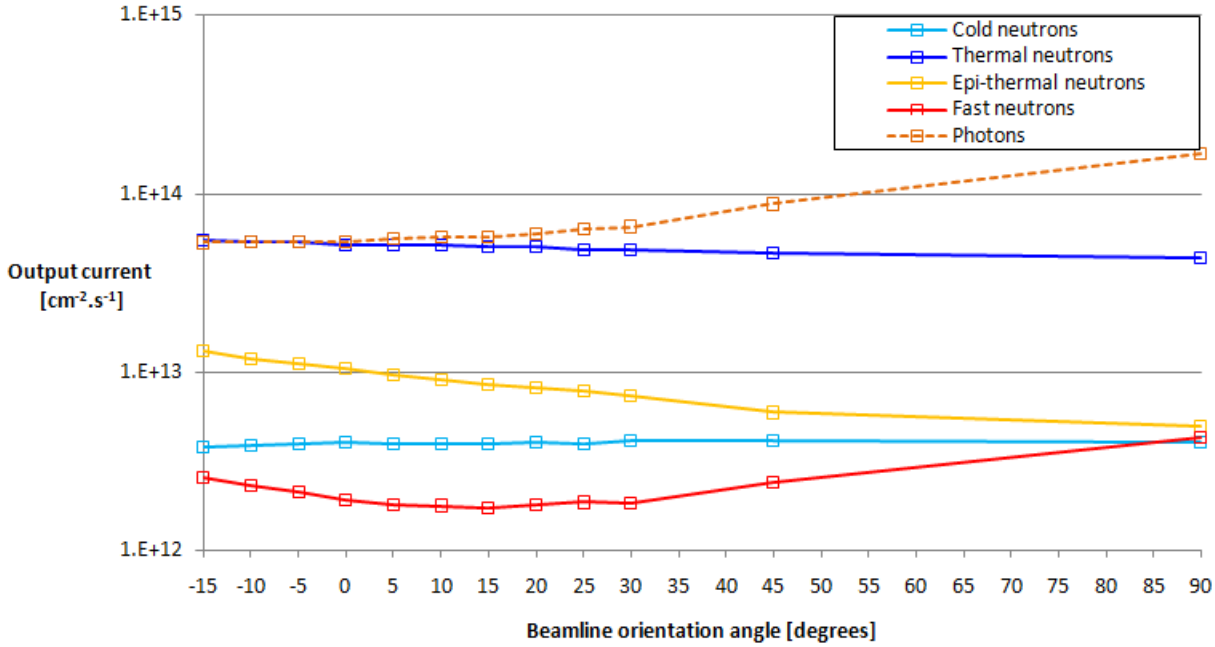

Figure 63 Beamline output current for a thermal neutron (E_n< 0.625 eV) beamline for the 4 by 4 core. Angular orientation is relative to the north core face. Values were calculated with MCNP5 utilizing DXTRAN-spheres.

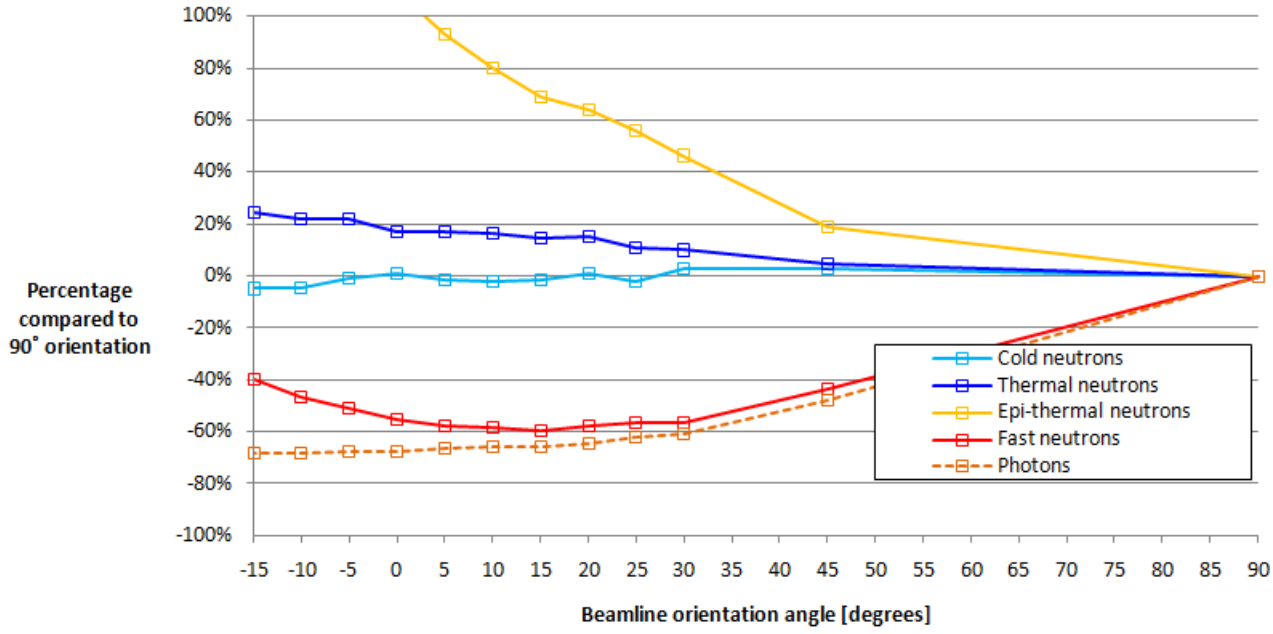

Figure 64 Beamline output current for a cold neutron (E_n< 5 meV) beamline for the 4 by 4 core. Angular orientation is relative to the north core face. Values were calculated with MCNP5 utilizing DXTRAN-spheres.

Table 18 Numerical values for the output currents, for the 4 by 4 core, at the end of the thermal beamline. The currents only includes directional values within a 5° difference of the output normal.

Orientation Angles (degrees)	Cold (E_n<5 meV)	Thermal (E_n<0.625 eV)	Epi-thermal (E_n 0.625 eV to 100 keV)	Fast (E_n>100 keV)	Photons (Total)
90	4.028E+12	4.406E+13	4.999E+12	4.289E+12	1.674E+14
45	4.147E+12	4.615E+13	5.936E+12	2.411E+12	8.752E+13
30	4.147E+12	4.845E+13	7.319E+12	1.853E+12	6.547E+13
25	3.945E+12	4.876E+13	7.799E+12	1.862E+12	6.306E+13
20	4.078E+12	5.067E+13	8.200E+12	1.821E+12	5.972E+13
15	3.970E+12	5.042E+13	8.455E+12	1.728E+12	5.711E+13
10	3.942E+12	5.123E+13	8.998E+12	1.785E+12	5.692E+13
5	3.968E+12	5.165E+13	9.645E+12	1.816E+12	5.608E+13
0	4.074E+12	5.168E+13	1.049E+13	1.915E+12	5.393E+13
-5	3.984E+12	5.380E+13	1.109E+13	2.111E+12	5.420E+13
-10	3.853E+12	5.387E+13	1.188E+13	2.296E+12	5.329E+13
-15	3.830E+12	5.491E+13	1.304E+13	2.584E+12	5.328E+13

Table 19 Numerical values for the output currents, for the 4 by 4 core, at the end of the thermal beamline as percentages of the 90° orientation. The currents only includes directional values within a 5° difference of the output normal.

Orientation Angles (degrees)	Cold (E_n<5 meV)	Thermal (E_n<0.625 eV)	Epi-thermal (E_n 0.625 eV to 100 keV)	Fast (E_n>100 keV)	Photons (Total)
90	100.0	100.0	100.0	100.0	100.0
45	102.9	104.7	118.7	56.2	52.3
30	103.0	110.0	146.4	43.2	39.1
25	97.9	110.7	156.0	43.4	37.7
20	101.2	115.0	164.0	42.4	35.7
15	98.6	114.4	169.1	40.3	34.1
10	97.9	116.3	180.0	41.6	34.0
5	98.5	117.2	192.9	42.4	33.5
0	101.1	117.3	209.8	44.7	32.2
-5	98.9	122.1	221.9	49.2	32.4
-10	95.7	122.3	237.7	53.5	31.8
-15	95.1	124.6	260.8	60.2	31.8

A2 4 X 5 CORE WITH A SINGLE IRRADIATION POSITION

The core configuration with this design is shown in the figure below:

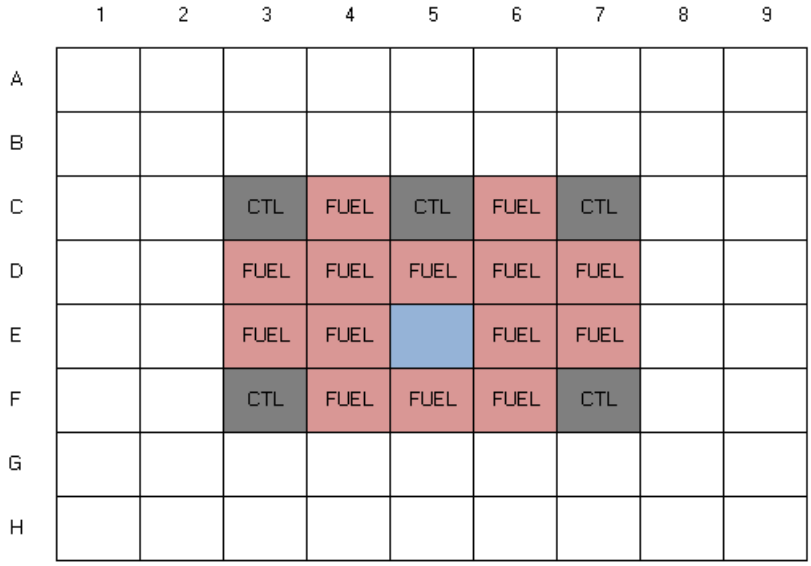

Figure 65 Diagram of the 4 by 5 core configuration.

A2.1 Loading pattern and equilibrium core power distribution

The core configuration is shown in figure 65. It includes five control assemblies and fourteen fuel assemblies. Control assembly fuel followers have 17 uranium-silicide fuel plates with a meat thickness of 0.066 cm resulting in 297 grams of ^{235}U per assembly. Fuel assemblies have 21 uranium-silicide fuel plates with a meat thickness of 0.066 cm resulting in 476 grams of ^{235}U per assembly. The reflector tank is modelled as a 260 cm diameter tank. Utilizing equation 21, figure 66table 20 shows the initial operating envelope.

Table 20 Initial operating envelope for a 4 by 5 core with 14 fuel assemblies and 5 control assemblies.

Parameter	Symbol	Value
Limiting power to prevent nucleate boiling	P_{ONB}	< 26.5 MW
Discharge burnup for 28 days of operation		
Discharge burnup, replacing 1 assembly per cycle	-	@25 MW > 100%
Discharge burnup, replacing 2 assemblies per cycle	-	@25 MW = 64%
Discharge burnup, replacing 3 assemblies per cycle	-	@25 MW < 50%

In this table, replacing 2 assemblies per cycle (of 28 days length) yields a suitable discharge burnup of approximately 64% which allows an operating envelope as indicated in figure 66.

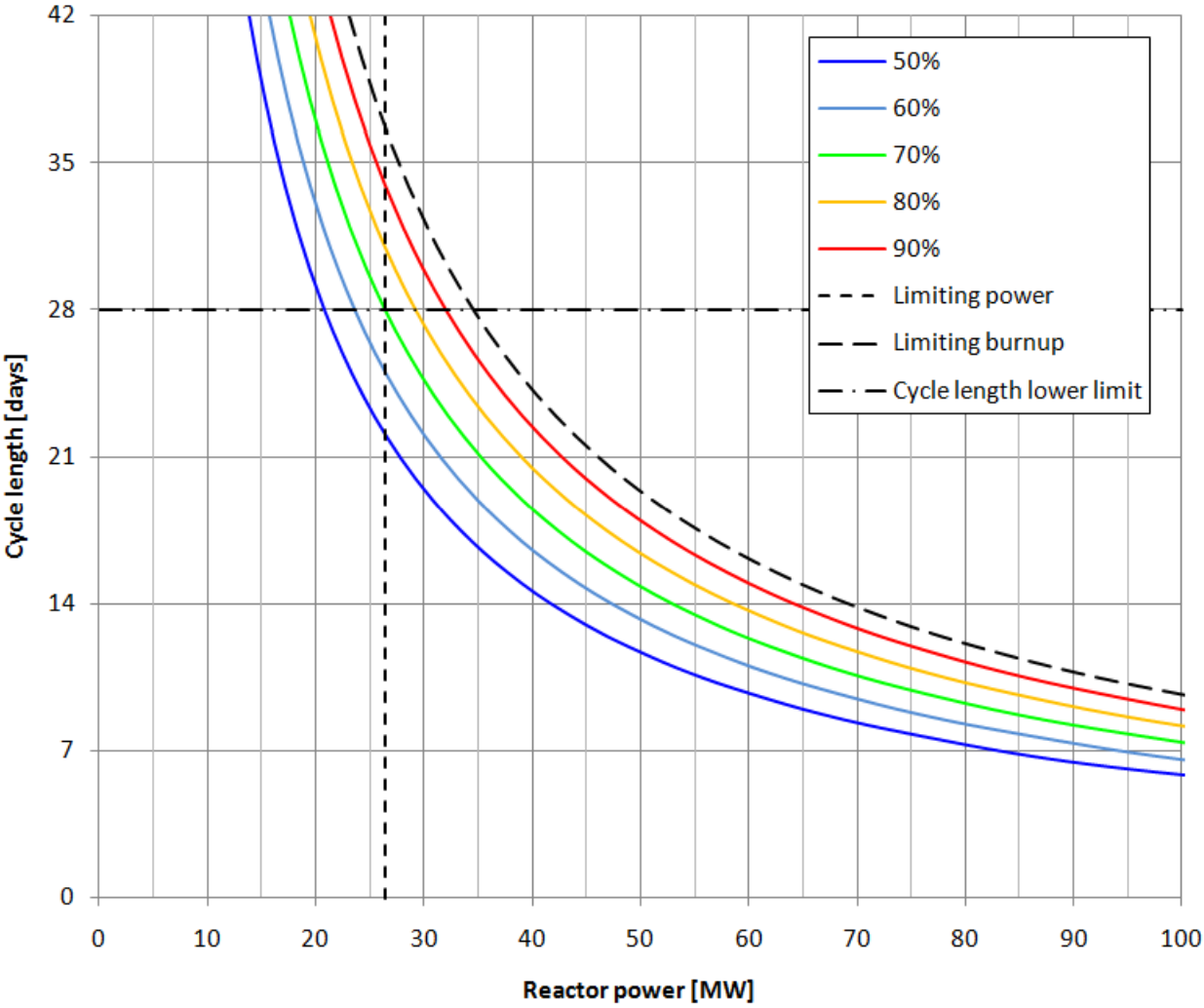

Figure 66 Operating envelope for the 4 by 5 core utilizing 5 control assemblies and 14 fuel assemblies. Two fuel assemblies are replaced per cycle.

Below is the equilibrium core mass distribution and reload pattern. A single control assembly and a pair of fuel assemblies were replaced every cycle. This loading sequence was the only applied sequence:

- Cycle A: 2 fuel assemblies + 1 control assembly
- Repeat starting at Cycle A

The reload path as indicated in figure 68 was used and the corresponding bank-height versus cycle progression is shown in figure 67 below.

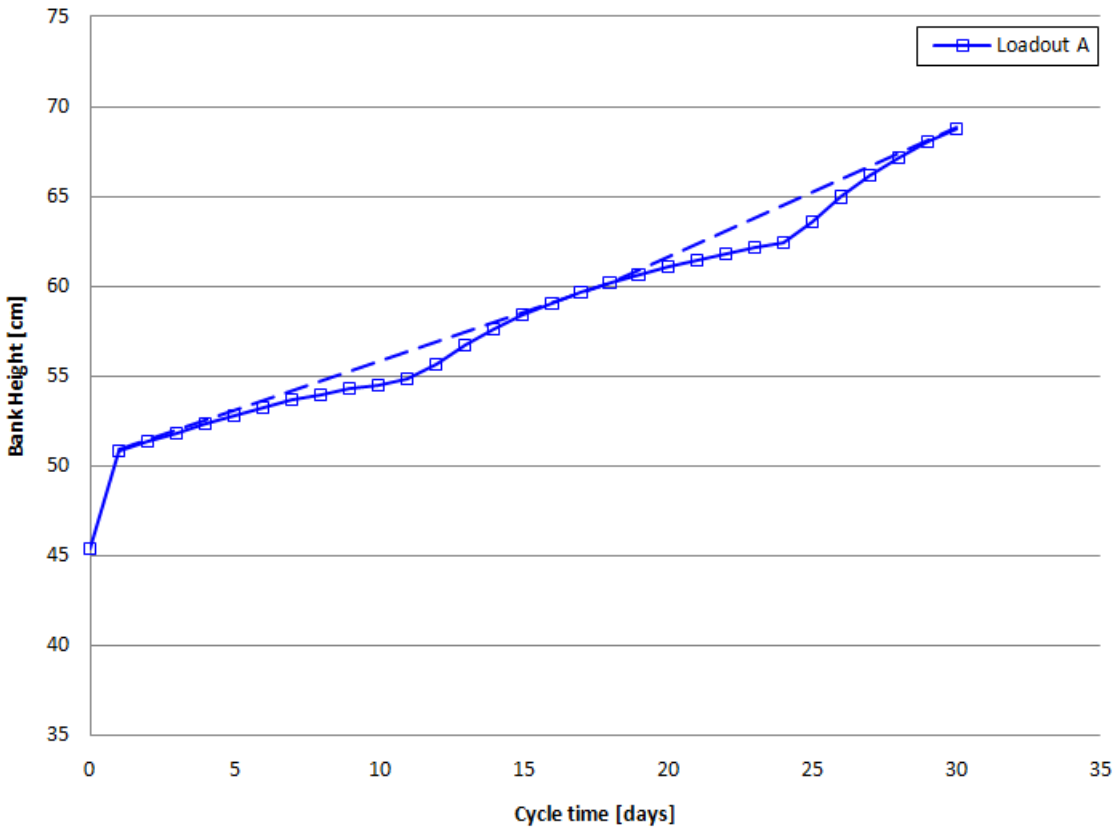

Figure 67 Bank height versus cycle length for the 4 by 5 core.

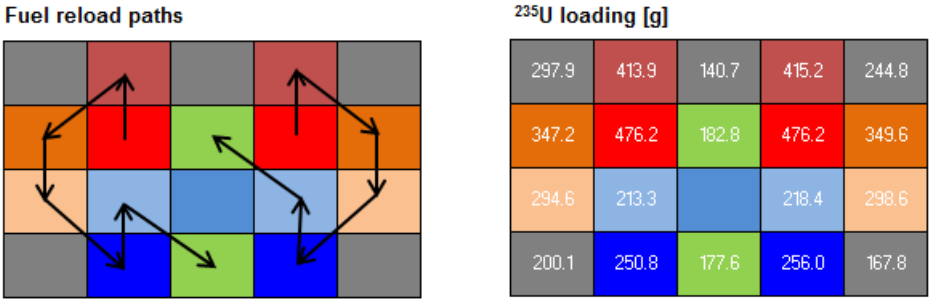

Figure 68 Loading pattern and mass distribution used to reload the 4 by 5 core. Numbers indicate ^{235}U content in grams.

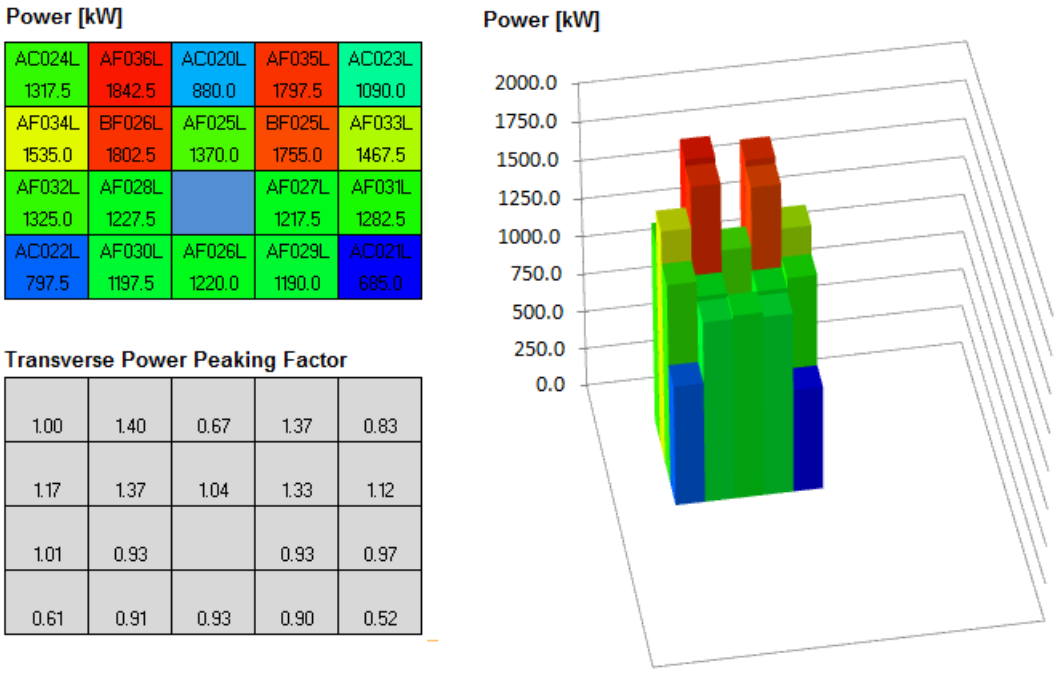

Figure 69 Core power distribution for the 4 by 5 core, for the most reactive cycle.

A2.2 Safety parameters

Table 21 List of relevant safety parameters associated with the 4 by 5 core.

Parameter	Value
BOC ^{235}U mass	5423 g
EOC ^{235}U mass	4566 g
Shutdown margin	-24 771 pcm (k_{eff} = 0.80147)
Excess reactivity	+8 497 pcm (k_{eff} = 1.09287)
Control bank reactivity worth	+33 268 pcm
Power peaking factor: - f_{xy} - f_z - f_p - PPF	1.46 1.40 1.3 (assumed) 2.66 (<3.5)
Limiting power to prevent the onset of nucleate boiling	26.5 MW
Limiting power to prevent bubble detachment instability	34.7 MW

A2.3 OSCAR-4 axially averaged thermal neutron flux distribution

	1	2	3	4	5	6	7	8	9
A	3.67E+14	4.14E+14	4.47E+14	4.70E+14	4.77E+14	4.61E+14	4.30E+14	3.94E+14	3.47E+14
B	4.04E+14	4.31E+14	4.18E+14	4.12E+14	4.39E+14	4.03E+14	4.03E+14	4.10E+14	3.81E+14
C	4.25E+14	4.02E+14	1.66E+14	1.50E+14	2.16E+14	1.46E+14	1.64E+14	3.81E+14	4.01E+14
D	4.29E+14	4.00E+14	1.43E+14	1.30E+14	2.22E+14	1.27E+14	1.36E+14	3.79E+14	4.05E+14
E	4.10E+14	3.82E+14	1.42E+14	1.72E+14	5.90E+14	1.68E+14	1.35E+14	3.63E+14	3.89E+14
F	3.74E+14	3.51E+14	1.46E+14	1.46E+14	2.00E+14	1.43E+14	1.48E+14	3.36E+14	3.57E+14
G	3.34E+14	3.49E+14	3.29E+14	3.21E+14	3.29E+14	3.16E+14	3.20E+14	3.36E+14	3.19E+14
H	2.93E+14	3.25E+14	3.45E+14	3.59E+14	3.64E+14	3.54E+14	3.36E+14	3.13E+14	2.80E+14

Figure 70 Thermal flux-distribution (E_n<0.625 eV) for the 4 by 5 core. Values calculated over the active core region (±30 cm) with OSCAR4.

A2.4 MCNP5 In-core axially averaged thermal neutron flux distribution

	1	2	3	4	5	6	7	8	9
A	3.29E+14	3.63E+14	3.81E+14	3.96E+14	4.00E+14	3.91E+14	3.72E+14	3.50E+14	3.17E+14
B	3.56E+14	3.68E+14	3.45E+14	3.43E+14	3.52E+14	3.36E+14	3.33E+14	3.52E+14	3.40E+14
C	3.69E+14	3.42E+14	1.73E+14	1.38E+14	2.11E+14	1.35E+14	1.70E+14	3.25E+14	3.50E+14
D	3.72E+14	3.34E+14	1.46E+14	1.31E+14	2.04E+14	1.27E+14	1.38E+14	3.18E+14	3.52E+14
E	3.60E+14	3.27E+14	1.48E+14	1.84E+14	5.55E+14	1.79E+14	1.41E+14	3.14E+14	3.45E+14
F	3.42E+14	3.15E+14	1.64E+14	1.51E+14	1.97E+14	1.47E+14	1.66E+14	3.05E+14	3.28E+14
G	3.18E+14	3.23E+14	3.01E+14	3.04E+14	3.14E+14	3.00E+14	2.95E+14	3.16E+14	3.09E+14
H	2.89E+14	3.13E+14	3.29E+14	3.42E+14	3.49E+14	3.40E+14	3.23E+14	3.05E+14	2.81E+14

Figure 71 Thermal flux-distribution (v<0.625 eV) for the 4 by 5 core, for the most reactive cycle. Values calculated over the active core region (±30 cm) with MCNP5.

A2.5 MCNP5 In-core axially averaged epi-thermal neutron flux distribution

	1	2	3	4	5	6	7	8	9
A	3.01E+13	5.75E+13	8.83E+13	1.10E+14	1.16E+14	1.07E+14	8.43E+13	5.43E+13	2.80E+13
B	5.63E+13	1.13E+14	1.74E+14	2.16E+14	2.19E+14	2.08E+14	1.65E+14	1.04E+14	5.21E+13
C	8.45E+13	1.70E+14	2.28E+14	2.70E+14	2.61E+14	2.61E+14	2.12E+14	1.56E+14	7.83E+13
D	1.01E+14	2.03E+14	2.65E+14	2.96E+14	2.81E+14	2.88E+14	2.52E+14	1.91E+14	9.48E+13
E	9.61E+13	1.90E+14	2.41E+14	2.57E+14	2.21E+14	2.52E+14	2.32E+14	1.81E+14	9.04E+13
F	7.35E+13	1.40E+14	1.81E+14	2.16E+14	2.16E+14	2.11E+14	1.72E+14	1.34E+14	6.91E+13
G	4.53E+13	8.81E+13	1.36E+14	1.74E+14	1.86E+14	1.69E+14	1.28E+14	8.32E+13	4.31E+13
H	2.33E+13	4.44E+13	6.91E+13	8.86E+13	9.55E+13	8.76E+13	6.63E+13	4.22E+13	2.25E+13

Figure 72 Epi-thermal flux-distribution (E_n>0.625 eV & E_n<100 keV) for the 4 by 5 core, for the most reactive cycle. Values calculated over the active core region (±30 cm) with MCNP5.

A2.6 MCNP5 In-core axially averaged fast neutron flux distribution

	1	2	3	4	5	6	7	8	9
A	3.52E+12	9.03E+12	1.71E+13	2.28E+13	2.33E+13	2.22E+13	1.65E+13	8.74E+12	3.54E+12
B	8.98E+12	3.14E+13	7.77E+13	1.11E+14	1.00E+14	1.09E+14	7.22E+13	2.88E+13	8.31E+12
C	1.68E+13	7.63E+13	2.47E+14	3.39E+14	2.70E+14	3.29E+14	2.24E+14	6.93E+13	1.52E+13
D	2.10E+13	1.02E+14	3.29E+14	4.05E+14	3.54E+14	3.94E+14	3.12E+14	9.68E+13	2.02E+13
E	1.98E+13	9.37E+13	2.95E+14	3.33E+14	2.11E+14	3.27E+14	2.84E+14	9.04E+13	1.90E+13
F	1.42E+13	6.02E+13	1.86E+14	2.65E+14	2.61E+14	2.60E+14	1.73E+14	5.64E+13	1.33E+13
G	7.39E+12	2.43E+13	5.88E+13	8.84E+13	9.33E+13	8.69E+13	5.53E+13	2.26E+13	6.87E+12
H	2.96E+12	7.12E+12	1.32E+13	1.84E+13	2.01E+13	1.84E+13	1.25E+13	6.60E+12	2.76E+12

Figure 73 Fast flux-distribution (E_n>100 keV) for the 4 by 5 core, for the most reactive cycle. Values calculated over the active core region (±30 cm) with MCNP5.

A2.7 MCNP5 Ex-core neutron flux distribution

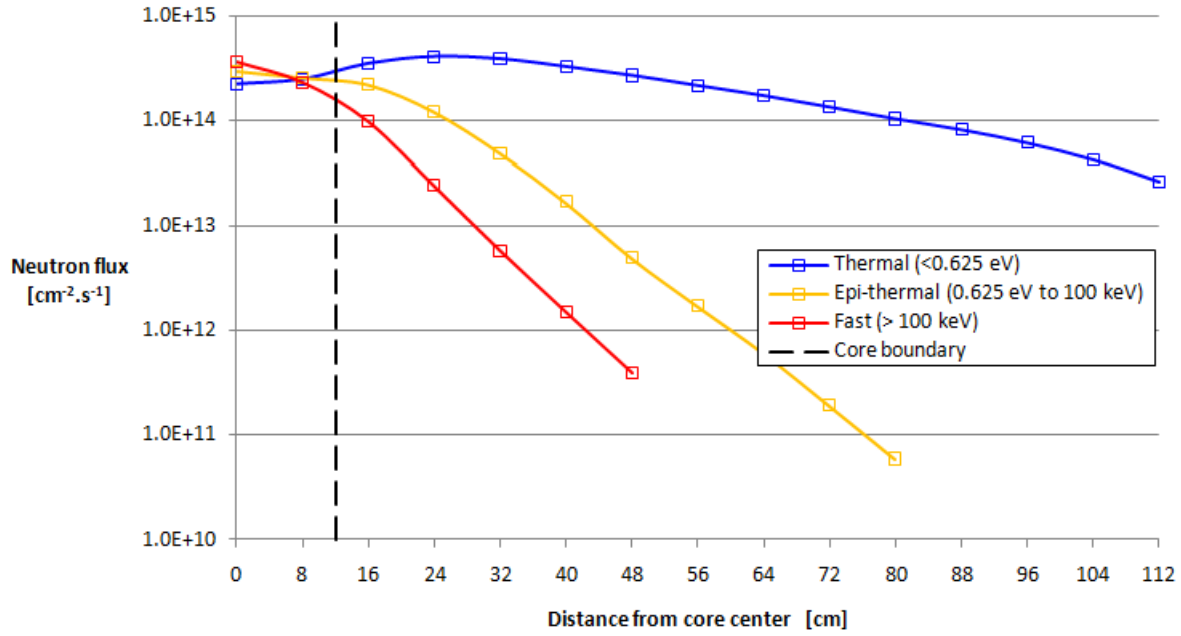

Figure 74 Flux-distribution in the reflector (blanket region) of the 4 by 5 core, for the most reactive cycle. Values were calculated over the active core region (±30 cm) with MCNP5 and only include statistically converged data.

Table 22 Numerical values for the Flux-distribution in the reflector (blanket region) of the 4 by 5 core, for the most reactive cycle. Values were calculated over the active core region (±30 cm) with MCNP5 and only include statistically converged data.

Distance from center [cm]	Thermal (E_n<0.625 eV)	Epi-thermal (E_n 0.625 eV to 100 keV)	Fast (E_n >100 keV)
0	2.26E+14	2.99E+14	3.68E+14
8	2.51E+14	2.59E+14	2.34E+14
16	3.54E+14	2.22E+14	9.82E+13
24	4.11E+14	1.22E+14	2.40E+13
32	3.90E+14	4.95E+13	5.76E+12
40	3.29E+14	1.69E+13	-
48	2.72E+14	4.98E+12	-
56	2.17E+14	-	-
64	1.74E+14	-	-
72	1.36E+14	-	-
80	1.05E+14	-	-
88	8.27E+13	-	-
96	6.23E+13	-	-
104	4.32E+13	-	-
112	2.63E+13	-	-

A2.8 MCNP5 Thermal neutron beamline characteristics

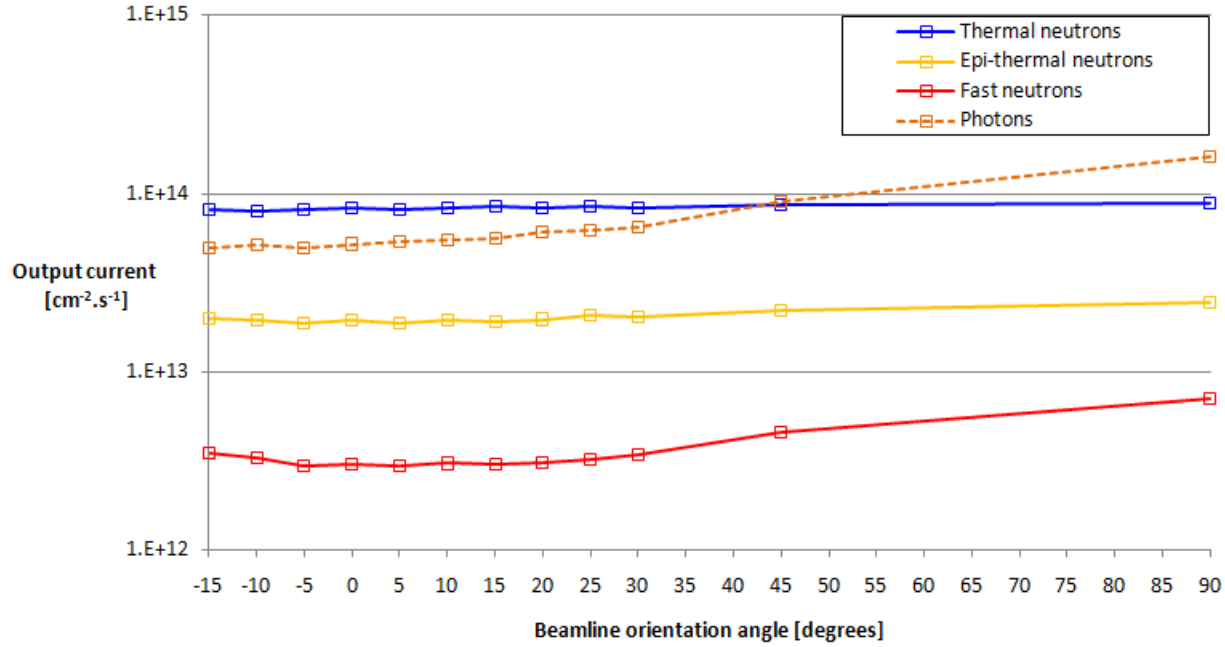

Figure 75 Beamline output current for a thermal beamline for the 4 by 5 core. Angular orientation is relative to the north core face. Values calculated with MCNP5 utilizing DXTRAN-spheres.

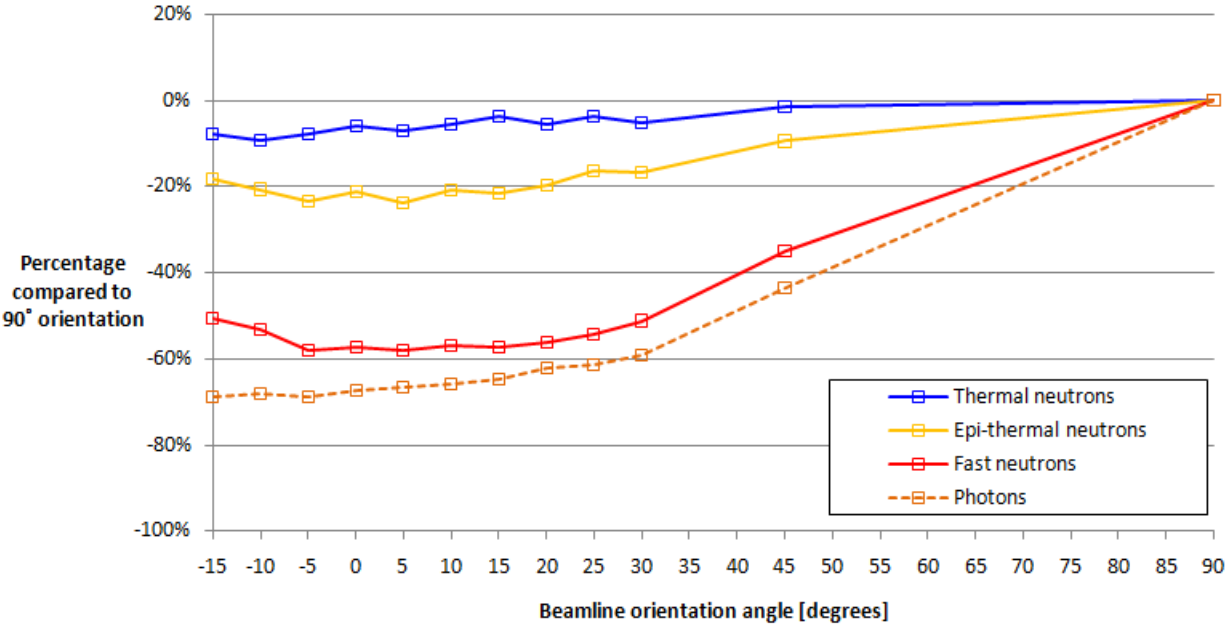

Figure 76 Beamline output current for a thermal beamline for the 4 by 5 core. Angular orientation is relative to the north core face. Values calculated with MCNP5 utilizing DXTRAN-spheres.

Table 23 Numerical values for the output currents, for the 4 by 5 core, at the end of the thermal beamline. The currents only includes directional values within a 5° difference of the output normal.

Orientation Angles (degrees)	Thermal (E_n<0.625 eV)	Epi-thermal (E_n 0.625 eV to 100 keV)	Fast (E_n>100 keV)	Photons (Total)
90	8.805E+13	2.456E+13	7.083E+12	1.600E+14
45	8.674E+13	2.224E+13	4.597E+12	9.010E+13
30	8.339E+13	2.049E+13	3.459E+12	6.528E+13
25	8.465E+13	2.058E+13	3.238E+12	6.170E+13
20	8.305E+13	1.970E+13	3.112E+12	6.040E+13
15	8.492E+13	1.927E+13	3.025E+12	5.646E+13
10	8.328E+13	1.941E+13	3.060E+12	5.446E+13
5	8.170E+13	1.871E+13	2.982E+12	5.361E+13
0	8.269E+13	1.936E+13	3.029E+12	5.214E+13
-5	8.130E+13	1.882E+13	2.977E+12	4.978E+13
-10	7.992E+13	1.949E+13	3.304E+12	5.117E+13
-15	8.129E+13	2.010E+13	3.498E+12	4.998E+13

Table 24 Numerical values for the output currents, for the 4 by 5 core, at the end of the thermal beamline as percentages of the 90° orientation. The currents only includes directional values within a 5° difference of the output normal.

Orientation Angles (degrees)	Thermal (E_n<0.625 eV)	Epi-thermal (E_n 0.625 eV to 100 keV)	Fast (E_n>100 keV)	Photons (Total)
90	100.00	100.00	100.00	100.00
45	98.52	90.54	64.90	56.30
30	94.71	83.41	48.83	40.79
25	96.15	83.78	45.71	38.56
20	94.33	80.19	43.94	37.74
15	96.44	78.44	42.71	35.28
10	94.59	79.02	43.19	34.03
5	92.79	76.18	42.10	33.50
0	93.92	78.82	42.76	32.58
-5	92.33	76.62	42.03	31.11
-10	90.76	79.36	46.65	31.97
-15	92.33	81.82	49.38	31.23

A2.9 MCNP5 Cold neutron beamline characteristics (Hydrogen source, H_2 at 20K)

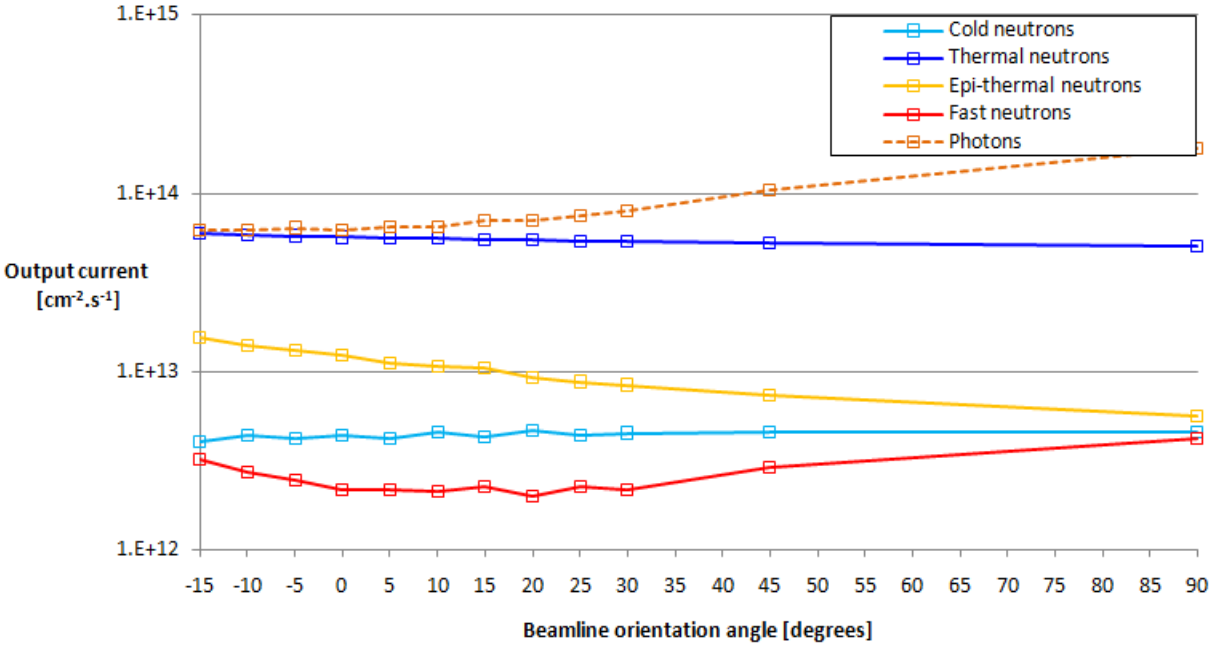

Figure 77 Beamline output current for a thermal beamline for the 4 by 5 core. Angular orientation is relative to the north core face. Values calculated with MCNP5 utilizing DXTRAN-spheres.

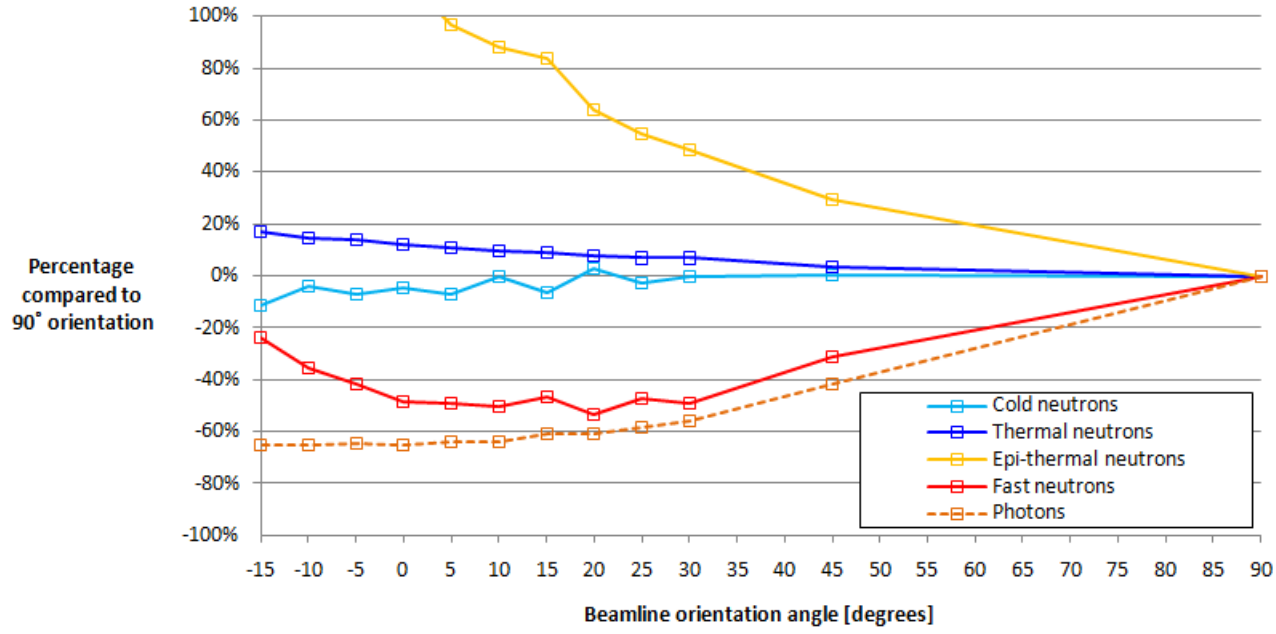

Figure 78 Beamline output current for a thermal beamline for the 4 by 5 core. Angular orientation is relative to the north core face. Values calculated with MCNP5 utilizing DXTRAN-spheres.

Table 25 Numerical values for the output currents, for the 4 by 5 core, at the end of the thermal beamline. The currents only includes directional values within a 5° difference of the output normal.

Orientation Angles (degrees)	Cold (E_n<5 meV)	Thermal (E_n<0.625 eV)	Epi-thermal (E_n 0.625 eV to 100 keV)	Fast (E_n >100 keV)	Photons (Total)
90	4.555E+12	5.061E+13	5.683E+12	4.251E+12	1.800E+14
45	4.569E+12	5.231E+13	7.343E+12	2.923E+12	1.052E+14
30	4.530E+12	5.408E+13	8.430E+12	2.156E+12	7.901E+13
25	4.427E+12	5.408E+13	8.790E+12	2.244E+12	7.530E+13
20	4.687E+12	5.451E+13	9.337E+12	1.989E+12	7.050E+13
15	4.266E+12	5.519E+13	1.044E+13	2.256E+12	7.083E+13
10	4.543E+12	5.554E+13	1.070E+13	2.121E+12	6.444E+13
5	4.235E+12	5.597E+13	1.118E+13	2.172E+12	6.435E+13
0	4.358E+12	5.666E+13	1.227E+13	2.182E+12	6.274E+13
-5	4.234E+12	5.780E+13	1.310E+13	2.479E+12	6.411E+13
-10	4.384E+12	5.801E+13	1.397E+13	2.736E+12	6.240E+13
-15	4.046E+12	5.930E+13	1.539E+13	3.245E+12	6.245E+13

Table 26 Numerical values for the output currents, for the 4 by 5 core, at the end of the thermal beamline as percentages of the 90° orientation. The currents only includes directional values within a 5° difference of the output normal.

Orientation Angles (degrees)	Cold (E_n<5 meV)	Thermal (E_n<0.625 eV)	Epi-thermal (E_n 0.625 eV to 100 keV)	Fast (E_n >100 keV)	Photons (Total)
90	100.00	100.00	100.00	100.00	100.00
45	100.30	103.36	129.22	68.77	58.48
30	99.46	106.86	148.35	50.72	43.90
25	97.20	106.86	154.69	52.80	41.84
20	102.90	107.71	164.32	46.80	39.18
15	93.66	109.05	183.69	53.07	39.36
10	99.73	109.74	188.27	49.89	35.81
5	92.98	110.59	196.75	51.09	35.76
0	95.67	111.96	215.85	51.33	34.86
-5	92.96	114.21	230.60	58.32	35.63
-10	96.24	114.63	245.89	64.37	34.68
-15	88.83	117.17	270.78	76.34	34.70

A3 5 X 5 CORE WITH FOUR IRRADIATION POSITIONS

The core configuration with this design is shown in the figure below:

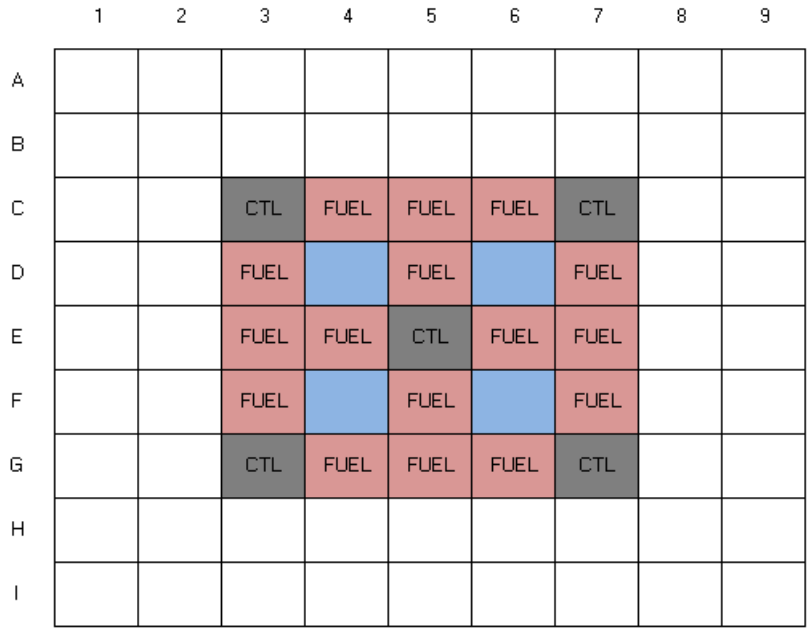

Figure 79 Diagram of the 5 by 5 core configuration.

A3.1 Loading pattern and equilibrium core power distribution

The core configuration is shown in figure 79. It includes 5 control assemblies and 14 fuel assemblies. Control assembly fuel followers have 17 uranium-silicide fuel plates with a meat thickness of 0.066 cm resulting in 297 grams of ^{235}U per assembly. Fuel assemblies have 21 uranium-silicide fuel plates with a meat thickness of 0.066 cm resulting in 476 grams of ^{235}U per assembly. The reflector tank is modelled as a 260 cm diameter tank. Utilizing equation 21, figure 80 shows the initial operating envelope.

Table 27 Initial operating envelope for a 5 by 5 core with 16 fuel assemblies and 5 control assemblies.

Parameter	Symbol	Value
Limiting power to prevent nucleate boiling	P_{ONB}	< 28.4 MW
Discharge burnup for 28 days of operation		
Discharge burnup, replacing 1 assembly per cycle	-	@28 MW > 100%
Discharge burnup, replacing 2 assemblies per cycle	-	@28 MW > 80%
Discharge burnup, replacing 3 assemblies per cycle	-	@28 MW = 50%
Discharge burnup, replacing 4 assemblies per cycle	-	@28 MW < 50%
Discharge burnup for 35 days of operation		
Discharge burnup, replacing 3 assembly per cycle	-	@28 MW = 66%

In this table, replacing 3 assemblies per cycle (of 35 days length) yields a suitable discharge burnup of approximately 66% which allows an operating envelope as indicated in figure 80.

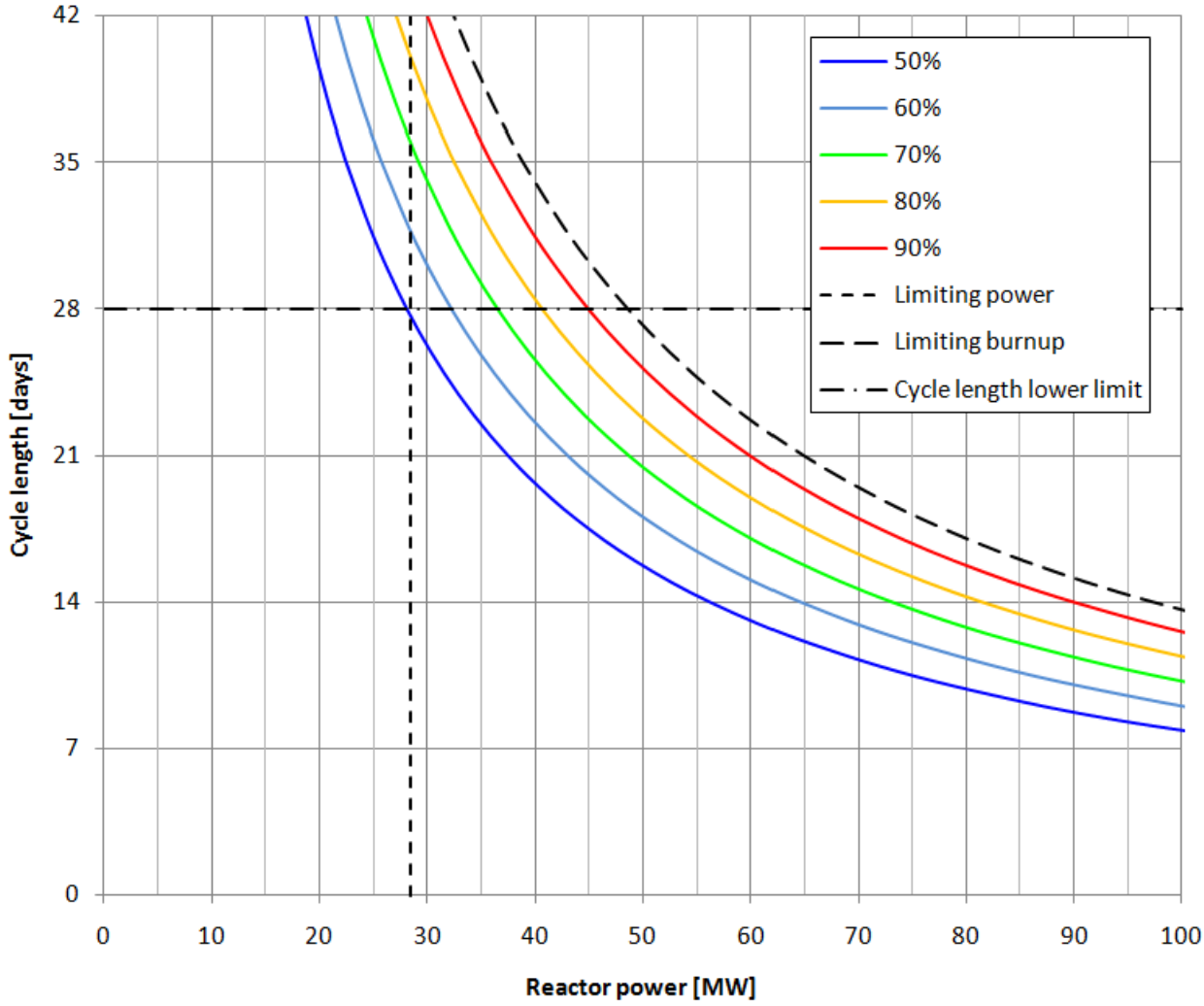

Figure 80 Operating envelope for a 5 by 5 core utilizing 5 control assemblies and 16 fuel assemblies. An average of 3 fuel assemblies are replaced per cycle.

Below is the equilibrium core mass distribution and reload pattern. In order to incorporate an average assembly replacement rate of 3 assemblies per cycle, two loading sequences were applied. These loading sequences are shown below:

- Cycle A: 4 fuel assemblies + 1 control assembly
- Cycle B: 2 fuel assemblies + 1 control assembly
- Repeat starting at Cycle A

For each cycle, the reload path as indicated in figure 82 figure 68was used and the corresponding bank-height versus cycle progression is shown in figure 81 figure 67below. In order to incorporate the differing amount of fuel assemblies being loaded, both loading

options followed the path depicted in figure 82, however, whenever the cycle A loading was done, the last 2 assemblies in the path were removed whilst moving each position along by 2 positions instead of one resulting in 2 empty locations per path (allowing for replacing 4 assemblies).

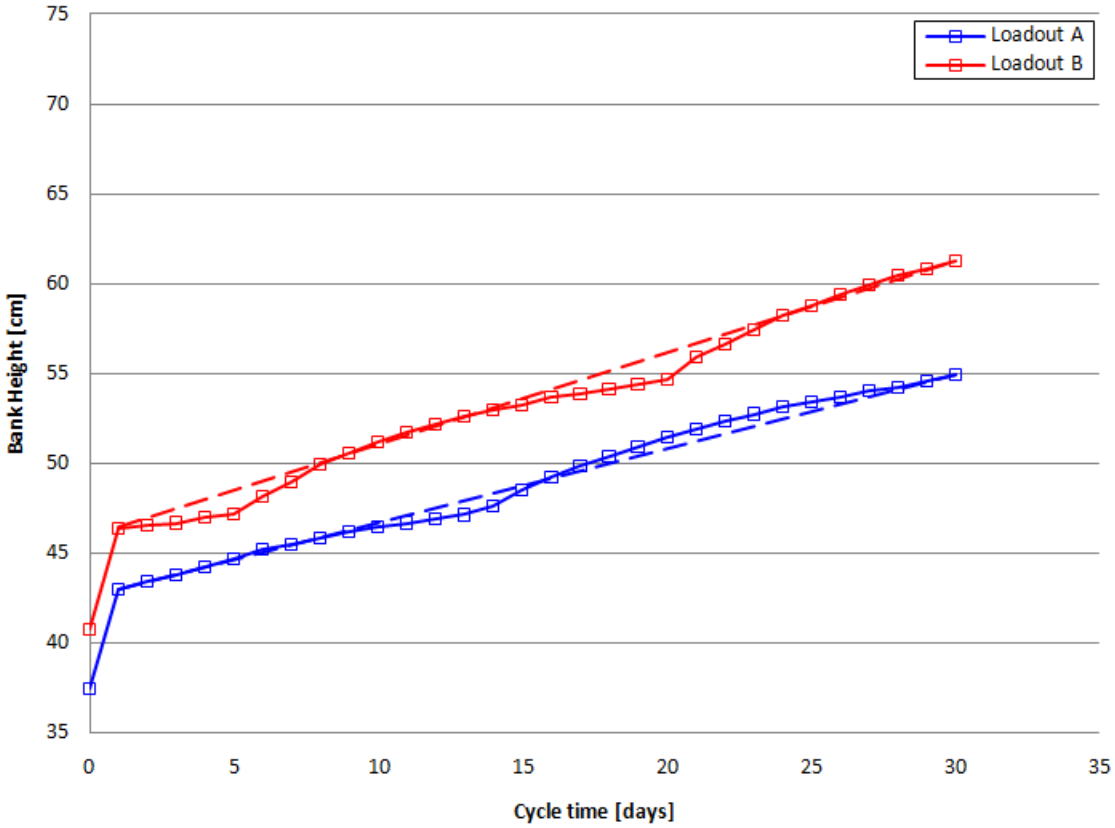

Figure 81 Bank height versus cycle length for the 5 by 5 core.

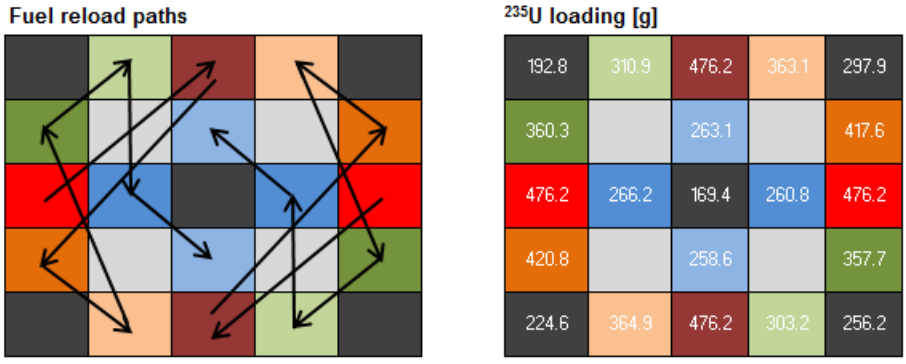

Figure 82 Loading pattern and mass distribution used to reload the 5 by 5 core. Numbers indicate ^{235}U content in grams.

Figure 83 Core power distribution for the 5 by 5 core, for the most reactive cycle.

A3.2 Safety parameters

Table 28 List of relevant safety parameters associated with the 5 by 5 core.

Parameter	Value
BOC ^{235}U mass	6993 g
EOC ^{235}U mass	6010 g
Shutdown margin	-11 483 pcm (k_{eff} = 0.89700)
Excess reactivity	+10 814 pcm (k_{eff} = 1.09287)
Control bank reactivity worth	+22 297 pcm
Power peaking factor: - f_{xy} - f_z - f_p - PPF	1.33 1.35 1.3 (assumed) 2.33 (<3.5)
Limiting power to prevent the onset of nucleate boiling	28.4 MW
Limiting power to prevent bubble detachment instability	37.3 MW

A3.3 OSCAR-4 axially averaged thermal neutron flux distribution

	1	2	3	4	5	6	7	8	9
A	2.68E+14	2.99E+14	3.26E+14	3.54E+14	3.71E+14	3.68E+14	3.51E+14	3.29E+14	2.98E+14
B	3.00E+14	3.11E+14	2.99E+14	3.07E+14	3.17E+14	3.18E+14	3.21E+14	3.43E+14	3.34E+14
C	3.33E+14	3.03E+14	1.23E+14	1.48E+14	1.28E+14	1.48E+14	1.21E+14	3.31E+14	3.68E+14
D	3.66E+14	3.34E+14	1.28E+14	4.90E+14	1.73E+14	5.15E+14	1.32E+14	3.61E+14	3.98E+14
E	3.84E+14	3.50E+14	1.15E+14	1.79E+14	1.45E+14	1.85E+14	1.21E+14	3.72E+14	4.09E+14
F	3.71E+14	3.37E+14	1.24E+14	4.96E+14	1.72E+14	4.97E+14	1.33E+14	3.52E+14	3.88E+14
G	3.40E+14	3.08E+14	1.21E+14	1.41E+14	1.25E+14	1.50E+14	1.17E+14	3.14E+14	3.50E+14
H	3.07E+14	3.17E+14	3.00E+14	3.01E+14	3.07E+14	3.04E+14	3.01E+14	3.20E+14	3.12E+14
I	2.71E+14	3.02E+14	3.26E+14	3.47E+14	3.57E+14	3.47E+14	3.26E+14	3.04E+14	2.75E+14

Figure 84 Thermal flux-distribution (E_n<0.625 eV) for the 5 by 5 core. Values calculated over the active core region (±30 cm) with OSCAR4.

A3.4 MCNP5 In-core axially averaged thermal neutron flux distribution

	1	2	3	4	5	6	7	8	9
A	2.67E+14	2.90E+14	3.08E+14	3.26E+14	3.34E+14	3.33E+14	3.21E+14	3.07E+14	2.84E+14
B	2.90E+14	2.92E+14	2.71E+14	2.80E+14	2.87E+14	2.86E+14	2.83E+14	3.10E+14	3.09E+14
C	3.09E+14	2.78E+14	1.43E+14	1.40E+14	1.26E+14	1.37E+14	1.42E+14	2.93E+14	3.28E+14
D	3.25E+14	2.87E+14	1.39E+14	4.58E+14	1.79E+14	4.75E+14	1.39E+14	3.00E+14	3.43E+14
E	3.33E+14	2.95E+14	1.26E+14	1.66E+14	1.69E+14	1.70E+14	1.30E+14	3.08E+14	3.48E+14
F	3.26E+14	2.88E+14	1.33E+14	4.61E+14	1.79E+14	4.62E+14	1.43E+14	2.98E+14	3.38E+14
G	3.12E+14	2.80E+14	1.41E+14	1.32E+14	1.25E+14	1.42E+14	1.38E+14	2.83E+14	3.20E+14
H	2.94E+14	2.96E+14	2.72E+14	2.77E+14	2.85E+14	2.81E+14	2.73E+14	2.99E+14	2.99E+14
I	2.70E+14	2.92E+14	3.08E+14	3.23E+14	3.33E+14	3.27E+14	3.12E+14	2.96E+14	2.74E+14

Figure 85 Thermal flux-distribution (E_n<0.625 eV) for the 5 by 5 core, for the most reactive cycle. Values calculated over the active core region (±30 cm) with MCNP5.

A3.5 MCNP5 In-core axially averaged epi-thermal neutron flux distribution

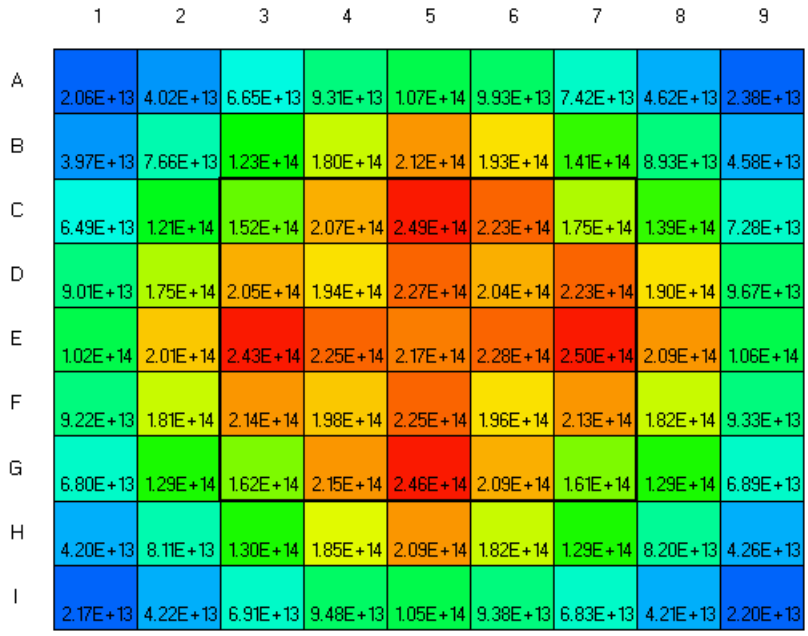

Figure 86 Epi-thermal flux-distribution (E_n>0.625 eV & E_n<100 keV) for the 5 by 5 core, for the most reactive cycle. Values calculated over the active core region (±30 cm) with MCNP5.

A3.6 MCNP5 In-core axially averaged fast neutron flux distribution

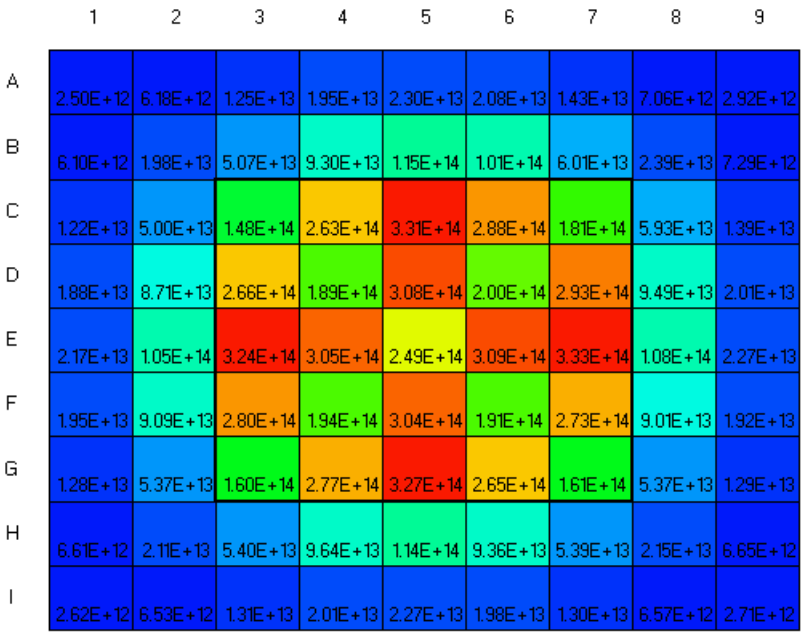

Figure 87 Fast flux-distribution (E_n>100 keV) for the 5 by 5 core, for the most reactive cycle. Values calculated over the active core region (±30 cm) with MCNP5.

A3.7 MCNP5 Ex-core neutron flux distribution

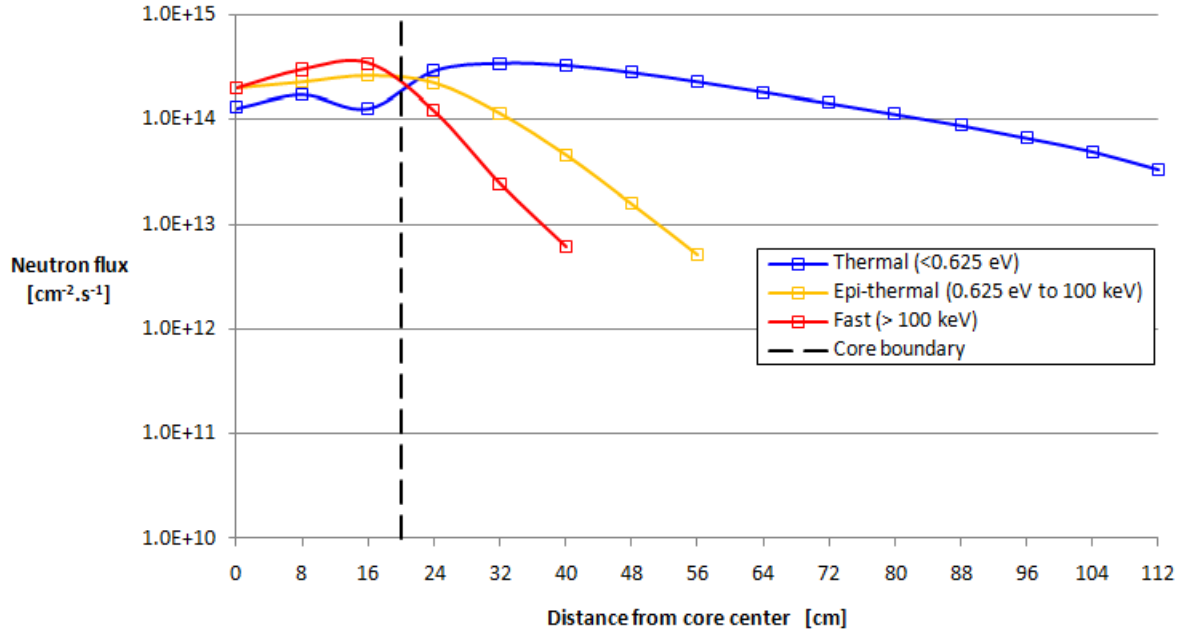

Figure 88 Flux-distribution in the reflector (blanket region) of the 5 by 5 core, for the most reactive cycle. Values were calculated over the active core region (±30 cm) with MCNP5 and only include statistically converged data.

Table 29 Numerical values for the Flux-distribution in the reflector (blanket region) of the 5 by 5 core, for the most reactive cycle. Values were calculated over the active core region (±30 cm) with MCNP5 and only include statistically converged data.

Distance from center [cm]	Thermal (E_n<0.625 eV)	Epi-thermal (E_n 0.625 eV to 100 keV)	Fast (E_n>100 keV)
0	1.30E+14	2.02E+14	2.01E+14
8	1.75E+14	2.30E+14	3.02E+14
16	1.29E+14	2.65E+14	3.48E+14
24	2.93E+14	2.27E+14	1.23E+14
32	3.47E+14	1.15E+14	2.46E+13
40	3.31E+14	4.64E+13	6.08E+12
48	2.83E+14	1.58E+13	-
56	2.31E+14	5.14E+12	-
64	1.84E+14	-	-
72	1.46E+14	-	-
80	1.14E+14	-	-
88	8.92E+13	-	-
96	6.73E+13	-	-
104	4.97E+13	-	-
112	3.34E+13	-	-

A3.8 MCNP5 Thermal neutron beamline characteristics

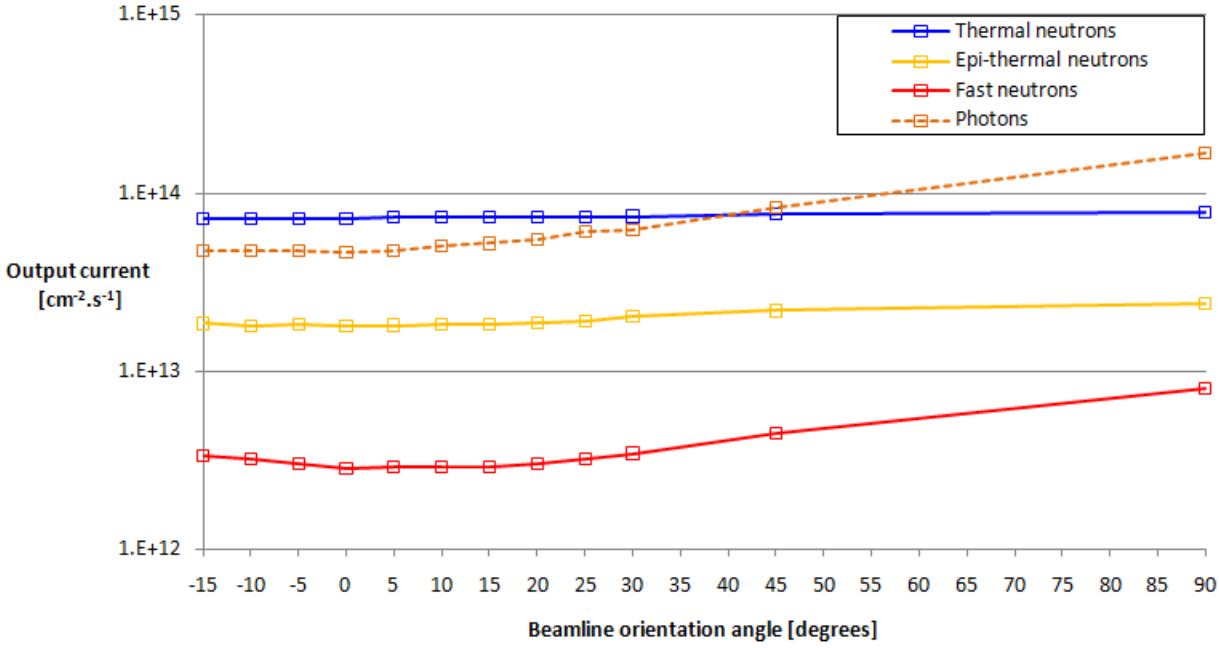

Figure 89 Beamline output current for a thermal beamline for the 5 by 5 core. Angular orientation is relative to the north core face. Values calculated with MCNP5 utilizing DXTRAN-spheres.

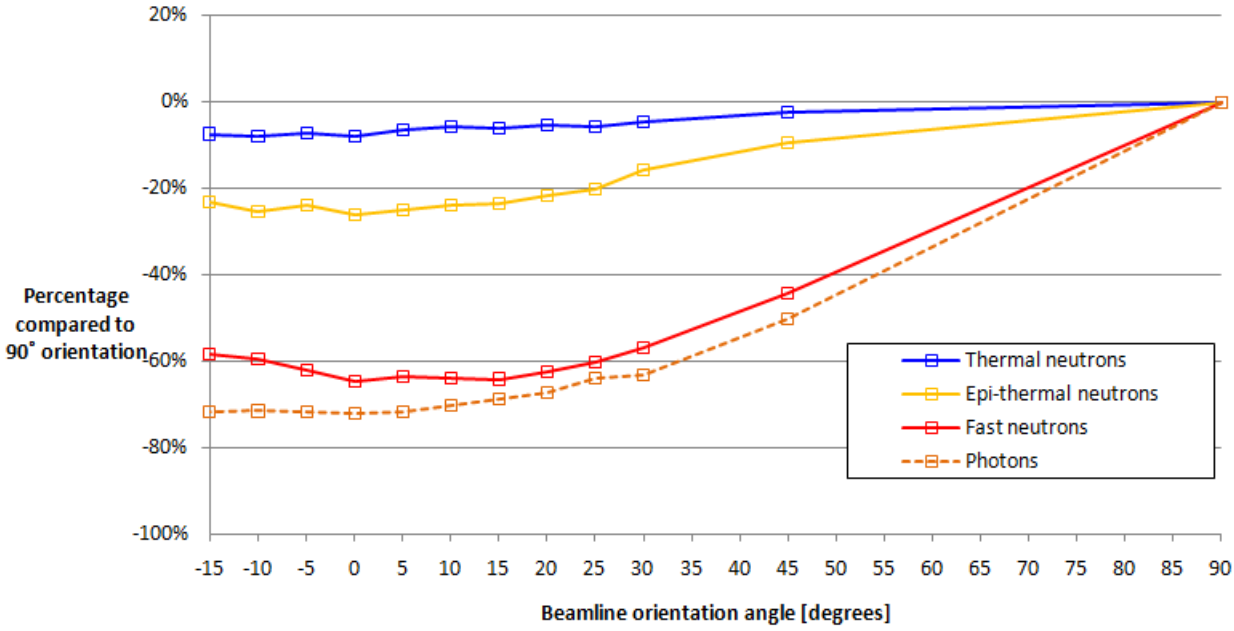

Figure 90 Beamline output current for a thermal beamline for the 5 by 5 core. Angular orientation is relative to the north core face. Values calculated with MCNP5 utilizing DXTRAN-spheres.

Table 30 Numerical values for the output currents, for the 5 by 5 core, at the end of the thermal beamline. The currents only includes directional values within a 5° difference of the output normal.

Orientation Angles (degrees)	Thermal (E_n<0.625 eV)	Epi-thermal (E_n 0.625 eV to 100 keV)	Fast (E_n>100 keV)	Photons (Total)
90	7.763E+13	2.411E+13	8.031E+12	1.677E+14
45	7.576E+13	2.187E+13	4.477E+12	8.340E+13
30	7.408E+13	2.036E+13	3.461E+12	6.163E+13
25	7.330E+13	1.923E+13	3.198E+12	6.057E+13
20	7.366E+13	1.889E+13	3.031E+12	5.519E+13
15	7.290E+13	1.849E+13	2.884E+12	5.218E+13
10	7.322E+13	1.838E+13	2.886E+12	5.020E+13
5	7.273E+13	1.813E+13	2.929E+12	4.746E+13
0	7.146E+13	1.784E+13	2.840E+12	4.690E+13
-5	7.207E+13	1.834E+13	3.035E+12	4.772E+13
-10	7.143E+13	1.803E+13	3.248E+12	4.778E+13
-15	7.193E+13	1.852E+13	3.343E+12	4.738E+13

Table 31 Numerical values for the output currents, for the 5 by 5 core, at the end of the thermal beamline as percentages of the 90° orientation. The currents only includes directional values within a 5° difference of the output normal.

Orientation Angles (degrees)	Thermal (E_n<0.625 eV)	Epi-thermal (E_n 0.625 eV to 100 keV)	Fast (E_n>100 keV)	Photons (Total)
90	100.00	100.00	100.00	100.00
45	97.59	90.71	55.74	49.75
30	95.43	84.46	43.09	36.76
25	94.42	79.77	39.82	36.13
20	94.88	78.35	37.74	32.92
15	93.90	76.69	35.91	31.13
10	94.32	76.22	35.93	29.95
5	93.69	75.19	36.47	28.31
0	92.05	73.98	35.36	27.98
-5	92.84	76.08	37.79	28.46
-10	92.01	74.78	40.44	28.50
-15	92.66	76.83	41.62	28.26

A3.9 MCNP5 Cold neutron beamline characteristics (Hydrogen source, H_2 at 20K)

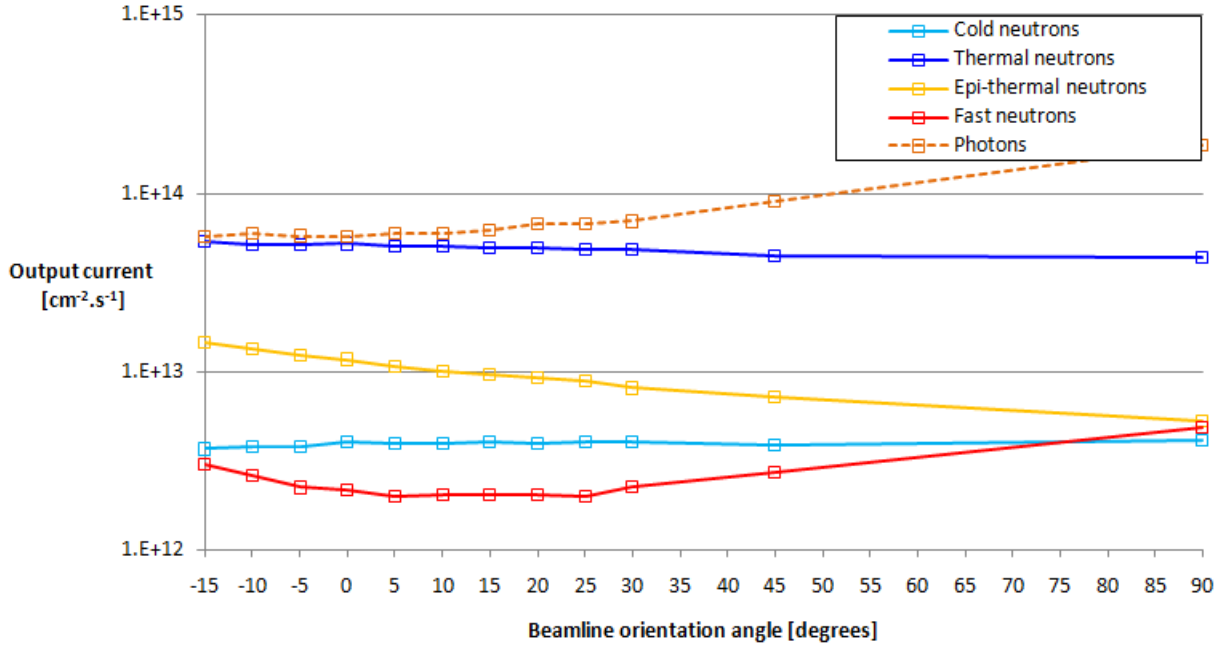

Figure 91 Beamline output current for a thermal beamline for the 5 by 5 core. Angular orientation is relative to the north core face. Values calculated with MCNP5 utilizing DXTRAN-spheres.

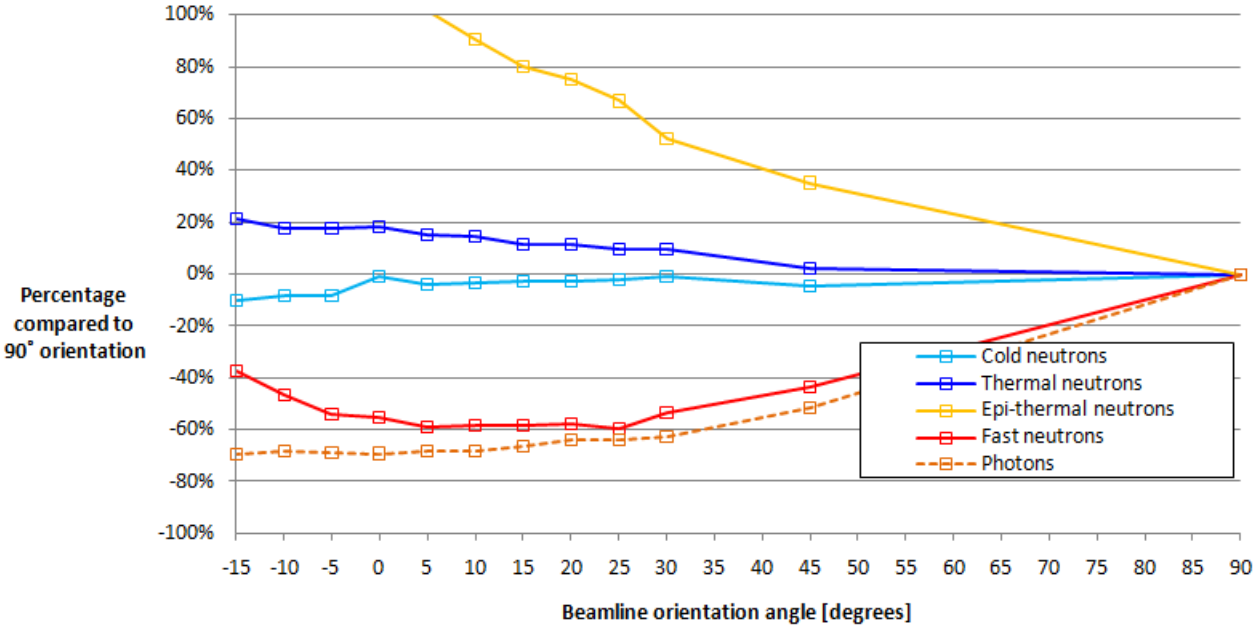

Figure 92 Beamline output current for a thermal beamline for the 5 by 5 core. Angular orientation is relative to the north core face. Values calculated with MCNP5 utilizing DXTRAN-spheres.

Table 32 Numerical values for the output currents, for the 5 by 5 core, at the end of the thermal beamline. The currents only includes directional values within a 5° difference of the output normal.

Orientation Angles (degrees)	Cold (E_n<5 meV)	Thermal (E_n<0.625 eV)	Epi-thermal (E_n 0.625 eV to 100 keV)	Fast (E_n>100 keV)	Photons (Total)
90	4.113E+12	4.409E+13	5.322E+12	4.879E+12	1.868E+14
45	3.917E+12	4.503E+13	7.199E+12	2.742E+12	9.037E+13
30	4.081E+12	4.833E+13	8.095E+12	2.269E+12	6.969E+13
25	4.025E+12	4.830E+13	8.879E+12	1.983E+12	6.741E+13
20	3.996E+12	4.906E+13	9.313E+12	2.050E+12	6.778E+13
15	4.007E+12	4.910E+13	9.594E+12	2.027E+12	6.222E+13
10	3.972E+12	5.057E+13	1.015E+13	2.041E+12	5.930E+13
5	3.946E+12	5.088E+13	1.075E+13	2.013E+12	5.929E+13
0	4.083E+12	5.218E+13	1.174E+13	2.173E+12	5.745E+13
-5	3.775E+12	5.188E+13	1.231E+13	2.242E+12	5.780E+13
-10	3.778E+12	5.192E+13	1.336E+13	2.598E+12	5.966E+13
-15	3.686E+12	5.352E+13	1.447E+13	3.052E+12	5.738E+13

Table 33 Numerical values for the output currents, for the 5 by 5 core, at the end of the thermal beamline as percentages of the 90° orientation. The currents only includes directional values within a 5° difference of the output normal.

Orientation Angles (degrees)	Cold (E_n<5 meV)	Thermal (E_n<0.625 eV)	Epi-thermal (E_n 0.625 eV to 100 keV)	Fast (E_n>100 keV)	Photons (Total)
90	100.00	100.00	100.00	100.00	100.00
45	95.23	102.13	135.27	56.20	48.39
30	99.24	109.60	152.11	46.52	37.31
25	97.87	109.55	166.83	40.64	36.09
20	97.15	111.26	175.00	42.03	36.29
15	97.44	111.37	180.27	41.55	33.32
10	96.59	114.69	190.64	41.84	31.75
5	95.95	115.39	202.07	41.26	31.75
0	99.27	118.34	220.53	44.55	30.76
-5	91.79	117.66	231.30	45.96	30.95
-10	91.86	117.76	250.98	53.25	31.94
-15	89.62	121.37	271.91	62.56	30.72

A4 7 X 7 CORE WITH 7 IRRADIATION POSITIONS

The core configuration with this design is shown in the figure below:

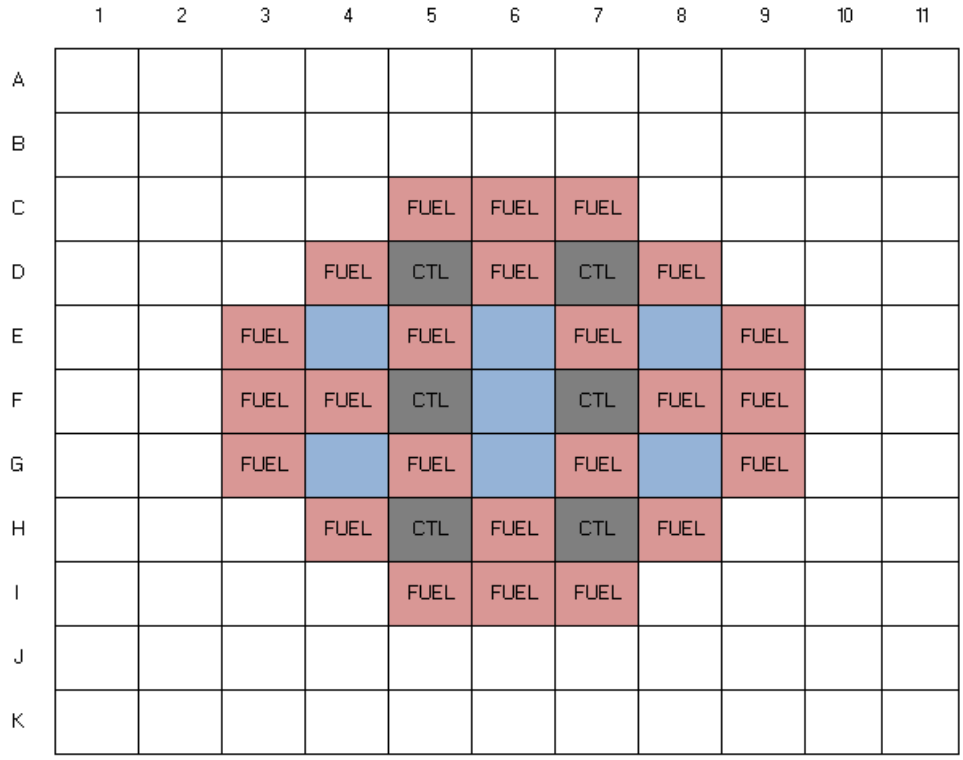

Figure 93 Diagram of the 7 by 7 core configuration.

A4.1 Loading pattern and equilibrium core power distribution

The core configuration is shown in figure 93. It includes 6 control assemblies and 24 fuel assemblies. Control assembly fuel followers have 17 uranium-silicide fuel plates with a meat thickness of 0.066 cm resulting in 297 grams of ^{235}U per assembly. Fuel assemblies have 21 uranium-silicide fuel plates with a meat thickness of 0.066 cm resulting in 476 grams of ^{235}U per assembly. The heavy water reflector tank is modelled as a 260 cm diameter tank and was selected as such to correspond approximately to the design of the OPAL reactor. Utilizing equation 21, figure 94 shows the initial operating envelope.

Table 34 Initial operating envelope for the 7 by 7 core with 24 fuel assemblies and 6 control assemblies.

Parameter	Symbol	Value
Limiting power to prevent nucleate boiling	P_{ONB}	< 40.6 MW
Discharge burnup for 28 days of operation		
Discharge burnup, replacing 3 assembly per cycle	-	@40 MW > 100%
Discharge burnup, replacing 4 assemblies per cycle	-	@40 MW = 60%
Discharge burnup, replacing 5 assemblies per cycle	-	@40 MW < 50%
Discharge burnup for 35 days of operation		

Discharge burnup, replacing 4 assembly per cycle	-	@40 MW = 78%

In this table, replacing 4 assemblies per cycle (of 35 days length) yields a suitable discharge burnup of approximately 78% which allows an operating envelope as indicated in figure 94.

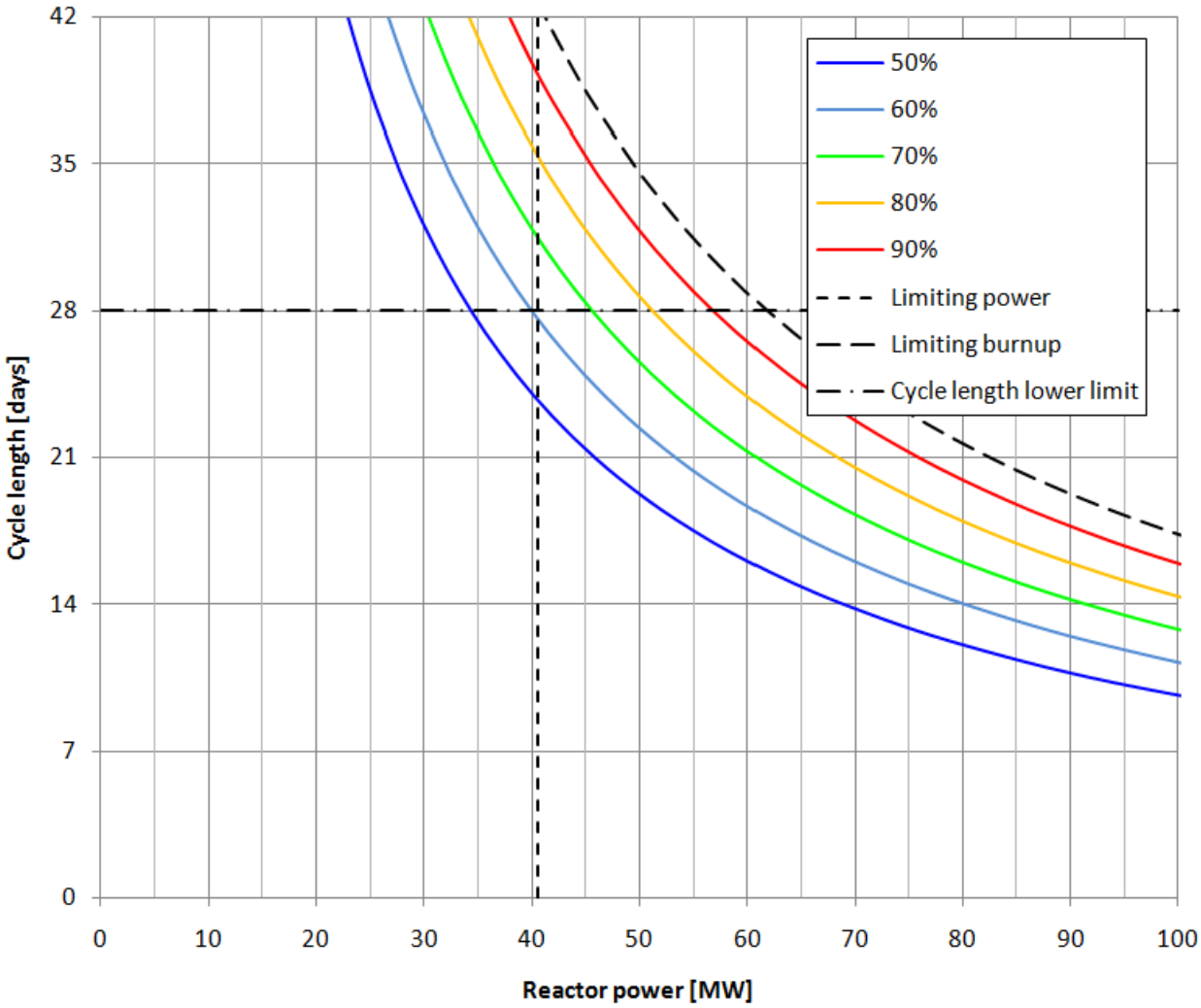

Figure 94 Operating envelope for the 7 by 7 core utilizing 6 control assemblies and 24 fuel assemblies. Four fuel assemblies are replaced per cycle.

Below is the equilibrium core mass distribution and reload pattern. A single loading sequence was applied:

- Cycle A: 4 fuel assemblies + 1 control assembly
- Repeat starting at Cycle A

The loading path for this reload pattern is shown in figure 96, however, since there are 4 symmetric loading paths only 2 are shown. The corresponding bank height versus cycle progression is shown in figure 95 below.

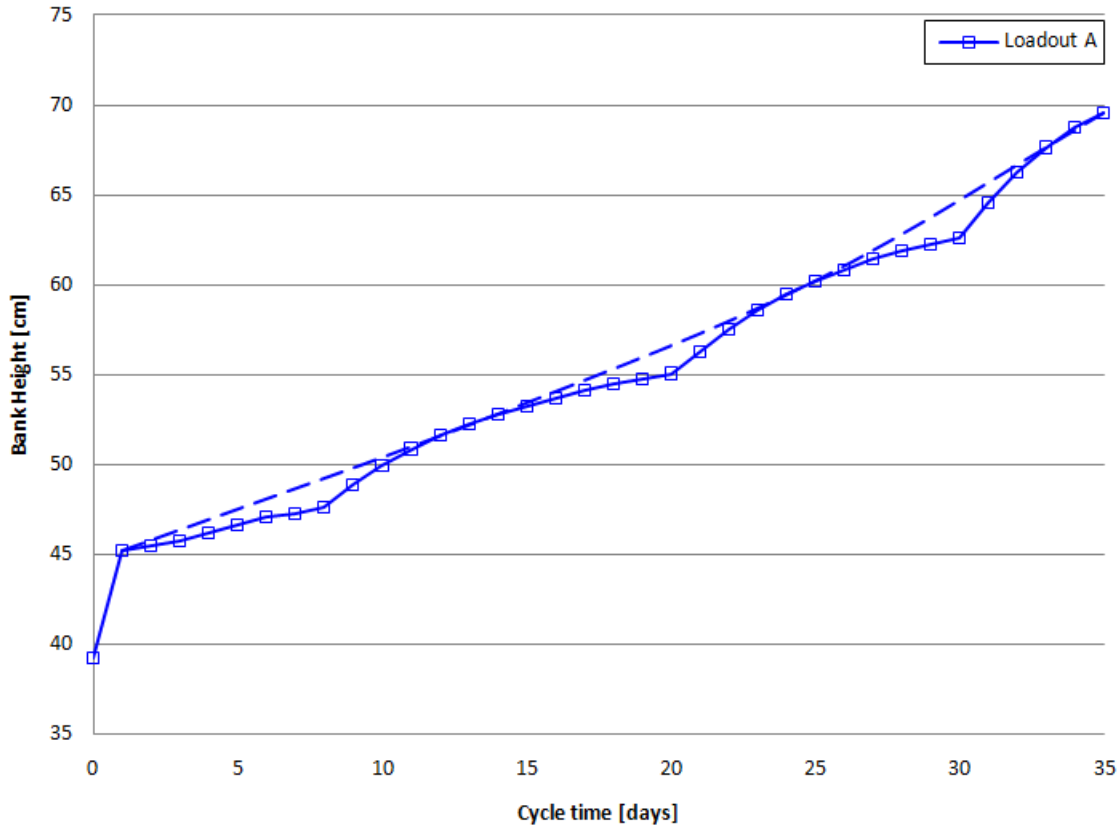

Figure 95 Bank height versus cycle length for the 7 by 7 core.

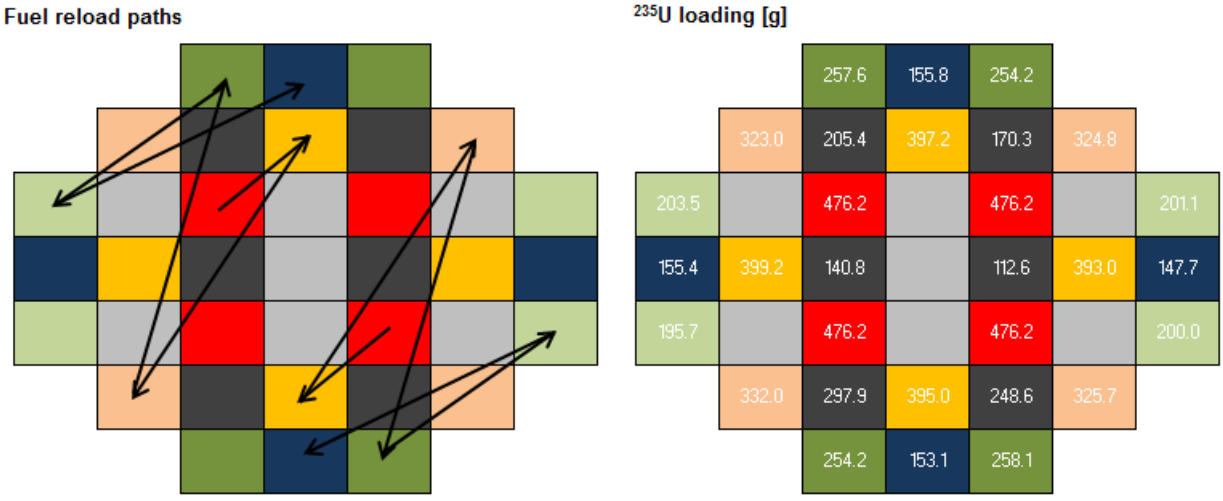

Figure 96 Loading pattern and mass distribution used to reload the 7 by 7 code numbers indicate ^{235}U content in grams.

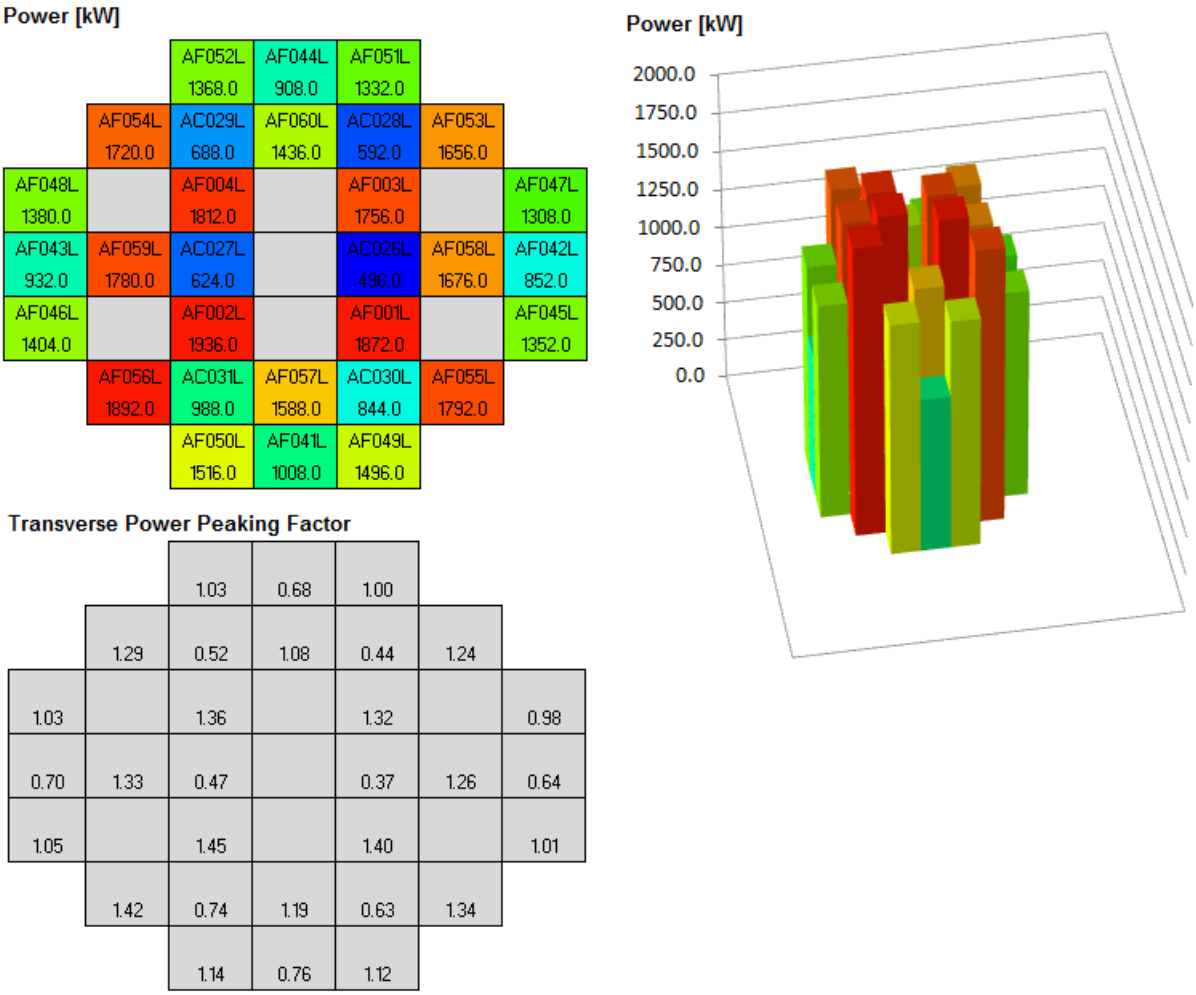

Figure 97 Core power distribution for the 7 by 7 core, for the most reactive cycle.

A4.2 Safety parameters

Table 35 List of relevant safety parameters associated with the 7 by 7 core.

Parameter	Value
BOC ^{235}U mass	8385 g
EOC ^{235}U mass	6778 g
Shutdown margin	-13 386 pcm (k_{eff} = 0.88194)
Excess reactivity	+9 325 pcm (k_{eff} = 1.10284)
Control bank reactivity worth	+22 711 pcm
Power peaking factor: - f_{xy} - f_z - f_p - PPF	1.45 1.32 1.3 (assumed) 2.49 (<3.5)
Limiting power to prevent the onset of nucleate boiling	40.6 MW

Limiting power to prevent bubble detachment instability	53.2 MW

A4.3 OSCAR-4 axially averaged thermal neutron flux distribution

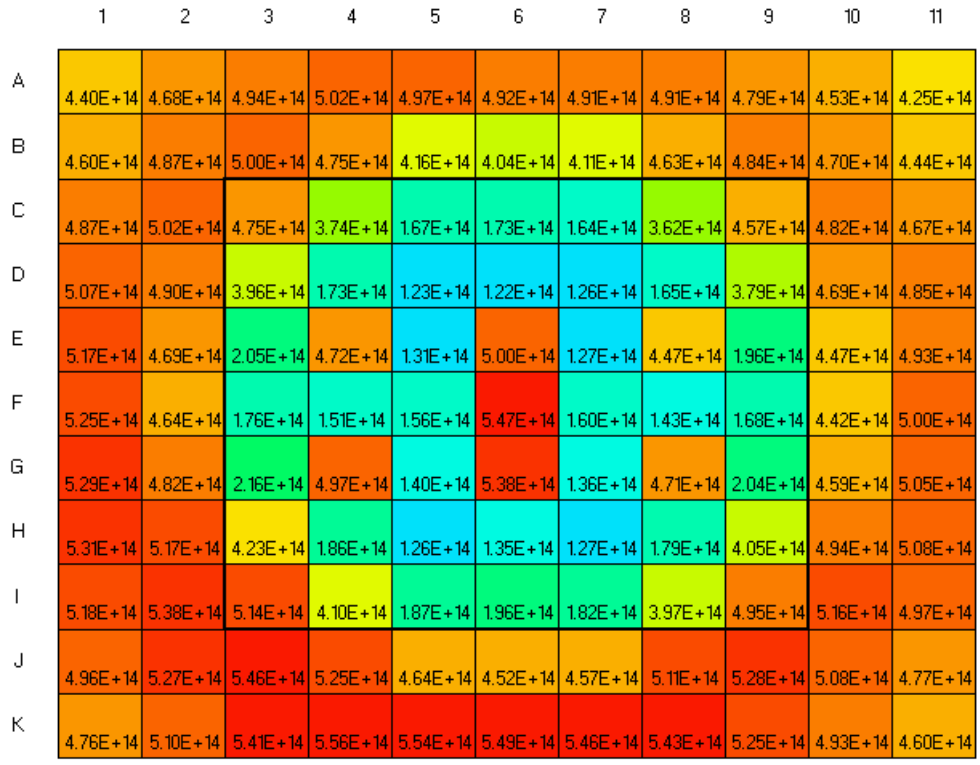

Figure 98 Thermal flux-distribution (E_n<0.625 eV) for the 7 by 7 core, for the most reactive cycle. Values calculated over the active core region (±30 cm) with OSCAR4.

A4.4 MCNP5 In-core axially averaged thermal neutron flux distribution

	1	2	3	4	5	6	7	8	9	10	11
A	2.86E+14	3.25E+14	3.54E+14	3.69E+14	3.74E+14	3.75E+14	3.73E+14	3.68E+14	3.53E+14	3.24E+14	2.87E+14
B	3.26E+14	3.65E+14	3.82E+14	3.73E+14	3.44E+14	3.40E+14	3.43E+14	3.72E+14	3.82E+14	3.63E+14	3.27E+14
C	3.58E+14	3.86E+14	3.77E+14	3.10E+14	1.61E+14	1.71E+14	1.62E+14	3.08E+14	3.75E+14	3.85E+14	3.57E+14
D	3.77E+14	3.84E+14	3.29E+14	1.65E+14	1.45E+14	1.17E+14	1.48E+14	1.62E+14	3.30E+14	3.85E+14	3.80E+14
E	3.88E+14	3.66E+14	2.10E+14	4.59E+14	1.39E+14	4.69E+14	1.39E+14	4.56E+14	2.11E+14	3.69E+14	3.89E+14
F	3.93E+14	3.65E+14	1.90E+14	1.44E+14	1.79E+14	5.10E+14	1.85E+14	1.44E+14	1.92E+14	3.65E+14	3.96E+14
G	3.97E+14	3.77E+14	2.22E+14	4.90E+14	1.50E+14	5.02E+14	1.47E+14	4.80E+14	1.85E+14	3.70E+14	3.97E+14
H	3.95E+14	4.06E+14	3.53E+14	1.68E+14	1.53E+14	1.31E+14	1.51E+14	1.91E+14	3.43E+14	4.02E+14	3.95E+14
I	3.80E+14	4.15E+14	4.10E+14	3.37E+14	1.82E+14	1.93E+14	1.77E+14	3.37E+14	4.03E+14	4.10E+14	3.77E+14
J	3.50E+14	3.96E+14	4.20E+14	4.11E+14	3.84E+14	3.80E+14	3.80E+14	4.07E+14	4.12E+14	3.91E+14	3.47E+14
K	3.12E+14	3.56E+14	3.91E+14	4.08E+14	4.16E+14	4.15E+14	4.11E+14	4.04E+14	3.83E+14	3.51E+14	3.08E+14

Figure 99 Thermal flux-distribution (E_n<0.625 eV) for the 7 by 7 core, for the most reactive cycle. Values calculated over the active core region (±30 cm) with MCNP5.

A4.5 MCNP5 In-core axially averaged epi-thermal neutron flux distribution

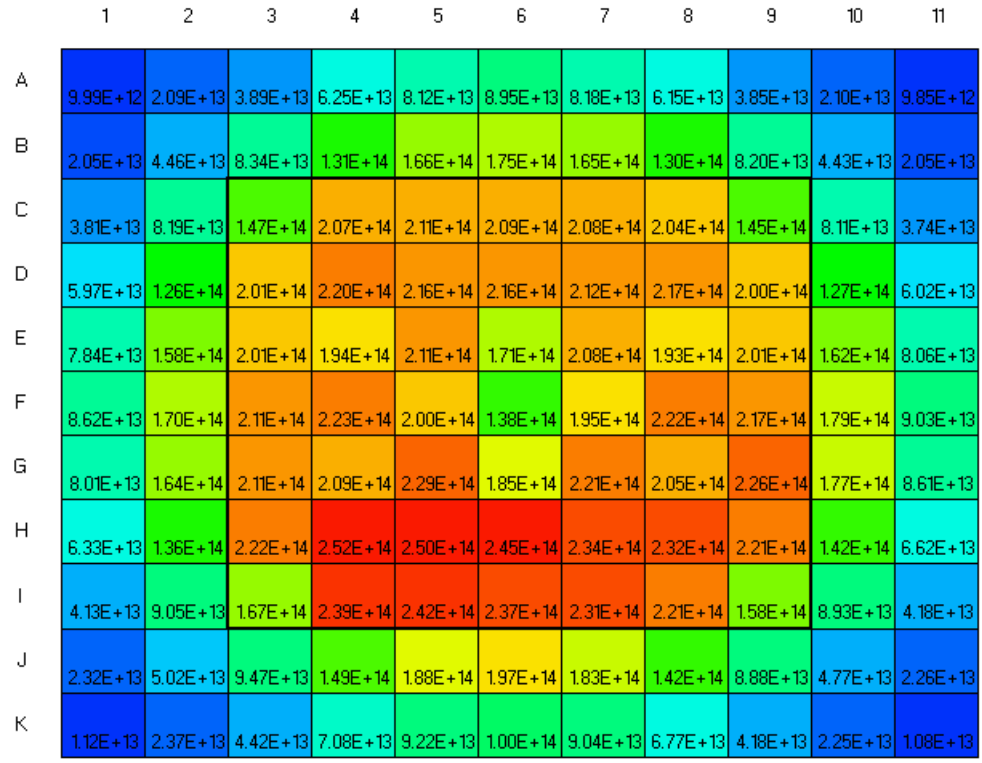

Figure 100 Epi-thermal flux-distribution (E_n>0.625 eV & E_n<100 keV) for the 7 by 7 core, for the most reactive cycle. Values calculated over the active core region (±30 cm) with MCNP5.

A4.6 MCNP5 In-core axially averaged fast neutron flux distribution

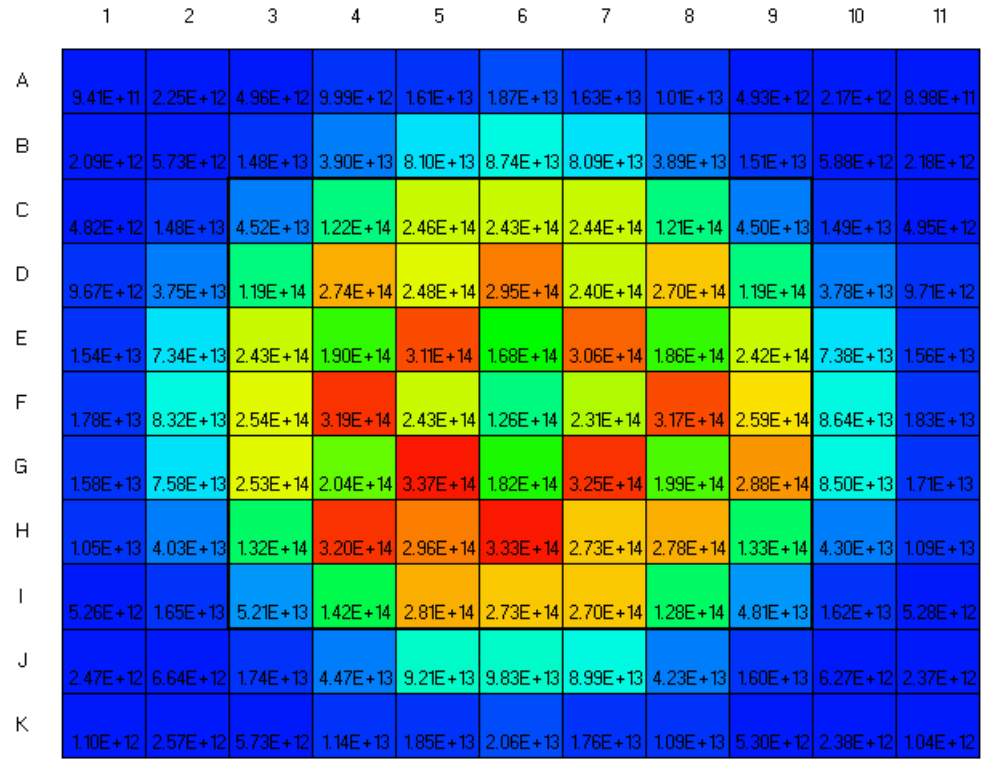

Figure 101 Fast flux-distribution (E_n>100 keV) for the 7 by 7 core, for the most reactive cycle. Values calculated over the active core region (±30 cm) with MCNP5.

A4.7 MCNP5 Ex-core neutron flux distribution

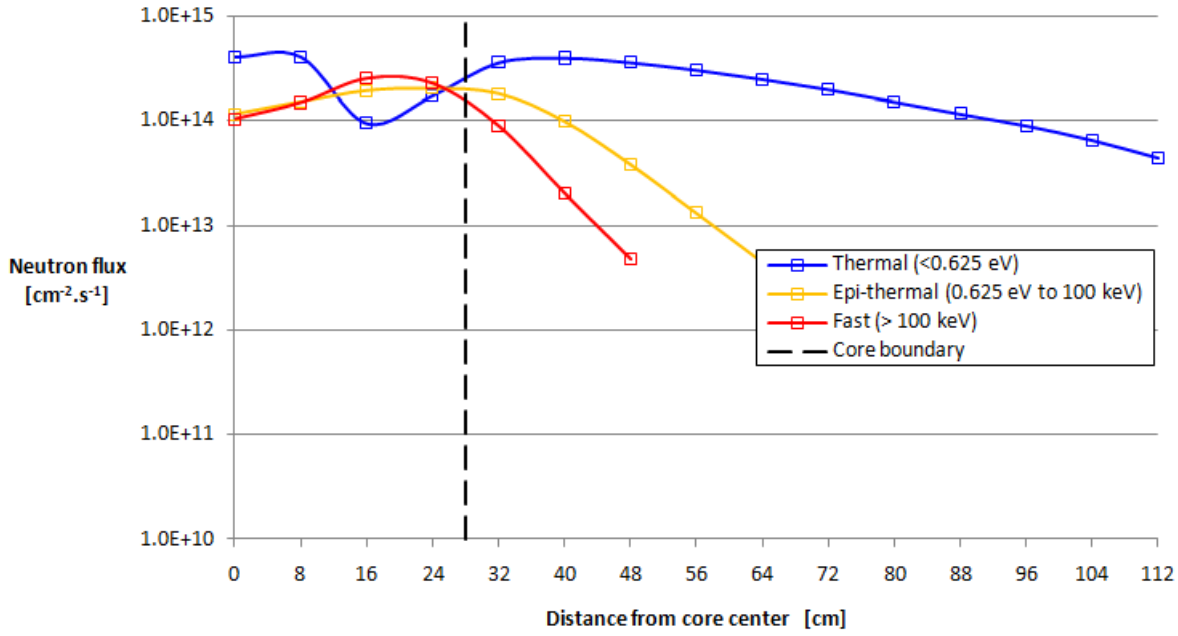

Figure 102 Flux-distribution in the reflector (blanket region) of the 7 by 7 core, for the most reactive cycle. Values were calculated over the active core region (±30 cm) with MCNP5 and only include statistically converged data.

Table 36 Numerical values for the Flux-distribution in the reflector (blanket region) of the 7 by 7 core, for the most reactive cycle. Values were calculated over the active core region (±30 cm) with MCNP5 and only include statistically converged data.

Distance from center [cm]	Thermal (E_n<0.625 eV)	Epi-thermal (E_n 0.625 eV to 100 keV)	Fast (E_n>100 keV)
0	4.11E+14	1.16E+14	1.04E+14
8	4.13E+14	1.52E+14	1.49E+14
16	9.58E+13	1.97E+14	2.56E+14
24	1.77E+14	2.06E+14	2.29E+14
32	3.63E+14	1.84E+14	8.92E+13
40	4.02E+14	9.88E+13	2.03E+13
48	3.63E+14	3.83E+13	4.76E+12
56	3.08E+14	1.31E+13	-
64	2.52E+14	4.41E+12	-
72	2.01E+14	-	-
80	1.54E+14	-	-
88	1.18E+14	-	-
96	9.10E+13	-	-
104	6.59E+13	-	-
112	4.44E+13	-	-

A4.8 MCNP5 Thermal neutron beamline characteristics

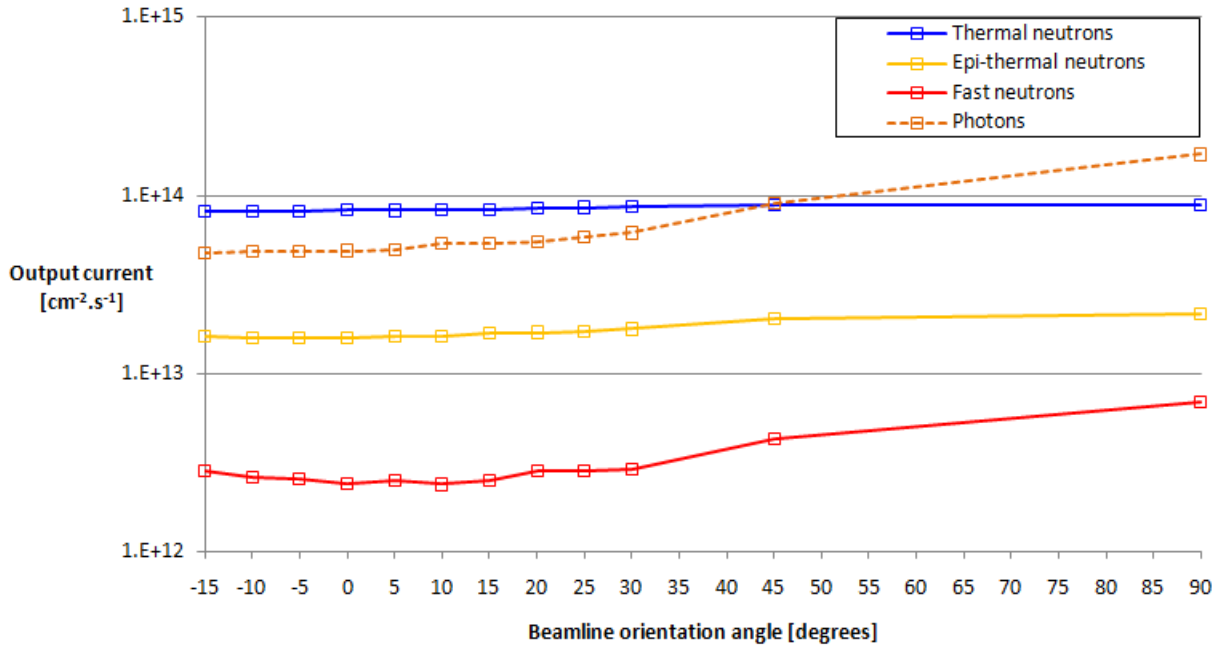

Figure 103 Beamline output current for a thermal beamline for the 7 by 7 core. Angular orientation is relative to the north core face. Values calculated with MCNP5 utilizing DXTRAN-spheres.

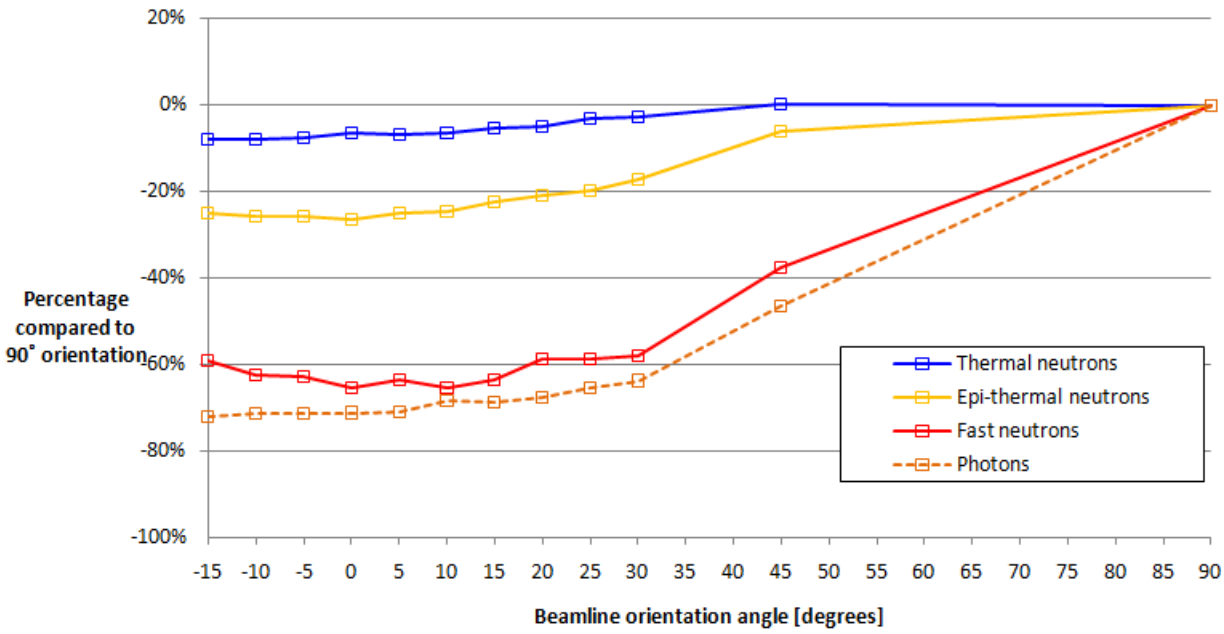

Figure 104 Beamline output current for a thermal beamline for the 7 by 7 core. Angular orientation is relative to the north core face. Values calculated with MCNP5 utilizing DXTRAN-spheres.

Table 37 Numerical values for the output currents, for the 7 by 7 core, at the end of the thermal beamline. The currents only includes directional values within a 5° difference of the output normal.

Orientation Angles (degrees)	Thermal (E_n<0.625 eV)	Epi-thermal (E_n 0.625 eV to 100 keV)	Fast (E_n>100 keV)	Photons (Total)
90	8.840E+13	2.150E+13	6.918E+12	1.698E+14
45	8.854E+13	2.021E+13	4.318E+12	9.094E+13
30	8.615E+13	1.778E+13	2.898E+12	6.158E+13
25	8.570E+13	1.725E+13	2.858E+12	5.892E+13
20	8.415E+13	1.704E+13	2.850E+12	5.476E+13
15	8.379E+13	1.673E+13	2.516E+12	5.328E+13
10	8.280E+13	1.620E+13	2.386E+12	5.397E+13
5	8.229E+13	1.615E+13	2.516E+12	4.919E+13
0	8.266E+13	1.585E+13	2.402E+12	4.898E+13
-5	8.165E+13	1.595E+13	2.578E+12	4.867E+13
-10	8.142E+13	1.598E+13	2.610E+12	4.848E+13
-15	8.142E+13	1.613E+13	2.830E+12	4.763E+13

Table 38 Numerical values for the output currents, for the 7 by 7 core, at the end of the thermal beamline as percentages of the 90° orientation. The currents only includes directional values within a 5° difference of the output normal.

Orientation Angles (degrees)	Thermal (E_n<0.625 eV)	Epi-thermal (E_n 0.625 eV to 100 keV)	Fast (E_n>100 keV)	Photons (Total)
90	100.00	100.00	100.00	100.00
45	100.16	94.01	62.43	53.56
30	97.46	82.72	41.90	36.27
25	96.94	80.23	41.31	34.70
20	95.19	79.26	41.20	32.25
15	94.78	77.80	36.37	31.38
10	93.67	75.34	34.50	31.79
5	93.09	75.14	36.37	28.97
0	93.51	73.71	34.72	28.85
-5	92.36	74.20	37.27	28.67
-10	92.11	74.33	37.74	28.56
-15	92.10	75.02	40.91	28.05

A4.9 MCNP5 Cold neutron beamline characteristics (Hydrogen source, H_2 at 20K)

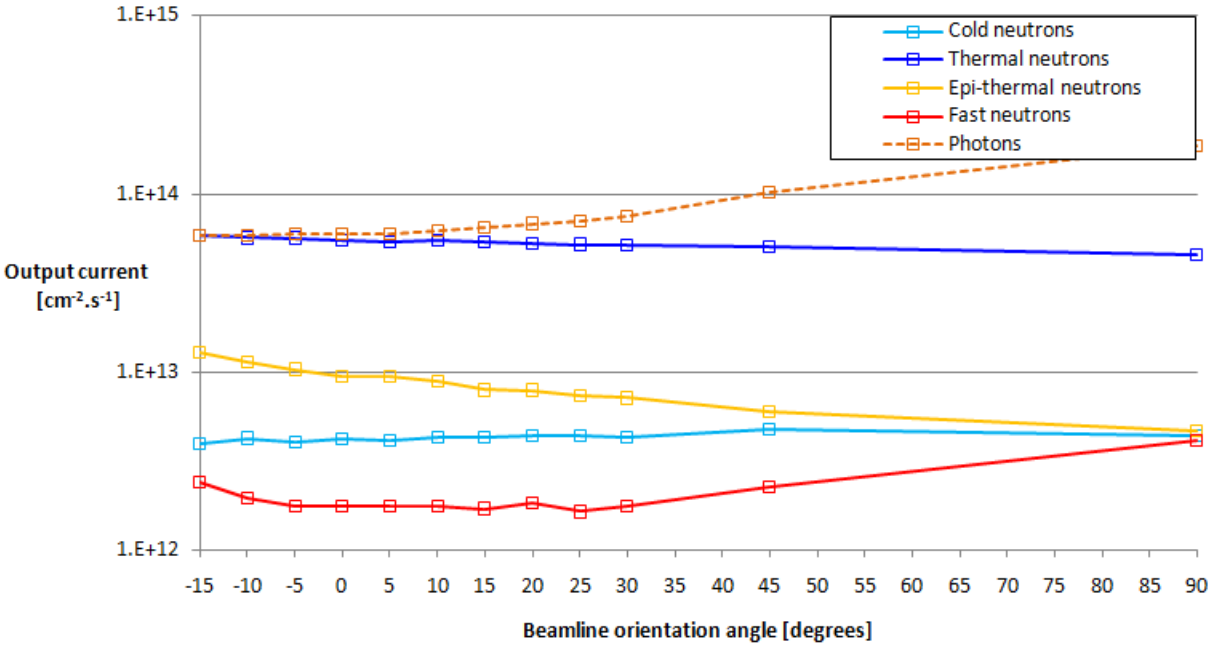

Figure 105 Beamline output current for a thermal beamline for the 7 by 7 core. Angular orientation is relative to the north core face. Values calculated with MCNP5 utilizing DXTRAN-spheres.

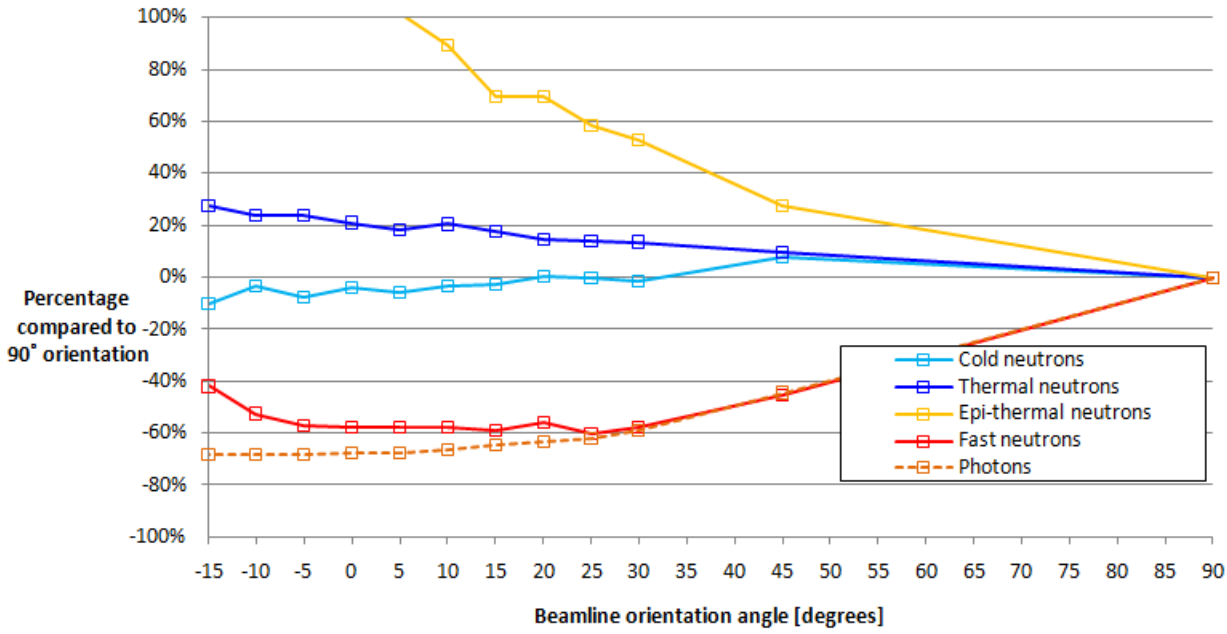

Figure 106 Beamline output current for a thermal beamline for the 7 by 7 core. Angular orientation is relative to the north core face. Values calculated with MCNP5 utilizing DXTRAN-spheres.

Table 39 Numerical values for the output currents, for the 7 by 7 core, at the end of the thermal beamline. The currents only includes directional values within a 5° difference of the output normal.

Orientation Angles (degrees)	Cold (E_n<5 meV)	Thermal (E_n<0.625 eV)	Epi-thermal (E_n 0.625 eV to 100 keV)	Fast (E_n>100 keV)	Photons (Total)
90	4.399E+12	4.578E+13	4.670E+12	4.164E+12	1.852E+14
45	4.731E+12	5.010E+13	5.952E+12	2.263E+12	1.028E+14
30	4.332E+12	5.202E+13	7.148E+12	1.753E+12	7.548E+13
25	4.397E+12	5.214E+13	7.411E+12	1.644E+12	7.013E+13
20	4.424E+12	5.238E+13	7.921E+12	1.845E+12	6.819E+13
15	4.276E+12	5.380E+13	7.933E+12	1.712E+12	6.511E+13
10	4.263E+12	5.515E+13	8.851E+12	1.753E+12	6.181E+13
5	4.140E+12	5.412E+13	9.434E+12	1.760E+12	5.985E+13
0	4.231E+12	5.542E+13	9.447E+12	1.758E+12	6.020E+13
-5	4.053E+12	5.661E+13	1.037E+13	1.783E+12	5.922E+13
-10	4.256E+12	5.665E+13	1.146E+13	1.976E+12	5.863E+13
-15	3.962E+12	5.846E+13	1.282E+13	2.416E+12	5.886E+13

Table 40 Numerical values for the output currents, for the 7 by 7 core, at the end of the thermal beamline as percentages of the 90° orientation. The currents only includes directional values within a 5° difference of the output normal.

Orientation Angles (degrees)	Cold (E_n<5 meV)	Thermal (E_n<0.625 eV)	Epi-thermal (E_n 0.625 eV to 100 keV)	Fast (E_n>100 keV)	Photons (Total)
90	100.00	100.00	100.00	100.00	100.00
45	107.54	109.44	127.45	54.35	55.51
30	98.47	113.64	153.07	42.08	40.75
25	99.95	113.91	158.69	39.47	37.86
20	100.56	114.43	169.62	44.30	36.81
15	97.20	117.52	169.87	41.11	35.15
10	96.91	120.47	189.54	42.09	33.36
5	94.09	118.22	202.02	42.25	32.31
0	96.18	121.05	202.30	42.22	32.50
-5	92.13	123.67	222.04	42.82	31.97
-10	96.75	123.75	245.45	47.45	31.65
-15	90.06	127.71	274.51	58.01	31.78

A5 8 X 9 CORE WITH 9 IRRADIATION POSITIONS

The core configuration for this design is shown in the figure below:

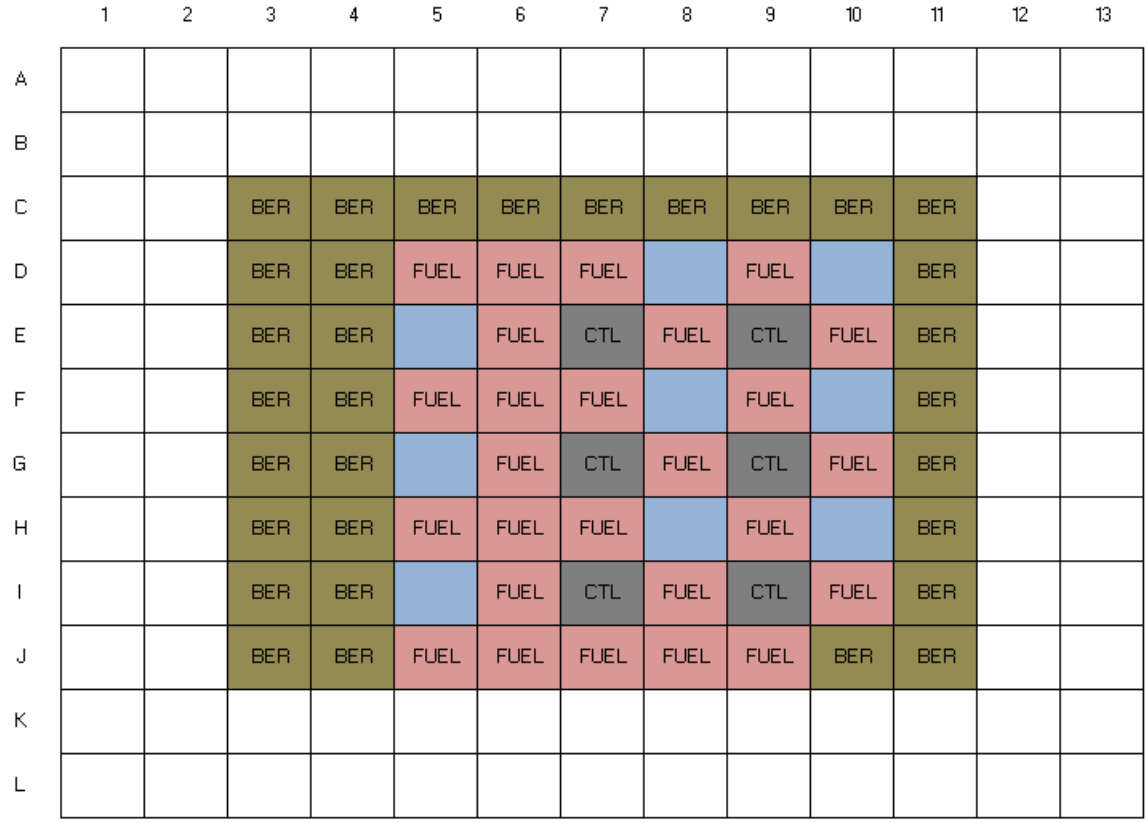

Figure 107 Diagram of the SAFARI-1 core configuration. The core is Beryllium reflected with a light water filled blanket region.

A5.1 Loading pattern and equilibrium core power distribution

In order for this design to correspond approximately to the SAFARI-1 core, a similar loading pattern was used. This loading pattern involves a high-mass to low-thermal-flux arrangement of fuel assemblies whereby a thermal neutron flux distribution is determined after which a list of core positions is then sorted from low- to high flux. Fuel assemblies are then loaded inversely (high mass to low mass). This pattern allows the core to: discharge spent assemblies, then add either fresh assemblies or assemblies stored in the storage pool and then to have the core locations “auto-assign” according to the mass sorting. The nominal relationship between the mass and the thermal flux is shown below:

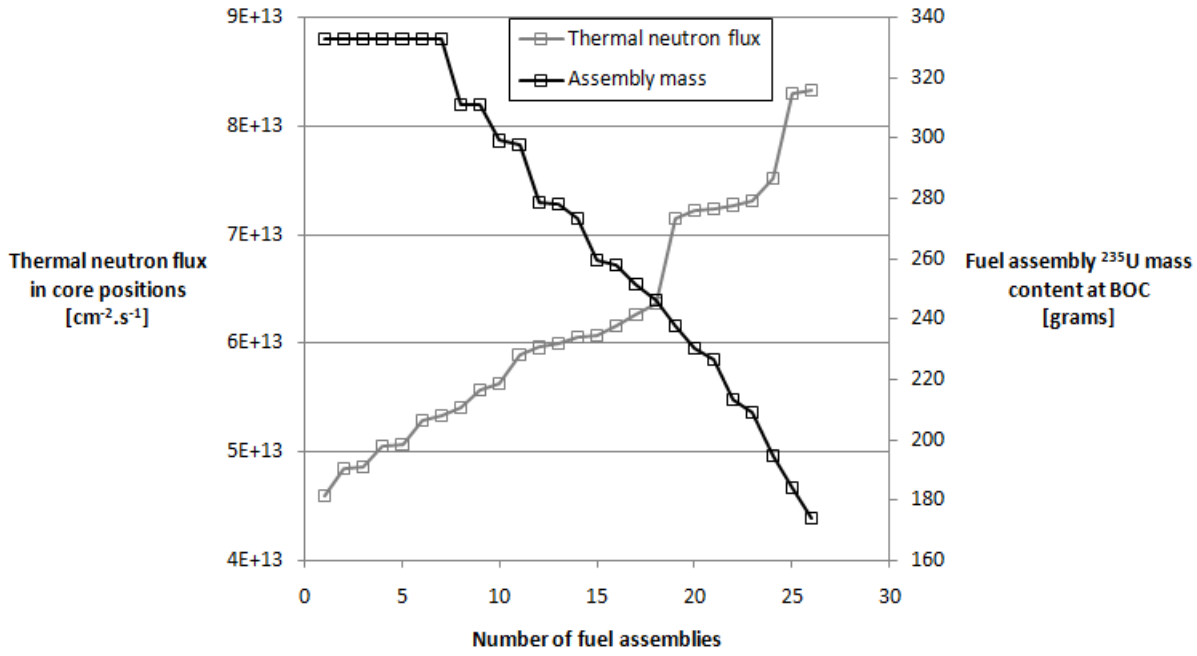

Figure 108 Relationship between the ^{235}U mass content and the thermal neutron flux within core positions as applied to the 8 by 9 core design.

Figure 109 ^{235}U mass distribution used to load the 8 by 9 core design.

Power [kW]

AF033L 606.0	BF037L 594.0	AF042L 602.0		AF029L 576.0	
	AF035L 588.0	AC004L 364.0	AF047L 676.0	AC006L 414.0	AF069L 656.0
BF004L 660.0	BF059L 604.0	BF048L 626.0		AF031L 652.0	
	BF051L 650.0	AC002L 388.0	AF030L 772.0	AC003L 404.0	AF068L 796.0
BF038L 688.0	BF057L 710.0	AF041L 760.0		AF037L 738.0	
	AF032L 682.0	AC001L 342.0	AF049L 752.0	AC005L 480.0	AF070L 750.0
AF054L 666.0	AF064L 690.0	AF065L 734.0	AF066L 712.0	AF067L 672.0	

Transverse Power Peaking Factor

0.97	0.95	0.96		0.92	
	0.94	0.58	1.08	0.66	1.05
1.06	0.97	1.00		1.04	
	1.04	0.62	1.23	0.65	1.27
1.10	1.14	1.22		1.18	
	1.09	0.55	1.20	0.77	1.20
1.07	1.10	1.17	1.14	1.07	

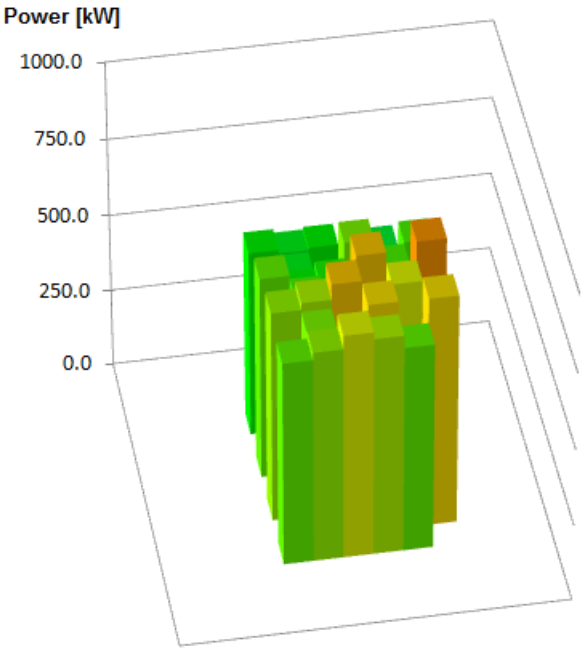

Figure 110 Core power distribution for the 8 by 9 core, for the most reactive cycle.

A5.2 OSCAR-4 axially averaged thermal neutron flux distribution

	1	2	3	4	5	6	7	8	9	10	11	12	13
A	1.04E+11	5.97E+11	2.07E+12	4.56E+12	7.18E+12	8.92E+12	8.91E+12	8.17E+12	6.37E+12	4.60E+12	2.34E+12	7.85E+11	1.66E+11
B	5.00E+11	4.42E+12	1.75E+13	3.19E+13	4.51E+13	5.40E+13	5.57E+13	5.17E+13	4.36E+13	3.25E+13	1.95E+13	5.58E+12	7.95E+11
C	1.42E+12	1.56E+13	5.50E+13	7.75E+13	8.18E+13	8.90E+13	1.01E+14	1.20E+14	8.86E+13	8.39E+13	6.28E+13	2.01E+13	2.47E+12
D	2.36E+12	2.49E+13	8.10E+13	1.08E+14	6.71E+13	6.16E+13	7.01E+13	1.89E+14	5.87E+13	1.33E+14	9.03E+13	3.61E+13	4.99E+12
E	3.02E+12	3.13E+13	1.03E+14	1.47E+14	1.94E+14	7.33E+13	6.83E+13	8.41E+13	5.50E+13	6.25E+13	1.08E+14	5.06E+13	7.51E+12
F	3.42E+12	3.55E+13	1.15E+14	1.56E+14	1.01E+14	8.23E+13	9.67E+13	2.61E+14	8.63E+13	2.03E+14	1.43E+14	6.27E+13	9.35E+12
G	3.62E+12	3.74E+13	1.23E+14	1.75E+14	2.31E+14	9.15E+13	9.06E+13	1.11E+14	7.98E+13	8.38E+13	1.45E+14	6.87E+13	1.04E+13
H	3.55E+12	3.67E+13	1.19E+14	1.63E+14	1.08E+14	8.47E+13	1.02E+14	3.03E+14	9.80E+13	2.36E+14	1.62E+14	7.07E+13	1.05E+13
I	3.11E+12	3.21E+13	1.06E+14	1.55E+14	2.17E+14	8.04E+13	8.96E+13	9.28E+13	7.27E+13	7.88E+13	1.30E+14	6.23E+13	9.32E+12
J	2.11E+12	2.25E+13	7.80E+13	1.09E+14	6.29E+13	6.29E+13	7.16E+13	7.13E+13	6.79E+13	1.11E+14	1.02E+14	4.34E+13	6.09E+12
K	9.00E+11	7.51E+12	3.09E+13	6.51E+13	9.70E+13	1.31E+14	1.50E+14	1.50E+14	1.27E+14	9.37E+13	5.07E+13	1.57E+13	2.57E+12
L	2.38E+11	1.42E+12	5.71E+12	1.53E+13	2.82E+13	3.99E+13	4.57E+13	4.52E+13	3.64E+13	2.24E+13	1.00E+13	3.08E+12	6.25E+11

Figure 111 Thermal flux-distribution (E_n<0.625 eV) for the 8 by 9 core, for the most reactive cycle. Values calculated over the active core region (±30 cm) with OSCAR4.

A5.3 MCNP5 In-core axially averaged thermal neutron flux distribution

	1	2	3	4	5	6	7	8	9	10	11	12	13
A	1.25E+11	5.77E+11	1.79E+12	4.08E+12	6.93E+12	9.09E+12	9.35E+12	8.54E+12	6.93E+12	4.68E+12	2.40E+12	9.16E+11	3.02E+11
B	4.41E+11	2.97E+12	1.14E+13	2.42E+13	3.86E+13	4.93E+13	5.21E+13	4.88E+13	3.92E+13	2.82E+13	1.55E+13	4.76E+12	9.44E+11
C	1.10E+12	9.29E+12	3.29E+13	5.49E+13	6.92E+13	8.40E+13	9.62E+13	1.11E+14	8.05E+13	7.21E+13	4.68E+13	1.59E+13	2.53E+12
D	1.71E+12	1.52E+13	4.96E+13	7.56E+13	6.14E+13	6.47E+13	7.75E+13	1.87E+14	6.44E+13	1.24E+14	7.44E+13	2.95E+13	4.86E+12
E	2.19E+12	1.93E+13	6.40E+13	1.08E+14	1.75E+14	8.35E+13	8.92E+13	9.09E+13	6.92E+13	6.18E+13	8.65E+13	4.19E+13	7.30E+12
F	2.52E+12	2.25E+13	7.26E+13	1.11E+14	9.66E+13	9.54E+13	1.16E+14	2.75E+14	1.00E+14	1.99E+14	1.22E+14	5.25E+13	9.01E+12
G	2.78E+12	2.40E+13	7.79E+13	1.30E+14	2.12E+14	1.07E+14	1.20E+14	1.22E+14	1.02E+14	8.43E+13	1.18E+14	5.75E+13	9.95E+12
H	2.79E+12	2.37E+13	7.57E+13	1.17E+14	1.03E+14	9.60E+13	1.19E+14	3.12E+14	1.12E+14	2.28E+14	1.37E+14	5.89E+13	9.89E+12
I	2.44E+12	2.08E+13	6.77E+13	1.17E+14	1.97E+14	9.09E+13	1.12E+14	1.02E+14	8.79E+13	7.84E+13	1.07E+14	5.24E+13	8.72E+12
J	1.73E+12	1.46E+13	4.97E+13	7.76E+13	5.73E+13	6.40E+13	7.39E+13	7.45E+13	7.15E+13	1.02E+14	8.70E+13	3.63E+13	5.89E+12
K	8.78E+11	5.49E+12	2.17E+13	5.22E+13	8.78E+13	1.25E+14	1.45E+14	1.47E+14	1.26E+14	8.92E+13	4.55E+13	1.39E+13	2.67E+12
L	3.87E+11	1.59E+12	5.51E+12	1.49E+13	2.85E+13	4.13E+13	4.78E+13	4.78E+13	3.89E+13	2.36E+13	1.07E+13	3.49E+12	9.40E+11

Figure 112 Thermal flux-distribution (E_n<0.625 eV) for the 8 by 9 core, for the most reactive cycle. Values calculated over the active core region (±30 cm) with MCNP5.

A5.4 MCNP5 In-core axially averaged epi-thermal neutron flux distribution

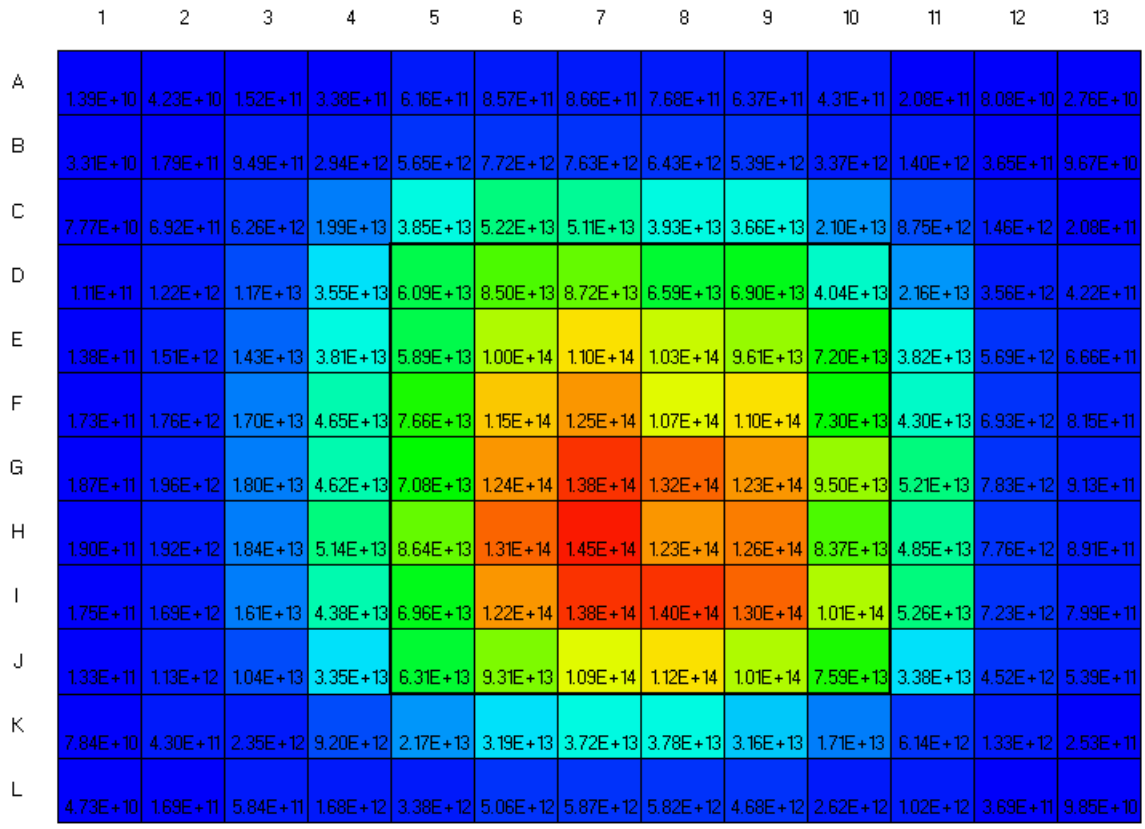

Figure 113 Epi-thermal flux-distribution (E_n>0.625 eV & E_n<100 keV) for the 8 by 9 core, for the most reactive cycle. Values calculated over the active core region (±30 cm) with MCNP5.

A5.5 MCNP5 In-core axially averaged fast neutron flux distribution

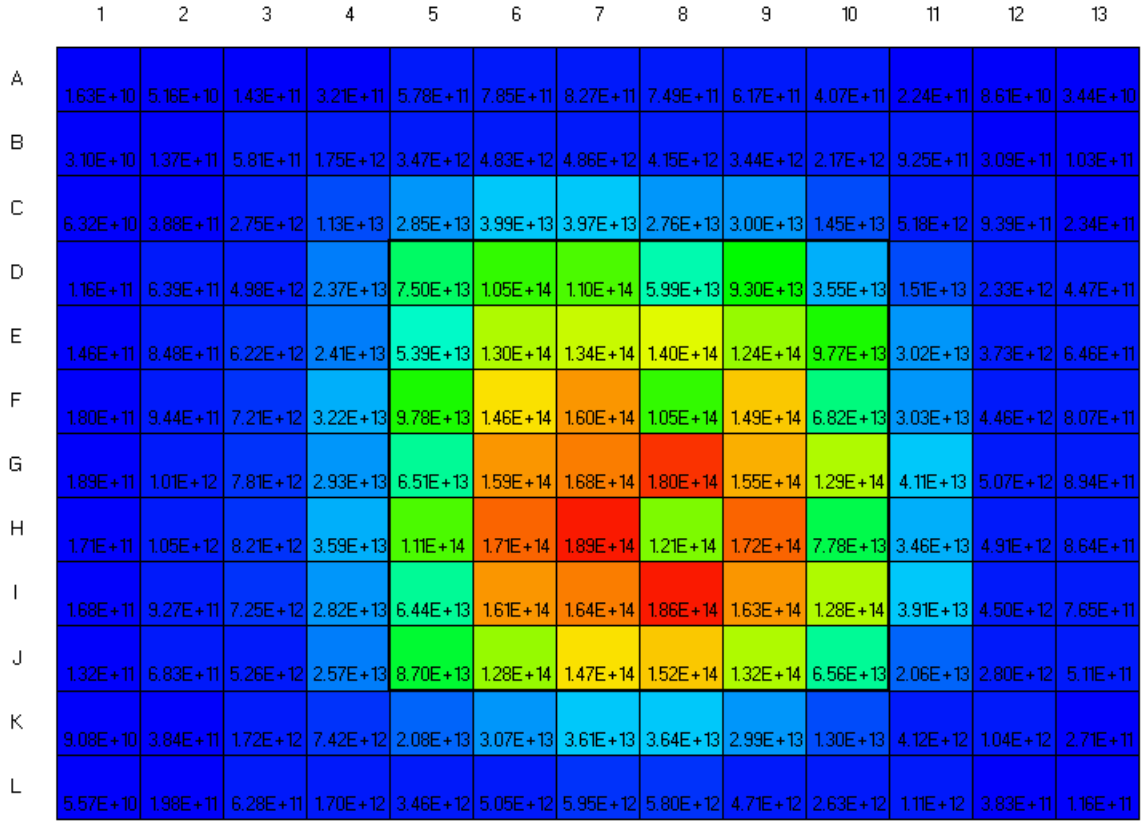

Figure 114 Fast flux-distribution (E_n>100 keV) for the 8 by 9 core, for the most reactive cycle. Values calculated over the active core region (±30 cm) with MCNP5.

A5.6 MCNP5 Thermal neutron beamline characteristics

Table 41 Numerical values for the output currents, for the 8 by 9 core, at the end of the thermal beamline. The currents only includes directional values within a 5° difference of the output normal.

Orientation Angles (degrees)	Thermal (E_n<0.625 eV)	Epi-thermal (E_n 0.625 eV to 100 keV)	Fast (E_n>100 keV)	Photons (Total)
90	3.002E+13	1.796E+13	2.004E+13	1.964E+14

A6 9 X 9 CORE WITH 19 IRRADIATION POSITIONS

The core configuration for this design is shown in the figure below:

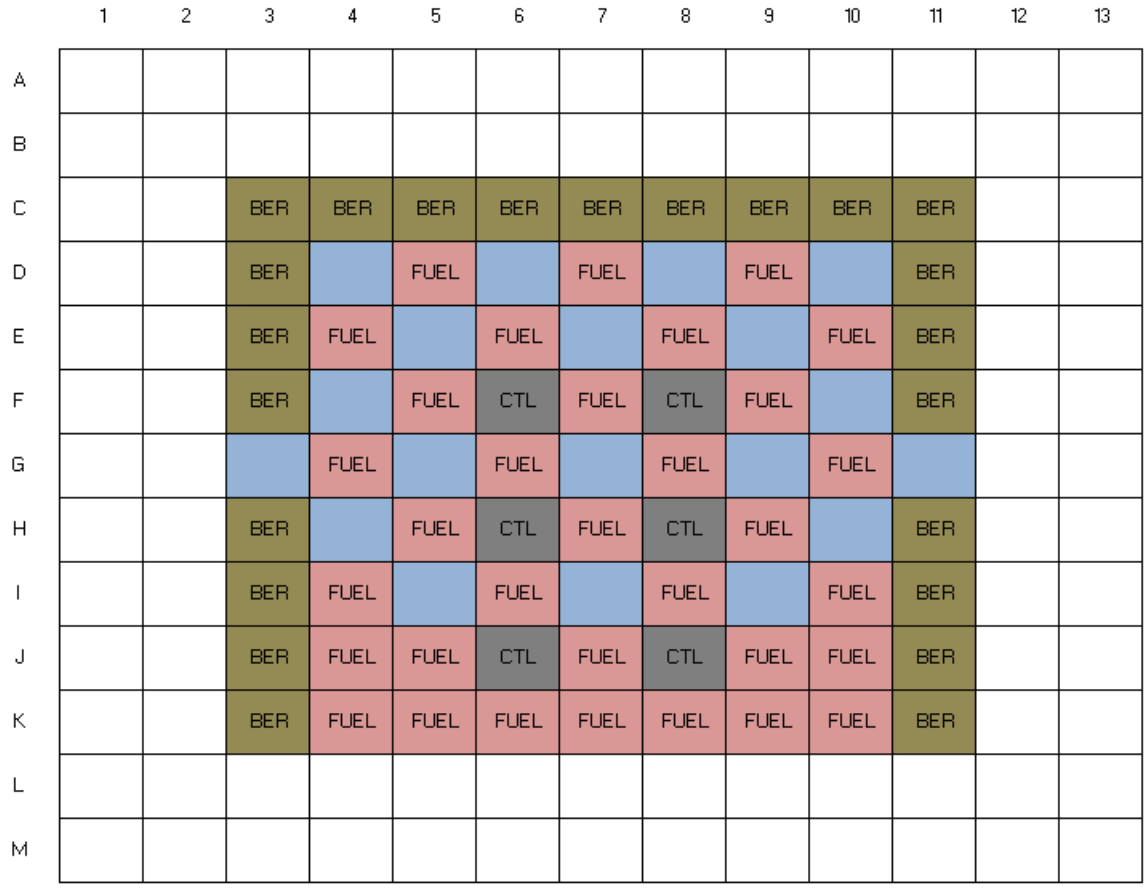

Figure 115 Diagram of a core design resembling that of the HFR Petten.

A6.1 Loading pattern and equilibrium core power distribution

Since the HFR Petten utilizes burnable absorbers, which fundamentally determines the loading strategy, the exact same loading pattern was not matched. Instead, the same loading strategy, as that for the 8 by 9 core design, was applied. The nominal relationship between the mass and the thermal flux is shown below:

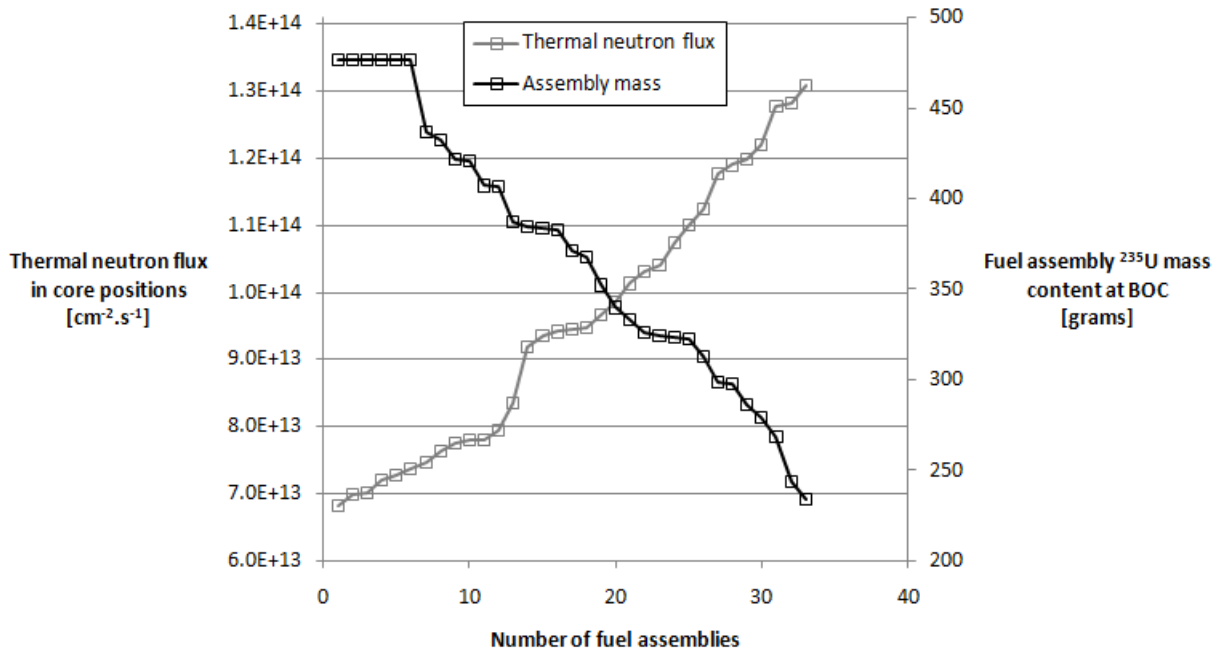

Figure 116 Relationship between the ^{235}U mass content and the thermal neutron flux within core positions as applied to the 9 by 9 core design.

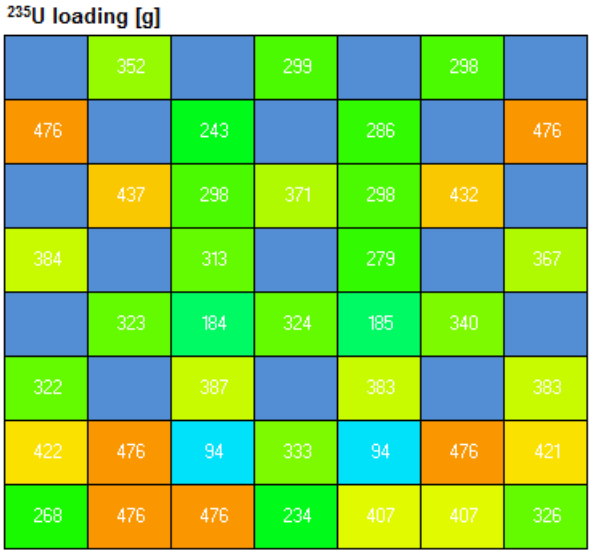

Figure 117 ^{235}U mass distribution used to load the 9 by 9 core design.

Power [kW]

	AF075L 1010.0		AF070L 1035.0		AF071L 905.0	
BF003L 1300.0		AF068L 1080.0		AF069L 1155.0		BF002L 1265.0
	AF089L 1630.0	ZC016L 865.0	AF086L 1530.0	ZC015L 855.0	AF088L 1600.0	
AF085L 1520.0		AF072L 1495.0		AF073L 1390.0		AF087L 1500.0
	AF078L 1720.0	ZC014L 740.0	AF081L 1710.0	ZC013L 750.0	AF079L 1810.0	
AF080L 1515.0		AF083L 1810.0		AF084L 1825.0		AF082L 1715.0
AF091L 1295.0	BF001L 1720.0	ZC012L 390.0	AF076L 1450.0	ZC011L 390.0	AF096L 1740.0	AF090L 1315.0
AF074L 895.0	AF095L 1325.0	AF094L 1395.0	AF067L 905.0	AF093L 1245.0	AF092L 1190.0	AF077L 1015.0

Transverse Power Peaking Factor

	0.79		0.81		0.71	
1.01		0.84		0.90		0.99
	1.27	0.67	1.19	0.67	1.25	
1.19		1.17		1.08		1.17
	1.34	0.58	1.33	0.59	1.41	
1.18		1.41		1.42		1.34
1.01	1.34	0.30	1.13	0.30	1.36	1.03
0.70	1.03	1.09	0.71	0.97	0.93	0.79

Power [kW]

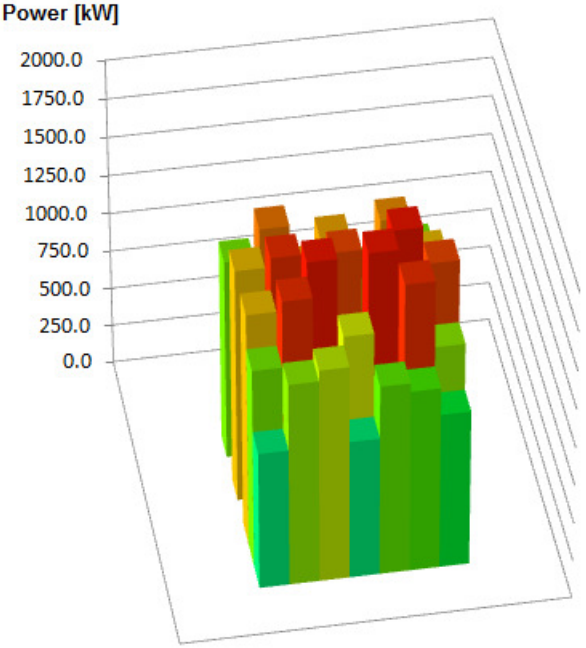

Figure 118 Core power distribution for the 9 by 9 core, for the most reactive cycle.

A6.2 OSCAR-4 axially averaged thermal neutron flux distribution

	1	2	3	4	5	6	7	8	9	10	11	12	13
A	2.74E+11	1.30E+12	3.82E+12	7.38E+12	9.81E+12	1.18E+13	1.15E+13	1.15E+13	9.35E+12	6.96E+12	3.61E+12	1.23E+12	2.61E+11
B	1.32E+12	9.22E+12	3.18E+13	5.19E+13	6.67E+13	7.51E+13	7.64E+13	7.35E+13	6.40E+13	4.94E+13	3.03E+13	8.80E+12	1.26E+12
C	4.16E+12	3.31E+13	1.01E+14	1.32E+14	1.32E+14	1.71E+14	1.51E+14	1.68E+14	1.29E+14	1.27E+14	9.70E+13	3.17E+13	4.00E+12
D	8.38E+12	5.96E+13	1.44E+14	2.12E+14	9.47E+13	2.78E+14	1.11E+14	2.72E+14	9.75E+13	2.04E+14	1.39E+14	5.76E+13	8.11E+12
E	1.22E+13	8.07E+13	1.67E+14	9.42E+13	3.21E+14	1.41E+14	3.58E+14	1.29E+14	3.14E+14	9.17E+13	1.63E+14	7.87E+13	1.19E+13
F	1.36E+13	9.25E+13	2.22E+14	3.19E+14	1.27E+14	1.05E+14	1.36E+14	1.04E+14	1.26E+14	3.15E+14	2.20E+14	9.12E+13	1.35E+13
G	1.49E+13	8.84E+13	2.52E+14	1.31E+14	4.27E+14	1.55E+14	4.91E+14	1.61E+14	4.28E+14	1.35E+14	2.55E+14	8.94E+13	1.51E+13
H	1.80E+13	1.21E+14	2.88E+14	3.98E+14	1.72E+14	1.41E+14	1.73E+14	1.42E+14	1.73E+14	4.11E+14	2.98E+14	1.26E+14	1.88E+13
I	2.21E+13	1.38E+14	2.56E+14	1.52E+14	5.04E+14	1.56E+14	5.24E+14	1.57E+14	5.16E+14	1.49E+14	2.65E+14	1.45E+14	2.33E+13
J	2.18E+13	1.35E+14	2.24E+14	1.03E+14	1.24E+14	1.55E+14	1.42E+14	1.55E+14	1.26E+14	1.05E+14	2.32E+14	1.42E+14	2.30E+13
K	1.59E+13	9.91E+13	1.91E+14	1.06E+14	9.60E+13	1.01E+14	1.22E+14	1.03E+14	9.85E+13	1.00E+14	1.96E+14	1.03E+14	1.68E+13
L	7.53E+12	4.37E+13	1.30E+14	2.05E+14	2.57E+14	2.68E+14	2.64E+14	2.58E+14	2.50E+14	2.05E+14	1.34E+14	4.57E+13	7.92E+12
M	2.03E+12	1.04E+13	3.15E+13	5.89E+13	7.96E+13	8.46E+13	8.26E+13	8.15E+13	7.70E+13	5.90E+13	3.26E+13	1.09E+13	2.14E+12

Figure 119 Thermal flux-distribution (E_n<0.625 eV) for the 9 by 9 core, for the most reactive cycle. Values calculated over the active core region (±30 cm) with OSCAR4.

A6.3 MCNP5 In-core axially averaged thermal neutron flux distribution

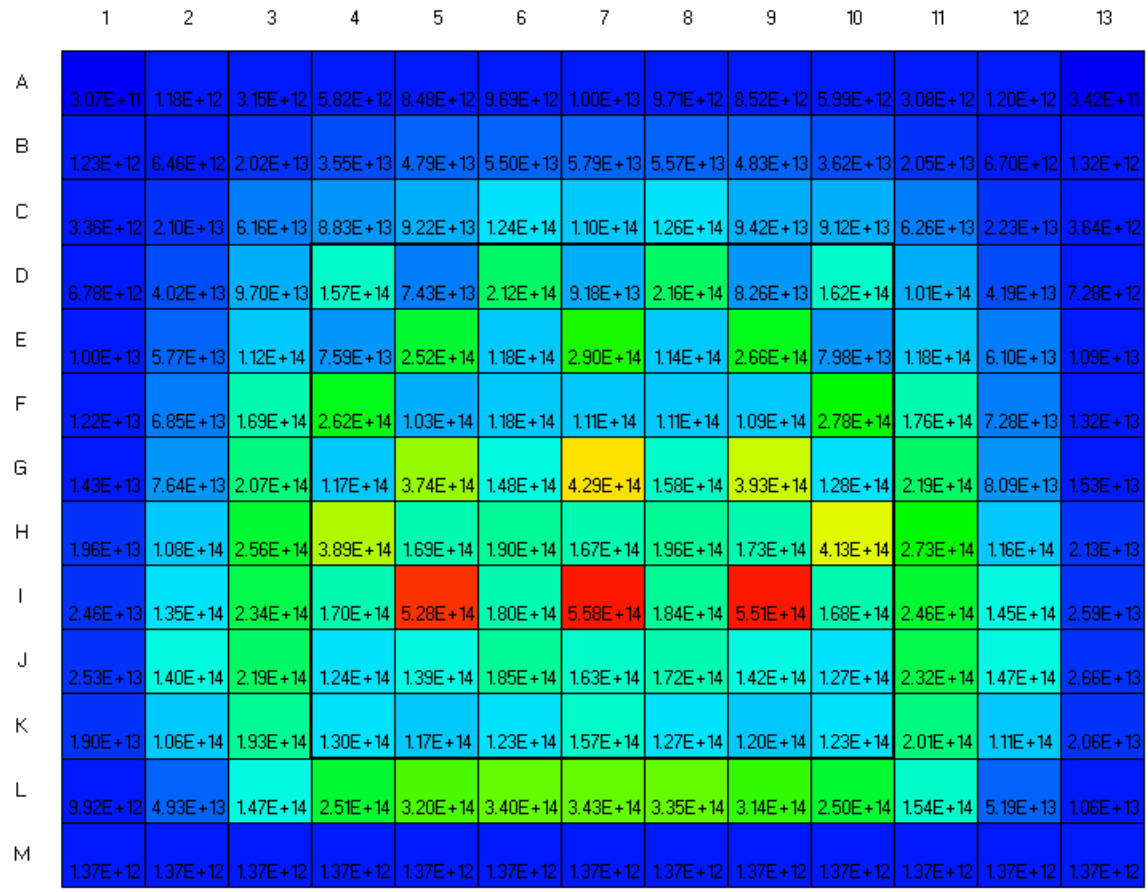

	1	2	3	4	5	6	7	8	9	10	11	12	13
A	3.07E+11	1.18E+12	3.15E+12	5.82E+12	8.48E+12	9.69E+12	1.00E+13	9.71E+12	8.52E+12	5.99E+12	3.08E+12	1.20E+12	3.42E+11
B	1.23E+12	6.46E+12	2.02E+13	3.55E+13	4.79E+13	5.50E+13	5.79E+13	5.57E+13	4.83E+13	3.62E+13	2.05E+13	6.70E+12	1.32E+12
C	3.36E+12	2.10E+13	6.16E+13	8.83E+13	9.22E+13	1.24E+14	1.10E+14	1.26E+14	9.42E+13	9.12E+13	6.26E+13	2.23E+13	3.64E+12
D	6.78E+12	4.02E+13	9.70E+13	1.57E+14	7.43E+13	2.12E+14	9.18E+13	2.16E+14	8.26E+13	1.62E+14	1.01E+14	4.19E+13	7.28E+12
E	1.00E+13	5.77E+13	1.12E+14	7.59E+13	2.52E+14	1.18E+14	2.90E+14	1.14E+14	2.66E+14	7.98E+13	1.18E+14	6.10E+13	1.09E+13
F	1.22E+13	6.85E+13	1.69E+14	2.62E+14	1.03E+14	1.18E+14	1.11E+14	1.11E+14	1.09E+14	2.78E+14	1.76E+14	7.28E+13	1.32E+13
G	1.43E+13	7.64E+13	2.07E+14	1.17E+14	3.74E+14	1.48E+14	4.29E+14	1.58E+14	3.93E+14	1.28E+14	2.19E+14	8.09E+13	1.53E+13
H	1.96E+13	1.08E+14	2.56E+14	3.89E+14	1.69E+14	1.90E+14	1.67E+14	1.96E+14	1.73E+14	4.13E+14	2.73E+14	1.16E+14	2.13E+13
I	2.46E+13	1.35E+14	2.34E+14	1.70E+14	5.28E+14	1.80E+14	5.58E+14	1.84E+14	5.51E+14	1.68E+14	2.46E+14	1.45E+14	2.59E+13
J	2.53E+13	1.40E+14	2.19E+14	1.24E+14	1.39E+14	1.85E+14	1.63E+14	1.72E+14	1.42E+14	1.27E+14	2.32E+14	1.47E+14	2.66E+13
K	1.90E+13	1.06E+14	1.93E+14	1.30E+14	1.17E+14	1.23E+14	1.57E+14	1.27E+14	1.20E+14	1.23E+14	2.01E+14	1.11E+14	2.06E+13
L	9.92E+12	4.93E+13	1.47E+14	2.51E+14	3.20E+14	3.40E+14	3.43E+14	3.35E+14	3.14E+14	2.50E+14	1.54E+14	5.19E+13	1.06E+13
M	1.37E+12	1.37E+12	1.37E+12	1.37E+12	1.37E+12	1.37E+12	1.37E+12	1.37E+12	1.37E+12	1.37E+12	1.37E+12	1.37E+12	1.37E+12

Figure 120 Thermal flux-distribution (E_n<0.625 eV) for the 9 by 9 core, for the most reactive cycle. Values calculated over the active core region (±30 cm) with MCNP5.

A6.4 MCNP5 In-core axially averaged epi-thermal neutron flux distribution

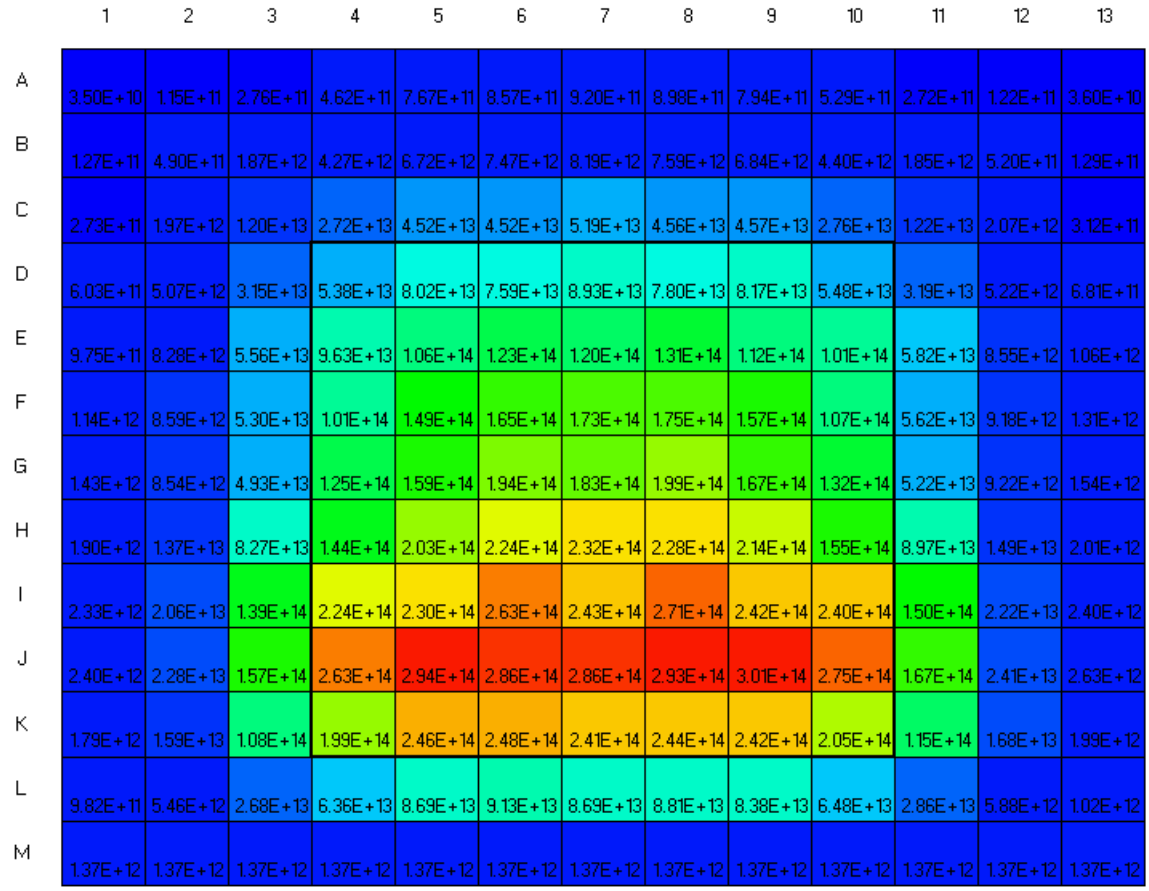

	1	2	3	4	5	6	7	8	9	10	11	12	13
A	3.50E+10	1.15E+11	2.76E+11	4.62E+11	7.67E+11	8.57E+11	9.20E+11	8.98E+11	7.94E+11	5.29E+11	2.72E+11	1.22E+11	3.60E+10
B	1.27E+11	4.90E+11	1.87E+12	4.27E+12	6.72E+12	7.47E+12	8.19E+12	7.59E+12	6.84E+12	4.40E+12	1.85E+12	5.20E+11	1.29E+11
C	2.73E+11	1.97E+12	1.20E+13	2.72E+13	4.52E+13	4.52E+13	5.19E+13	4.56E+13	4.57E+13	2.76E+13	1.22E+13	2.07E+12	3.12E+11
D	6.03E+11	5.07E+12	3.15E+13	5.38E+13	8.02E+13	7.59E+13	8.93E+13	7.80E+13	8.17E+13	5.48E+13	3.19E+13	5.22E+12	6.81E+11
E	9.75E+11	8.28E+12	5.56E+13	9.63E+13	1.06E+14	1.23E+14	1.20E+14	1.31E+14	1.12E+14	1.01E+14	5.82E+13	8.55E+12	1.06E+12
F	1.14E+12	8.59E+12	5.30E+13	1.01E+14	1.49E+14	1.65E+14	1.73E+14	1.75E+14	1.57E+14	1.07E+14	5.62E+13	9.18E+12	1.31E+12
G	1.43E+12	8.54E+12	4.93E+13	1.25E+14	1.59E+14	1.94E+14	1.83E+14	1.99E+14	1.67E+14	1.32E+14	5.22E+13	9.22E+12	1.54E+12
H	1.90E+12	1.37E+13	8.27E+13	1.44E+14	2.03E+14	2.24E+14	2.32E+14	2.28E+14	2.14E+14	1.55E+14	8.97E+13	1.49E+13	2.01E+12
I	2.33E+12	2.06E+13	1.39E+14	2.24E+14	2.30E+14	2.63E+14	2.43E+14	2.71E+14	2.42E+14	2.40E+14	1.50E+14	2.22E+13	2.40E+12
J	2.40E+12	2.28E+13	1.57E+14	2.63E+14	2.94E+14	2.86E+14	2.86E+14	2.93E+14	3.01E+14	2.75E+14	1.67E+14	2.41E+13	2.63E+12
K	1.79E+12	1.59E+13	1.08E+14	1.99E+14	2.46E+14	2.48E+14	2.41E+14	2.44E+14	2.42E+14	2.05E+14	1.15E+14	1.68E+13	1.99E+12
L	9.82E+11	5.46E+12	2.68E+13	6.36E+13	8.69E+13	9.13E+13	8.69E+13	8.81E+13	8.38E+13	6.48E+13	2.86E+13	5.88E+12	1.02E+12
M	1.37E+12	1.37E+12	1.37E+12	1.37E+12	1.37E+12	1.37E+12	1.37E+12	1.37E+12	1.37E+12	1.37E+12	1.37E+12	1.37E+12	1.37E+12

Figure 121 Epi-thermal flux-distribution (E_n>0.625 eV & E_n<100 keV) for the 9 by 9 core, for the most reactive cycle. Values calculated over the active core region (±30 cm) with MCNP5.

A6.5 MCNP5 In-core axially averaged fast neutron flux distribution

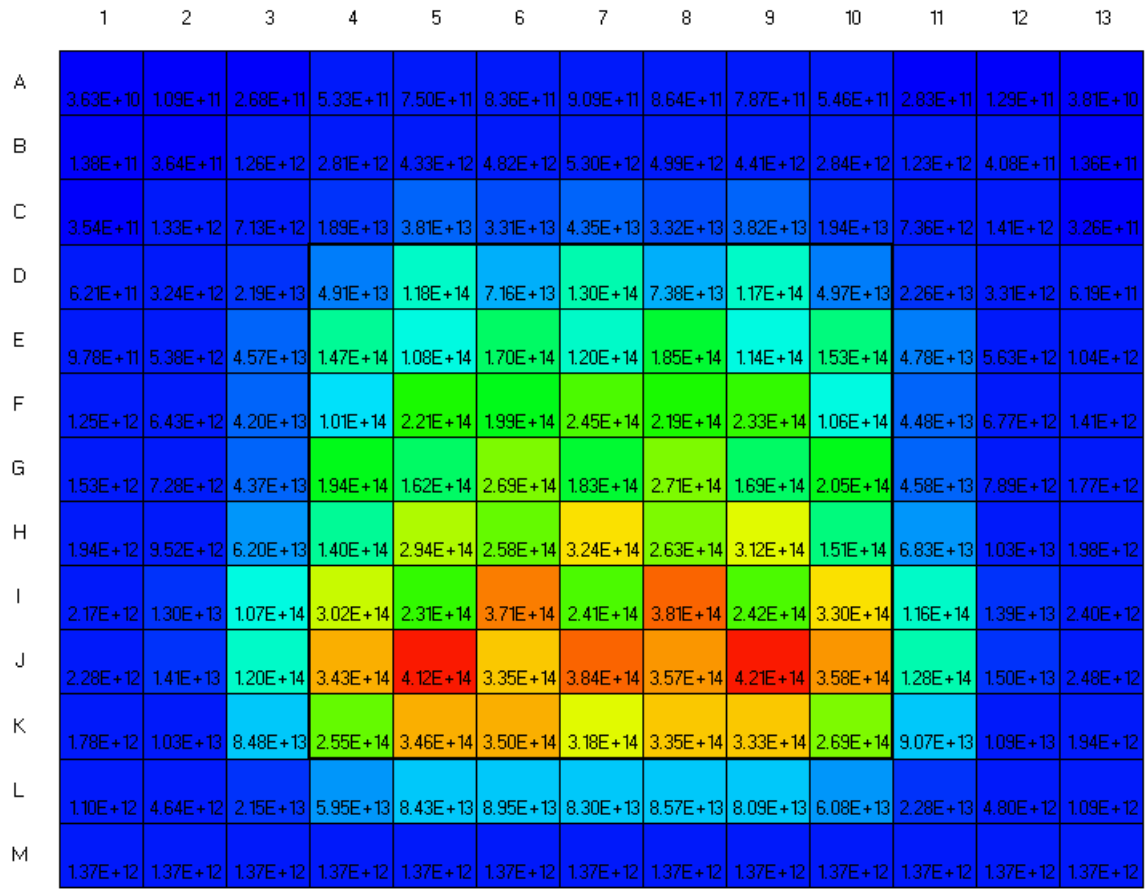

Figure 122 Fast flux-distribution (E_n>100 keV) for the 9 by 9 core, for the most reactive cycle. Values calculated over the active core region (±30 cm) with MCNP5.

A6.6 MCNP5 Thermal neutron beamline characteristics

Table 42 Numerical values for the output currents, for the 9 by 9 core, at the end of the thermal beamline. The currents only includes directional values within a 5° difference of the output normal.

Orientation Angles (degrees)	Thermal (E_n<0.625 eV)	Epi-thermal (E_n 0.625 eV to 100 keV)	Fast (E_n>100 keV)	Photons (Total)
90	1.722E+13	8.075E+12	1.006E+13	1.364E+14

ANNEXURE B. COLD NEUTRON SOURCE VOLUME

In order to assess the optimal volume to use as a cold-neutron source; a hydrogen (H_2), cylindrical source was modelled in the peak neutron flux region of a 5 by 5 core design with 4 in-core irradiation positions. The cylinder was modelled with a height to diameter ratio equal to unity. The hydrogen material was specified with S(α,β)-treatments for a mixture of 50% para-hydrogen and 50% ortho-hydrogen.

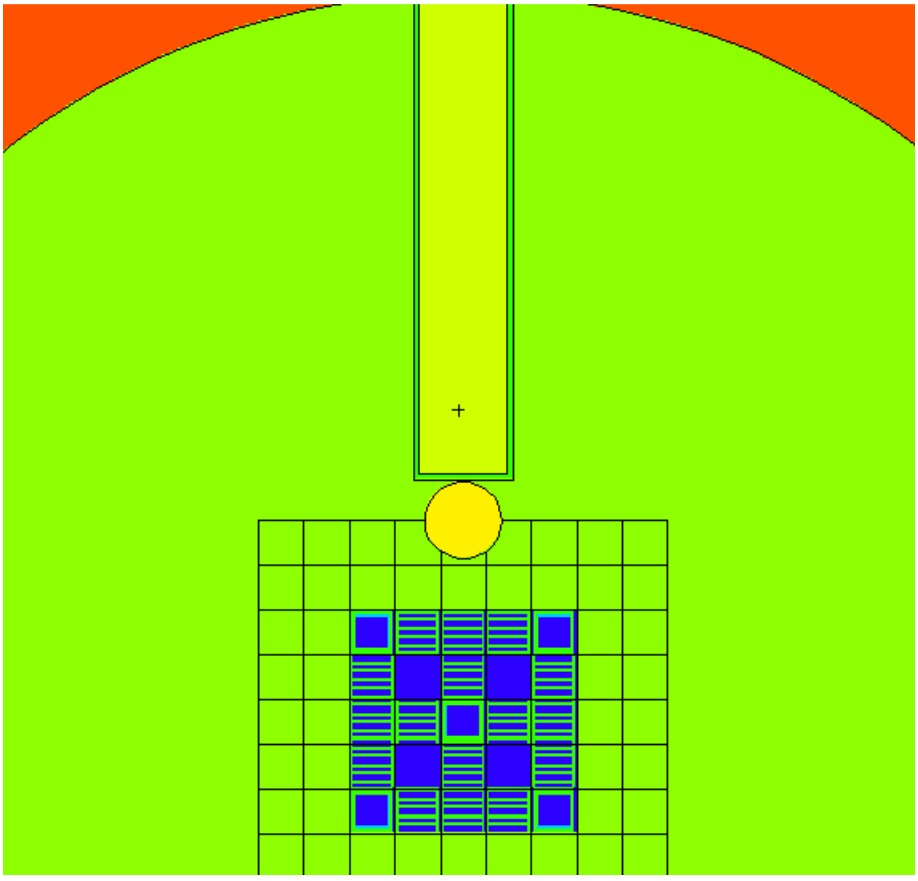

Figure 123 Visualization of the MCNP model used to evaluate the optimal liquid H_2 cold-neutron source.

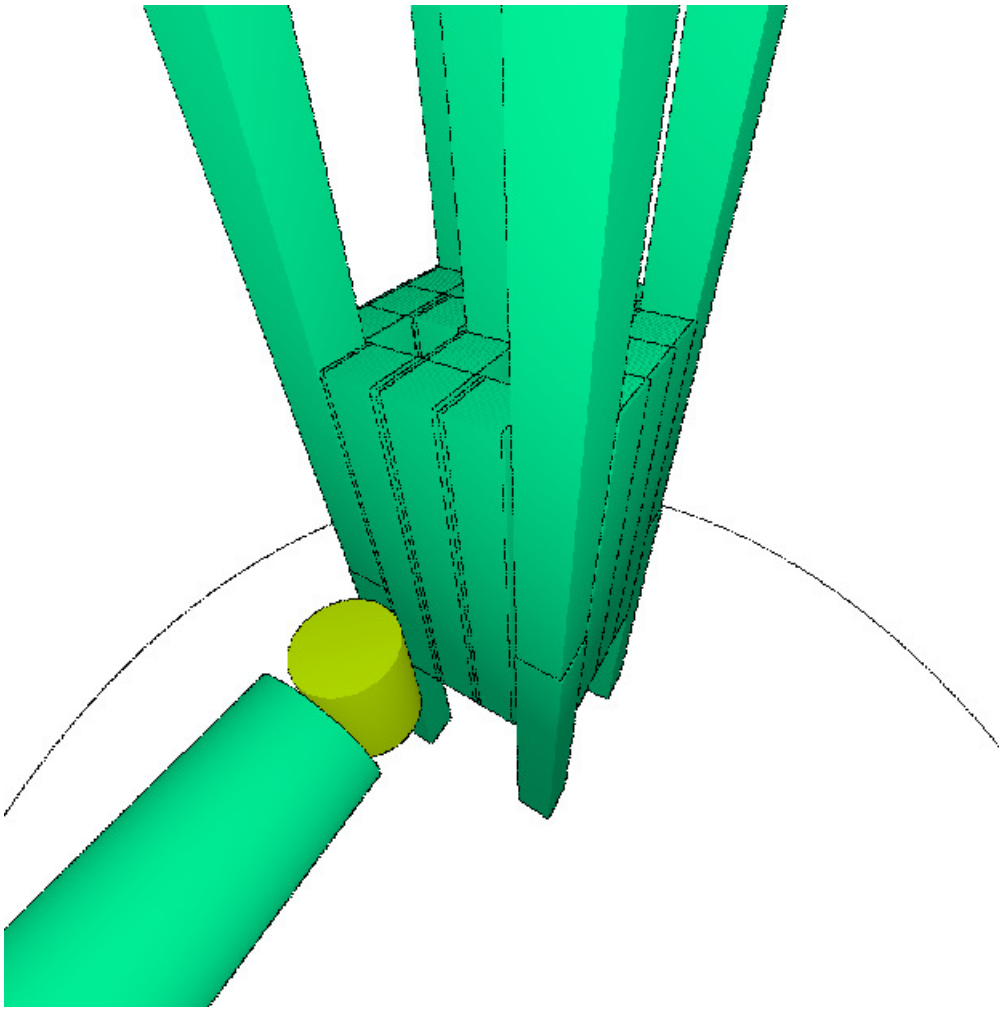

Figure 124 Three-dimensional visualization of the MCNP5 model used to model a cold neutron source.

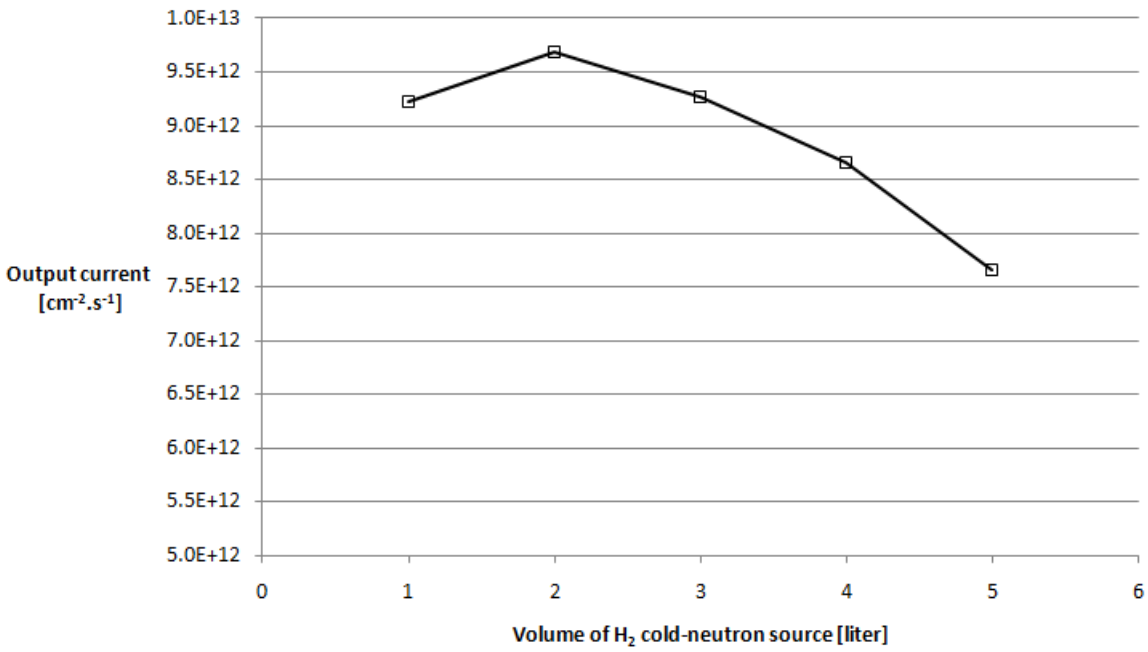

Figure 125 Output current of cold-neutrons for varying volumes of liquid H_2.

In this figure the optimal source volume was shown to be approximately 2 litres (2000 cm^3).

ANNEXURE C. HEADE ENERGY GROUP STRUCTURES

Table 43 Energy group structure used by the fine-group collision probabilities code HEADE.

Group	Upper Boundary [eV]	Lower Boundary [eV]	Group	Upper Boundary [eV]	Lower Boundary [eV]	Group	Upper Boundary [eV]	Lower Boundary [eV]
1	1.96E+07	1.73E+07	59	7.49E+02	6.77E+02	117	1.15E+00	1.13E+00
2	1.73E+07	1.49E+07	60	6.77E+02	4.54E+02	118	1.13E+00	1.11E+00
3	1.49E+07	1.38E+07	61	4.54E+02	3.72E+02	119	1.11E+00	1.10E+00
4	1.38E+07	1.16E+07	62	3.72E+02	3.04E+02	120	1.10E+00	1.07E+00
5	1.16E+07	1.00E+07	63	3.04E+02	2.04E+02	121	1.07E+00	1.05E+00
6	1.00E+07	8.19E+06	64	2.04E+02	1.49E+02	122	1.05E+00	1.04E+00
7	8.19E+06	6.70E+06	65	1.49E+02	1.37E+02	123	1.04E+00	1.02E+00
8	6.70E+06	6.07E+06	66	1.37E+02	9.17E+01	124	1.02E+00	9.96E-01
9	6.07E+06	5.49E+06	67	9.17E+01	7.57E+01	125	9.96E-01	9.86E-01
10	5.49E+06	4.49E+06	68	7.57E+01	6.79E+01	126	9.86E-01	9.72E-01
11	4.49E+06	3.68E+06	69	6.79E+01	5.56E+01	127	9.72E-01	9.50E-01
12	3.68E+06	3.01E+06	70	5.56E+01	5.16E+01	128	9.50E-01	9.30E-01
13	3.01E+06	2.47E+06	71	5.16E+01	4.83E+01	129	9.30E-01	9.10E-01
14	2.47E+06	2.23E+06	72	4.83E+01	4.55E+01	130	9.10E-01	8.60E-01
15	2.23E+06	2.02E+06	73	4.55E+01	4.02E+01	131	8.60E-01	8.50E-01
16	2.02E+06	1.65E+06	74	4.02E+01	3.73E+01	132	8.50E-01	7.90E-01
17	1.65E+06	1.35E+06	75	3.73E+01	3.37E+01	133	7.90E-01	7.80E-01
18	1.35E+06	1.22E+06	76	3.37E+01	3.05E+01	134	7.80E-01	7.05E-01
19	1.22E+06	1.11E+06	77	3.05E+01	2.76E+01	135	7.05E-01	6.25E-01
20	1.11E+06	1.00E+06	78	2.76E+01	2.50E+01	136	6.25E-01	5.40E-01
21	1.00E+06	9.07E+05	79	2.50E+01	2.26E+01	137	5.40E-01	5.00E-01
22	9.07E+05	8.21E+05	80	2.26E+01	1.95E+01	138	5.00E-01	4.85E-01
23	8.21E+05	6.08E+05	81	1.95E+01	1.59E+01	139	4.85E-01	4.33E-01
24	6.08E+05	5.50E+05	82	1.59E+01	1.37E+01	140	4.33E-01	4.00E-01
25	5.50E+05	4.98E+05	83	1.37E+01	1.12E+01	141	4.00E-01	3.91E-01
26	4.98E+05	4.50E+05	84	1.12E+01	9.91E+00	142	3.91E-01	3.50E-01
27	4.50E+05	4.08E+05	85	9.91E+00	9.19E+00	143	3.50E-01	3.20E-01
28	4.08E+05	3.02E+05	86	9.19E+00	8.32E+00	144	3.20E-01	3.15E-01
29	3.02E+05	2.73E+05	87	8.32E+00	7.52E+00	145	3.15E-01	3.00E-01
30	2.73E+05	2.47E+05	88	7.52E+00	6.16E+00	146	3.00E-01	2.80E-01
31	2.47E+05	1.83E+05	89	6.16E+00	5.35E+00	147	2.80E-01	2.48E-01
32	1.83E+05	1.23E+05	90	5.35E+00	5.04E+00	148	2.48E-01	2.20E-01
33	1.23E+05	1.11E+05	91	5.04E+00	4.13E+00	149	2.20E-01	1.89E-01
34	1.11E+05	8.23E+04	92	4.13E+00	4.00E+00	150	1.89E-01	1.80E-01

35	8.23E+04	6.74E+04	93	4.00E+00	3.38E+00	151	1.80E-01	1.60E-01
36	6.74E+04	5.52E+04	94	3.38E+00	3.30E+00	152	1.60E-01	1.40E-01
37	5.52E+04	4.09E+04	95	3.30E+00	2.77E+00	153	1.40E-01	1.34E-01
38	4.09E+04	3.70E+04	96	2.77E+00	2.72E+00	154	1.34E-01	1.15E-01
39	3.70E+04	2.93E+04	97	2.72E+00	2.60E+00	155	1.15E-01	1.00E-01
40	2.93E+04	2.74E+04	98	2.60E+00	2.55E+00	156	1.00E-01	9.50E-02
41	2.74E+04	2.48E+04	99	2.55E+00	2.36E+00	157	9.50E-02	8.00E-02
42	2.48E+04	1.66E+04	100	2.36E+00	2.13E+00	158	8.00E-02	7.70E-02
43	1.66E+04	1.50E+04	101	2.13E+00	2.10E+00	159	7.70E-02	6.70E-02
44	1.50E+04	1.11E+04	102	2.10E+00	2.02E+00	160	6.70E-02	5.80E-02
45	1.11E+04	9.12E+03	103	2.02E+00	1.93E+00	161	5.80E-02	5.00E-02
46	9.12E+03	7.47E+03	104	1.93E+00	1.84E+00	162	5.00E-02	4.20E-02
47	7.47E+03	5.53E+03	105	1.84E+00	1.76E+00	163	4.20E-02	3.50E-02
48	5.53E+03	5.00E+03	106	1.76E+00	1.67E+00	164	3.50E-02	3.00E-02
49	5.00E+03	3.53E+03	107	1.67E+00	1.59E+00	165	3.00E-02	2.50E-02
50	3.53E+03	3.35E+03	108	1.59E+00	1.50E+00	166	2.50E-02	2.00E-02
51	3.35E+03	2.25E+03	109	1.50E+00	1.48E+00	167	2.00E-02	1.50E-02
52	2.25E+03	2.03E+03	110	1.48E+00	1.45E+00	168	1.50E-02	1.00E-02
53	2.03E+03	1.51E+03	111	1.45E+00	1.37E+00	169	1.00E-02	6.90E-03
54	1.51E+03	1.43E+03	112	1.37E+00	1.34E+00	170	6.90E-03	5.00E-03
55	1.43E+03	1.23E+03	113	1.34E+00	1.30E+00	171	5.00E-03	3.00E-03
56	1.23E+03	1.01E+03	114	1.30E+00	1.24E+00	172	3.00E-03	1.00E-05
57	1.01E+03	9.14E+02	115	1.24E+00	1.17E+00			
58	9.14E+02	7.49E+02	116	1.17E+00	1.15E+00			

Table 44 Energy group structure used by the intermediate energy group collision probabilities code STYX.

Group	Upper Boundary [eV]	Lower Boundary [eV]	Group	Upper Boundary [eV]	Lower Boundary [eV]	Group	Upper Boundary [eV]	Lower Boundary [eV]
1	1.96E+07	2.23E+06	9	2.76E+01	9.91E+00	17	4.00E-01	3.00E-01
2	2.23E+06	8.21E+05	10	9.91E+00	4.00E+00	18	3.00E-01	2.48E-01
3	8.21E+05	6.74E+04	11	4.00E+00	2.10E+00	19	2.48E-01	1.40E-01
4	6.74E+04	5.53E+03	12	2.10E+00	1.13E+00	20	1.40E-01	5.00E-02
5	5.53E+03	1.43E+03	13	1.13E+00	9.72E-01	21	5.00E-02	4.20E-02
6	1.43E+03	3.72E+02	14	9.72E-01	9.10E-01	22	4.20E-02	2.50E-02
7	3.72E+02	7.57E+01	15	9.10E-01	6.25E-01	23	2.50E-02	1.50E-02
8	7.57E+01	2.76E+01	16	6.25E-01	4.00E-01	24	1.50E-02	1.00E-05

Table 45 Energy groups used for the generation of homogenized few-group (6 groups) cross-sections by the HEADE code.

Group	Upper Boundary [eV]	Lower Boundary [eV]
1	1.96E+07	8.21E+05
2	8.21E+05	5.53E+03
3	5.53E+03	4.00E+00
4	4.00E+00	6.25E-01
5	6.25E-01	1.40E-01
6	1.40E-01	1.10E-04

BIBLIOGRAPHY

Ahmed, R., Aslam & Ahmad, N., 2005. Effect of high-density fuel loading on criticality of low enriched Uranium fueled material test research reactors. *Annals of Nulcear Energy*, 32(1), pp.29-62.

ANL, 2012. *Reduced Enrichment for Research and Test Reactors (RERTR) [Nonproliferation]*. [Online] Available at: http://www.rertr.anl.gov/ [Accessed 3 May 2012].

Bakkari et al., 2010. Monte Carlo modeling of TRIGA research reactor. *Radiation Physics and Chemistry*, 79(1), pp.1022-30.

Ball, G. & Weiss, Z.J., 1993. STYX-I: A Benchmarking Program for Neutron Transport Calculations in Fuel-Assembly Type Geometries. *Annals of Nuclear Energy*, 20, pp.59-70.

Benham, P.P., Crawford, R.J. & Armstrong, C.G., 1996. *Mechanics of Engineering Materials*. 2nd ed. Essex: Pearson Prentice Hall.

Bergles AE, R.W., 1964. The determination of forced convective surface boiling heat transfer. *Journal of Heat Transfer, ASME*, 86(Series C), p.365.

Cengel, Y.A., 2006. *Heat and Mass Transfer*. Third (SI units) ed. McGraw-Hill.

D'Arcy A.J., J.E., 2010. Theoretical ageing assessment of the SAFARI-1 core structure. *NECSA*.

De Beer, F.C., 2005. Characteristics of the neutron/X-ray tomography system at the SANRAD facility in South Africa. *Nuclear Instruments and Methods in Physics Research*, A(542), pp.1-8.

De Beer, F.C. et al., 2009. Archaeology benefits from neutron tomography investigations in South Africa. *Nuclear Instruments and Methods in Physics Research*, A(605), pp.167-70.

Duderstadt, J.J. & Hamilton, L.J., 1976. *Nuclear Reactor Analysis*. John Wiley & Sons.

Finlay, M.R., Hofman, G.L. & Snelgrove, J.L., 2004. Irradiation behaviour of Uranium Silicide compounds. *Journal of Nuclear Materials*, 325(1), pp.118-28.

Flocchini, H., Liu, H. & Boussoufi, M., 2007. *Development of a Large-Field Cold Neutron Source at the University of California, Davis, McClellan Nuclear Radiation Center (UCD-MNRC)*. Project report. California: University of California.

Hyde, T.H., Luo, R. & Becker, A.A., 2005. Elastic–plastic response of unpressurised pipes subjected to axially-long radial indentation. *International Journal of Mechanical Sciences*, (47), pp.1949-71.

IAEA Safety Standards Series NS-R-4, 2005. *NS-R-4 Safety standards series*. Safety Series. Vienna: IAEA International Atomic Energy Agency.

IAEA-RRDB, 2011. *Research Reactor Databases - IAEA NEFW*. [Online] Available at: http://www.iaea.org/OurWork/ST/NE/NEFW/Technical_Areas/RRS/databases.html [Accessed 3 May 2012].

IAEA-TECDOC-133, 1980. *Research Reactor Core Conversions from the use of highly enriched Uranium to the use of low enriched Uranium fuels - Guidebook*. Vienna: International Atomic Energy Agency.

IAEA-TECDOC-643, 1992. *Research reactor core conversion guidebook Volumes 1 to 5*. Vienna: IAEA.

Irwin, A. & De Lorenzo, N., 2007. OPAL: Commissioning a New Research Reactor.

Joubert, W.R. & Weiss, Z.J., 1992. A Nodal Solution of the Interface Current Equations. In *Proceeding of the Top Meeting Advances in Reactor Physics*. Charleton USA, 1992.

Kahn, L.H., 2008. The potential dangers in medical isotope production. *Bulletin of the atomic scientists*.

Kasai, H., Dino, W.A. & Muhida, R., 2003. Surface science-based reaction design: Increasing the ortho-para hydrogen conversion yield via molecular orientation, a case study. *Progress in Surface Science*, (72), pp.53-86.

Kim, H.K. et al., 1997. Characterization of U-2 wt% Mo and U-10 wt% Mo alloy powders prepared by centrifugal atomization. *Journal of Nuclear Materials*, 245(1), pp.179-84.

Lamarsh, J.R. & Baratha, A.J., 2001. *Introduction to Nuclear Engineering*. Third Edition ed. Prentice Hall.

MCNP5: MCNP. X-5 Monte Carlo Team, 2003. *A General Monte Carlo N-Particle Transport Code, Version 5, LA-UR-03-1987*. Los Alamos National Laboratory.

Miller, D.R., 1958. *KAPL-1954 Critical flow velocities for collapse of reactor parallel-plate fuel assemblies*. Knolls Atomic Power Laboratory.

NECSA - Research and Development, n.d. *Feasibility study for a new large neutron source for NECSA*.

NUREG-1313, 1988. *Safety Evaluation Report related to the evaluation of Low-Enriched Uranium Silicide-Aluminium dispersion fuel for use in Non-Power Reactors.* United States Nuclear Regulatory Commission.

Ooi, M. et al., 2006. Measurements of the change of neutronic performance of a hydrogen moderator at Manuel Lujan Neutron Scattering Center due to conversion from ortho- to para-hydrogen state. *Nuclear Instruments and Methods in Physics Research*, A(566), pp.699-705.

RR-SAR-0005, 2008. *SAFARI-1 Safety Analysis Report, Chapter 5:Description of the SAFARI-1 Reactor*. Pretoria: NECSA.

RR-TGL-1103, 2003. *Material specification: Low neutron poison Aluminium extrusion alloy plates and sheets.* Pretoria: NECSA.

Shen, F. & Yuan, L., 2002. Conceptual study of cold-neutron source in China Advanced Research Reactor. *Physics*, B(311), pp.152-57.

Sinha, V.P. et al., 2008. Development of powder metallurgy technique for synthesis of U3Si2 dispersoid. *Journal of Nuclear Materials*, 383(1), pp.196-200.

Stander, G. & et.al., 2008. OSCAR-4 Code System Application to the SAFARI-1 Reactor. In *International Conference on Reactor physics, Nuclear Power: A Sustainable Resource, PHYSOR2008.* Interlaken, Switzerland, 2008.

Thijssen, P.J.M., 2006. HEU/LEU Conversion of the Petten HFR. *Transactions of the 10th International Topical Meeting on Research Reactor Fuel Management*, I(1), pp.250-54.

Vogel, D.L. & Weiss, Z.J., 2011. A General, Multigroup Formulation of the Analytical Nodal Method. In *International Topical Meeting on Advances in Research Reactor Physics*. Charleston USA, 2011.

Wikipedia, 2011. *Beamline*. [Online] Available at: http://en.wikipedia.org/wiki/Beamline [Accessed 3 October 2011].

Xoubi N., P.R.T., 2004. *ORNL/TM-2004/251, Modelling of the High Flux Isotope Reactor Cycle 400*. UT-Batelle.